Modelling of the cavitating propeller noise by means of semi-empirical and data driven approaches

By
Leonardo Miglianti

Supervised by
prof. Michele Viviani
dr. Giorgio Tani

A thesis presented for the degree of
Doctor of Philosophy

**UNIVERSITÀ DEGLI STUDI
DI GENOVA**

Electrical, Electronics and Telecommunication Engineering
and Naval Architecture Department (DITEN)

University of Genoa, Italy

28 April 2020

This page was intentionally left blank.

Abstract

Historically, the mitigation of the ship radiated noise in the water was a prerogative of naval ships due to quiet requirements. In the last decades, the need for merchant ships and pleasure craft to ensure high standards of comfort on board in terms of on board radiated noise and structural vibrations lead also, indirectly, towards the reduction of underwater radiated noise. Nowadays, the greater awareness about the damages to the marine ecosystem as a result of the ship noise pollution is leading governments and international institutions towards the study of possible limits to acoustic emissions, which could be applied, to different levels, to protected marine areas and to more general navigation routes.

Propeller, when cavitating, is the main source of radiated noise for conventional ships together with the engines; propeller cavitation, contrarily to machinery, is not linked to single frequencies, being a broadband noise. Its reduction is thus becoming one of the objectives in new propellers design. One of the most effective and common way to assess the propeller cavitation noise is by experimental tests in model scale. This procedure is rather expensive and time consuming, thus it is rather difficult to include it in an iterative design loop.

The aim of the present PhD thesis is the development of semi-empirical methods for the prediction of the propeller cavitating noise, in order to provide the designer with a tool capable of allowing prediction of underwater radiated noise at early design stages. Moreover, the same method can be applied in order to enhance the capability of prediction of underwater radiated noise from model scale tests, allowing to obtain indications also for operating conditions not directly reproducible due to scaling effects.

Attention has been devoted to the most common cavitation phenomena, i.e. back sheet cavitation and tip vortex.

The considered methods are derived from physical formulations available in literature and purely data driven models coming from the machine learning field, exploiting also the advantages of their combination in hybrid models. In order to build and test the noise models, a dataset of propeller cavitating noise has been collected and processed, including relevant information on the input characteristics (i.e. propeller geometry, working point, ship wake description) and corresponding radiated noise. The experimental campaigns have been performed at the cavitation tunnel of the University of Genoa, considering three controllable pitch propellers in twin screw configuration. The dataset has been exploited to build different models of increasing complexity, to predict the radiated noise spectrum.

The methodologies proposed allowed to obtain encouraging results providing a valuable basis for further investigations and developments of this approach.

This page was intentionally left blank.

Acknowledgements

I would like to thank my tutors Michele Viviani and especially Giorgio Tani, who have made this long journey possible. I wish to express my gratitude to Fincantieri MM-ARC office in Genoa, in particular Francesco Conti and Ottavio Pinto, which kindly provided the propeller models used in this work.

I would like to acknowledge Prof. Luca Oneto and Eng. Francesca Cipollini for the fundamental contribution in the understanding and the development of the machine learning methods, and into have forced me to learn the art of writing with LaTeX.

My sincere thanks also go to Prof. Stefano Gaggero who kindly carried out the BEM computations exploited in this thesis. Lastly, I would to thank Dr. Mario Felli for his assistance.

This page was intentionally left blank.

Contents

This page was intentionally left blank.

List of Figures

This page was intentionally left blank.

List of Tables

List of Symbols

Acronyms

ADDM	Advanced Data Driven Model	
BAR	Blade Area Ratio	
BEM	Boundary Element Method	
BP1	Break Point 1	
BP2	Break Point 2	
BPF	Blade Passage Frequency	Hz
BTS	Bootstrap	
CDDM	Conventional Data Driven Model	
CFD	Computational Fluid Dynamics	
CI	Confidence Interval	
CPP	Controllable Pitch Propeller	
D. TVC	Detached Tip Vortex Cavitation	
DDDM	Deep Data Driven Model	
DDES	Detached Eeddy Simulation	
DDM	Data Driven Model	
DES	Design	
DNN	Deep Neural Network	
ELM	Extreme Learning Machine	
ERM	Empirical Risk Minimisation	
FM	Feature Map	
FR	Feature Ranking	
FS	Feature Set	
FS	Full Scale	
HM	Hybrid Model	
HSV	High Speed Videos	
HUB VC	Stable Hub Vortex Cavitation	
IMO	International Maritime Organization	
INT HUB VC	Intermittent Hub Vortex Cavitation	
ITTC	International Towing Tank Conference	
KRLS	Kernel Regularized Least Squares	

LDV	Laser Doppler Velocimetry	
LES	Large Eddy Simulation	
MAE	Mean Absolute Error	
MAPE	Mean Absolute Percentage Error	
ML	Machine Learning	
MS	Model Scale	
MS	Model Selection	
MST	Model Scale Test	
N-S	Navier-Stokes equations	
NSP	Noise Spectrum Parametrization	
OTO	One-Third Octave	
P.S.	Pressure Side	
P.S. RB	Pressure Side Root Bubbles	
P.S. S	Pressure Side Sheet	
P.S. TVC	Pressure Side Tip Vortex Cavitation	
PM	Physical Model	
PPMCC	Pearson Product-Moment Correlation Coefficient	
RANSE	Reynolds Averaged Navier-Stokes Equations	
RelPre	tunnel Relative Pressure	Pa
RLS	Regularized Least Squares	
RNL	Radiated Noise Level	$\mathrm{dB\,re\,1\mu Pa^2m^2}$
SPL_b	Sound Pressure Level background	$\mathrm{dB\,re\,1\mu Pa^2/Hz}$
SPL_n	Sound Pressure Level net	$\mathrm{dB\,re\,1\mu Pa^2/Hz}$
SPL_t	Sound Pressure Level total	$\mathrm{dB\,re\,1\mu Pa^2/Hz}$
$SPL_{1/3}$	Sound Pressure Level in one-third octave band	$\mathrm{dB\,re\,1\mu Pa^2}$
S.S.	Suction Side	
S.S. B	Suction Side Bubbles	
S.S. RB	Suction Side Root Bubbles	
S.S. S	Suction Side Sheet	
S.S. S 0°	Suction Side Sheet at 0°	
SDDM	Shallow Data Driven Model	
SE	Standard deviation of the Error	
SL	Source Level	$\mathrm{dB\,re\,1\mu Pa^2m^2}$
SNR	Signal to Noise Ratio	
SPIV	Stereoscopic Particles Image Velocimetry	
SPL	Sound Pressure Level	$\mathrm{dB\,re\,1\mu Pa^2/Hz}$
TF	Transfer Function	$\mathrm{dB\,re\,1\mu Pa^2m^2}$
TVC	Tip Vortex Cavitation	
TVC 0°	suction side Tip Vortex Cavitation at 0°	

TVC 90°	suction side Tip Vortex Cavitation at 90°	
TVI	Tip Vortex Index	
UNIGE	University of Genoa	
URN	Underwater Radiated Noise	
VFSF	Vortex From Sheet Face	
WP	Working Point	

Constants

g	gravitational acceleration	$9.8066\,\mathrm{m^2/s}$
μ	dynamic viscosity	$10^{-3}\,\mathrm{Pa\,s}$
ν	kinematic viscosity	$10^{-6}\,\mathrm{m^2/s}$
π	Archimedes' constant	3.1415
p_{ref}	reference pressure in water	$1\,\mu\mathrm{Pa}$
r_{ref}	distance from the acoustic source and the reference receiver	$1\,\mathrm{m}$
ρ	water density	$10^3\,\mathrm{kg/m^3}$

Greek Symbols

α	Brown's formula parameter	
α	RNL decay between break-point 1 and vortex peak	dB/oct
$\alpha_G(r,\theta)$	propeller geometric angle of attack	°
$\alpha_i, \boldsymbol{\alpha}$	KRLS weights, weights vector	
α_s	dynamometer shaft inclination	°
β	Proctor's formula parameter	
β	RNL decay between vortex peak and break-point 2	dB/oct
$\beta(r,\theta)$	propeller advance angle	°
$\Delta\Phi$	difference between actual and design propeller pitch	°
η_o	propeller efficiency	
$\boldsymbol{\varphi}$	feature map	
$\Phi(r)$	propeller pitch	°
Φ_{pp}	power spectral density function	$\mathrm{Pa^2/Hz}$
Γ	blade circulation	$\mathrm{m^2/s}$
γ	RNL decay between break-point 2 and last point	dB/oct
Γ_∞	vortex strength	$\mathrm{m^2/s}$
$\overline{\Gamma}$	mean circulation on the blade	$\mathrm{m^2/s}$
Γ_{adim}	non-dimensional blade circulation	
Γ_{tip}	blade tip circulation	$\mathrm{m^2/s}$
λ	regularisation parameter	
μ	true map function among inputs and outputs	
σ	generic cavitation number	
σ_n	cavitation number, $V_{ref} = nD$, $h = h_s$	
$\tilde{\sigma}_n$	ratio of cavitation number to a reference value	

σ_{ntip}	cavitation number, $V_{ref} = nD$, $h = h_{tip}$	
σ_{tip}	cavitation number, $V_{ref} = \sqrt{V_a^2 + (\pi nD)^2}$, $h = h_{tip}$	
σ_v	cavitation number, $V_{ref} = V_a$, $h = h_s$	
σ_x	standard deviation	
τ	relative loading between blade and tip	
θ	angular coordinate in cylindrical reference system	°
θ	blade angular position	°
θ	hybrid model parameter	
ζ	Proctor's formula parameter	

Subscripts

1/3	one-third bandwidth	
b	spectrum ending point at 100 kHz	
bp1	spectrum first break-point	
bp2	spectrum second break-point	
c	spectrum central peak	
i	inception	

Roman Symbols

A_C	swept area of cavitation	m^2
A_D	propeller disc area	m^2
A_E	blade expanded area	m^2
$\mathscr{A}_{\mathcal{H}}$	learning algorithm	
$\mathcal{B}$	RNL dimensionless decay	
c/D	chord ratio at $0.7R$	
c	blade chord	m
$C(\cdot)$	complexity measure	
C_p	coefficient of pressure	
D	propeller diameter	m
$\mathcal{D}_n$	building set	
E	generic error	
E_1	exponential integral	
f_{max}/c	camber ratio at $0.7R$	
f	blade camber	m
f	frequency	Hz
Fr	Froude number	
f_{max}	blade maximum camber at $0.7R$	m
f_p	p-th harmonic frequency	Hz
$\mathcal{H}$	hyperparameters	
$\mathfrak{H}$	hyperparameters set	
h	generic data driven model	

h	propeller reference point immersion	m
h_s	shaft immersion at propeller disk center	m
h_{tip}	propeller top dead immersion	m
I	identity matrix	
J	advance coefficient	
$\mathcal{K}$	RNL decay	dB/dec
K	kernel function	
K_Q	propeller torque coefficient	
$\tilde{K}_T$	ratio of thrust coefficient to a reference value	
K_T	propeller thrust coefficient	
$\ell(\cdot)$	loss function	
l	number of samples in training set	
$\mathcal{L}_l$	training set	
$\mathcal{M}$	RNL decay	dB/oct
m	McCormick exponent	
m	number of samples in test set	
n	Rate of propeller rotation	Hz
n	number of samples in the building set	
n_r	number of Bootstrap iterations	
P	propeller pitch	m
p	local pressure	Pa
p	number of samples in the original set	
p	positive integer number	
p_∞	undisturbed pressure	Pa
p_{atm}	ambient pressure inside cavitation tunnel	Pa
P/D	ratio of propeller pitch to diameter	
p_i	pressure of cavitation inception	Pa
$p_{static,ref}$	static pressure	Pa
p_v	vapour pressure of water	Pa
Q	Gram matrix	
Q	propeller torque	$\mathrm{kg_f}$ cm
r	distance from the acoustic source and the receiver	m
Re	Reynolds number	
R	propeller radius	m
r	radial coordinate in cylindrical reference system	m
r_c	vortex cavity radius	m
r_{hub}	hub radius	m
r_ν	viscous core radius	m
$\mathcal{S}_p$	original set	

$\mathcal{T}_m$	test set	
t_{max}/c	thickness ratio at $0.7R$	
T	propeller thrust	$\mathrm{kg_f}$
t	blade thickness	m
t	time	s
t_{max}	blade maximum thickness at $0.7R$	m
u	radial velocity in cylindrical reference system	m/s
V	undisturbed axial flow velocity	m/s
v	azimuthal velocity in cylindrical reference system	m/s
v	number of samples in validation set	
V_a	axial flow velocity	m/s
V_{ref}	reference velocity for cavitation index	m/s
$\mathcal{V}_v$	validation set	
$\overline{w}$	mean wake fraction	
w	axial velocity in cylindrical reference system	m/s
w	axial wake fraction	
$\mathcal{X}$	model input variables	
x	blade section chordwise coordinate	m
$\mathcal{Y}$	model output variables	
y/R	transversal coordinate in local reference system	
Z	propeller blade number	
z	axial coordinate in cylindrical reference system	m
z/R	vertical coordinate in local reference system	

Chapter 1

Introduction

This chapter makes an introduction to the research presented in this thesis including the motivation and aims of thesis as well as its layout.

1.1 Acoustic pollution in the oceans

For marine mammals and many deeper sea fish, hearing is the most important sense. Noise pollution adversely affect these animals inducing hearing loss, reduced communications, internal damaging, stress and disorientation, driving up the occurrences of mass strandings. The speed of sound in water is 4.5 times greater than in air, then some Underwater Radiated Noise (URN) can be heard by marine life over distances of dozens of kilometres. Anthropogenic sources of sound in the marine environment are commonly related to transport, mining, fishing, military and construction. Ships tend to produce low-frequency sound (<1000 Hz) that can spread over huge distances and is the most common source of ocean noise, moreover the noise input can be continuous for a long time. There is no global map of ocean noise, but researchers agree that ship traffic approximately doubled between 1950 and 2000, boosting sound contributions by about 3 decibels per decade. That translates to a doubling of noise intensity every 10 years.

The main sources of noise on board of a generic vessel are machineries and propellers (Figure 1.1). Other sources can be present according to the specific employ. The first contributor is the main propulsion system (diesel engine, turbines, reduction gears); noise components from rotating auxiliary machinery and other shipboard equipment contribute to the ship overall noise signature, but usually at lower levels than propulsion systems.

Different phenomena can occur and generate noise from the propeller as the flow noise, direct radiation, hull vibration at blade rate harmonics, mechanical frictions, cavitation and propeller singing. The acoustical energy produced by these sources is not only spread in sea but, in part, is converted in vibrations on-board of the ship causing discomfort on personnel and passenger, other than potential damage to structures and components. In this framework, international organisations and class societies started in the early 2000's to emanate non-mandatory guidelines to reduce the noise emission. For instance, the additional DNV-GL QUIET class notation, RINA DOLPHIN additional class and LR UWN notation. Quantities and procedures for description and measurement of underwater sound from ships are periodically updated by ISO standard as the last ISO 17208-1:2016 (2016) and ISO

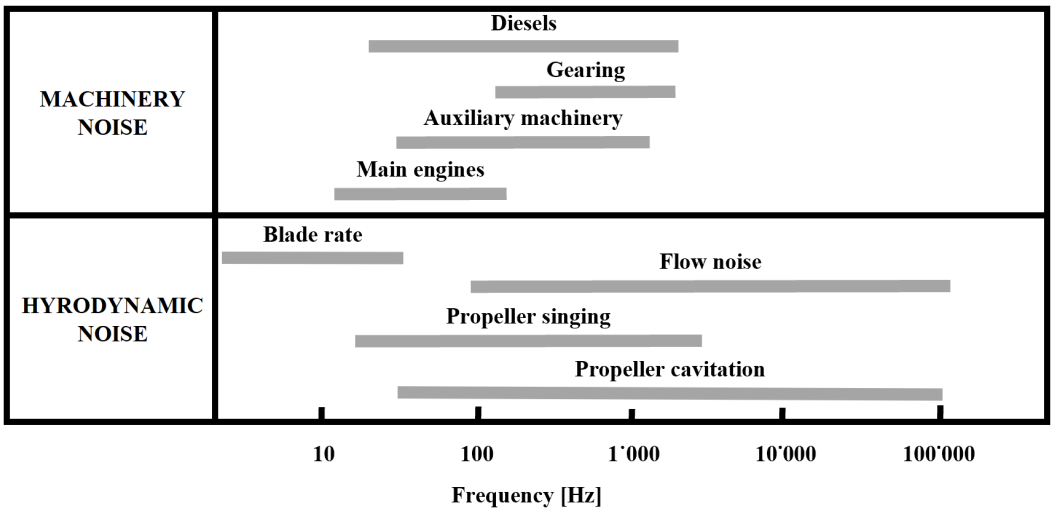

Figure 1.1: Ship sources of URN and their characteristic frequencies (data from Norwood (*Noise from vessels and its control*)).

17208-2:2019 (2019).

In the European Union, the adoption of the Marine Strategy Framework Directive (*MSFD 2008/56/EC*), and specifically of Descriptor 11, establishes a framework within which the Member States shall take the necessary measures to achieve or maintain good environmental status in the marine environment by the year 2020 at the latest.

In 2008, the IMO Marine Environment Protection Committee (MEPC) agreed to develop non-mandatory technical guidelines to minimise the introduction of incidental noise from commercial shipping operations into the marine environment to reduce potential adverse impacts on marine life. Later, the approved guidelines IMO MEPC.1/Circ.833, summarised the countermeasures to reduce noise emission from commercial shipping. Given the complexities associated with ship design and construction, the guidelines focus on primary sources of underwater noise, namely on propellers, hull shape, on-board machinery, and various operational and maintenance recommendations. Some instructions are to operate below cavitation inception, reduce speed and avoid abrupt acceleration, keep clean the hull and maintain the propeller, insulate ship engines, modify route to avoid sensitive marine areas, reduce propeller susceptibility to cavitate during re-fits or new vessel construction.

When adopting the guidelines, it was noted that there were still significant knowledge gap, and that sound levels in the marine environment and the contribution from various sources was a complex issue, so setting future targets for underwater sound levels emanating from ships was premature and more research was needed, in particular on the measurement and reporting of underwater sound radiating from ships.

In this context, the last two EU FP7 projects AQUO (Achieve QUieter Oceans) and SONIC (Suppression Of underwater Noise Induced by Cavitation) allowed to enhance the understanding of noise generated by vessels, to validate predictions of noise levels for individual ships, and to classify ships based on simplified noise models. Moreover, project partners developed techniques to model cavitation noise through the use of experiments in model scale (MS) and through computer sim-

ulations. Also it has been gained insight into the sensitivity of different marine species to shipping noise by carrying out dedicated bio acoustic experiments. One finding shows that the MSFD criterion for the underwater noise descriptor needs to be revised to include higher frequencies.

1.2 Propeller noise assessment

The prediction of propeller cavitation noise can be addressed by means of different approaches, as summarised in Figure 1.2.

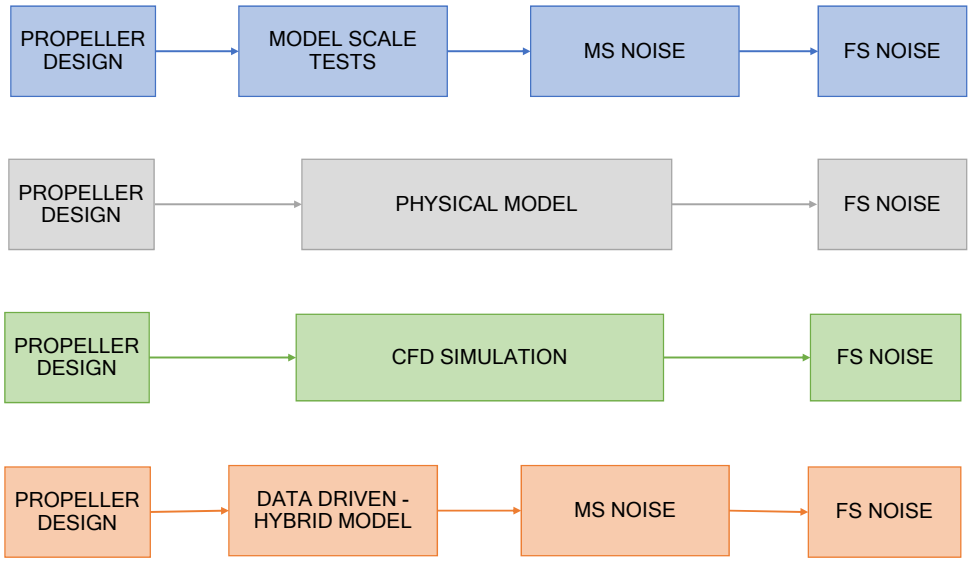

Figure 1.2: Cavitation noise prediction methodologies: CFD, MST, PM, DDM, and HM.

Traditionally, Model Scale Tests (MST) in cavitation tunnels are considered the most reliable method for cavitation noise prediction. MST makes use of a model of the propeller, manufactured using the geometry from the design papers, which is tested reproducing the full scale (FS) working conditions. Scale effects must be carefully taken into account in order to retrieve the full scale noise from MST.

Among the different cavitation typologies affecting the propeller, the most common and often unavoidable is Tip Vortex Cavitation (TVC) generated by the flow motion induced by the pressure drop at the tip of the blade. The development of TVC is significantly influenced by the Reynolds number (McCormick, 1962); the onset of TVC in model scale occurs at significantly lower cavitation number than on the full scale propeller. For some ship operational conditions then, it is not trivial to correctly reproduce the cavitation pattern in MST. For instance, if for a certain full scale condition only a tiny TVC is present, it is plausible that to obtain the same vortex (i.e. diameter and extent) in MST, it could be necessary to reach lower cavitation number respect to the full scale propeller. This might lead to the simultaneous presence of other cavitation kinds, or reinforce the ones already existing. Noise prediction is then worthless in the prediction of the full scale noise, if scale

effects are not correctly evaluated. Moreover, MST are quite expensive and time-consuming; it is not feasible to include them in the early stage of the design where many alternative designs are considered.

If MSTs cannot be undertaken it is still possible to make estimates of the cavitating propeller noise from simplified Physical Models (PM) combined with empirical relations based on historical data; examples of such approaches are represented by the work of Raestad (1996), Matusiak (1992), Brown (1976) and Bosschers (2018a). The limitation of these PM lies in the fact that, due to the undergoing simplifications, they are not able to accurately describe the phenomenon of cavitation noise taking into account all the complex aspects involved in the cavities dynamics. Consequently, the quality of the results may not be completely satisfactory requiring following tuning on experimental data by means of fitting parameters.

Large part of the ongoing research on ship hydroacoustics focuses on Computational Fluid Dynamics (CFD) models (Li, Hallander, and Johansson, 2018; Fujiyama and Nakashima, 2017). The advantage of this method is the direct full-scale prediction without the need of model propeller manufacturing and MSTs. Unfortunately, CFD-based models are still under development and their high computational requirements limit their use to the field of research, making it impractical in a conventional propeller design loop.

In this context, the availability of a tool able to predict propeller noise, based on the information available at the design stage, would be of great interest. Such a tool should be reliable, user friendly and able to manage a great quantity of parameters. Lastly, cost and time effectiveness are essential features for a tool intended to be used also in the propeller design loop.

For this aim, approaches based on the adoption of Data Driven Models (DDM) are proposed in present work. These methods are able to build models exploiting robust statistical inference procedures and data collected in previous experiments in order to make predictions about previously unseen cases, i.e. cases that are different from those used to build the models. A possible advantage of these methods is represented by the fact that there is no need of any a-priory knowledge about the mathematical expression governing the physical system. Furthermore, thanks to the nature of these approaches, it is possible to exploit even data regarding particular phenomena that cannot be easily modelled with a PM. DDM have proved to be valuable instruments in many marine applications (Petersen, Winther, and Jacobsen, 2012; Smith et al., 2013; Coraddu et al., 2017; Cipollini et al., 2018) and recently Aktas, 2017 proposed a promising Artificial Neural Network approach for the prediction of the propeller cavitation noise in full scale given a number of design parameters and a large collection of noise samples from cavitation tunnel tests. However, DDM usually produce black-box (non-parametric) models that are not supported by any physical interpretation; this, despite representing a possible advantage, as mentioned above, may limit the capability of the models themselves, without exploiting important knowledge about the phenomena of interest.

For the above reasons, a hybrid approach is considered, namely Hybrid Models (HM), in order to take advantage of the best characteristics of both PMs and DDMs by combining them together. In fact, HMs are able to combine the statistical information acquired by analysing the collected data, with the physical equations describing the occurring phenomenon, thus considering both the theoretical and the empirical sides of a model scale experiment. HMs are widely used in those contexts

were the experience on the field brought by PMs can enhance the DDMs prediction (Coraddu et al., 2017).

1.3 Aim of the thesis

The object of the present work is the development of semi-empirical methods for the prediction of the propeller cavitating noise at early design stages, with special emphasis to suction side cavitation, namely tip vortex and sheet. In order to exploit ML methods such as DDMs and HMs, the availability of a significant amount of data is needed. Considering the ship radiated noise, full scale measurements carried out during sea trials should be used, however, this kind of data presents some practical issues. One of the major problem is that the availability of such data is very limited; moreover, it is not trivial to identify and separately study the propeller contribution in full scale measurements. Historical data of full scale noise could be used in place of a MST campaign, but the question of homogeneity in data, arises. On the other hand, MST provide the opportunity to collect a large amount of data from dedicated experiments in a controlled environment where it is easier to reproduce the required condition and pick-up the desired quantities. For these reasons, it was decided to define models based on MST data, this guarantees the possibility to build up a proper dataset by means of dedicated experimental campaigns. Such a model is able to replace MST and predict model scale noise, which must then be extrapolated to full-scale using some scaling formulations such as the ITTC (ITTC Specialist Committee on Hydrodynamic Noise, 2017, Chapter 3) or the Lovik (1981). The analysis of effectiveness of the formulations is beyond the scopes of this thesis.

In order to develop and test the models proposed, a dataset has been firstly collected by means of an extensive set of cavitation tunnel tests for two controllable pitch propellers of twin screw ships. Test have been performed applying all the measurements devices available at the UNIGE cavitation tunnel to get all the useful explanatory variables. The test matrix has been defined in such a way to explore the operating range (with different functioning points at different thrust coefficient and cavitation number values) and to better stimulate some cavitation types. Later, another propeller tested previously, again in twin screw configuration, has been added to the dataset.

The modelisation of only the continuous spectrum (broadband) of cavitation noise is addressed in this work, neglecting tonal components. The cavitation typologies of interest are the phenomena on the back of the propeller, such as the TVC and sheet cavitation, since these phenomena are the most common ones for marine propellers. Data regarding other kinds of cavities have also been sampled but not yet employed. The attention is to focus on combinations of propellers/configurations/cavitation typologies that better represent the typical functioning of propellers of twin screw vessels.

The model building approach has been implemented in two alternative ways.

- The first attempt (Approach 1) considers a simplified definition of the input and output variables to better fit more basic PM/DDM/HM. Both input and output are numeric scalars obtained from main descriptors and general quantities, when needed. For instance, the target is represented by a simplified description of the noise spectrum and the features are general parameters

such as propeller operating parameters, mean wakes, advance velocity etc. The amount of data to be treated is then lower and simpler models can be applied.

- In the second phase (Approach 2) more complex models are tackled to fully exploit the information contained in input data. The goal is to obtain a better predictor tool able to model the entire spectrum in one-third levels. Then, the inputs are not only general descriptors but also point by point 2D or 3D matrix e.g. the pressure distribution on the blade.

The main difference between these two approaches is that in the first one the ML computational time is lower but the definition of output and input requires more work and a deep knowledge of the phenomenon. In the second, the computational time in the modelisation increases considerably but the variables definition is almost immediate and the possibility of mistakes decreases.

1.4 Layout of the dissertation

The thesis is organised in ten chapters. Chapter 1 is a brief introduction to the ocean noise pollution, the research behind this topic and the aims of the present study. The following Chapter 2 provides the basic knowledge of the cavitating propeller and its noise. Emphasis is given to the mechanics of the cavities dynamics in relation to ship wake and to the definition of all the different kind of cavitation affecting the propeller. The second part of the chapter deals with the noise generated by the cavitation, a deep insight is dedicated to the resulting spectrum and its characteristic trends when some of the fundamental parameters are varied.

Chapter 3 introduces the machine learning terminology. This chapter is intended as a generic introduction to the main concepts and to the techniques to build and validate data driven models.

Chapter 4 presents all the models scale tests performed, the facility where surveys have been carried out and the main measurements devices utilised. The propeller test cases, their set-up and the functioning points selection are described. Lastly, the post-processing of noise data is reported.

Chapter 5 describes in detail the additional post-processing of the noise data. This includes the repeatability check and the definition of three alternative targets, of increasing complexity.

In Chapter 6 all the possible input parameters collected by model scale tests, or from the propeller design or by CFD calculations are described. Again, as for the targets, different levels of complexity have been accounted.

In Chapter 7 some vortex model are described together with the procedure to compute the vortex cavity radius. Later the theory to obtain the vortex resonance frequency and its acoustic power level according to the data available is presented: the formulations here shown will provide the physical-models employed.

In Chapter 8 and Chapter 9 the two alternative physical, data-driven and hybrid models approaches are presented, respectively. The first considers a simplified version of the problem and then less complex predictive algorithms. The last accounts for sophisticated targets and features, and a more demanding modelisation.

Finally, in Chapter 10, the main conclusions of this thesis are drawn and possible improvements for future works are presented.

Due to confidentiality issues, sensitive data like propeller geometries, working conditions, and noise levels will be omitted or altered by means of normalisation with respect to appropriate reference values.

This page was intentionally left blank.

Chapter 2

Propeller cavitation and noise

In this chapter the main sources of underwater noise from marine propeller are presented. A special emphasis is given to the cavitation typologies and to the scale effects influencing the cavitation extent.

2.1 Introduction

The propeller is, in most cases, the main source of underwater radiated noise when considering ships in regular navigation. The noise contributions from the propeller may be divided in two types: non-cavitating noise and cavitating noise.

The former is always present and depends on the geometry of the blades, their load, the propeller inflow, the forces fluctuations and the shaft arrangement. The typical frequency spectrum of non-cavitating propeller noise (Figure 2.1) is composed by some discrete tones at blade passage frequency (BPF) and its harmonics, and broadband noise at higher frequencies (up to 20 000 Hz for ships). During the revolution the blade encounters the flow with different angle of attack because of the ship wake (see Section 6.5), that induces a periodical fluctuation of loads acting on propeller blades and consequently on the whole shaft-line. This system can be compared to fluctuating forces acting on rigid bodies, which is a typical dipole source and produce noise at frequencies corresponding to BPF ($Z\,n$) and harmonics (tonals); usually only the first three harmonics are visible (ITTC Specialist Committee on Hydrodynamic Noise, 2014). The harmonics frequencies are:

$$f_p = p\,Z\,n\,, \tag{2.1}$$

where Z is the blade number, n is the propeller revolutions per second and p is a positive integer number.

The broadband part of the noise spectrum is caused by the turbulence in the incident flow, in the boundary layer and in the propeller slipstream; these noise sources are comparable to quadrupole, hence they are the less efficient kind of source and they are usually overcomed by the cavitation noise if present. Blade-rate forces transmitted by propeller shaft may produce hull vibration. In particular, when these vibratory forces coincide with low-frequency hull resonances, severe vibrations may occur. Also vortex shedding sounds, that are responsible for the phenomenon known as propeller singing, are an important source of noise. Every rigid body placed close to the propeller (rudder etc.) is affected by propeller flow and propeller near field pressure fluctuations and as a consequence it behaves as a dipole in its

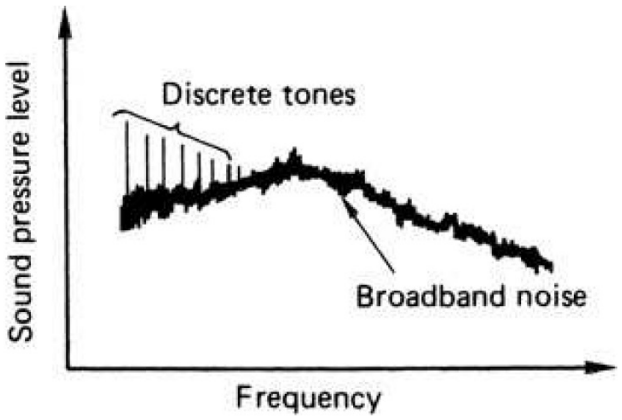

Figure 2.1: Frequency spectrum by a non-cavitating propeller (image taken from Carlton (2007)).

turn. In addition, fluid structure interactions may become relevant and noise may be produced also by structures vibrations not only at blade rate, depending on structure characteristic frequencies. The contribution of all the noise mechanisms to the ship acoustic signature is generally comparable to other contributions, such as the machinery noise: the relative importance of all these phenomena may vary case by case and depends on considered frequencies. On the other hand, the sound pressure level of a non-cavitating propeller is typically lower than that generated by a cavitating propeller, which usually becomes the dominant component in the noise signature.

2.2 Physics and typologies of cavitation on ship propellers

In fluids subjected to local change in velocity or pressure, small cavities filled in vapour or gas can appear. These voids are generally unstable and they are prone to return to the liquid phase with an implosion that can generate strong pressure waves. This phenomenon, that recalls the boiling, is called cavitation and affects every machine in which a fluid is used to generate forces like turbines, pumps and propellers. Actually, the relative motion of a solid body into the water may cause significant disturbances in the velocity and pressure fields close to the body. As a result the local pressure may be locally reduced to very low value, comparable with the vapour tension of water. As a first simple approximation, cavitation occurs when somewhere in the flow, the local pressure is equal or lower than the vapour tension. In real cases, for the cavitation inception to occur, the drop of pressure below the vapour pressure may be not sufficient to overcome the water tensile strength which counteracts the formation of cavities into the fluid. In general, more a fluid is pure and more force (depression) is necessary to create visible cavities. Liquids considered in practical applications contain a variable percentage of dissolved gas, air or solid particles, which act as an interface (cavitation nuclei) where cavities can grow and reach visible size when the external pressure decrease.

According to the cavity content, two main kinds of cavitation exist: vaporous

and gaseous cavitation, but in most cases it is a combination of both. The gaseous cavitation is less dangerous because the gas tends to not merge with the water and then the collapse is not complete and the pressure wave level is lower. The collapse of a bubble starts when the travelling bubbles reach a region where the pressure is higher or because, following its expansion, the inner pressure becomes smaller than the external.

The process of implosion of a bubble near a solid surface has been studied, among other, by Plesset and Chapman (1971) and is showed in Figure 2.2. The bubble collapse is not symmetrical due to the wall and the fluid motion, attracted from the bubble implosion, is faster towards the wall than in the opposite direction. The microjet of water can reach the velocity of 1000 m/s, and its repeated action on a surface leads to erosion in a matter of hours in the worst cases. The collapse rarely

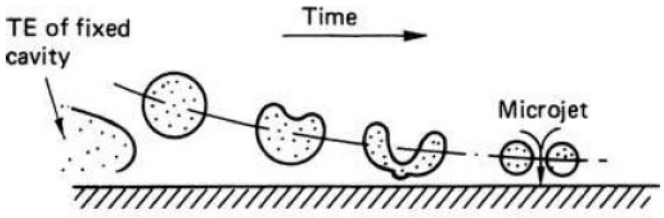

Figure 2.2: Bubble collapse in proximity of a wall (image taken from Carlton (2007)).

is complete, more often the cavities rebound and form new bubbles that collapse again, this process can occur four or five times until visible bubbles are dissolved (Figure 2.3).

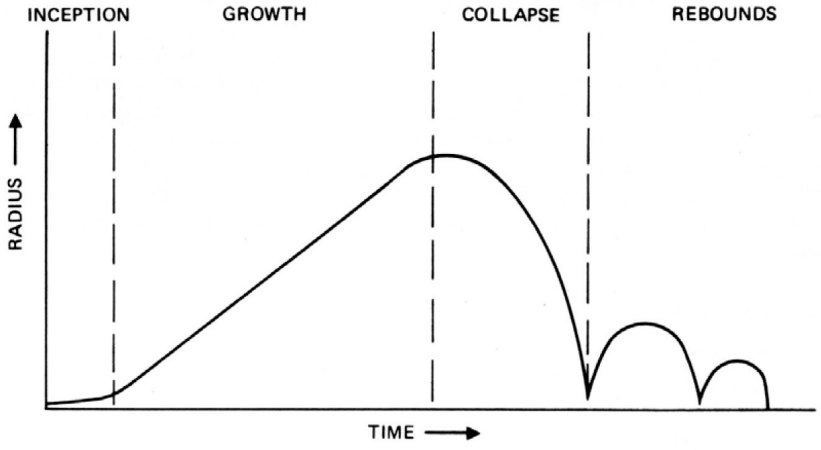

Figure 2.3: Cavity rebounds dynamic (image taken from Ross (1976)).

The ratio of the static to dynamic head of the flow is named cavitation number and it represents the fluid's reserve of static pressure before cavitation inception.

$$\sigma = \frac{p_{static,ref} - p_v}{0.5\rho V_{ref}^2}\,, \tag{2.2}$$

where $p_{static,ref}$ is the static pressure head at a reference point, p_v the vapour pressure and $0.5\rho V_{ref}^2$ is the dynamic pressure head with V_{ref} a reference velocity. As long as this reserve is greater than any drop in the local static pressure coefficient C_p, no cavitation will theoretically occur.

$$C_p = \frac{p - p_{static,ref}}{0.5\rho V_{ref}^2}\,, \tag{2.3}$$

where p is the local pressure.

According to the simplest cavitation inception scheme, the pressure at which cavitation occurs should be $p_i = p_v$, but this pressure is dependent from the presence of cavitation nuclei: if they are insufficient in number, p_i can be considerably lower than the vapour pressure, as sometimes happens in MSTs, thus inducing some scaling effects.

In marine propellers the combination of pressure field, turbulence in the flow, blade geometry and the three-dimensional effects give rise to many cavitation phenomena. In propellers three main groups of cavitation can be distinguished: vortex cavitation, sheet cavitation and bubble cavitation.

The vortex cavitation origins in the low pressure core of the shed vortices from the propeller tip, from the blades leading edge or from the boss cap. The travelling cavities which are convected inside the vortices enlarge until they become visible, this usually happens first some distances downstream the propeller due to wake roll-up (detached tip vortex, Figure 2.4). Later, if the cavitation index is lowered, the cavitating vortex becomes attached to the blade. If operating in a non-uniform flow, the tip vortex may be distorted or even collapse or burst, which in return causes large pressure fluctuations and hence high levels of noise. The hub vortex cavitation

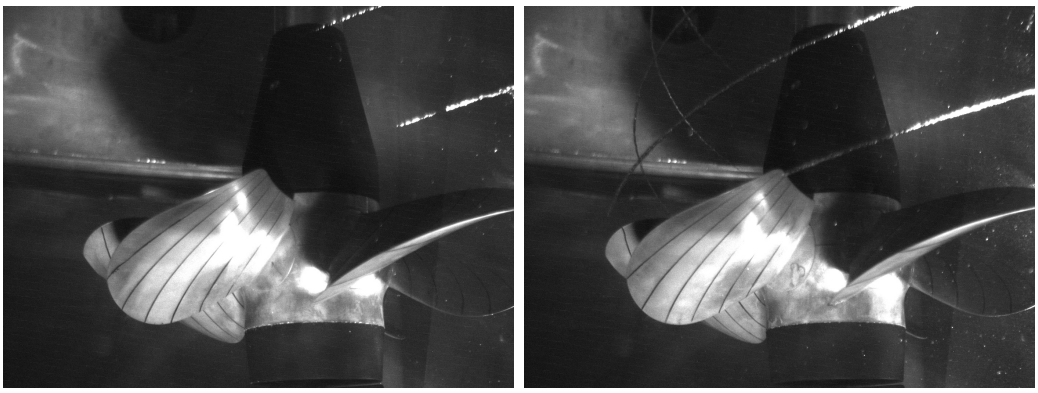

Figure 2.4: Suction side tip vortex, detached (left), attached (right).

is the outcome of the shed vortices at the blades roots, which, individually, are not so intense to cavitate, however the intensity of the vortex resulting from their combination may lead to cavitation; the presence of a cavitating hub vortex may be critical since it can (Figure 2.5) impinge on the rudder, leading to its erosion.

The sheet cavitation is an aggregation of bubbles on the blade surface to form a rather continuous sheet; it arises on the leading edge or in proximity of the tip where the pressure on the blade profile can reach sharp negative peak when the angle of attack is high. It appears on the back side (suction side S.S.) if the angle of attack is positive, or on the propeller face (pressure side P.S.) in the angle is reduced or even negative. If the cavitation number decreases or if the angle of attack gets larger, the

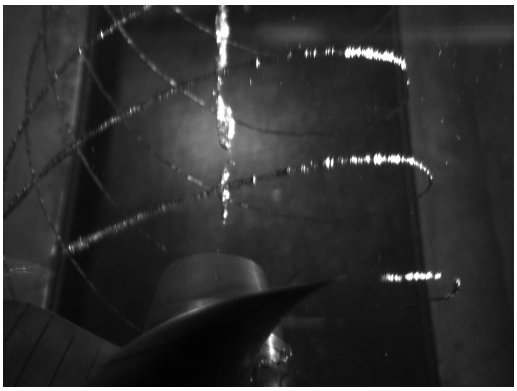

Figure 2.5: Hub vortex cavitation.

sheet expands over the blade. When the sheet area is considerably large it can lead to thrust reduction. The sheet cavitation is highly subjected to the circumferential varying inflow and its surface can grow and shrink periodically adversely affecting the total noise radiated. In Figure 2.6 the effect of the abrupt change of the inflow wake on the sheet extent,is reported for a propeller behind twin screw wake.

At the end of the vapour sheet, it forms a re-entrant jet responsible for noise emission and erosion; furthermore, the jet can break-off the sheet in many small bubbles that implode downstream or reinforce the vortex cavitation.

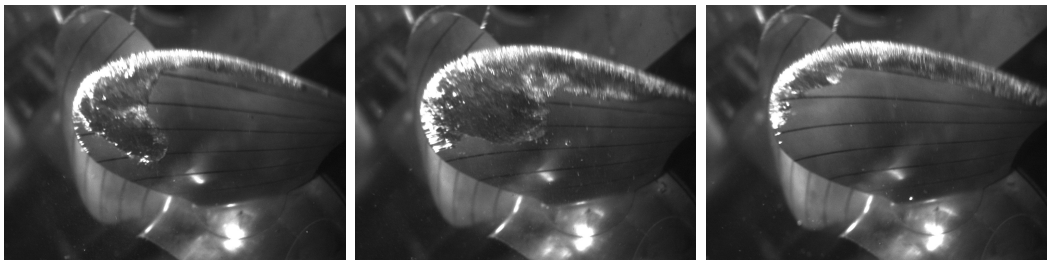

Figure 2.6: Suction side sheet cavitation for a blade in three subsequent time-steps.

The P.S. sheet cavitation (Figure 2.7) is visible in a propeller working in unloaded condition with respect to design point. The low pressure areas where cavitation occurs are usually limited in extent and close to the blade leading edge. Actually, due to the effect of blade camber, the local pressure grows rapidly while moving towards the trailing edge. This steep recovery of pressure causes the violent collapse of cavities shed by pressure side cavitation, as a consequence the sheet cavitation on pressure side is significantly more unstable with respect to suction side cavitation, with cavities collapsing just after leaving the local low pressure area.

In some cases, both on suction side and pressure side, vortices may be generated at the leading edge of the blade at intermediate radial sections, due to local flow separation. In the case of pressure side vortices, the cavities burst and vanish quite close to the blade as for the P.S. sheet cavitation. The vortex collapse is an impulsive and noisy phenomenon which usually generates also a significant amount of bubbles splitting and collapsing at vortex tail.

Bubble cavitation, in model-scale, appears as well defined individual bubbles, which grow and implode rather quickly. It occurs mainly on the mid-chord section of the profiles because of high suction pressure due to the combination of section

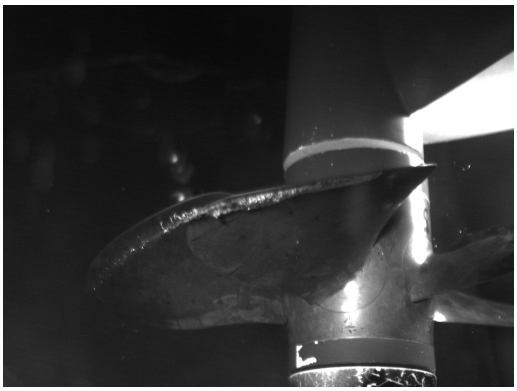

Figure 2.7: Pressure side sheet and vortex from sheet face.

thickness (especially at the root) and camber (at mid and outer radii); if the cavitation number decreases they can cover large areas of the blade (Figure 2.8). The angle of attack is not particularly influential in the bubble dynamic. The collapse of bubble cavities is one of the most violent phenomena, if it occurs near to the blade surface, it can lead to erosion fast and its noise easily overwhelms all the other cavitating sources.

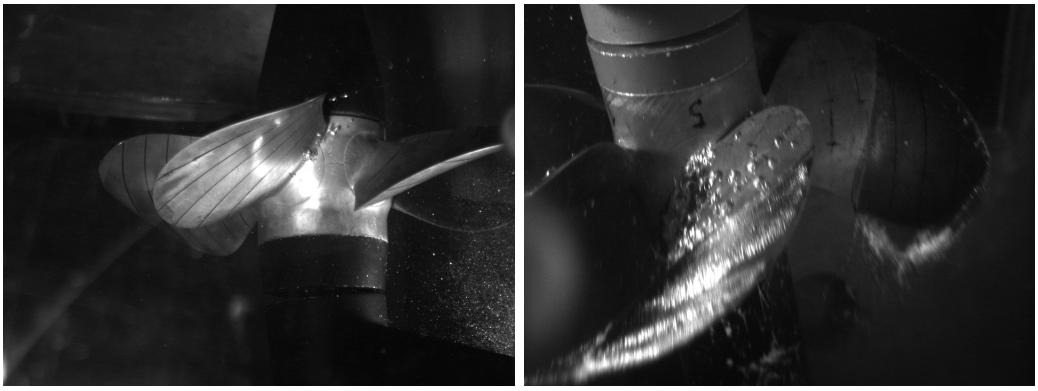

Figure 2.8: Suction side blade bubbles on the root (left) on the surface (right).

When the angle of attack is small or negative (for instance when the blade is operating on inclined flow) a kind of bubbles can show even at the face root from the break-off of thick and unstable laminar sheet on the blade surface. Needless to say, this cavitation is extremely dangerous and must be avoided.

2.3 Scale effects on cavitation

Cavitation tests are carried out on propeller models in dedicated facilities, which can be divided in three main typologies: cavitation tunnel, circulation channel and depressurised towing tank. When operating in model-scale the main challenge is to simulate correctly the whole full-scale environment or, conversely, to be able to scale the measured quantities from model to full-scale. If the cavitation noise is the subject of study, the full-scale cavitation pattern should be reproduced. The scale effects on cavitation are generally understood to be due to three main causes (Billet and Holl, 1979): the viscous nature of the flow, the dynamics of bubbles, and the

effects of gravity. The former and the latter are accounted with Reynolds (Equation 2.4) and Froude (Equation 2.5) number identity respectively. But, being impossible to respect in model scale both the identities, the effects of gravity are neglected in favour of the viscous effects which are more relevant for this subject.

$$Re = \frac{nD^2}{\nu}\,. \qquad (2.4) \qquad\qquad Fr = \frac{nD}{\sqrt{gD}}\,. \qquad (2.5)$$

Unfortunately, the Reynolds identity is neither accomplished due to limitations in tunnel size and speed. Tests are usually carried out keeping the Reynolds number as high as possible, nevertheless the Re in model-scale is one or two order of magnitude smaller than that of the full-scale. Due to this, both the free stream turbulence and the blade boundary layer (which is also related to the manufacture roughness) is different from the full-scale propeller.

The wake inflow, in smaller facilities, is usually reproduced by means of dummy model coupled with a suitable wake screen. Due to Reynolds number difference, the full-scale wake field may present wake with narrower decelerated peak and larger gradient, lower values of the average wake fraction and a reduced strength of bilge vortices if present. Furthermore, in cavitation tunnel, when the dynamometer is runned in pushing-configuration (Figure 4.15) the propeller can be invested by the wake of the dynamometer itself. However, this wake is not representative of the full-scale one, weak and usually limited to lower radii of the propeller and its influence on the cavitation in negligible.

Past studies focused on the observation of small bubbles in turbulent boundary layer (Daily, 1956) found that cavitation always occurred at a value of local wall pressure that was greater than the vapour pressure and further that cavitation inception occurred predominately in the center of the boundary layer. Arndt and Ippen (1968) made similar experiments above a roughened surface and reported that negative pressure peaks, of a magnitude many times larger than the root mean square value of the turbulent pressure fluctuations, are responsible for cavitation. Turbulent intensity in a boundary layer adjacent to both rough and smooth walls is a function of wall shear that in turn is dependent on a Reynolds number based on displacement thickness and corrected for the effect of roughness. Therefore, the Reynolds similarity is fundamental to reproduce the same boundary layer.

The boundary layer on the suction side can be laminar over a considerable region of the propeller blade in model-scale, especially for unloaded sections, while it is almost totally turbulent in full-scale (Kuiper, 1981). In Figure 2.9, in the loaded tip region, a laminar separation bubble (A-B) quickly lead to the onset of the turbulent boundary layer, in accordance with the expected full-scale. Otherwise, the laminar layer extends for large part of the blade. The transition points (C-D-E) are a function both of load, geometry and local Reynolds number. Under this circumstance, the inception could be delayed and the cavitation to be rather intermittent. The boundary layer on the pressure side of a propeller blade is generally less complex. In normal operating conditions no laminar separation occurs on the pressure side and a significant laminar region exists near the leading edge. Transition often occurs more gradually than on the suction side due to a favourable pressure gradient.

The transition from laminar to turbulent on a blade boundary layer can be driven by the turbulence level of the inflow wake that provides the initial disturbance (Mack, 1977). In a facility test section this can be achieved running the

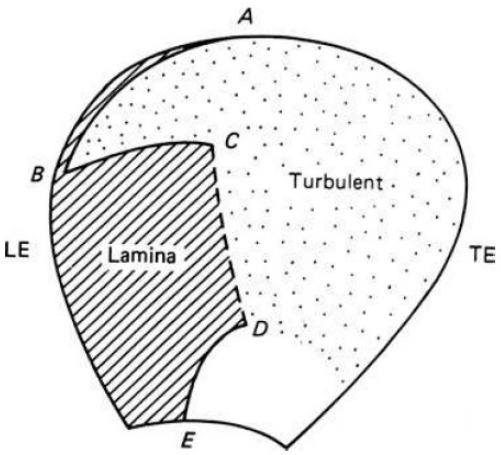

Figure 2.9: Sketch of a boundary layer on the back of the model-scale propeller (image taken from Carlton (2007)).

propeller behind suitable wire screens or other similar devices which alter inflow free-stream turbulence without modifying the distribution of average velocity. Another countermeasure is to run cavitation tests at the highest achievable revolution rate in order to maximise the Reynolds numbers, however this can be not sufficient to shift the transition region close to the leading edge (Kuiper, 1978). Surface irregularities (roughness) and manufacturing tolerances of the model propeller blades are different from those of ship propeller blades, therefore, some researchers (Kuiper, 1981; van Rijsbergen and van Terwisga, 2010; Korkut, 2000) have used artificial stimulators, such as carborundum grain, to stimulate the boundary layer into being turbulent. Moreover, maintain a proper amount of nuclei into the water through nuclei seeding techniques (as electrolysis) enhances the cavitation inception (van Rijsbergen and van Terwisga, 2010).

All these strategies may allow to enhance significantly results obtained from model-scale cavitation experiments but the consistent application of some of these techniques (e.g. artificial roughness added on blades leading edge) is not straight forward and requires some experience.

Other parameters that must be treated with great attention are the size and distribution of cavitation nuclei, which affect the bubble dynamic. As seen, they are essential to reduce the water tensile strength and stimulate cavitation. Tension of a fluid depends upon the number, size, distribution and content of nuclei in the fluid. When the size and number of nuclei are suppressed, relatively large values of tension can be sustained (Arndt and Maines, 1998). Therefore, if the fluid has not enough nuclei, it can resist up to very low pressure without the cavitation occurring. The nuclei population should not be aimed to reproduce the one in full-scale, which is usually very high, because it can overstimulate the bubble density in the model scale facilities, deteriorating the visibility and increasing the damping on the measured noise. Hence the optimum air content for a given cavitation tunnel should be determined by long-established experience (ITTC Specialist Committee on Hydrodynamic Noise, 2017). It has been demonstrated that cavitation inception tests performed without controlling the amount of nuclei may lead to inconsistent results (Keller, 1984). The cavitation nuclei can be directly measured, e.g. by mean

of optical methods or indirectly by measuring the water tensile strength (cavitation susceptibility meter). These two alternative approaches can be too demanding to be inserted in routinely tunnel operations, hence some facilities check only for the presence of dissolved gas (especially oxygen) through simple membrane sensors. This kind of measurement does not provide a description of the nuclei spectrum, however, for a given facility a correlation exists between the nuclei spectrum and the gas content (when the gas content is low, the mean diameter of nuclei decrease), as a consequence the gas content can be used to control and set the water quality for cavitation (ITTC Specialist Committee on Water Quality and Cavitation, 2002).

2.3.1 Viscous effects: the case of the tip vortex inception

The aforementioned scale effects can be minimised with proper strategies, however the viscous effect, on the delay of the tip vortex cavitation, inception is still not resolvable with technical procedures.

Tip vortex cavitation is very often the first form of cavitation to occur on full-scale propellers, and its presence is often unavoidable above a certain speed, even for properly designed propellers. On the other hand it is usually the unique phenomenon present in ordinary navigation regime for ships designed to have a limited acoustic signature. The prediction of the onset of this type of cavitation is particularly important in the design of silent propellers as for navy vessels or researcher ship, since it determines the velocity above which vessel noise increases significantly. The physical phenomena previously discussed have an influence on tip vortex inception, however in this case, the viscous effects are even more important. Considering a vortex in fully wet conditions, i.e. no cavitation, the vortex flow is characterised by the presence of a viscous core. The dimension of the viscous core depends on the thickness of the blades boundary layers and the shear stresses, consequently it varies with the Reynolds number. This causes different azimuthal velocity distribution and different pressure inside the vortex core. The smaller the vortex core, the lower the pressure. The variation of pressure has of course an effect on cavitation inception, being the local low value of pressure responsible for it to occur. As far as a stable cavitating core is formed, viscous effects in the vortex core become negligible and cavitation similarity based on the cavitation number can be achieved (Kuiper, 2001).

As a result of the above, the inception of an isolated vortex at model-scale, will be significantly delayed by the lower Reynolds number respect to the full-scale, as expressed in the McCormick rule (McCormick, 1962):

$$\frac{\sigma_{FS}}{\sigma_{MS}} = \left(\frac{Re_{FS}}{Re_{MS}}\right)^{m}. \tag{2.6}$$

The exponent m is depending upon the testing facility and range in 0.3-0.5.

To reproduce the same full-scale vortex radius from the model-scale bucket, the full-scale cavitation index of interest, should be scaled according to McCormick rule. Formally, the cavitation tests are performed with similar σ/σ_i but the McCormick rule (with fixed exponent) is valid only at the inception, indeed when the vortex radius enlarges the difference in Reynolds number becomes gradually negligible; this can be accounted for applying formula as the one proposed by Shen, Gowing, and Jessup (2009) where the values of m decrease as the values of Re_{MS} increase.

However, the presence of other cavitation typologies does not scale accordingly: bubble cavitation is not delayed by viscous effects, whereas sheet cavitation scaling

for viscosity is still under discussion, the effect of the Reynolds number on the inception of sheet cavitation is lower than that on the inception of vortex cavitation. In proximity of the inception in model-scale, this leads to two cases:

1. the TVC inception curve can be scaled without moving to the back sheet inception curve as in Figure 2.10a (green area). In this case the scaled TVC is representative of the full-scale cavitation extent;

2. the scaling of the TVC inception leads to the appearance of other cavitation patterns or the TVC inception is already under other phenomena as in Figure 2.10b. The presence of bubble cavitation or sheet cavitation may also alter the extent and the dynamic behaviour of the tip vortex itself and the full-scale cavitation pattern can not be consistently reproduced in model-scale.

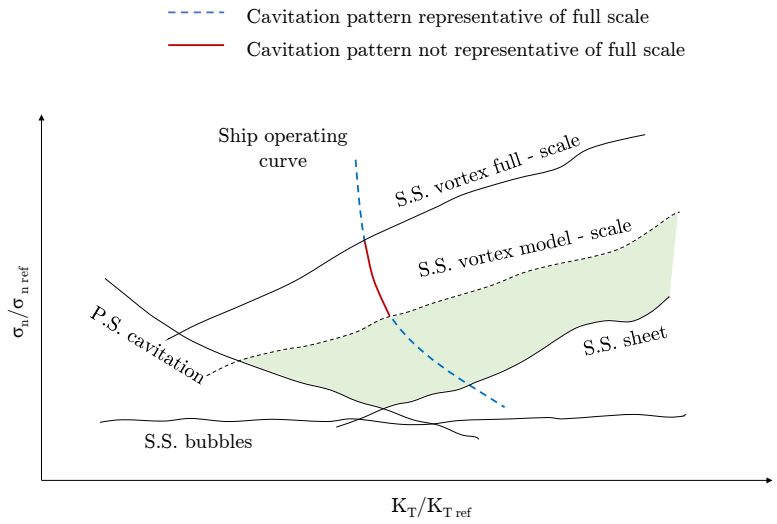

(a) Cavitation bucket with an isolated tip vortex in model scale.

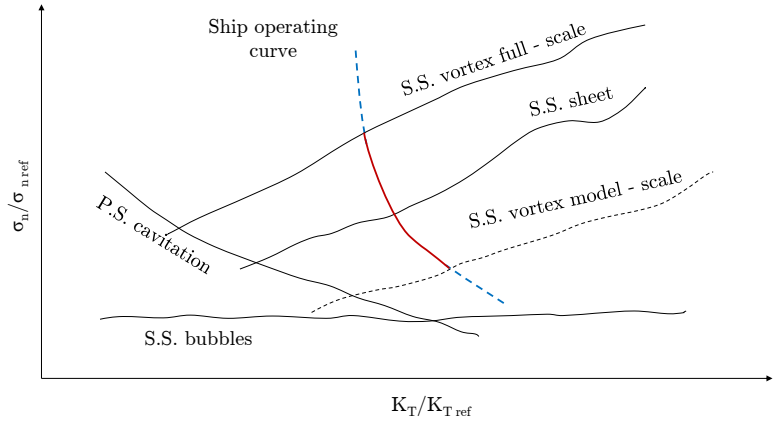

(b) Cavitation bucket without isolated tip vortex in model-scale.

Figure 2.10: Cavitation inception curves in model and full scale (images adapted from ITTC Specialist Committee on Hydrodynamic Noise (2017)).

When the cavitation pattern is fully developed, the similitude in cavitation index can be used to retain the cavitation extent. The previous consideration must be taken carefully in account when the aim of the tests is the noise assessment of the full-scale propeller. If unwanted phenomena are present (as in case 2.) the acquired noise may include the contribution of such phenomena, consequently it should be disregarded because not representative of the full-scale noise.

2.4 Summary

A marine propeller generate thrust thanks to a difference in pressure between the two sides of a blade. If the negative pressure peak reaches particularly high values, small cavities filled in vapour or gas can appear on the blade surfaces, or in its neighbourhood. The drawbacks of such phenomenon are thrust reduction, noise emission, vibrations and, in the most severe cases, material erosion.

The three main typologies of marine cavitation are vortices, sheets and bubbles; further classification comes from the location on which it appears (back, face, tip, root, leading edge, trailing edge, etc.) and on the trigger, as inflow wake or blade geometry. Cavitation tests are usually performed on model propellers for the undoubted advantages of operating in a controlled environment. But, when operating in model-scale, the main challenge is to reproduce correctly the whole full-scale environment or, conversely, to be able to scale the measured quantities from model to full-scale.

The are several scale effects, but the viscous effects are more relevant for this subject. Unfortunately, due to limitations in tunnel size and speed the tests are usually carried out keeping the Reynolds number as high as possible, but never reaching the full-scale value which is one or two order of magnitude bigger than the model-scale. Due to this, both the free stream turbulence and the blade boundary layer is different from the full-scale propeller. Under this circumstance, the cavitation inception could be delayed, the cavity extent altered and the cavitation can be rather intermittent. This has an impact especially on tip vortex cavitation which is very often the first and unique phenomenon present in ordinary navigation regime for ships designed to have a limited acoustic signature.

The inception of an isolated vortex at model-scale, will be significantly delayed by the lower Reynolds number respect to the full-scale, as expressed in the McCormick rule (Equation 2.6), allowing other phenomena to arise concurrently. If unwanted phenomena are present the measured noise may include the contribution of such phenomena, consequently it should be disregarded because not representative of the full-scale noise.

The problem of the inception of the tip vortex, and its consequences in the noise prediction, will be discussed in the Chapters 8 and 9 .

This page was intentionally left blank.

Chapter 3

Machine learning theoretical background

In this chapter an overview of the machine learning theoretical background is given, outlining the typical workflow used to build a reliable machine learning tool. Some of the common failures and relative countermeasures are described. Finally one regression method, used in the first noise modelisation approach in the thesis, named the kernel regularised least square, is described in detail.

3.1 Introduction

Computer software are widely used by decades to resolve a multitude of tasks in scientific disciplines. Formally, they are set of instructions written in a programming language that can be read and ran by the computer to solve specific tasks. The biggest limitation lies in the request of a priori knowledge of the mathematical expressions governing the phenomenon under examination: without them no software can exist. In real life application a myriad of problems, situations and tasks exist where the physical model is unknown or it is too complex to be modelled with the available techniques or the problem itself is not suited to be mapped by mathematical expressions. Some examples can be: pattern recognition (differentiate object or faces in images, understand spoken words), anomaly detection (bank fraud, industrial plant monitoring), prediction (stock exchange prices, polling techniques).

For these cases the best approach comes with Machine Learning (ML). To build a ML tool a suitable amount of data and a learner are needed. Data includes inputs and outputs (called features and targets, respectively). The learner observes the dataset and maps the inner function that approximates the relation among the outputs and the inputs. A good learner must be able to accurately predict such outcomes, for unseen cases belonging to the same features domain (generalisation). This is called programming by example or learning from data or data analysis. This approach is useful when a pattern is to be found, there is data availability, computational capacity, and when effectiveness is more important than precision (prediction errors are tolerated).

Learning can be grouped in two macro categories: supervised and unsupervised learning. Given a set of input variables $\mathcal{X}$ and the corresponding outputs $\mathcal{Y}$, through supervised learning it is possible to model an approximating function h able to predict the outputs for a new set of inputs. It is called supervised because the function

h is modified iteratively until the prediction is accurate as needed. The regression and classification may be considered belonging to the group of the supervised learning algorithms (Bishop, 2006) tasks. In classification the output is a label or class, the inputs (also called features, explanatory variables or independent variables) can be numerical and/or class. For instance, assessing if a bank note is forged (output yes/no) or cataloguing animals depicted in a photo are classification problems. The aim of this task is hence to build hyperplanes to separate the classes (Figure 3.1).

In regression frameworks both entry and exit variables are numerical. Here the aim is to find a pattern in the data, that is a generalization rules among the inputs and the outputs (also named targets, response variables or dependent variables), in other words to compute an hyperplane which approximates the points. As an example a car fuel consumption (response variable) is reasonably a regression of some explanatory variables such as engine characteristics, tires, weights, road surface etc. The unsupervised learning aims to subdivide data on the basis of a similarity

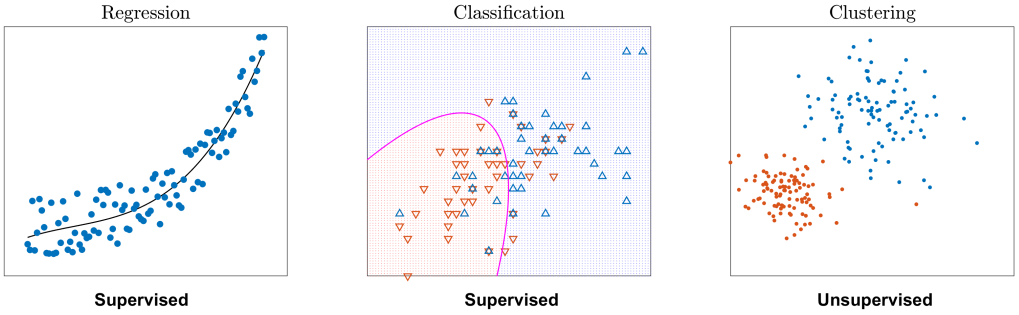

Figure 3.1: Main typologies of machine learning algorithms.

measure to extract useful information from data itself. The user is not involved in the training process then neither features and target exist, nor a priori knowledge on possible groups. Unsupervised learning problems are further grouped into clustering and association problems. Clustering (Jain and Dubes, 1988) deals with finding a structure or pattern in a collection of uncategorised data. Clustering algorithms process data and find natural clusters (groups) if they exist in the data.

Association mining (Agrawal et al., 1996) allows to establish associations among data objects inside large databases. This unsupervised technique is about discovering interesting relationships between variables in large databases. This, for instance, can be applied in advance to a supervised learning to reduce features dimensionality discarding redundant features. In spite of the power of these techniques, they are computationally complex and the user needs to spend time interpreting the classes which follow that classification, which can be ambiguous. Indeed, a correct answer, as in supervised learning, cannot exist.

The choice of the learning type depends upon the problem to be faced; there are a multitude of machine learning algorithms belonging to these two macro categories, among which the most suitable one must be chosen according to goals, computational time, hardware, accuracy etc.

In the context of cavitating propeller noise studies, attempting a full analytical description of the phenomenon is practically unfeasible. Data from previous observations of the phenomenon may be available thanks to experimental tests in a cavitation tunnel and design papers, the output data types are numerical, and errors

in target prediction are accepted to a certain extent. Therefore the problem here considered can be straightforwardly mapped in a typical machine learning regression problem.

In the remainder of the chapter, some of the main concepts and terminologies related to the supervised learning will be introduced. The principal steps needed to build a ML tool are presented, together with the reliable estimation of the generalisation error. Lastly, the algorithm used in Chapter 8 is discussed.

3.2 Supervised learning

The supervised learning can be used both in regression and in classification analyses. Only the former will be here accounted for, but many concepts are applicable also to the classification case.

The goal is to learn an artificial simplification h of the unknown relation μ, namely the relation between the inputs $\boldsymbol{x} \in \mathcal{X}$ and the outputs $y \in \mathcal{Y}$. In general, the supervised learning is made up of the following steps, summarised in Figure 3.2:

- raw data collection
- outputs and inputs definition
- data processing and dataset construction (Subsection 3.2.1)
- selection of the machine learning algorithm
- machine learning training (Subsection 3.2.2)
- model selection (Subsection 3.2.3)
- final model evaluation (Subsection 3.2.4)
- new data prediction (example in Subsection 3.3.1).

Data collection is the process of measuring and gathering information on the realisation of the phenomenon, to build a dataset. The single row in a dataset, composed by features and targets, is called sample. The sample set is just a subset on the population, that is the complete set of elements that possess some common characteristic: for instance, in this study a sample of propeller loading conditions, from three propellers, have been extracted (sampled) from all the possible loading conditions (population). Therefore, to be representative, the samples must reflect the characteristics of the population.

Collecting data allows to capture a record of past events so that they can be used to extract information to find recurring patterns. From those patterns, the predictive models are built using machine learning algorithms. Predictive models are only as good as the data from which they are built, so good data collection practices are crucial to develop high-performing models. The data need to be free of noise as possible and contain relevant information for the task at hand.

These phases are here not further investigated because strongly correlated with the case under study. A detailed description about the raw data collection and the post-processing carried out in this thesis are visible in Chapters 4, 5, and 6.

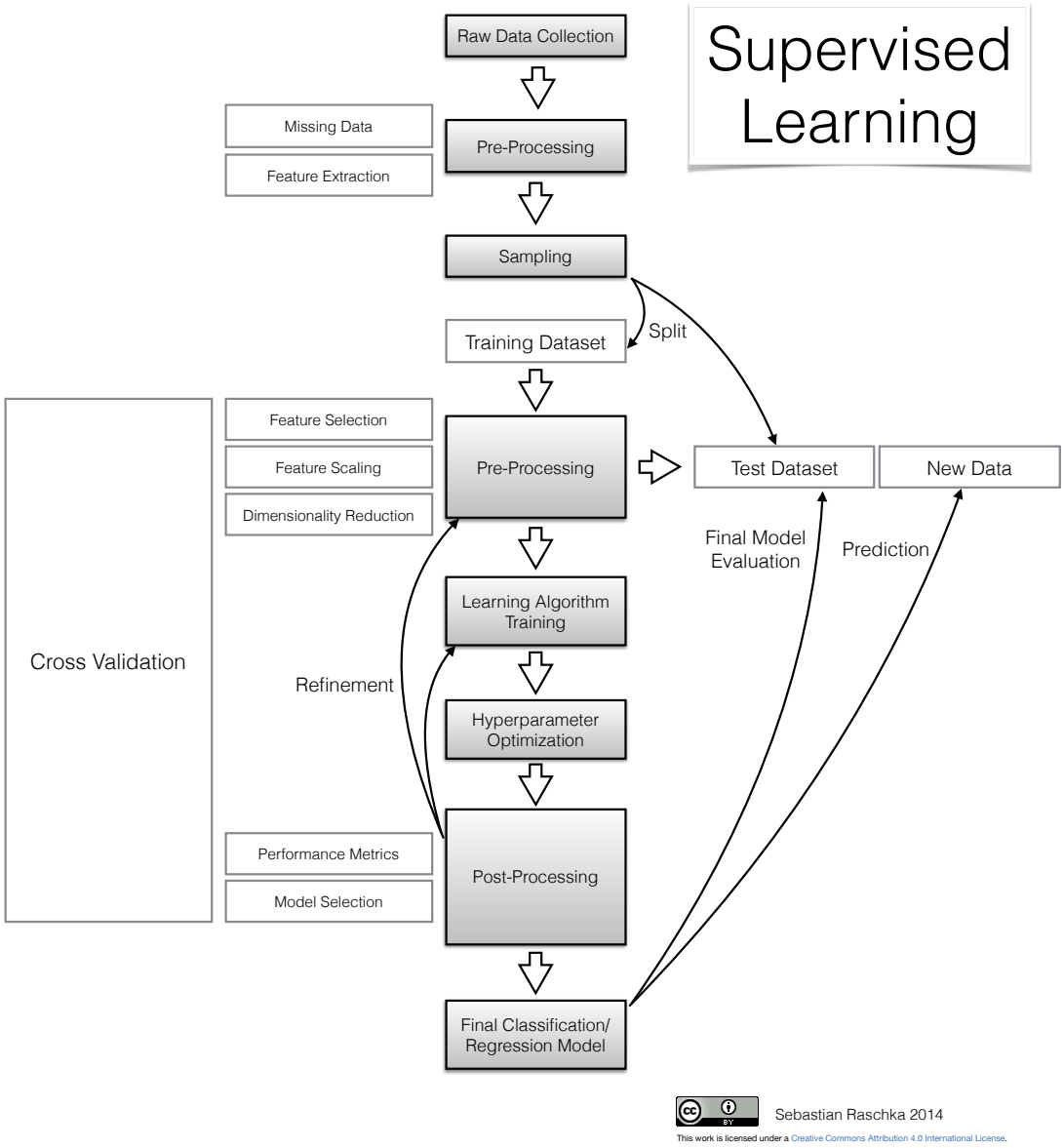

Figure 3.2: Machine learning flowchart (image taken from Raschka, S.).

3.2.1 Data processing and dataset construction

The data preparation phase is crucial for the success of the whole learning. Usually, data picked-up by sensors are inhomogeneous in format (numerical, text, categorical, images) and dimension (scalar, array, matrix), some values can be missing or they can assume anomalous values due to failures or to the nature of the phenomenon. Hence, they have to be treated before they can be used for processing (data portability).

The raw data collected by multiple sources are processed and integrated into a single database for processing. The data format depends upon the chosen ML algorithm and computational resources: e.g. scalar values are easily managed compared to multi dimensional matrices, and less sophisticated tools can be adopted. In this context, all data are numerical, therefore no transformation of features have been performed (categorical to numerical or images to numerical, for instance).

The dataset has to be checked for missing, erroneous, and inconsistent entries. The samples are removed from the data if identified as outliers, or corrected if possible (e.g. fault in sensors or human error in early processing).

The targets definition is generally straightforward as the desired outputs are defined in the initial phase of the project. However, in some cases, the same phenomenon output can translate in different targets. For instance, in this study, the spectral noise can be seen with different levels of complexity (narrow band, one-third octave or octave bands), but all refer to the same physical effects.

The features extraction is needed to obtain clean, organised, coherent and meaningful variables from the raw data. This phase is demanded both to experts in the field and to data scientists. Indeed, some features can be defined straightforwardly by theory or experimental evidence, in other cases ML is applied also to create, evaluate and enhance features. This is the case of feature extraction from images, or from multidimensional arrays, or the feature selection process used to discard redundant and needless variables. An application of these methodologies, also referred to as feature engineering, has been explained in Appendix A.1.

The collected data may be expressed in very different scales. In some algorithms, this may result in an involuntary weighting of the features. Therefore, it is important to normalise the different variables according to the information sought. Numerical variables x can be scaled in the interval [0-1]

$$x' = \frac{x - min(x)}{max(x) - min(x)} \tag{3.1}$$

but this approach can suppress the effect of outliers and in some situations they are needed to find non frequent patterns. A less disruptive way to normalise data is to apply z-score method:

$$x' = \frac{x - \overline{x}}{\sigma_x} \tag{3.2}$$

where $\overline{x}$ is the mean and σ_x the standard deviation. The features will be rescaled so that they will have the properties of a standard normal distribution with zero mean and unitary standard deviation.

In the present study the normalisation 0-1 has been used in the ML approaches of Chapter 8, instead in Chapter 9 has been used the z-score.

3.2.2 Machine learning training

The training is the phase in which the samples are presented to the algorithm to learn and build the mapping function h among inputs and outputs. The chosen learning algorithm $\mathscr{A}_{\mathcal{H}}$ must satisfactorily adapt to data typology and purposes and other needs as time, precision and number of parameters and hyperparameters. Different algorithms can be exploited and then the best one picked up.

Most of ML algorithms come both with parameters and hyperparameters $\mathcal{H}$ to be tuned. When the best set of parameters has been found, the learned function h is known. Hence, within the same algorithm, many models exist, each characterised by different values of the parameters.

A model parameter is a variable that is internal to the model and whose value is estimated from data. For instance the coefficients of a linear regression or the weights of a neural network are parameters. The estimation of parameters by data

fitting is called model training. Model parameters can be estimated using a brute force method (trying all possible combinations), when they are few in number and the search domain is limited, or by an optimisation algorithm, which is an efficient search through possible parameter values.

Conversely, hyperparameters are set a priori according to data scientist experience and tuned with a trial and error procedure. It must be said that, even for complex models the hyperparameters are usually in limited number. As an example, hyperparameters can be the degree of a polynomial regression or, for a neural net, the number of neurons on each layer.

Independently from the chosen algorithm, every model needs to be tested on a real-world scenario to assess the generalisation performances. In order to assess the performance of the model and detect the optimum set of parameters and hyperparameters, a rigorous procedure must be followed, otherwise the accuracy of the model could be too optimistically biased. Therefore, the common approach is to split the dataset in three subsets called respectively training, validation and test set.

The training set is exploited to tune the model's parameters, hence the model see and learns only from this data.

The validation set is needed to seek for the best set of hyperparameters and it provides an unbiased evaluation of the model fitted on the training set. Moreover, it can be used for some techniques of regularisation (see Subsection 3.2.3.1) to prevent memorisation on the training set instead of generalisation. Therefore, the validation and the training set are employed to build the model and hence the accuracy must be assessed on a group of data totally new.

The test set is a completely new set of data, which allows to check the model predictive performances in unseen cases.

It is important to note that the test set is needed since the error that h would commit over the training or the validation set would be too optimistically biased since they have been used to tune h. The split must be random to keep the same probability distribution over the subsets. A typical splitting percentage is 70% in the training set, 20% in the validation set, and the remain 10% in the test set. The percentages can be changed according to specific situations, for instance if there are many hyperparameters to be tuned, it can be useful to enlarge the validation set.

3.2.3 Model selection

In real applications, the mere split of the dataset in three parts is not sufficient to achieve a well performing tool neither to get a trustful estimation of the error that h would commit on unseen data, as the performance estimation relies on the random selection of the test set.

This subsection describes the main sources of error in the prediction of unseen cases, and the procedures used to get an unbiased estimate of predictive accuracy.

The term Model Selection (MS) refers to all the techniques and procedures used to select the hyperparameters (or the algorithm) producing the mapping function with the smallest generalisation error.

The generalisation error is the error committed predicting targets for previously unseen data, using h in place of μ. This error (Shalev-Shwartz and Ben-David, 2014) can be decomposed in:

- approximation error, that is the minimum error achievable when considering a specific algorithm and hyperparameters domain (hypothesis class) in modelling a real-life phenomenon. This error is related to a wrong choice of the algorithm (e.g. a linear regression to shape data distributed with a quadratic trend or search the best hyperparameters in a wrong subset of their domain);

- estimation error is the smallest error achievable on the available sample set. The estimation error results because the predictor is built minimising the error on the sample set, that is only an estimate of the true error on the population.

Another way to analyse the error decomposition is respect to the so called bias variance trade-off.

Learning bias is the effect of erroneous assumptions in machine learning processes that causes it to over-generalise and underfit the data. This can be generated by the contents of the data, e.g. if the data samples are not representative of the population, if there are a conspicuous number of outliers, or the noise is dominant, or even the features are not able to describe the physical context. Lastly, the chosen algorithm can be not suited to solve the problem under study.

In contrast, the variance is the sensitivity to small fluctuations in the data and it causes the model to memorise instead to generalise. This is the typical problem of too complex models such as high polynomial regressors, or neural networks with too layers/neurons. Hence, the number of parameters is too large compared to the number of samples. Bias and variance are the outcome of opposite errors in the process used to create a ML tool, hence, the countermeasures to face the bias lead to an increase in variance and viceversa. In Figure 3.3 the bias variance trade-off is depicted, the model to be found is the one that minimise the generalization error.

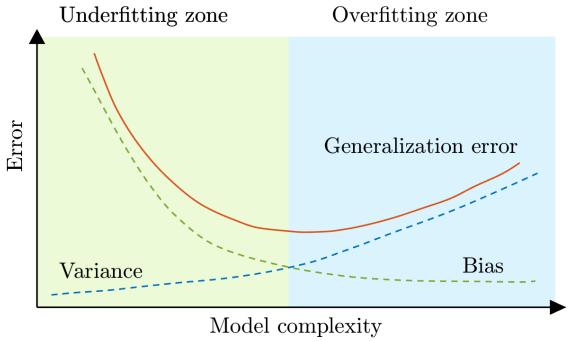

Figure 3.3: Bias-variance trade off.

3.2.3.1 Overfitting and underfitting

In models affected by high variance and low bias overfitting occurs. A model overfits the data when it memorises the training data instead of learning the generic pattern. This situation is easily detected observing that the error in the training set is much smaller than the one computed on the validation (or test) set. Figure 3.4 presents some examples of fitting on experimental data distributed along a third degree polynomial, plus some noise that is naturally contained in experimental data. If the

model considered is too complex (an higher degree polynomial regressor), overfitting occurs, meaning that the model shapes the noise instead of the inherent trend. In this way the error on the training set is ridiculously low, but on the validation set it is unacceptably high.

Conversely, underfitting occurs when a model cannot capture the underlying trend of the data; usually it occurs in models with a low variance and a high bias. For instance, when fitting a linear model to non-linear data as in Figure 3.4. In this case the performance is degraded in both training and validation set.

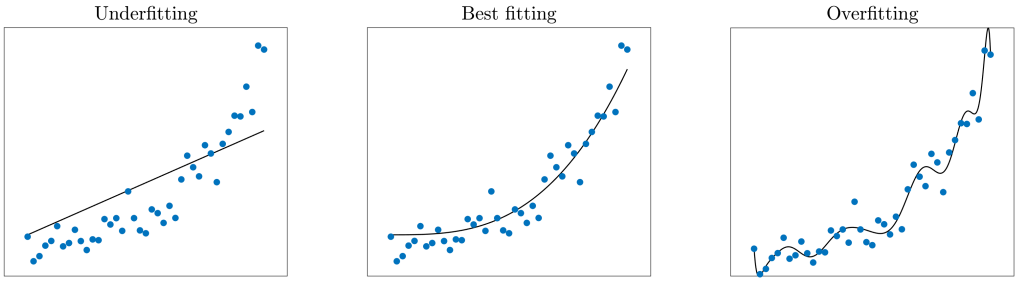

Figure 3.4: Overfitting and underfitting in regression.

A model with an high error on the training set is a model with a high bias, instead a model with a small error in the training set but high error on the validation (or test) is a model with high variance. Furthermore, in high variance models, the error on the validation set is strongly fluctuating depending on the selection of the sample subsets.

A possible solution to the underfitting is to improve step by step the model complexity and select a better representative training set, if possible adding more meaningful data. Increasing the dataset is applicable also to reduce variance, and in general it is a countermeasure adopted to face up many problems in ML.

Other countermeasures to reduce the variance are the reduction of the model complexity, the reduction of the number of features (especially if they are too many respect to the sample size), the regularisation and the early stopping.

Regularisation refers to a wide range of techniques used to force the model to be simpler, adding a penalty to the error when the model tends to increase its complexity. The method depends on the type of learner used. For instance, when performing polynomial regression, the degree of the polynomial is a hyperparameter that has to be found. If no regularisation is considered, the model will be prone to overfitting increasing the polynomial degree.

During the training phase, the quality of the learned function $h(\boldsymbol{x})$ can be measured according to a loss function $\ell(h(\boldsymbol{x}), y)$ (Rosasco et al., 2004) that is a method to evaluate the model predictive performance; the resulting empirical error is

$$\hat{L}_n(h) = \frac{1}{n} \sum_{i=1}^{n} \ell(h(\boldsymbol{x}_i), y_i)\,. \tag{3.3}$$

Several loss functions exist depending on the problem; for regression the most popular are the square error loss, and the absolute error loss (Equation 8.1). A simple criterion for selecting the final model during the training phase could then consist

in simply choosing the approximating function that minimises the empirical error $\hat{L}_n(h)$. This approach is known as Empirical Risk Minimisation (ERM) (Vapnik, 1998). However, ERM is usually avoided in ML as it leads to severe overfitting of the model on the training dataset. As a matter of fact, in this case the training process could choose a model, complicated enough to perfectly describe all the training samples (including noise, which afflicts them).

A more effective approach is to minimise a loss function where the trade-off between accuracy on the training data and a measure of the complexity of the selected model is achieved (Tikhonov and Arsenin, 1979), implementing the simple regularisation principle

$$h^* : \quad \min_h \quad \hat{L}_n(h) + \lambda \, C(h) \, . \tag{3.4}$$

In other words, the best approximating function h^* is chosen as the one that is complicated enough to learn from data without overfitting them. In particular, $C(\cdot)$ is a complexity measure depending on the exploited ML approach (an example is visible in Sections 3.3 and A.1). Instead, $\lambda \in [0, \infty)$ is a hyperparameter, that must be aprioristically set and is not obtained as an output of the optimisation procedure: it regulates the trade-off between the overfitting tendency, related to the minimisation of the empirical error, and the underfitting tendency, related to the minimisation of $C(\cdot)$. The optimal value for λ is problem-dependent, and tuning this hyperparameter is a non-trivial task, as it will be discussed in Section 8.3 and Section A.1.

3.2.3.2 Cross validation

A useful technique to improve estimate accuracy and detect overfitting is the cross-validation. A primitive way has been presented in the previous subsection and it consists in randomly splitting the dataset $\mathcal{S}_p$ in train, validation and test sets. The first two subsets ($\mathcal{D}_n$) are used to build the model, the latter ($\mathcal{T}_m$) is instead used to evaluate it. This method is misleading when the original dataset size is limited, because some important information can be missed, or when input data are not drawn from the same distribution, hence they may follow different patterns. The accuracy so evaluated can be largely biased.

More advanced techniques are the leave one out and the resampling methods. In leave one out, the training is performed on the whole dataset but one point is left out as validation sample, and then the procedure is iterated for each data-point. The final performance metrics are the mean of the performance computed for each iteration, usually together whit their t-student 95% confidence interval.

An advantage of using this method is that all the information is retained and hence it results in low bias. The major drawback of this method is that it leads to severe variation in the testing performances, and it requires significant execution time since it iterates over the entire dataset. More statistically robust approaches are the sampling methods, like the well-known k-Fold Cross Validation (Kohavi et al., 1995) or the nonparametric Bootstrap BTS (Efron and Tibshirani, 1994); they represent the state-of-the-art MS approaches when targeting real-world applications. The dataset $\mathcal{D}_n$ is resampled once or many (n_r) times, to build two independent training and validation sets, called respectively $\mathcal{L}_l^r$ and $\mathcal{V}_v^r$, with $r \in \{1, \cdots, n_r\}$. Note that $\mathcal{L}_l^r \cap \mathcal{V}_v^r = \oslash$, $\mathcal{L}_l^r \cup \mathcal{V}_v^r = \mathcal{D}_n$; n, l, v are the number of samples contained

respectively in the building, in the training and in the validation set. Then, in order to select the best combination of hyperparameters $\mathcal{H}$ in a set of possible ones $\mathfrak{H} = \{\mathcal{H}_1, \mathcal{H}_2, \cdots\}$ for the algorithm $\mathscr{A}_{\mathcal{H}}$ or, in other words, to perform the MS phase, the following procedure has to be applied:

$$\mathcal{H}^* : \quad \min_{\mathcal{H}\in\mathfrak{H}} \frac{1}{n_r}\sum_{r=1}^{n_r}\frac{1}{v}\sum_{(\boldsymbol{x}_i,y_i)\in\mathcal{V}_v^r} \ell(\mathscr{A}_{\mathcal{H},\mathcal{L}_l^r}(\boldsymbol{x}_i), y_i)\,, \tag{3.5}$$

where $\mathscr{A}_{\mathcal{H},\mathcal{L}_l^r}$ is a model built with the algorithm $\mathscr{A}$ with its set of hyperparameters $\mathcal{H}$ and with the data $\mathcal{L}_l^r$. Since the data in $\mathcal{L}_l^r$ are independent from those in $\mathcal{V}_v^r$, the idea is that $\mathcal{H}^*$ should be the set of hyperparameters allowing to achieve a small error on a data set that is independent from the training set. The quality of the prediction is measured by the loss function $\ell(h(\boldsymbol{x}_i, y_i))$ (e.g. mean square error).

In the k-fold cross validation, $\mathcal{D}_n$ is at first shuffled, then randomly divided in k subset: one of the subset is used as validation set, the others k-1 are the training set (see Figure 3.5a, in each box multiple items of $\mathcal{D}_n$ are contained).

For each validation fold, a model is fitted on the k-1 training folds and the performance metrics evaluated on validation fold. The number of samples is equally subdivided among the folds, and every item is considered only once. Hence k-fold is a resampling method without replacement, and $l < n$, $v = n - l$. A typical application is the 10-fold cross validation.

Note that, each observation in the data sample is assigned to an individual group and stays in that group for the duration of the procedure. This means that each sample is used in the validation set 1 time and used to train the model k-1 times. Generally, if the number of splits k is increased, the variance will increase and bias will decrease as the number of element in the validation set is reduced. On contrast, if k is reduced, the bias will increase and variance will decrease. The average error is found as

$$\overline{E} = \frac{1}{k}\sum_{i=1}^{k} E_i\,, \tag{3.6}$$

where E_i is the error computed on each validation fold. In the bootstrap, $\mathcal{D}_n$ is at first shuffled, then for the k-th bootstrap cycle: n items are sampled with replacement from $\mathcal{D}_n$ to be placed in the training set; then all values in the dataset have an equal probability of being selected multiple times.

The remaining items are put in the validation set, hence $l = n$ and v change over iterations. In Figure 3.5b, the dataset is composed by ten items (x_i), at every bootstrap iteration the training set can be made up of repeated values to get $l = n$. For each validation set, a model is built on its training set and evaluated. This method is useful when the number of samples is too limited to efficiently build a model, compared with the number of parameters. With Bootstrap the training set has always the same size of $\mathcal{D}_n$. The averaged error is found again by Equation 3.6. Lastly, the t-student 95% confidence interval is computed as follows. The standard deviation of the errors on the iterations is

$$SE = \sqrt{\frac{1}{n_r - 1}\sum_{i=1}^{n_r}(E_i - \overline{E})^2}\,, \tag{3.7}$$

(a) k-fold cross validation.

(b) Bootstrap.

Figure 3.5: Resampling procedures for model evaluation.

where n_r is the number of fold or bootstrap iterations. From the Student's t-distribution table, given $\alpha = 0.95$ (confidence level of 95%) and the degree of freedom $n_r - 1$, the 95-th percentile of the cumulative distribution function t is found.

The confidence interval is then

$$CI = \overline{E} \pm t \frac{SE}{\sqrt{n_r}}. \tag{3.8}$$

3.2.4 Final model evaluation

In the previous subsections the problems affecting the ML training and the procedures to get unbiased estimation of the models have been described. Up to now, nothing has been said on $\mathcal{T}_m$ and how to choose the best model to perform the task at hand. In the previous explanation, the complete dataset $\mathcal{S}_p$ has been divided once in $\mathcal{D}_n$ and $\mathcal{T}_m$, later the focus has been put on the iterative procedures (k-fold and bootstrap) to get the training set and the validation set from $\mathcal{D}_n$. The main reason to perform the split iteratively is to ensure the statistical relevance, otherwise a particular lucky split (training/validation) will results in optimistically biased performances.

The same applies to the subdivision $\mathcal{T}_m/\mathcal{D}_n$. If performed only once, nothing can be said on the sensitivity of the performance to different test sets. Therefore, the MS techniques (leave-one-out, k-fold and bootstrap) should be carried out both on the $\mathcal{T}_m/\mathcal{D}_n$ split and on the $\mathcal{L}_l^r / \mathcal{V}_v^r$ split.

In Figure 3.6 an example of a nested k-fold cross validation is shown.

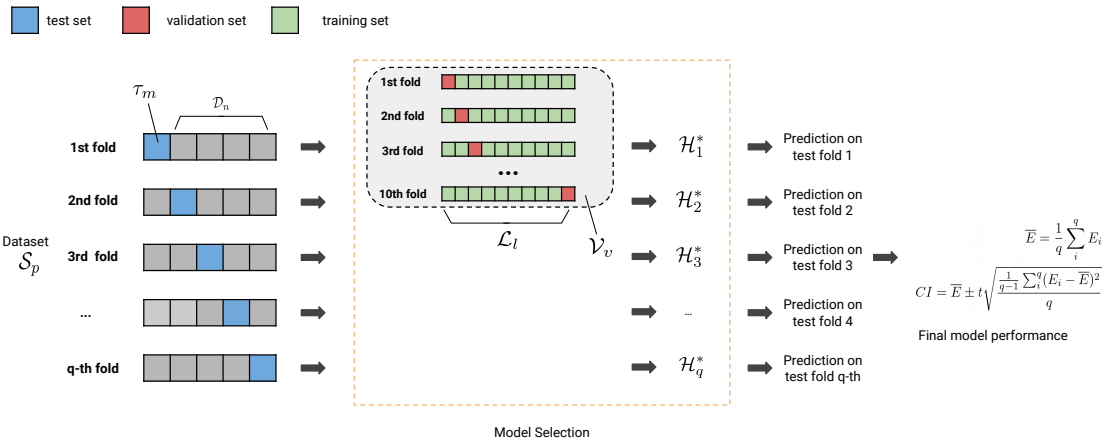

Figure 3.6: Nested cross-validation.

The procedure can be summarised as follow:

1. random subdivision of the dataset $\mathcal{S}_p$ in test set $\mathcal{T}_m$ and $\mathcal{D}_n$ (with k-fold or other methods)
2. for each combination of $\mathcal{T}_m$ and $\mathcal{D}_n$
   - 2.1. random subdivision of $\mathcal{D}_n$ (with k-fold or other method) in many training set $\mathcal{L}^l$ e validation set $\mathcal{V}_v$
   - 2.2. for each set of hyperparameters
     - 2.2.1. the learning phase on each $\mathcal{L}_l$ is performed to get the model parameters, then the accuracy is evaluated on the respective validation set
   - 2.3. for each $\mathcal{D}_n$ only the set $\mathcal{H}^*$ (hence only the best model) that result in the minimum average error on the validation sets is kept
3. the targets of the test set $\mathcal{T}_m$ are predicted and the accuracy evaluated
4. the performance indexes are averaged and confidence intervals calculated

At this stage, the prediction accuracy for unseen cases is found but the model is not ready to be used because the final hyperparameters are unknown. The last step, called new data prediction (Subsection 3.3.1), consists in use the complete dataset $\mathcal{S}_p$ and evaluate the definitive hyperparameters to be used for future predictions.

3.2.5 Feature mapping

Let us consider a classification problem where the inputs are real number x in the range $[-10, 10]$, the labels are +1 for $|x| > 2$ and -1 otherwise. An hyperplane able to efficiently separate the two classes does not exist in $\mathbb{R}$. A possible approach is to consider a space of higher dimension and learn an hyperplane in that domain. For instance, the mapping function $\boldsymbol{\varphi(x)} = (x, x^2)$ transforms $\mathbb{R} \to \mathbb{R}^2$. The graphical representation of this new features space is shown in Figure 3.7. In $\boldsymbol{\varphi}(x)$ the data can be easily explained by the hyperplane (which is a line in $\mathbb{R}^2$): $h(x) = sign(\boldsymbol{w} \cdot \boldsymbol{\varphi}(x) - b)$ with $\boldsymbol{w} = (0, 1)$ and b = 5 (Table 3.1).

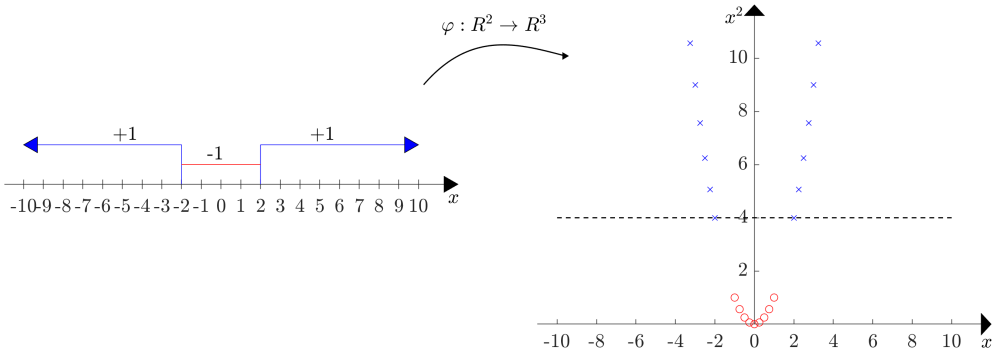

Figure 3.7: Feature mapping $\mathbb{R} \rightarrow \mathbb{R}^2$.

Table 3.1: Classification problem after feature mapping.

x	$\varphi(x)$	$h(x)$
-10	(-10,100)	+1
...	...	...
-3	(-3,9)	+1
-2	(-2,4)	-1
-1	(-1,1)	-1
0	(0,0)	-1
1	(1,1)	-1
2	(2,4)	-1
3	(3,9)	+1
...	...	...

Another example is the classification of samples with respect to their distance from the origin. In Figure 3.8 the data whose distance from (0,0) is lower than one belong to class 1, the other to class 2. They can be easily discriminated in $\mathbb{R}^3$ by an hyperplane according to the feature map $\varphi(x_1, x_2) : (z_1, z_2, z_3) = (x_1^2, \sqrt{2}x_1x_2, x_2^2)$.

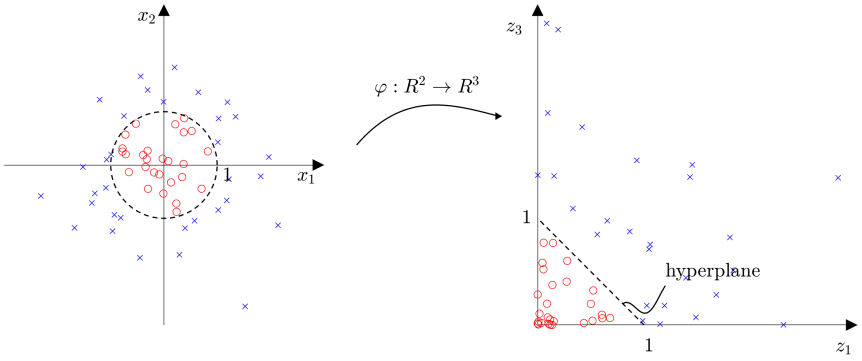

Figure 3.8: Feature mapping $\mathbb{R}^2 \rightarrow \mathbb{R}^3$.

Therefore, a Feature Map (FM) is a non-linear function which maps data vector from the feature space to a new space (Shalev-Shwartz and Ben-David, 2014), usually of higher dimension, where a linear regressor or classifier can be learned. Remapping data can allow non-linearly separable data to become linearly separable by a hyperplane in a higher dimension. The main aim is to present to the learning algorithm data that it is better able to regress or classify, to enhance accuracy in

prediction.

Infinite types and combinations of feature mapping exist, according to the specific problem under study; for instance a FM is used in Chapter 8.

The FM is a powerful solution to afford complex task but it come with some drawbacks. Firstly, when working in higher dimension, the number of parameters to be learned increases. In the first example, in the original feature space the hyperplane is reduced to a point but after the feature mapping it transforms to a line and the parameters to be learnt become three ($\boldsymbol{w}$ and b).

If the range of $\boldsymbol{\varphi}(x)$ is very large, the amount of data needed to support the result often grows exponentially with the dimensionality. Moreover, moving to higher spaces increases the sparsity of the data (curse of dimensionality) because the inner distance between data point increases, hence patterns can be lost. Eventually, performing computation in high dimension can be unfeasible.

A possible solution to this concern is use of kernel based learning: this technique allows to retain the advantages of performing FM but at the same time it reduces the number of calculations required, avoiding the direct computation in the higher dimension space.

The learning approaches considered in present thesis may be divided in two main families: the first one is based on Kernel Regularised Least Squares while the second is based on neural networks. Both approached have been developed and implemented in collaboration with a research group of the University of Genoa specialised in data science. Since the study of theory and implementation of the first method has been an important part of present thesis, it is briefly described in Section 3.3. On the contrary the description of the second approach is reported only in appendix, being its development outside the scope of the thesis.

3.3 Kernel Regularised Least Squares

In this thesis, a method from the ML kernel methods family, called Kernel Regularized Least Squares (KRLS), has been adopted in order to predict the cavitating noise spectrum $\boldsymbol{y} \in \mathcal{Y}$. Given a suitable set of features $\boldsymbol{x}$ belonging to the features space $\mathcal{X}$, in KRLS models are defined as

$$h(\boldsymbol{x}) = \boldsymbol{w}^T \boldsymbol{\varphi}(\boldsymbol{x}) \,, \tag{3.9}$$

where $\boldsymbol{w}$ is an unknown weight vector, and $\boldsymbol{\varphi}$ is an a priori defined feature mapping (Shalev-Shwartz and Ben-David, 2014), which strongly depends on the particular problem under examination and will be described in Section 8.3, allowing to keep the structure of $h(\boldsymbol{x})$ linear.

During the training phase, the quality of the learned function $h(\boldsymbol{x})$ can be measured according to a loss function $\ell(h(\boldsymbol{x}), y)$ (Rosasco et al., 2004); the resulting empirical error is

$$\hat{L}_n(h) = \frac{1}{n} \sum_{i=1}^{n} \ell(h(\boldsymbol{x}_i), y_i) \,. \tag{3.10}$$

Recalling the regularisation approach discussed in Sub subsection 3.2.3.1 to prevent overfitting, the complexity of the models, in KRLS, is measured as

$$C(h) = \|\boldsymbol{w}\|^2 \,, \tag{3.11}$$

i.e. the Euclidean norm of the set of weights describing the regressor, which is a quite standard complexity measure in ML (Shalev-Shwartz and Ben-David, 2014). Regarding the loss function, the square loss is typically adopted because of its convexity, smoothness, and statistical properties (Rosasco et al., 2004)

$$\hat{L}_n(h) = \frac{1}{n}\sum_{i=1}^{n} \ell(h(\boldsymbol{x}_i), y_i) = \frac{1}{n}\sum_{i=1}^{n} \left[h(\boldsymbol{x}_i) - y_i\right]^2 . \tag{3.12}$$

Consequently, Problem (3.4) can be reformulated as

$$\boldsymbol{w}^* : \quad \min_{\boldsymbol{w}} \quad \sum_{i=1}^{n} \left[\boldsymbol{w}^T \boldsymbol{\varphi}(\boldsymbol{x}) - y_i\right]^2 + \lambda \|\boldsymbol{w}\|^2 . \tag{3.13}$$

By exploiting the Representer Theorem (Schölkopf, Herbrich, and Smola, 2001), the solution h^* of the RLS Problem (3.13) can be expressed as a linear combination of the samples projected in the space defined by $\boldsymbol{\varphi}$

$$h^*(\boldsymbol{x}) = \sum_{i=1}^{n} \alpha_i \boldsymbol{\varphi}(\boldsymbol{x}_i)^T \boldsymbol{\varphi}(\boldsymbol{x}) . \tag{3.14}$$

It is worth underlining that, according to the kernel trick, it is possible to reformulate $h^*(\boldsymbol{x})$ without an explicit knowledge of $\boldsymbol{\varphi}$, and consequently avoiding the course of dimensionality of computing $\boldsymbol{\varphi}$, by using a proper kernel function $K(\boldsymbol{x}_i, \boldsymbol{x}) = \boldsymbol{\varphi}(\boldsymbol{x}_i)^T \boldsymbol{\varphi}(\boldsymbol{x})$

As an example, let us consider $\boldsymbol{a}, \boldsymbol{b} \in \mathbb{R}^2$ and the transformation in $\mathbb{R}^4$ by means of $\varphi(a_1, a_2) = (a_1 a_2, a_2 a_1, a_1^2, a_2^2)$; in this case

$$\begin{aligned} &\varphi(a_1, a_2) \cdot \varphi(b_1, b_2) = \\ &\quad = (a_1 a_2, a_2 a_1, a_1^2, a_2^2)^T \cdot (b_1 b_2, b_2 b_1, b_1^2, b_2^2) = a_1^2 b_1^2 + 2 a_1 a_2 b_1 b_2 + a_2^2 b_2^2 , \end{aligned} \tag{3.15}$$

that is 4x2 operations to get the feature mapping, and 3 operations to get the scalar product.

Conversely, it can be noticed that

$$(\boldsymbol{a}^T \boldsymbol{b})^2 = ((a_1, a_2)^T \cdot (b_1, b_2))^2 = (a_1 b_1 + a_2 b_2)^2 = a_1^2 b_1^2 + 2 a_1 a_2 b_1 b_2 + a_2^2 b_2^2 , \tag{3.16}$$

allows to obtain the same results but with 3 operations only. The last expression is equivalent to a polynomial kernel of second degree $K(\boldsymbol{a}, \boldsymbol{b}) = (\boldsymbol{a}^T \boldsymbol{b})^2$. The main advantage of such algorithms is that they implement linear separators in high dimensional feature spaces without having to specify points in that space explicitly (corresponding to the second term in Equation 3.15).

Several kernel functions can be retrieved in literature (Scholkopf, 2001; Cristianini and Shawe-Taylor, 2000), each one with a particular property that can be exploited based on the problem under exam.

The solution in Equation 3.14 can be rewritten as

$$h^*(\boldsymbol{x}) = \sum_{i=1}^{n} \alpha_i K(\boldsymbol{x}_i, \boldsymbol{x}) . \tag{3.17}$$

The KRLS problem of Equation (3.13) can be reformulated by exploiting kernels as

$$\boldsymbol{\alpha}^* : \quad \min_{\boldsymbol{\alpha}} \quad \|Q\boldsymbol{\alpha} - \boldsymbol{y}\|^2 + \lambda \boldsymbol{\alpha}^T Q \boldsymbol{\alpha}\,, \tag{3.18}$$

where $\boldsymbol{y} = [y_1, \ldots, y_n]^T$, $\boldsymbol{\alpha} = [\alpha_1, \ldots, \alpha_n]^T \in \mathbb{R}^n$, the matrix Q such that $Q_{i,j} = K(\boldsymbol{x}_j, \boldsymbol{x}_i)$, and the identity matrix $I \in \mathbb{R}^{n \times n}$. Equation 3.18 is convex in $\boldsymbol{\alpha}$, and by setting equal to zero the gradient with respect to $\boldsymbol{\alpha}$ it is possible to state that

$$(Q + \lambda I)\, \boldsymbol{\alpha}^* = \boldsymbol{y}\,, \tag{3.19}$$

that is a linear system for which effective solvers have been developed over the years, allowing coping with even very large sets of training data (Young, 2003).

The problems that still have to be faced is how to choose $\boldsymbol{\varphi}$, the kernel K, and how to set up the hyperparameter λ. They will be discussed in Section 8.3.

3.3.1 New data prediction

When the training phase is completed, the ML tool is almost ready to predict new data. At this stage the developer has found: the best algorithm, the optimal MS procedure, the performance indexes (such as mean square error, mean absolute error, R-squared etc.) and their confidence intervals. Therefore, the final regressor can be built. The procedure here depicted is relative to the KRLS but the concepts are the same for every ML algorithm.

1. On the whole dataset ($\mathcal{S}_p$, total number of samples $p = n + m$) the MS is performed to found the final set of hyperparameters. Hence $\mathcal{S}_p$ is repeatedly splitted in training set and validation set to solve Problem 3.5.

2. The best set of hyperparameters $\mathcal{H}^*$ so found is adopted to compute the final set of coefficients

$$\boldsymbol{\alpha^*} = \frac{Q + \lambda I}{\boldsymbol{y}}\,, \tag{3.20}$$

   where $\boldsymbol{y} = [y_1, \ldots, y_p]^T \in \mathbb{R}^p$, $\boldsymbol{\alpha^*} = [\alpha_1, \ldots, \alpha_p]^T \in \mathbb{R}^p$, the matrix $Q \in \mathbb{R}^{p \times p}$ such that $Q_{i,j} = K(\boldsymbol{x}_j, \boldsymbol{x}_i)$, and the identity matrix $I \in \mathbb{R}^{p \times p}$.

3. Hereinafter, every new blind prediction will be simply done as

$$y_{blind} = Q_{blind}\, \boldsymbol{\alpha^*}\,, \tag{3.21}$$

   with $Q_{blind} = [K(\boldsymbol{x}_1, \boldsymbol{x}_{blind}), ..., K(\boldsymbol{x}_p, \boldsymbol{x}_{blind})]$; $\boldsymbol{x}_{blind}$ is the array of features of the new case.

Chapter 4

Experimental tests

This chapter describes the facility where tests have been carried out, the model propellers characteristics and how tests have been designed and performed.

4.1 Introduction

Data acquisition is a fundamental step to succeed in ML and should be performed wisely. The physical phenomenon under examination should be fully characterised; this means as much as possible test cases (samples) in different working conditions and different types of acquisitions (sound, numerical data from sensors, video etc.). The quantities to be collected should be at first the input for the PMs, then other suitable variables can be included as well; if some will be unnecessary or redundant, they will be automatically discarded by DDM/HM training algorithm. If the phenomenon involved specimen and working configurations (as in this case are the propeller-pitch-wake) they should be homogeneous and the samples should be evenly distributed. The tests must be reliable, repeatable and must follow well established procedures and regulations if applicable.

In this chapter the procedure built at UNIGE cavitation tunnel for data acquisitions is outlined. A special emphasis will be reserved to the blocks most important to the ML purposes. In Section 4.2 a quick overview of the tunnel characteristics and of the measurement devices is given. In Section 4.3 the model propellers are presented and in Sections 4.4 and 4.5 the wakes adopted and the cavitation tests. A better insight is dedicated to the radiated noise tests in Section 4.6 and to the immediate post-processing.

4.2 UNIGE cavitation tunnel

Experiments carried out for the development of models presented in this thesis have been performed at the cavitation tunnel of the University of Genoa. The facility (Figure 4.1) is a Kempf & Remmers K22 closed-circuit tunnel with a squared testing section of $0.57\,\mathrm{m} \times 0.57\,\mathrm{m}$, 2 m long. The distance between horizontal limbs is 4.54 m, while between the vertical ones is 8.15 m. Thrust, torque and revolution rate of the propeller are measured by a Kempf & Remmers H39 dynamometer. Maximum flow speed allowed in test section is 8.5 m/s and the maximum revolution rate is 50 Hz. The maximum torque sustainable by the dynamometer is $500\,\mathrm{kg_f\,cm}$

and the maximum thrust 100 kg_f. Due to strength limits of the model propellers and to the above maximum loads allowed on the dynamometer, the usual operating range of rate of rotation is between 15 and 35 Hz. Two vacuum pumps are arranged to reduce the pressure into the tunnel. No cavitation nuclei counter are present,

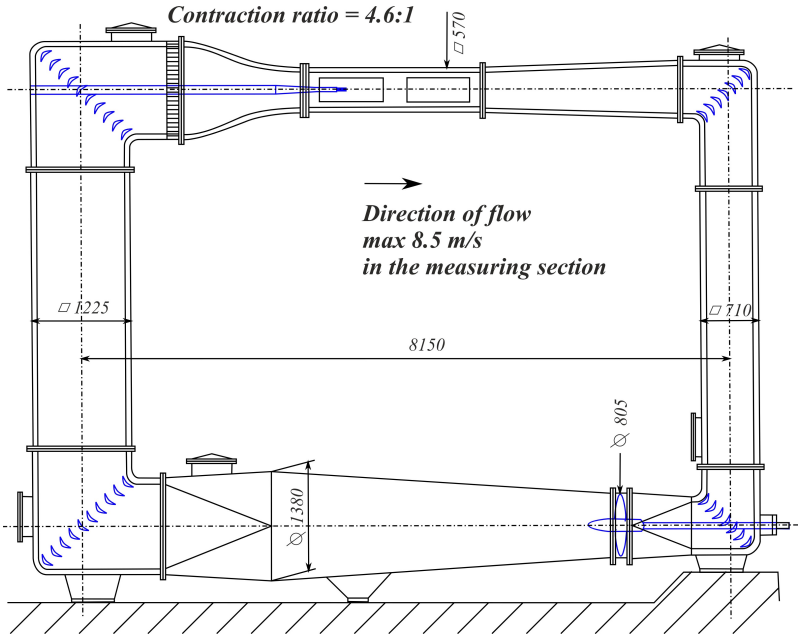

Figure 4.1: University of Genoa cavitation tunnel.

the water susceptibility to cavitation is estimated by the dissolved oxygen content which is monitored by an ABB sensor model 8012/70, coupled with the ABB AX 400 analyser. The optimal air content depends on the facility as well as on the operative conditions. For tests considered in present work, the optimum value is mostly comprised between 3.7 and 4.5 ppm.

The cavitation phenomena are visualised with a stroboscope and two hand lamps, while photos are taken with three Allied Vision Tech Marlin F145B2 Firewire cameras, with a resolution of 1392 × 1040 pixels (Figure 4.2). The tunnel is equipped with a Laser Doppler Velocimetry system with back-scatter collection optics by Dantec (Figure 4.3), for detailed non-intrusive flow measurements. The laser head is the model 177G-0232 provided by Spectra Physics, 5 W argon-ion laser, air-cooled, with a beam diameter of 0.82 mm. The 2D laser system is composed by a green light (wavelength of 514 nm) and a blue light (wavelength of 488 nm); the measuring volume is an ellipsoid whose minor and major diameters are 190 μm and 4 mm respectively. Propeller noise measurements are picked up with two hydrophones (namely a Bruel & Kjaer 8103, as in Figure 4.4b, and a Reson TC4013), connected to two Bruel & Kjaer 2635 amplifiers. For pressure pulses surveys, five differential Kulite XTL-190M-5G transducers are available (Figure 4.4a).

4.3 Propeller test cases and set-ups

Model scale tests have been performed on two controllable pitch propellers (CPP), respectively referred to as Propeller 1 (P1) and Propeller 2 (P2), at various pitches. Another CP propeller, P3, whose tests have been performed previously, has been

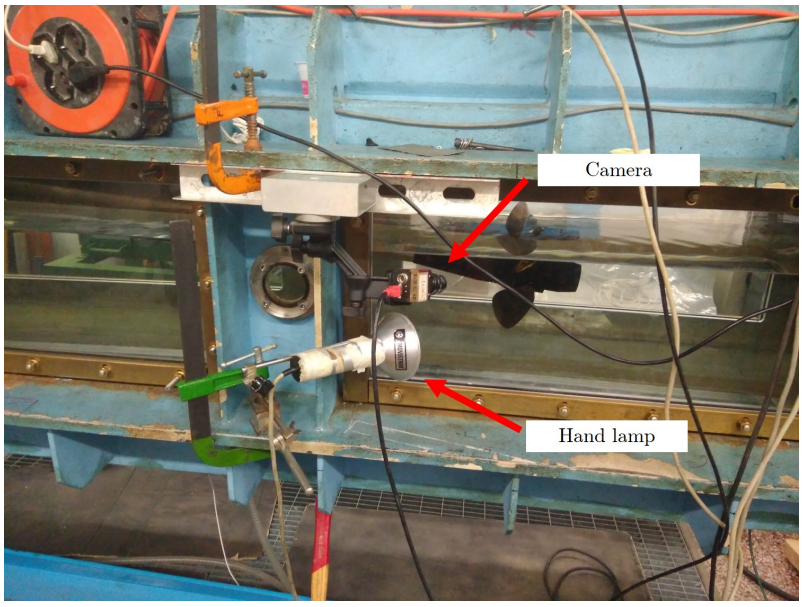

Figure 4.2: Photographs set-up.

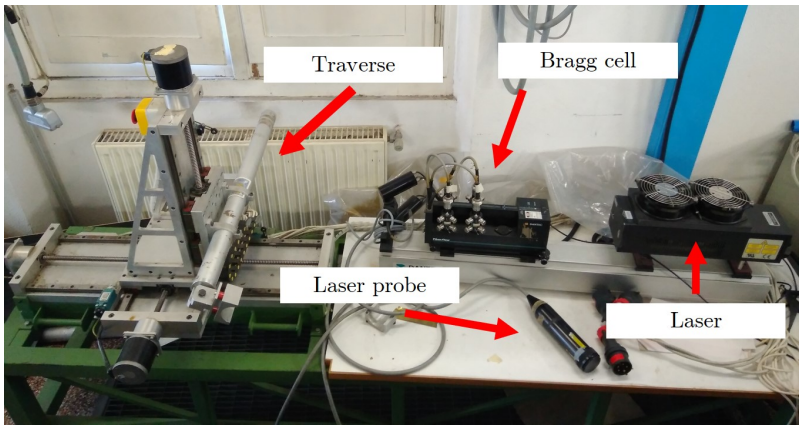

Figure 4.3: LDV arrangement for wake survey.

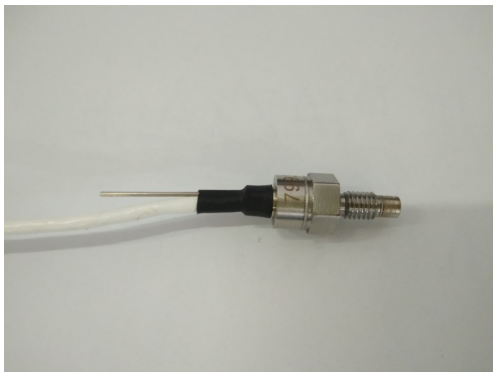

(a) Pressure transducer Kulite XTL-190M-5G.

(b) Hydrophone Bruel & Kjaer 8103.

Figure 4.4: Main sensors.

included in the current dataset. All the tests on P3 have been conducted following the same methodologies and the same instruments here described. The main

characteristics of the propellers are reported in Table 4.1.

Table 4.1: The model propellers characteristics.

Variable	*abbr.*	P1	P2	P3
Number of blades		5	5	5
Diameter		0.25 m	0.25 m	0.2639 m
BAR		0.755	0.6129	0.6549
Direction of rotation		Right	Right	Right
Design pitch ratio at $0.7R$	DES	1.385	1.156	1.440
Reduced (-3°) pitch ratio at $0.7R$	RED3	1.229	1.013	
Reduced (-5°) pitch ratio at $0.7R$	RED5	-	0.938	
Reduced (-6°) pitch ratio at $0.7R$	RED6	1.082	-	
Incremented (+2°) pitch ratio at $0.7R$	INC2	-	1.256	
Shaft inclination		6.8°	2.5°	6.4°

To obtain a complete characterisation of the cavitation pattern and its influence in the sound generation, for each configuration a complete set of tests have been conducted as wake survey, cavitation bucket, cavitation pattern, pressure pulses and radiated noise measurements in a large set of operational conditions.

The propeller loading conditions for model tests (also called functioning points or working points WP) are defined by the pair (K_T, σ_n), where K_T is the thrust coefficient and σ_n is the cavitation number based on rotational speed. The first coefficient represents the kinematic condition of the propeller while the cavitation number defines a cavitation similarity criterion.

4.4 Wake survey

The full scale propeller arrangement of interest is that typical of twin screw vessel, hence propeller inflow is set reproducing in the cavitation tunnel the characteristics of typical wake fields of this kind. The axial wake fields are simulated for propeller P1 and P2 by means of a mock-up of the shaft line with brackets and a small dummy hull on which wake screens are mounted (see Figure 4.5); the propeller is settled in pulling configuration. Shaft inclination is adopted in order to reproduce the significant upward velocity component present on the propeller disk for twin screw ships.

For each propeller a dedicated wake field have been simulated (see Table 4.2 for all combinations of propeller/wake), then only for P1 at design pitch, also the uniform inflow case, with inclined shaft, has been considered. In the latter case (named W2) the propeller is mounted in pushing configuration to make the hub vortex visible. Hence, the only disturbance in the water inflow is the tiny wake of the dynamometer shaft, whose effect on cavitation is negligible. P3 has been tested

Table 4.2: Propeller set-ups.

Pitch \ Propeller	P1	P2	P3
Design	×	●	▲
Reduced (-3°)	■	●	
Reduced (-5°)		●	
Reduced (-6°)	■		
Incremented (+2°)		●	

×W1 - W2 ■ W1 ● W3 ▲ W4 - W5 - W6

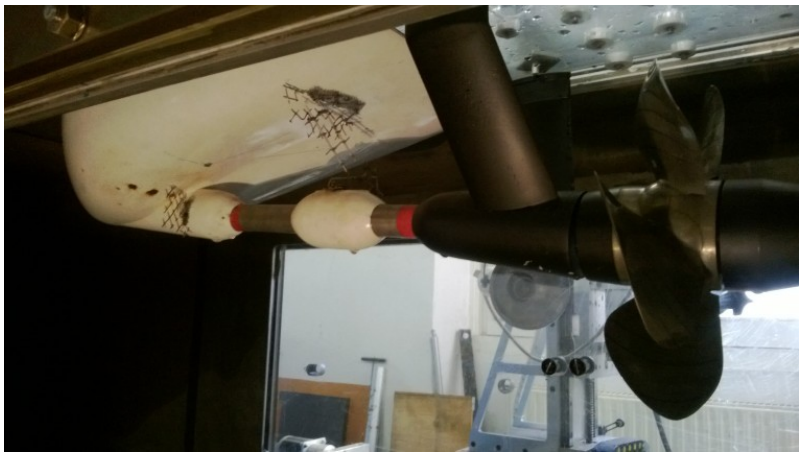

Figure 4.5: Dummy model and wire screen used in wake modelling for W1 and W3.

in pushing configuration too but shaft brackets are adopted (called W5, Figure 4.6) coupled with ad-hoc wake screen (W4, see Figure 4.7a) or parallel plates wake stimulator (W6, see Figure 4.7b). The wake W5 is similar to W2, indeed the only disturbance is given by the dynamometer vortices and in this case by the brackets too.

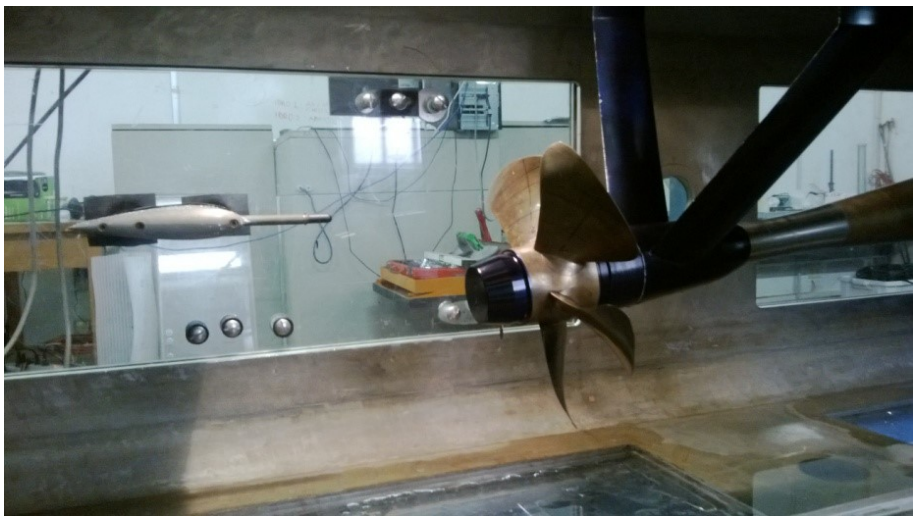

Figure 4.6: Shaft brackets and inclined shaft used in W5 modelling.

The compliance of the wake is checked by LDV survey: the laser collects the flow speed V_a point by point in compliance to measured wake in towing tank. Measured values are compared with the undisturbed flow velocity V, again sampled by LDV; the latter must be collected in the test section away from disturbance like dummy model, appendages or walls. The axial wake fraction w follows as $(1 - w) = V_a/V$. The survey is performed in absence of the propeller hence the result of the measurement is the nominal wake field.

Wakes are shown in Figure 4.8 with respect to vertical z/R and transversal y/R coordinate with reference to the propeller centerline, both normalised to the propeller radius R. The polar coordinate are set by the radial section r/R and the angle θ starting at the top dead center and increasing in the propeller direction of

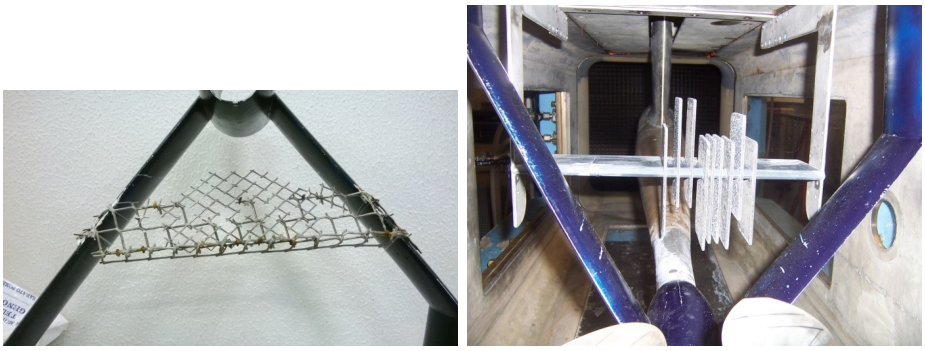

(a) Wake stimulator for W4. **(b)** Wake stimulator for W6.

Figure 4.7: Detail of the wake screen mounted on brackets for P3.

rotation. The wake W2 has not been collected by LDV, but it is similar to W5.

The complete description of these wakes and the extrapolated quantities are widely described in Section 6.4.

4.5 Cavitation tests

When the propeller set-up has been reproduced and the hydrodynamic performance of the propeller (in terms of propeller thrust and torque) evaluated, its cavitating behaviour can be assessed. In model scale tests the ship velocity is represented by the couple K_T and σ_n, in this way it is possible to simulate the full scale propeller functioning operating both on the flow velocity, the propeller speed and the tunnel internal pressure. The propeller speed is usually the maximum achievable without exceeding the maximum loads on the dynamometer, so to increase as much as possible the Reynolds number (commonly 25 Hz). Cavitation inception tests consist in the definition of the inception index for each cavitation typology of interest and for varying propeller kinematic conditions. This is achieved choosing a reasonable grid of thrust coefficients, centred around the propeller design point, and for each of them to lower gradually the pressure until the appearance of the cavitation type under study. During this descent the inceptions of cavitation are visually detected with the aid of the stroboscopic lamps. In the UNIGE tunnel it is not possible to over pressurise the tunnel, hence if at atmospheric pressure the cavitation is already visible, the good practice is to increase the cavitation number by lowering the revolution speed. For this reason a few tests have been carried out at 20 or 22.5 Hz.

Bubble cavitation is usually the most simple cavitation phenomenon to be detected, it appears almost instantly and it is less correlated to nuclei content and more to the local blade geometry which causes high suction pressures in the mid-chord region; hence the inception is usually well repeatable. Sheet cavitation is slightly less repeatable than bubble cavitation and more susceptible to Reynolds number and nuclei content. When there is not solution of continuity between the sheet and the tip vortex it is difficult to assess precisely the inception of the former. A rule of thumb can be to consider sheet cavitation when the cavity surface reaches the $0.9R$ or $0.95R$ of the blade.

The vortex cavitation may occur at the blade tip, at the leading edge and at the hub of the propeller. Cavitating vortices are generated by the travelling nuclei

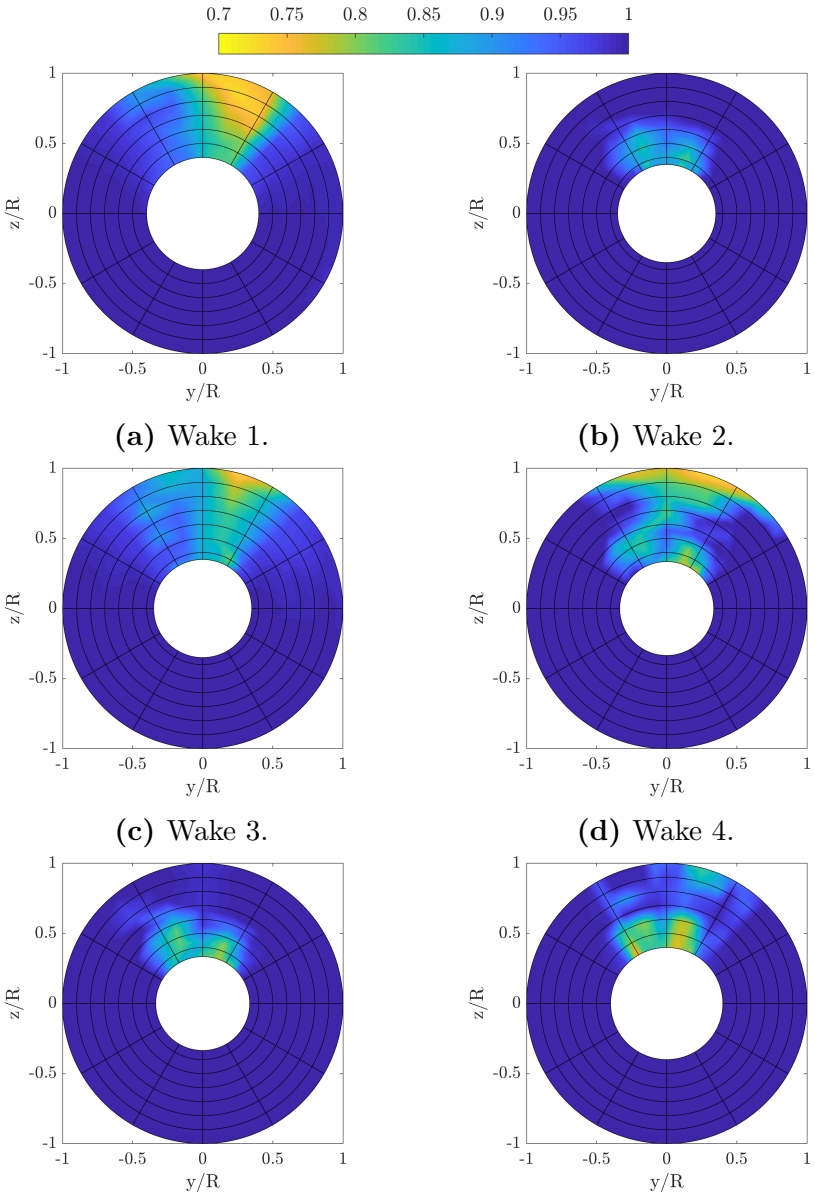

(a) Wake 1. **(b)** Wake 2.

(c) Wake 3. **(d)** Wake 4.

(e) Wake 5. **(f)** Wake 6.

Figure 4.8: Axial wake $(1 - w)$ for the P1, the P2, and for P3.

entrained in the low-pressure core of the shed vortices. The hub vortex is formed by the combination of the individual vortices shed from each blade root and, although individually these vortices are unlikely to cavitate given the weak bound circulation at inner radii, under the influence of a converging boss cap the combination of the blade root vortices has a high susceptibility to cavitate. This typology of cavitation is usually rather stable and moderately noisy.

The inception of the tip vortex is usually more complex to be defined and may be characterised by significant repeatability problems. Tip vortex cavitation can be first observed some distance behind the tips of the propeller blades (detached tip vortex) because the fluid roll-up boosts the negative pressure peak, but when the vortex strength increase because of lower σ_n or higher K_T, it becomes attached to the blade tip. The tip vortex inception usually occurs with some weak and sporadic flashes of the vortex, which become more and more frequent as the cavitation number

is lowered or the thrust coefficient is increased, until persistent vortices are formed. When a large amount of free bubbles is present these bubbles may track the vortex also at cavitation indices significantly higher than inception index. This phenomenon is usually called gaseous cavitation and is in general less violent, with low noise emissions.

In this study the exact inception of tip vortex and sheet cavitation is of outmost importance because only the noise generated by these phenomena are of interest. For this reason, every inception curve is the outcome of a series of repetitions of inception tests. From these repetitions, the definitive value of inception is chosen either removing the anomalous values and averaging the most meaningful. An idea of the inception scattering is provided in Figure 4.9 for the tip vortex cavitation at 0°, the VFSF and S.S. root bubbles. The thrust and the cavitation index are normalised respect to a mid-load working condition to ensure confidentiality. It is evident how the vortices are the most intermittent, while the bubble inception is very well repeatable. The criterion chosen for the definition of the inception point relies on

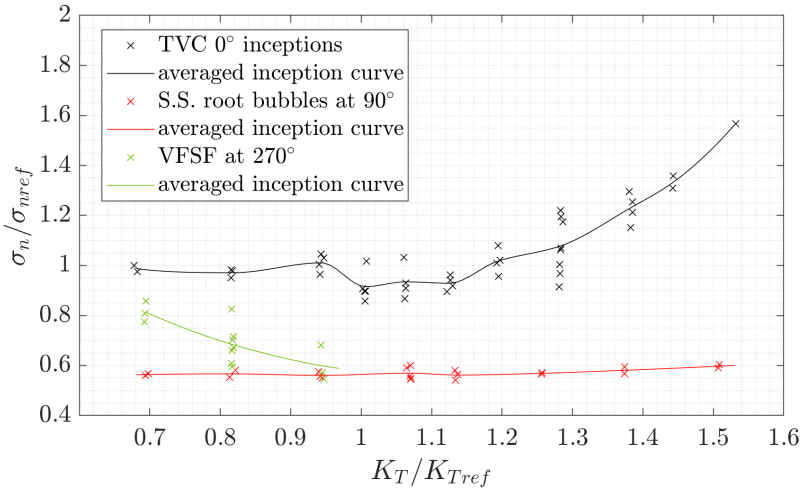

Figure 4.9: Scattering of the inception indexes for three different cavitation phenomena, propeller P2-DES.

the experience of operator, and it is based on the visualisation of a certain number of flashes separated by a sufficiently short time, occurring on most of the blades in case evident differences between blades are present. The latter consideration is troubled when the focus is not on the inception itself but on the noise emitted: if some blades show evident anomalous behaviour they are not considered as representative of the cavitation inception but they negatively affect the noise measure. To overcome issues related to cavitation intermittency and outliers, the noise acquisitions are repeated many times as will be showed in Section 4.6.

The inceptions of different cavitation phenomena are plotted on a diagram called the cavitation bucket, which reports the inception as a function of K_T and σ_n. Some examples of cavitation buckets are visible in the following pictures. Propeller P1 and P2 were tested behind a dummy model, reproducing the wake fields typical of twin screw ships. The flow in the first half of the first quadrant is slightly decelerated. This leads to an over stimulation of vortices and sheets in the position θ labelled as 0° as it is pointed out comparing Figure 4.10 (P1-DES) and Figure 4.11 (P1-W2). The TVC 0° persist for the entire first quadrant for P1-DES whereas the TVC

for P1-W2 appears when the angle of attack reaches its maximum, that is at 90° for the configuration with uniform inflow and inclined shaft. Obviously the hub vortex cannot be observed when the propeller is mounted in pulling configuration. Sheet and vortex cavitation follow the same trends: the suction side phenomena are

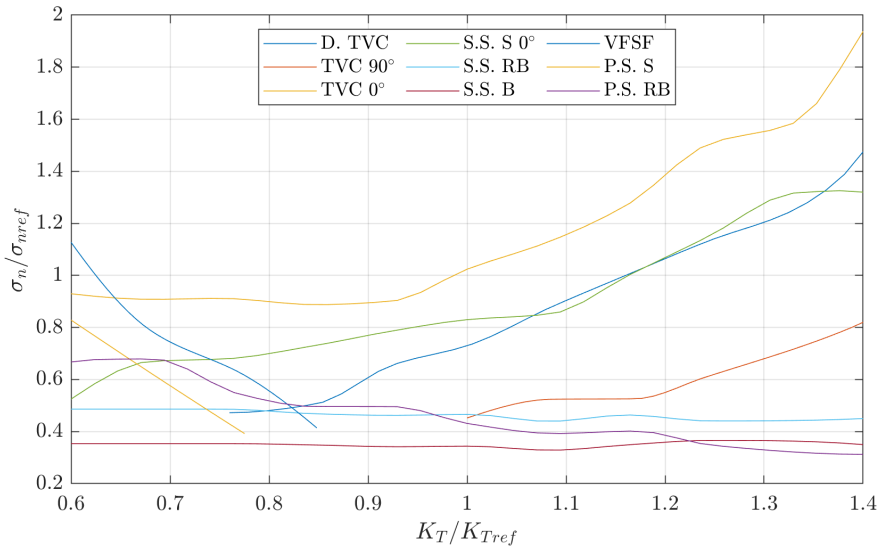

Figure 4.10: Cavitation bucket of P1 at design pitch.

anticipated at higher loads, the pressure side ones at lower loads. Instead the bubble cavitation inception, depending mostly on blade local geometry, is quite constant with respect to kinematic conditions. Varying the pitch setting, the behaviour of

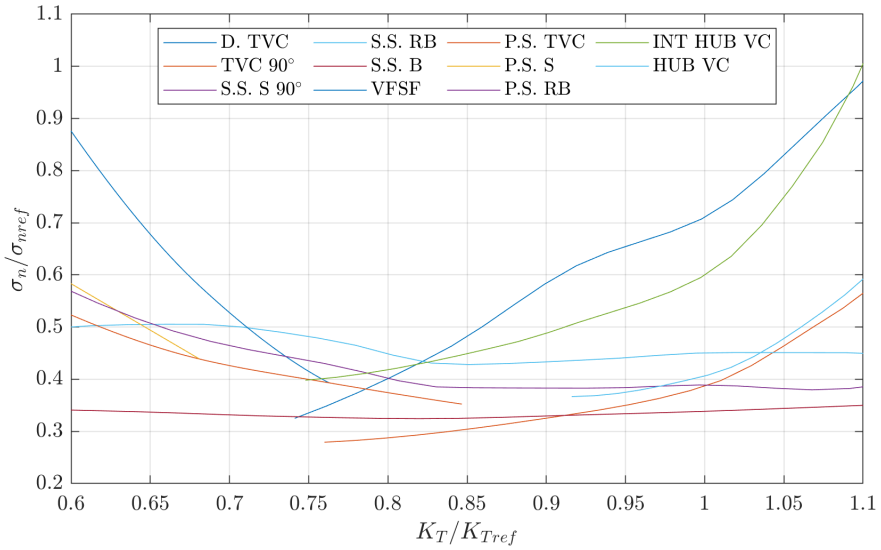

Figure 4.11: Cavitation bucket of P1 at design pitch, in uniform inflow.

the cavities changes accordingly. Lower angle of attack results in faster flow motion on the blade face and slower on the back, then the pressure on the face decreases. This condition can be dangerous because the face cavitation stands on a blade portion that normally is over pressurised and these low pressure areas are really unstable during propeller revolution. Potentially cavities grow and shrink rapidly

hence the face cavitation is particularly noisy. For instance in Figure 4.12 the P1-RED3 has a lower angle of attack with respect to P1-DES, resulting in predominant face cavitation for wide interval of thrust. The contrary applies when the angle of attack is increased.

For a limited set of functioning points also written notes of the cavitation pattern and photographs have been taken but they are not used in ML computation.

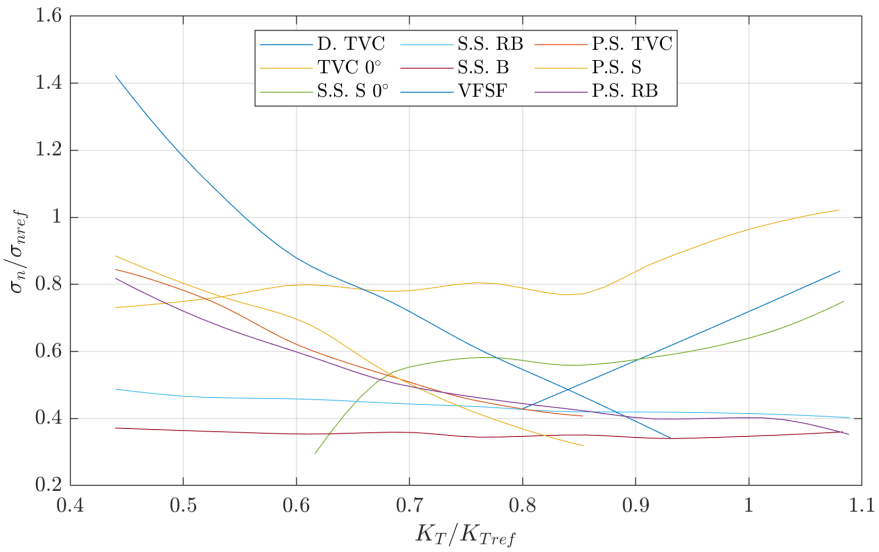

Figure 4.12: Cavitation bucket of P1 at pitch -3°.

4.6 Radiated noise tests

Radiated noise measurements were carried out with two hydrophones, one (Figure 4.13b) is mounted on a fin immersed in the tunnel flow, the other (Figure 4.13a) is located inside a water filled tank, attached to the tunnel observation window present on the bottom of the test section, below the propeller.

(a) Hydrophone H1.

(b) Hydrophone H2.

Figure 4.13: Hydrophones arrangement.

The position of hydrophone H2 is chosen in a way to be not too much close to the propeller, so to attenuate near-field components, but also not too much far from it, in order to achieve a sufficient Signal to Noise Ratio (SNR) and limiting the corrupting effect of wall reflections. The external hydrophone H1 is adopted to reduce hydrophone self noise and improve SNR, especially for conditions characterised by

very high flow rate in the test section. The presence of a Plexiglas interface between the source and the device is responsible of a mutate acoustic pattern that must be properly accounted with a dedicated transfer function. In this thesis only the acquisitions of H2 are considered.

Test set-up schema for propeller P1 and P2 in pulling configuration is represented in Figure 4.14, the missing dimensions are written in Table 4.3.

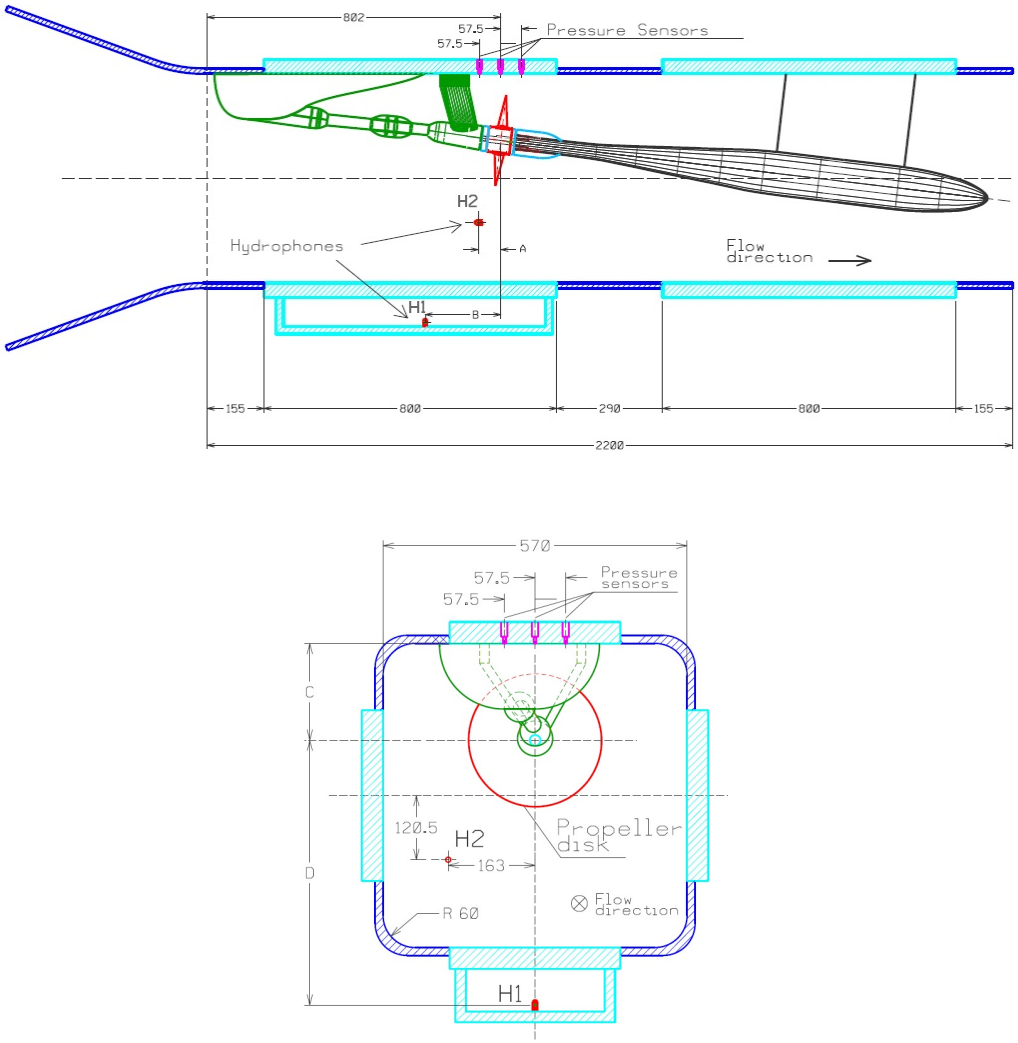

Figure 4.14: P1-P2 test set up, longitudinal view (top) and vertical (bottom).

Table 4.3: Pulling configuration set up.

Variable	P1	P2
α_s	2.5°	6.8°
A	75.7 mm	61.6 mm
B	221.1 mm	207 mm
C	169.95 mm	181.7 mm
D	508 mm	496.4 mm

Test set-up schema for propeller P1 in pushing configuration (P1-W2) and P3 is represented in Figure 4.15, again the missing dimensions are written in Table 4.4.

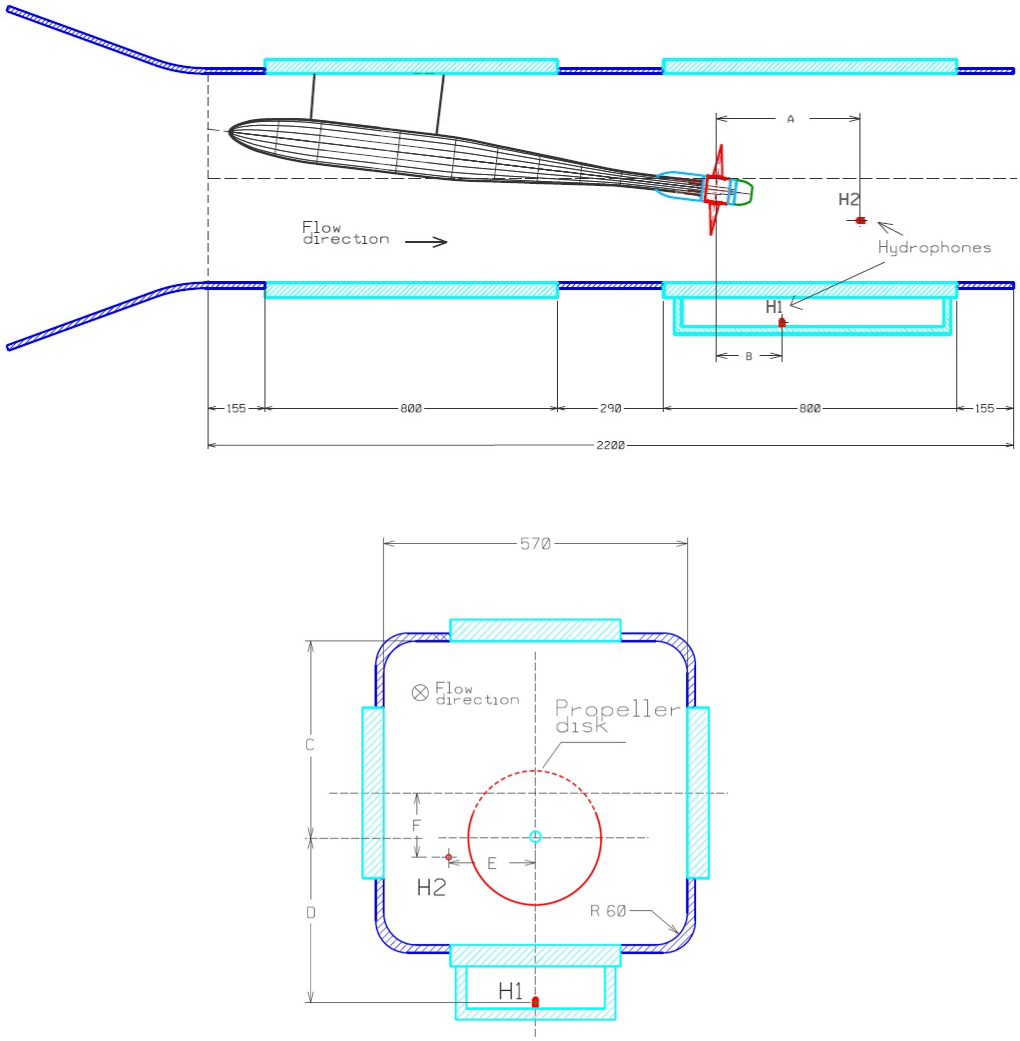

Figure 4.15: P1-W2 and P3 test set up, longitudinal view (top) and vertical (bottom).

Table 4.4: Pushing configuration set up.

Variable	P1	P3
α_s	2.5°	6.4°
A	14.8 mm	172.7 mm
B	64.1 mm	97.7 mm
C	248.8 mm	NA
D	392.8 mm	360.6 mm
E	130.7 mm	162.5 mm
F	94.5 mm	NA

Measurements were carried out mainly with a shaft rate equal to 25 Hz. Lower

rotational rates (22.5 or 20 Hz) were adopted when necessary to avoid exceeding dynamometer maximum allowed loads. For what concerns the measurement procedure, tests have been performed following the ITTC model scale noise measurement guidelines (ITTC Specialist Committee on Hydrodynamic Noise, 2017). The working conditions, for which noise samples are collected, have been chosen in order to provide an exhaustive characterisation of cavitation noise, including also very off-design conditions. As an example, in Figure 4.16 the URN measuring points for propeller P2-INC are reported.

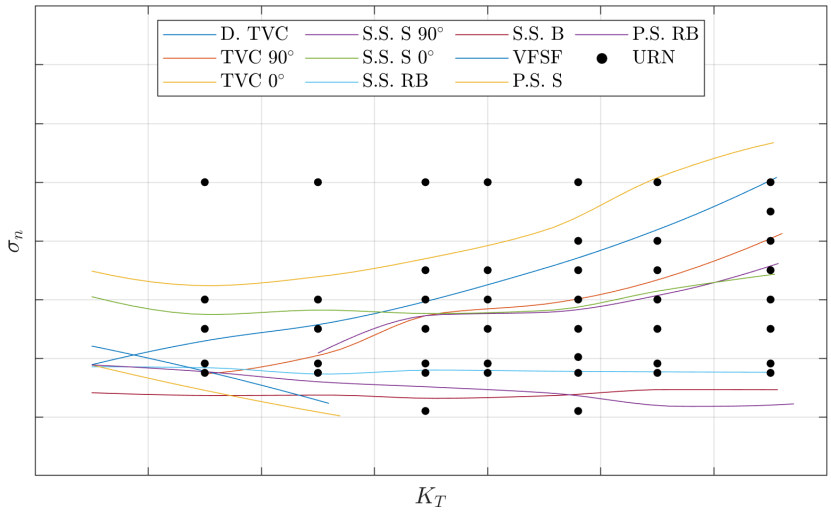

Figure 4.16: Cavitation bucket of P2-INC2 and radiated noise sample points.

Within all possible cavitation typologies, the attention is voluntarily focused on those phenomena more interesting for the real propeller functioning.

From the point of view of noise requirements, the most important phenomenon is probably the tip vortex since it is usually the first cavitation type occurring on a full scale propeller and the more difficult to be avoided also for those propellers suitably designed to limit cavitation. Other phenomena of relevance are the suction side sheet cavitation and pressure side cavitation, both sheet and vortex like. The first one is rather common in propellers operating in non-uniform wake field, especially for single screw ships, and generally when the propeller load is rather high, as it may happen in correspondence to higher velocities of ships, also for the twin screw configuration. Pressure side cavitation is usually not present in design conditions; its avoidance is one of the requirements of the propeller design due to its erosive nature and to the rather high noise levels connected to its presence. However, it may occur when a controllable pitch propeller is operated at reduced pitch and/or at design pitch when large shaft inclinations are present (such as in typical leisure boat configurations); as a consequence also its study is deemed of great interest in principle but it is postponed to future studies and not included in present thesis. Bubble cavitation is very noisy and erosive but it is reasonably absent in the region of operation of a well-designed propeller and consequently the modelling of its noise is beyond the purpose of this work.

Having defined the measuring points according to the above considerations, for each point, four to six repetitions have been carried out in different days, always

with almost constant oxygen content. The goal was to check the repeatability of acoustic measurements, especially for close to inception conditions. Indeed, it is hard to perfectly control the many parameters that concur to cavitation development, in particular cavitation nuclei size and distribution. Propeller blades are not build perfectly identical, this leads to discrepancies in the inception; one or more blades can anticipate cavitation while other can delay it.

The total number of working points tested is 658, but those considered for ML purpose are 258. These are chosen on the basis of cavitation bucket and noise spectrum: e.g. those samples for which the corresponding weak cavitation noise has not been captured by hydrophones are discarded, also those conditions for which bubble cavitation and pressure sides cavitation were present have been disregarded. These collected samples are not equally subdivided among the different configurations as reported in Table 4.5, as expected for the reduced pitches the valuable points for ML are lower than for the design pitch configurations. Actually, for reduced pitch settings, pressure side cavitation occurs for a large part of the operational conditions considered. Instead, for the configurations of P3, the test matrix have not been expressly designed for the purpose of the full characterisation of the suction side noise, that is the reason why P3-W5 (the weakest wake) has so few points suitable for the ML.

Table 4.5: Number of acquired functioning points.

Configuration	Collected	ML dataset
P1-DES	77	43
P1-RED3	62	20
P1-RED6	67	7
P1-W2	73	26
P2-DES	59	42
P2-INC2	46	37
P2-RED3	57	9
P2-RED5	57	5
P3-W4	53	26
P3-W5	39	7
P3-W6	68	36

4.6.1 Noise data presentation

The spectral representation of a pressure signal $p(t)$ is computed through Fast Fourier Transform using Welch's method of averaging modified spectrograms, to get the Power Spectral Density function $\Phi_{pp}(f, \Delta f)$ in $\mathrm{Pa}^2/\mathrm{Hz}$. The Sound Pressure Level $\mathrm{SPL}(f, \Delta f)$ is formulated as:

$$\mathrm{SPL}\,(f, \Delta f) = 10 \log_{10} \left(\frac{\Phi_{pp}(f, \Delta f)}{p_{ref}^2} \right), \tag{4.1}$$

for a constant bandwidth the unit of measure is $\mathrm{dB\,re\,1}\mu\mathrm{Pa}^2/\mathrm{Hz}$. The reference pressure for water is $1\,\mu\mathrm{Pa}$.

For a proportional bandwidth as one-third octave band, levels are:

$$\mathrm{SPL}_{1/3}\,(f, \Delta f) = 10 \log_{10} \left(\frac{\Phi_{pp}(f, \Delta f)}{p_{ref}^2} \right) + 10 \log_{10}(\Delta f)\,, \tag{4.2}$$

and the unit of measure is dB re $1\mu Pa^2$.

The noise picked-up by the hydrophone includes the contribution of noise sources different from cavitation, like: dynamometer gears, turbulence, mechanical vibrations of the tunnel structure or of other components, electrical noise, propeller non-cavitating noise etc. Each of these disturbs should be quantified and subtracted from the collected noise, however the estimation of all the components is tricky, then some simplification must be done. The background noise is measured replacing the propeller with a dummy hub and running the tunnel at the same operational conditions used for noise measurements (namely same flow rate, shaft rate and vacuum level). By doing this, some unwanted noise levels are lost or not correctly estimated; for instance when the dynamometer shaft is loaded with a propeller, its mechanical noise is greater compared to the case of unloaded shaft, i.e. with a dummy hub. The same applies for the noise due to structural vibrations induced by the propeller and by the cavitation. Even random noise can be present like sporadic debris cavitation or accidental noise external to the tunnel.

Net noise Sound Pressure Levels (SPL_n) are calculated by means of a logarithmic subtraction of the background noise (SPL_b) from the total one (SPL_t).

$$\mathrm{SPL_n} = 10\log_{10}\left[10^{\left(\frac{\mathrm{SPL_t}}{10}\right)} - 10^{\left(\frac{\mathrm{SPL_b}}{10}\right)}\right]. \tag{4.3}$$

This applies for frequencies where the SNR, computed as $\mathrm{SPL}_t - \mathrm{SPL}_b$, is at least equal to 3 dB, otherwise the frequency is dominated by background noise and must be discarded. If SNR ≥ 10, the background noise is irrelevant and $\mathrm{SPL}_n = \mathrm{SPL}_t$.

Distance normalisation is required to account for the power decay due to the distance r to the acoustic source from the hydrophones, as it heavily influences the measured noise. Following the hypothesis of spherical spreading loss, the Radiated Noise Levels (RNL) referred to the r_{ref} distance of 1 m are:

$$\mathrm{RNL} = \mathrm{SPL_n} + 20\log_{10}\left(\frac{\mathrm{r}}{\mathrm{r}_{ref}}\right). \tag{4.4}$$

The distance r is calculated considering an equivalent source at the propeller disk center. The unit of measure is, in one-third octave band levels, dB re $1\mu Pa^2m^2$. The RNL thus defined is the power seen from a receiver placed at 1 m from a punctual, omnidirectional source . In the UNIGE tunnel the ratio $\mathrm{r}/\mathrm{r}_{ref}$ is always less than one, then the correction is negative.

4.6.2 Transfer functions measurement

The correction for spherical propagation is not accurate in a confined environment like a cavitation tunnel test section. Especially in the smaller facilities, the acoustic pattern may become very complex, with the presence of reflections, echoes and reverberation due to walls, devices and interfaces.

With the aim to predict the full-scale noise or the comparison among different set-up configurations or even different facilities, the free-field noise must be assessed by means of Transfer Functions (TF) (Tani et al., 2017; Briançon, Fournier, and Fréchou, 2013) to correct the measurements carried out in the confined space.

The transfer functions measure consists in two phases: the first is the acoustic characterisation of a known noise source in a free-field environment (as a large towing

tank, a lake or a sea), the second is the measure of the acoustic emission of the same source in the facility. The procedure consists in the emission of a logarithmic sine sweep signal ($x(t)$) by the source, the noise is collected by the hydrophone ($y(t)$), connected to an amplifier, and later filtered and processed. The technique adopted in present work exploit sine sweep signals and the definition of a proper inverse filter, such that its convolution with the sweep signal gives a dirac delta. The filter $f(t)$ is defined as:

$$x(t) \ : \ x(t) * f(t) = \delta(t) \, . \tag{4.5}$$

The impulse response of the system is obtained convolving its response $h(t)$ to the sweep signal with the inverse filter.

$$h(t) = y(t) * f(t) \, . \tag{4.6}$$

The frequency response is computed as the Fourier transform of the impulse response.

The choice of the acoustic source is a compromise between the dimension and the SNR of the emitter at low frequency. A larger source improves the signal to noise ratio at lower frequencies (where the cavitation contribute is still relevant) but if its dimension is too big compared to the propeller diameter, the source can not well represent the acoustic pattern of a localised extent of cavitation. The acoustic source adopted in this study is the ITC 1001 which is a spherical broadband omnidirectional underwater transducer of about 10 cm of diameter (visible in Figure 4.17).

The impulse response in open-field has been measured at sea with a depth of about 35 m, the source has been placed at 5 m depth under the free surface, in order to postpone the time of the reflected waves. The receiving hydrophone has been placed at the same depth of the source at 1 m distance from it. The entire emitting-acquiring chain is a reproduction of the same adopted in the cavitation tunnel.

The impulse response of the cavitation tunnel has been measured approximating as well as possible the configuration adopted for propeller tests, especially in terms of source and sensors position. In Figure 4.17 the source is placed in the set-up for propeller P1 and P2, behind dummy model.

Figure 4.17: Transfer function test set-up for propellers P1-P2 behind wake.

The cavitating propeller, from the acoustic point of view, is an ensemble of monopole sources. This means that in the design phase of an experimental campaign focused on radiated noise of a cavitating propeller, the characterisation of the test section should be carried out considering the source positions where noise is more likely to be generated. For tests considered in present work, the cavities are mostly found in the suction side of the blade and in the angular sectors behind the decelerated wake peak if present, or in the range 90° to 180° for the only inclined shaft configurations. Consequently, the source has been located in correspondence of the propeller disk, in different locations to simulate the most common cavitation sources for each propeller configuration. The characterisation test has been performed using the cavitation tunnel test section filled up, with water at rest and in atmospheric condition. The cavitation tunnel frequency response is found applying the inverse filter to the hydrophone collected signal as in Equation 4.6.

In accordance with previous considerations, the effect of source position may vary significantly from frequency to frequency and it is in general relevant, thus when possible it should be taken into account.

For the propellers 1 and 2 behind wakes W1 and W3, respectively, the source have been located in the radial positions $0.7R$ and $0.9R$, at the angle θ=0-15-30-45-60-90-135-180-225-270-315; some transfer functions are visible in Figures 4.18 and 4.19. The TF has been obtained averaging for the two radial positions, the TFs in the sector 0° to 90°, hence where the most interesting cavitation extent is present.

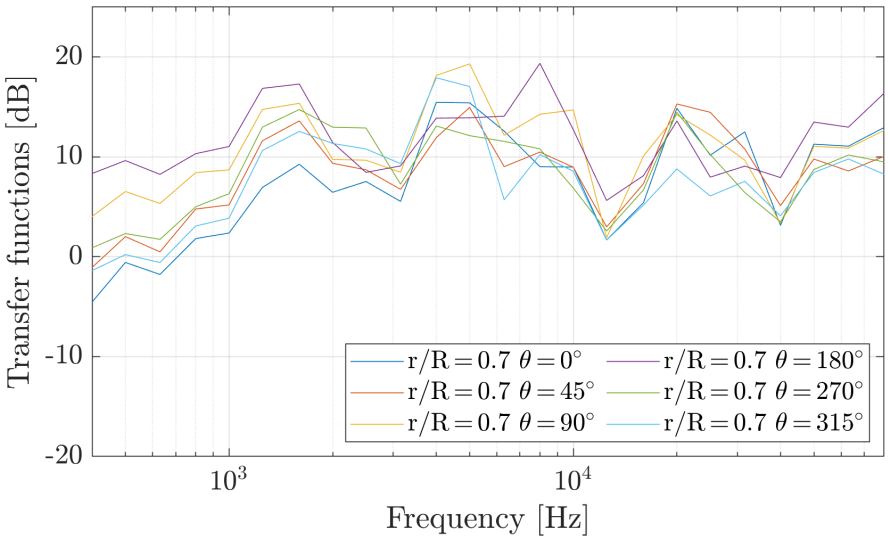

Figure 4.18: Transfer functions measured for different source positions at $0.7R$ for the propellers P1, and P2 behind twin screw wake.

The same consideration applies for P1-W2, hence the propeller working in uniform inflow. In this case only the radial section $0.7R$ and the positions θ=0-45-90-120-150-180-225-270-315 have been tested (Figure 4.20). In this set-up, the cavitation arise in proximity of the maximum angle of attack that is located, due to shaft inclination, at 90° and persist around for all the second quadrant. Hence, the TF results from the averaging on the sector 120° to 180°.

For the propellers 3, the source have been located in the radial positions $0.7R$, at the angle θ=0-45-90-135-180-225-270-315; the transfer functions are visible in

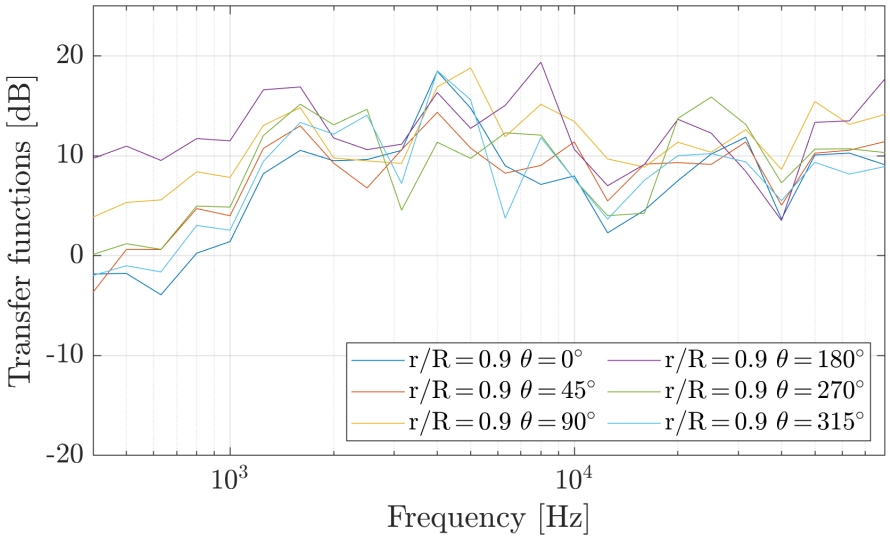

Figure 4.19: Transfer functions measured for different source positions at $0.9R$ for the propellers P1, and P2 behind twin screw wake.

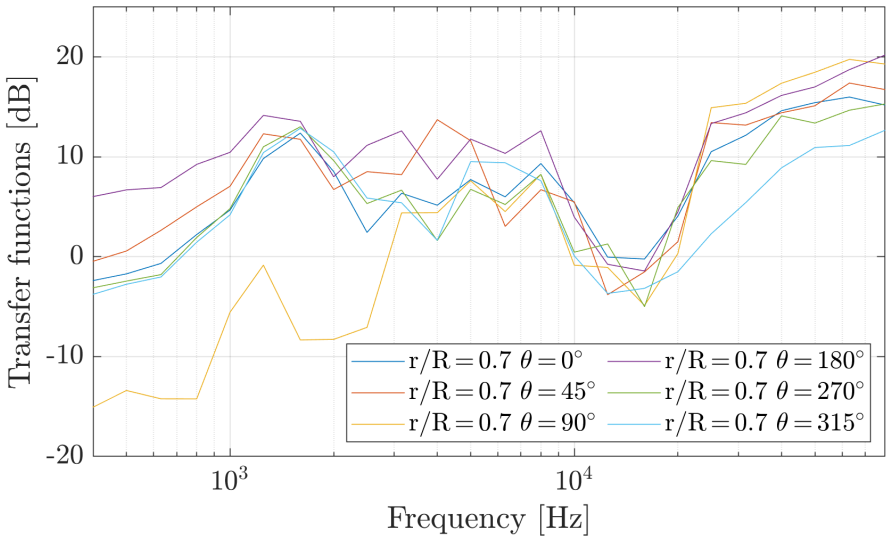

Figure 4.20: Transfer functions measured for different source positions at $0.7R$ for the propeller P1 in uniform wake inflow.

Figure 4.21. The TFs have been obtained averaging for the angular positions most representative for the expected cavitation pattern.

The resulting transfer function are shown in Figure 4.22. The obtained transfer functions can be adopted to correct measurement in order to estimate sound ideally radiated from the propeller in free-field condition at 1 m distance from it. The Source strength Levels (SL) is computed in one-third band levels as:

$$\mathrm{SL} = \mathrm{SPL_n} - \mathrm{TF}\,, \tag{4.7}$$

the unit is again $\mathrm{dB\,re\,1}\mu\mathrm{Pa^2m^2}$.

The TFs, differently from the spherical spreading loss, are not constant for the whole frequency range, since the confined environment effects typically depends on

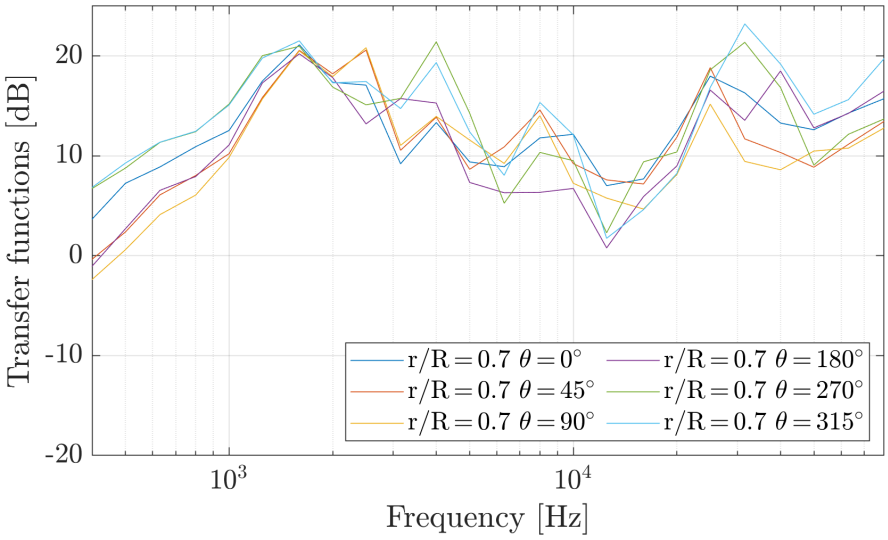

Figure 4.21: Transfer functions measured for different source positions at 0.8R for the propeller P3.

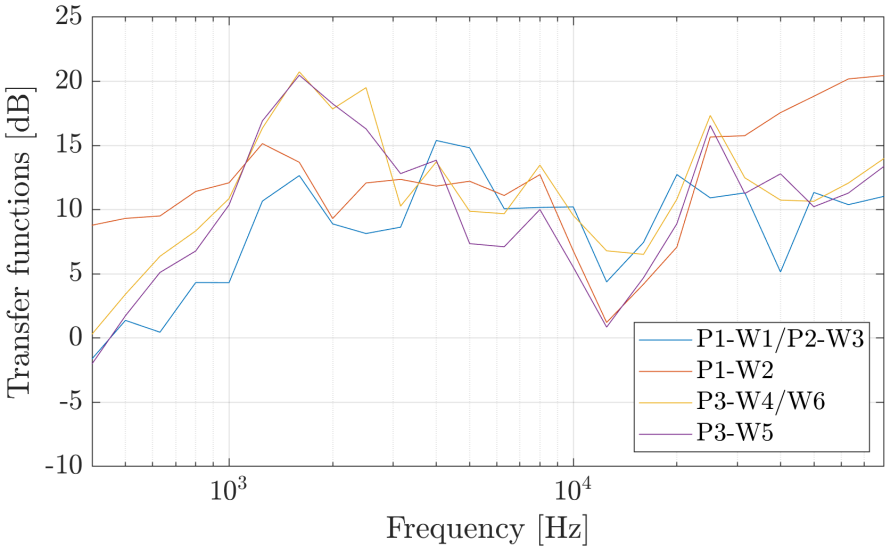

Figure 4.22: Transfer functions in one-third octave band for the propellers P1, P2 and P3.

frequency. Furthermore, as discussed in detail in Tani et al. (2019), measured transfer functions typically feature a rather irregular shape, with large oscillations of the frequency response and many peaks and hollows. These characteristics are generated by specific acoustical phenomena, such as the excitation of separated modes in the facility and wave interference. The characterisation of these phenomena is within the aims of the measurement, however their relative importance may depend also on the characteristics of the emitting source: the acoustic propagation process associated with a single deterministic source, as the electronic transducer, is strongly characterised by these phenomena, while they are less important when the noise is generated by cavitation, consisting in a distribution of uncorrelated noise sources acting simultaneously and moving through the domain. As a result, peaks

and hollows observed in transfer functions are larger, and generally different from those present in cavitating noise spectra. This issue is partially managed considering the incoherent average of transfer functions measured for many source positions and further averaging the noise measured by different hydrophones, however this aspect is still a matter of research.

From a practical point of view, free-field spectra obtained applying the transfer functions are globally more consistent, however their shape may be characterised by the same irregularities present in transfer functions.

Due to this, the identification of the spectral hump and other important spectral characteristics using SL spectra is in some cases quite complex. In Section 5.3 the effects of propeller loading condition on the spectral shape are analysed, while some SL spectra obtained applying the TF correction are considered for the sake of comparison. Consequently, the analyses relying on the knowledge of the spectral peak, such as the definition of the simplified spectrum used in Section 8, have been carried out considering the RNL spectra.

4.7 Summary

Three CP propeller models have been tested in a dedicated campaign aimed to obtain useful data to employ in training a ML tool for the prediction of cavitation noise. Both propellers have been tested behind two typical twin screw ship wakes, one for each. One propeller has been tested also in absence of wake to investigate the effect of the decelerated peak on sheet and tip vortex cavitation. From the devices at disposal the most important information regarding wakes, tunnel operation conditions, propeller working points and cavitation patterns have been extracted, analysed and reported compatibly with the ML algorithm, as it will be discussed in Chapters 5 and 6.

Cavitation noise has been processed in a double way: the first neglects the confined environment effects on noise propagation, the second, more realistic, considers these effects by dedicated transfer functions. TF are not always available and their measurements can be tough, hence both radiated noise definitions will be applied in the machine learning phase.

Chapter 5

Noise samples and target post processing

In this chapter the post-processing of noise acquisitions and the procedure to obtain ML targets ready to use are described in detail.

5.1 Introduction

The data acquisition and processing is a task strictly related to the physical problem under examination and even similar problem can be faced up from different points of view, thus the first definition of targets and features are usually defined by experts in the field under study, in order to characterise the phenomenon properly. In this case the transformation from raw data, collected experimentally, and input data for the ML, requires some calculations and careful considerations. For each WP many noise records have been collected to check measurements repeatability and, if needed, cope with possible issues selecting the most reliable acquisitions on the basis of the expected cavitation types, as discussed in Section 5.2. The compliance of spectra with typical shape from literature is checked in Section 5.3 and the target definition for the machine learning analysis is discussed in Subsection 5.3.1.

5.2 Repeatability analysis

As anticipated, the cavitation inception is highly subjected to nuclei content, blade geometry, viscous effects, free stream turbulence, etc. In addition, inception could be intermittent hence the assessment of the inception index σ_{ninc} may be ambiguous.

It is not surprising that multiple noise test, at the same WP, can result in very different noise spectra, especially if the WP is close to the inception. Especially given that the first kind of cavitation to appear is the tip vortex which is probably the most affected by the aforementioned factors. In Figure 5.1 the cavitation bucket for P2 at design pitch is reported as a function of reference value $\tilde{K}_T = K_T/K_{Tref}$ and $\tilde{\sigma}_n = \sigma_n/\sigma_{nref}$ corresponding to a mid-loading condition of propeller. The dots represent the noise samples: the green points are the ones in which the noise acquired in different days shows a good repeatability; usually these points include the cavitation free conditions, since they are dominated by background noise that is very repeatable. The inception and the volume dynamic of the TVC is highly

susceptible to the instantaneous water quality and tip blade load; these parameters can slightly change by the ones noted during inception test resulting in very different noise acquisitions (intermittent noise). After the first phenomenon inception, the noise spectra repeatability is constantly improving lowering the cavitation number because the cavitation process becomes steady.

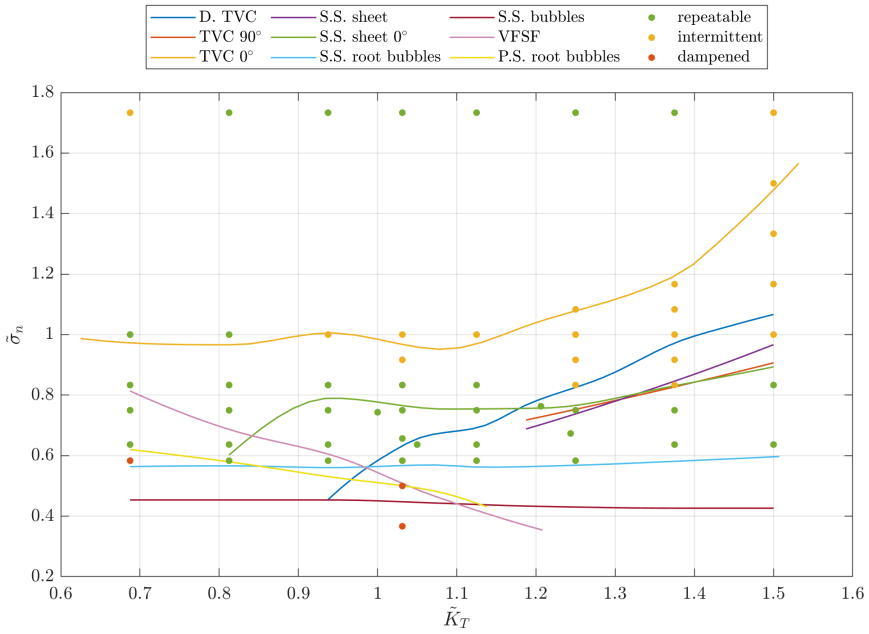

Figure 5.1: Cavitation bucket of P2 at design pitch and URN samples.

Further decreasing the pressure inside the tunnel another unwanted phenomenon appears, that is the acoustic damping. When the pressure is too low the number and size of free bubbles increase rapidly and due to the restricted vertical distance between the upper and the lower branch of the tunnel, these bubbles are not efficiently destroyed by the pressure head when they pass in the lower branch; the test section is soon filled by gaseous bubbles that act as damper.

In Figure 5.2 for $\tilde{K_T} = 1.03$ the RNL spectra for different cavitation index is reported; at lower cavitation number ($\tilde{\sigma}_n = 0.5$ and 0.37) is visibly dampened at mid-high frequency (>2 kHz), indeed the dBs decrease inspite the strong bubble cavitation which should produce ideally a flat spectrum similar to the spectrum of impulsive noise. It is reasonable to assume that the acoustic absorption affects also spectra measured for higher cavitation numbers, but it is not discernible nor quantifiable. Anyway, from experimental tests performed with an acoustic source (Tani et al., 2019), it was proven that, for the WPs of interest the absorption is negligible. Given that, the obvious dampened spectra are neglected (red dots). This is not a great loss because these spectra are always located under the bubble inception curve.

To analyse the effect of the inception uncertainties on the noise spectra, the noise acquired on different days for $\tilde{K_T} = 1.25$ is reported. The non cavitating condition of Figure 5.3 ($\tilde{\sigma}_n = 1.73$) is perfectly reproducible as expected. The condition in Figure 5.4 ($\tilde{\sigma}_n = 1.08$) it is at the turn of the first inception: the days 1, 4, 5 and 6 are comparable with the non cavitating noise, the other two days show some sign

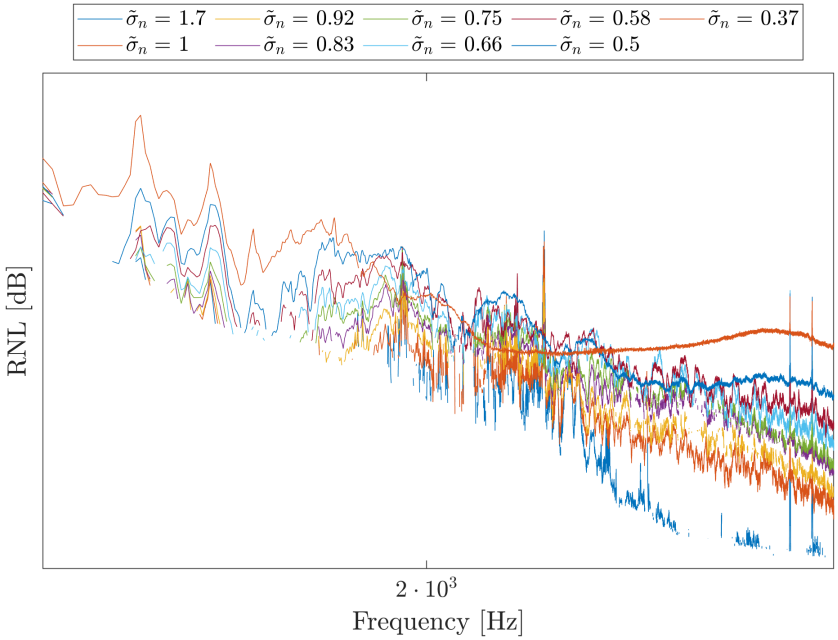

Figure 5.2: Acoustic damping, propeller P2-DES at $\tilde{K}_T = 1.03$.

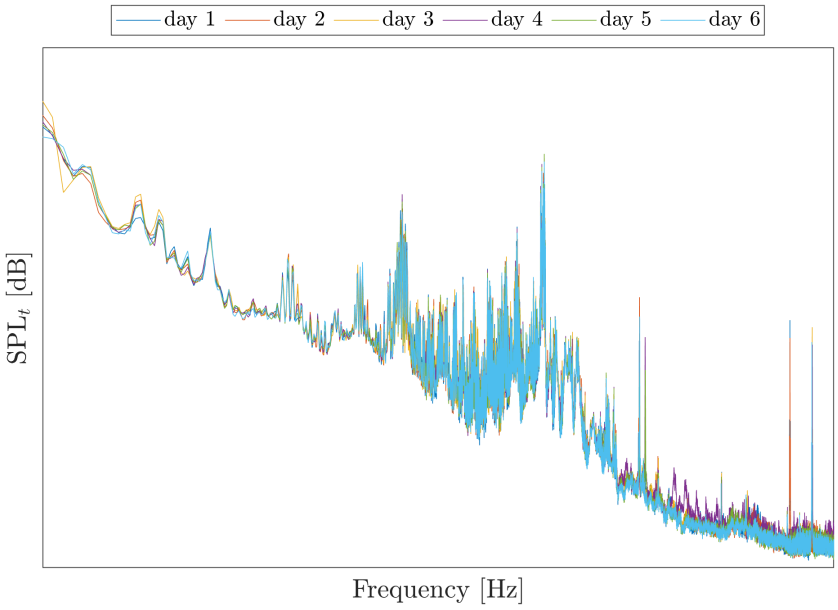

Figure 5.3: P2-DES ($\tilde{K}_T = 1.25, \tilde{\sigma}_n = 1.73$), repeated noise acquisition at cavitation free condition.

of cavitation, as an increase in noise levels, in the range 10 kHz-100 kHz and in the small peak at 1300 Hz (black arrow).

In Figure 5.5 ($\tilde{\sigma}_n = 1$) and Figure 5.6 ($\tilde{\sigma}_n = 0.92$) the cavitation number is further decreased, and based purely on the bucket of Figure 5.1 one should expect a fully developed tip vortex and a stable noise emission, instead at $\tilde{\sigma}_n = 1$ only days 1 and 3 show evidences of cavitation and for $\tilde{\sigma}_n = 0.92$ only day 3. The other acquisitions

are almost cavitation free.

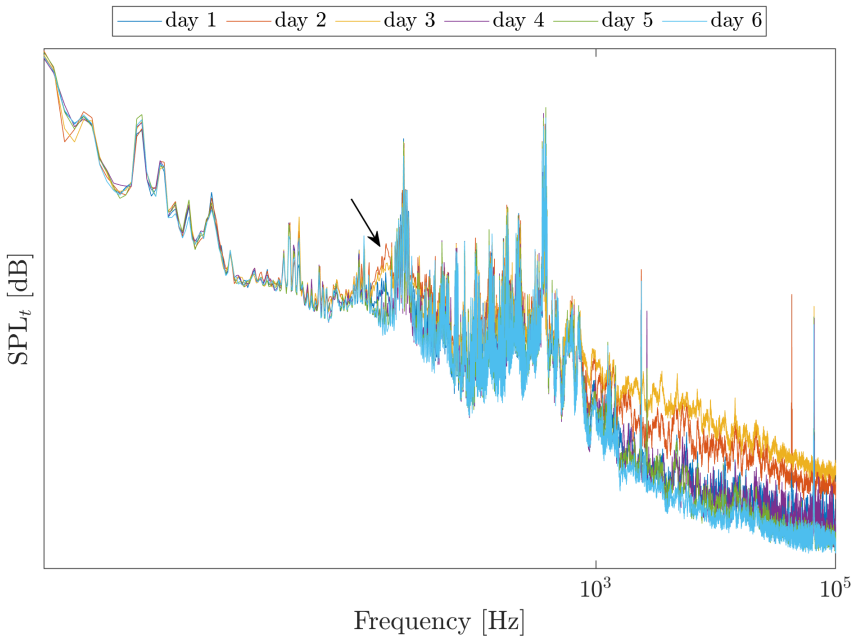

Figure 5.4: P2-DES ($\tilde{K}_T = 1.25, \tilde{\sigma}_n = 1.08$), repeated noise acquisition in proximity of inception.

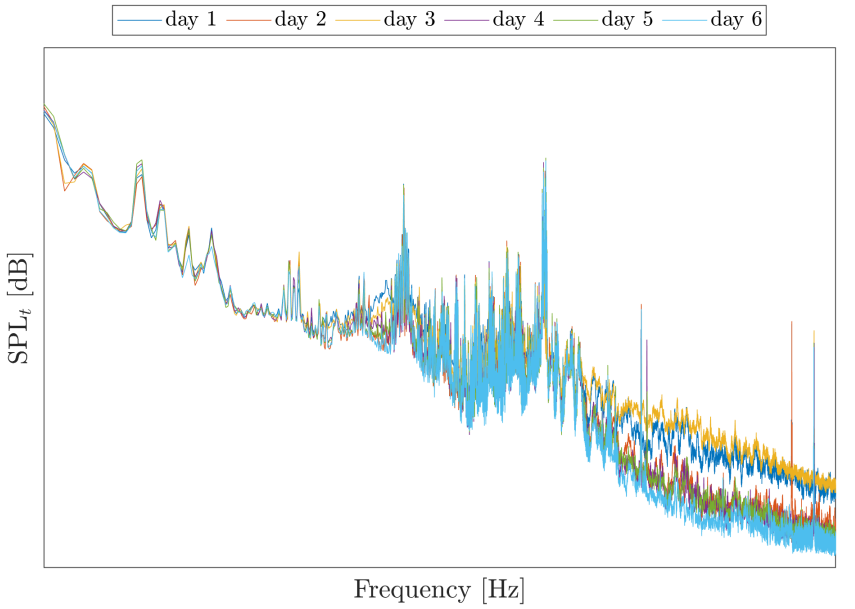

Figure 5.5: P2-DES ($\tilde{K}_T = 1.25, \tilde{\sigma}_n = 1$), repeated noise acquisition at the tip vortex inception.

In the end for $\tilde{\sigma}_n = 0.75$ in Figure 5.7, the cavitation is fully developed and rather stable, no intermittency is visible. The delay (or the advance) could be random for a given day, for instance the day 1 for $\tilde{\sigma}_n = 1$ seem to have cavitated but for $\tilde{\sigma}_n =$

0.92 the noise levels decrease, this could be explainable by the intermittency of the TVC, after the inception, due to temporary passage of nuclei, free bubbles or even debris.

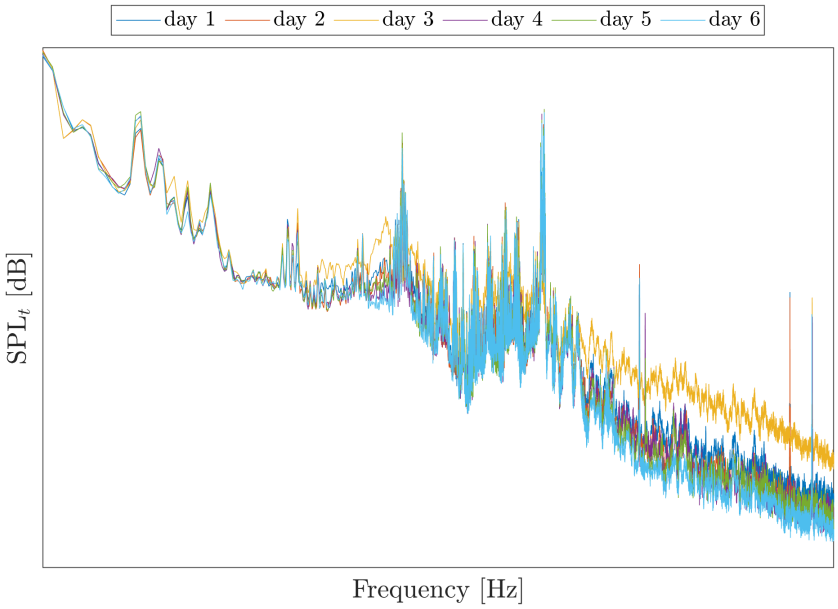

Figure 5.6: P2-DES ($\tilde{K}_T = 1.25, \tilde{\sigma}_n = 0.92$), repeated noise acquisition for well developed tip vortex.

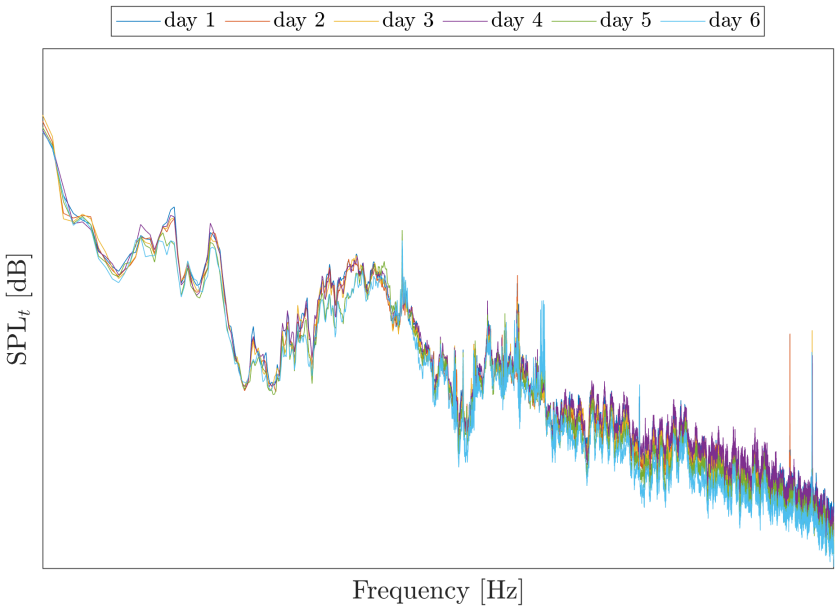

Figure 5.7: P2-DES ($\tilde{K}_T = 1.25, \tilde{\sigma}_n = 0.75$), repeated noise acquisition at suction side sheet inception.

Among the different repetitions, for each working point, one meaningful spectrum must be obtained. When the WP is strongly repeatable it is sufficient to take

the arithmetic mean of the spectra among the days, otherwise some considerations are required. Cavitation intermittency is generally due to scale effects or other experimental issues that prevent a stable development of cavitation. Consequently in most cases, the cavitation intermittency is usually regarded as an unwanted feature of cavitation that should be corrected with proper techniques, including special experimental techniques (e.g. electrolysis, artificial roughness etc.) and post processing techniques as the one here described. Taking as reference the cavitation bucket, the noise spectra have to reflect the expected trends exposed in Section 5.3. Given that, for the WP of Figure 5.6 the TVC is expected to be fully developed, hence the reasonable spectrum to take is the one of day 3. The same applies for Figure 5.5 where the final spectrum shall be taken by the average from day 1 and day 3.

The inception point is always the most tricky and it should be treated carefully. The first thing to do is to compare the spectra to the neighbouring ones (same or similar cavitation index but different $\tilde{K}_T$). Moving from the center of the bucket (at around $\tilde{K}_T = 1$) towards higher $\tilde{K}_T$ the noise at similar $\tilde{\sigma}_n$ is expected to increase slightly and steadily, this could be helpful to choose the representative spectrum for each WP. Based on the above mentioned considerations, all the spectra for the different WPs have been analysed, in order to choose the final ones to be employed on the modelisation phase. Furthermore, if the spectra levels were too low, the time record can be re-analysed with a larger number of sampling windows, keeping only those with a spectral power greater than the non-cavitating one. This technique called cavitation selection is described in Tani (2015, pp 108-130). When the repeatability analysis is concluded, the definitive spectra can be plotted together (Figure 5.8) to check the compliance with the expected trends.

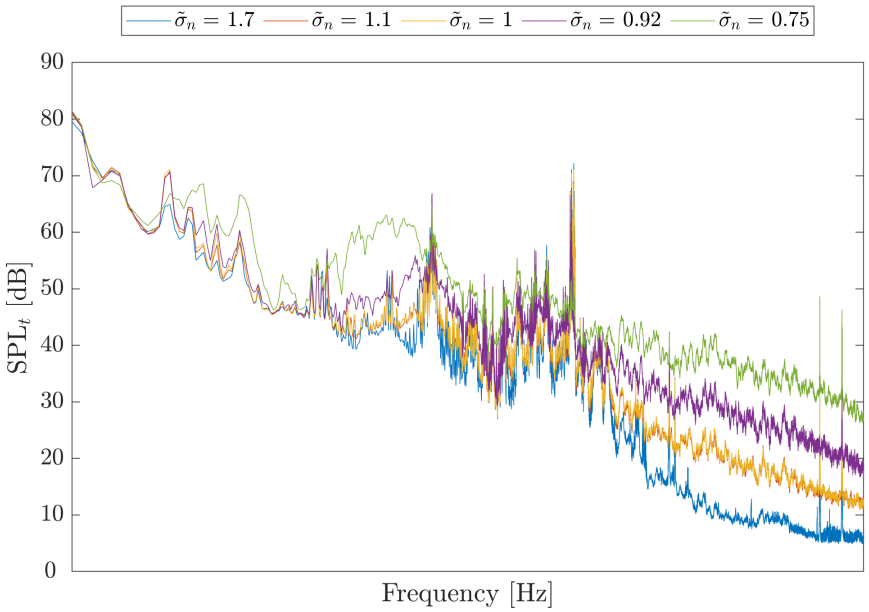

Figure 5.8: P2-DES, definitive curve of radiated noise after the repeatability analysis for $\tilde{K}_T = 1.25$.

The background noise is almost independent from the tunnel depressurisation for

a wide range of cavitation indexes, then the repeatability analysis is not required. In Figure 5.9 for the same operational conditions of Figure 5.8 the corresponding background noise, is shown. The values on the vertical axis are just for comparison purpose, not the actual dB values. The different curves are almost identical one another, the only difference is at $\tilde{\sigma}_n = 0.75$ because the pressure in the tunnel is reasonably very low then the devices inside the tunnel (screens, brackets, fins etc.) are likely to cavitate.

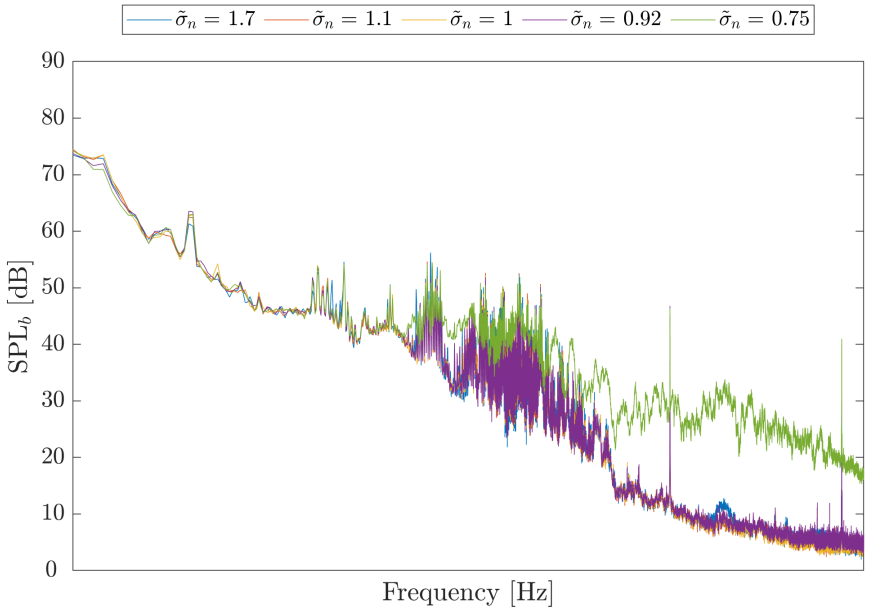

Figure 5.9: P2-DES, background noise for $\tilde{K}_T = 1.25$.

5.3 Analysis of the shape of noise spectra

As found by numerous studies (Ross, 1976; Fitzpatrick and Strasberg, 1956; Urick, 1983), cavitation noise spectrum is strongly related to cavitation extent and volume, then this problem is in principle suitable to be faced-up by ML techniques. Aim of this section is to check the compliance of this assumption examining the shapes of the spectra when the governing parameters are modified. Recalling, spectra are characterised by the presence of some tones in correspondence to the blade passage frequency and its multiples (Blake, 1984). These components, associated to the fluctuating load on propeller blades and to the periodic variation of cavitation volume are not analysed in present work.

The spectrum is usually characterised by a maximum, located at slightly higher frequency than blade passage tones, but still in the medium-low frequency range. Depending on the characteristics of cavitation, the maximum of the spectrum may appear as a prominent peak, sometimes characterised by a trapezoidal shape (Pennings, Westerweel, and van Terwisga, 2016). This peak is typical of the noise generated by tip vortex cavitation and it is of utmost importance in the study of ships radiated noise; the characteristics of this peak, as well as its presence, depend not only on the presence and dimensions of tip vortex cavitation, but also on the effect of the

surface cavitation, eventually attached to the vortex, that alters its dynamics. Moving away from the peak, the power levels decrease towards higher frequencies (van Wijngaarden, Bosschers, and Kuiper, 2005) with a certain decay law which again depends on cavitation dimensions and dynamics (van Wijngaarden, 1994; Buist, 1993; Brown, 1976). This part of the spectrum may be caused by different phenomena, such as sheet cavitation, bubbles and the tip vortex itself. As a general indication, the high frequency spectrum features higher levels and lower decay when cavitation dynamics are characterised by more violent events like collapses and bursting. On the contrary, when cavitation is more stable, levels are lower and decay faster moving to higher frequencies.

The first examples of noise spectra are reported in the following three figures and considering three operational conditions for P2-DES characterised respectively by a propeller load, lower, similar and higher than that corresponding to the design functioning of the propeller. The cavitation bucket of this configuration is already reported in Figure 5.1. As it can be seen, spectra are not continuous on the whole frequency range: the missing parts are those discarded because of the insufficient signal to noise ratio, according to the procedure presented in Section 4.6

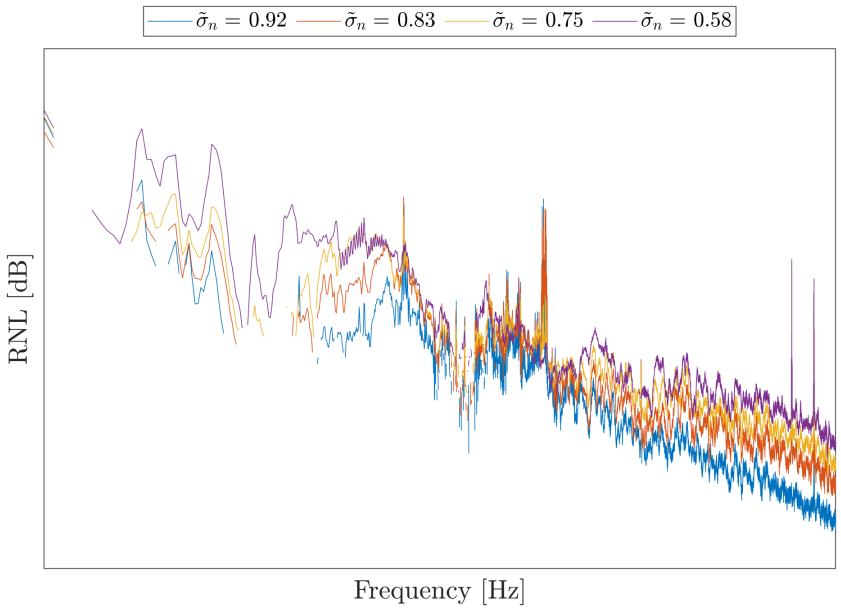

Figure 5.10: P2, RNL for propeller load $\tilde{K}_T = 1.25$

In Figure 5.10 a high load condition is shown; the lower curve refers to an isolated tip vortex behind the wake decelerated zone (TVC 0°), the red curve corresponds to the noise measured with a more developed TVC 0°. Lowering further the cavitation index (yellow and purple curve) all vortices get larger, tip vortex occurring also at 90° because of the effect of the inclined shaft and suction side sheet cavitation occurs at 0° − 90°. The TVC persists also for some diameters downstream (D. TVC). This sheet cavitation is highly non stationary because of the characteristics of the wake field, its presence is highlighted by a sudden increase of noise levels, especially at high frequency. In addition, it interacts with the TVC altering its dimensions and its behaviour. According to the larger dimensions of vortices when reducing

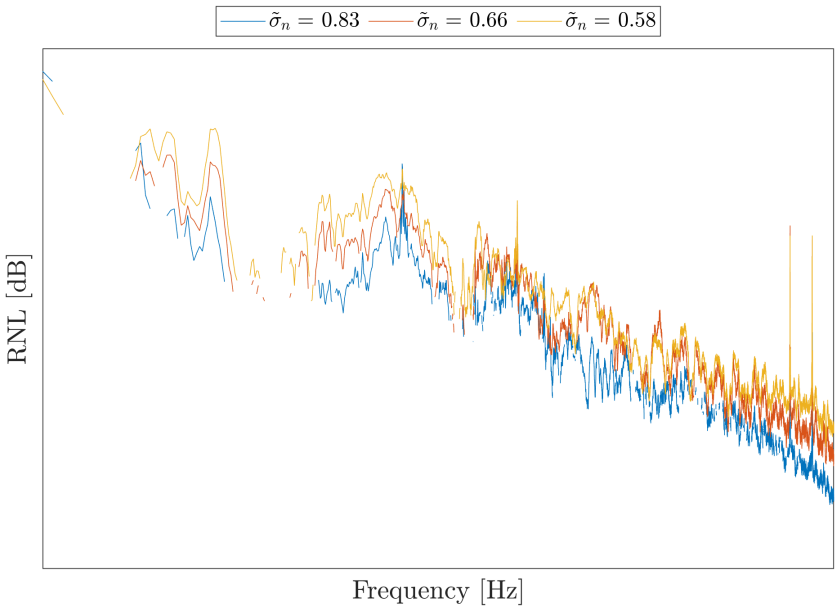

Figure 5.11: P2, RNL for propeller load $\tilde{K}_T = 1.03$

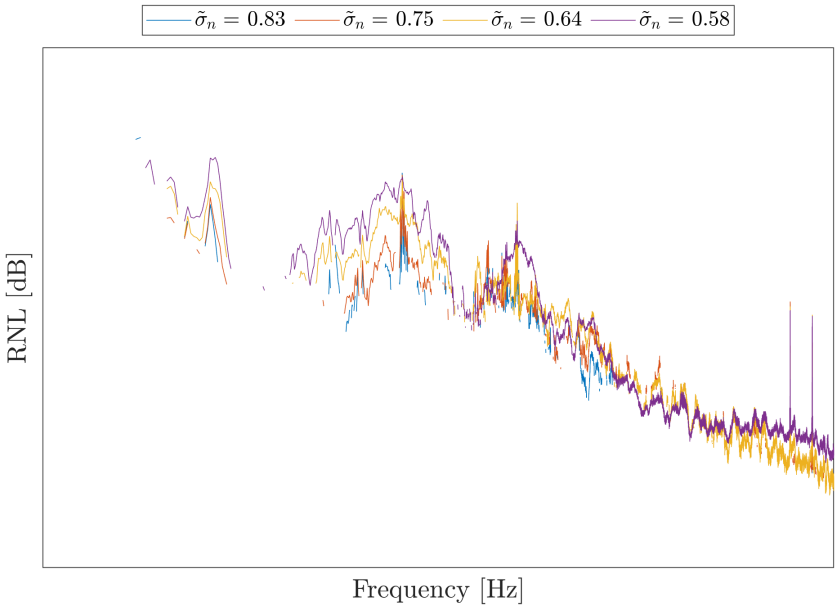

Figure 5.12: P2, RNL for propeller load $\tilde{K}_T = 0.81$

the cavitation index, the peak in the spectrum tends to shift progressively to lower frequency. In addition, it gets wider, probably because of the bursts and collapses induced by the interaction with the sheet cavities.

In Figure 5.11 a mid load condition is shown; the cavitation patterns are similar to those described for the previous plot but, due to the lower propeller load, phenomena are slightly reduced in intensity and they are suppressed before reaching the end of the first quadrant (90°). For what concerns the characteristics of noise spectra

it is observed that the frequency of the maximum of the spectrum remains almost unvaried reducing the cavitation number. This fact is likely due to a combined effect of the reduced dimensions of the TVC, as before mentioned, and its dynamics. Actually, the dynamic behaviour of the tip vortex for current configuration is strongly driven by the characteristics of the wake field: the vortex cavity is formed as soon as the blade enters the decelerated flow at about 0°, then it is subjected to a sudden growth and successively it collapses while the blade quits this decelerated area.

When the vortex dimensions increase (at higher propeller loading), this behaviour becomes more stable, cavities are more persistent and noise is radiated through the pulsation mechanism. On the other hand, when the tip vortex is smaller, the evolution of the cavity volume driven by the inflow, together with impulsive events like collapses and bursts, becomes dominant. Consequently, in the latter case the characteristic frequencies of the spectrum may be less influenced by the cavity size.

For the lower $\tilde{K}_T$ in Figure 5.12, spectra display in general the same characteristics described for the medium load conditions whit the addition effect of the pressure side cavitation. The blue and red spectra are associated with TVC 0° at different stage of development while for the other two conditions also P.S. cavitation is present, namely vortex from sheet face cavitation (VFSF). Despite the onset of this new, and usually noisy, phenomenon, the main features of the spectra remain unvaried; levels are significantly increased but in such a case it is not trivial to assess if this is due to the presence of pressure side cavitation or simply to the larger extent of tip vortex cavitation at 0°. The yellow curve is also nearby the inception of the P.S. root bubbles inception, it is possible that at this stage the free bubbles in the tunnel were too much in number, starting to produce some acoustic absorption as visible from the hollow at high frequency.

As seen, the center peak is an interesting and meaningful portion of the spectrum. Now considering all the before mentioned WPs of interest (dominant phenomena TVC and S.S. sheet cavitation) an overall view of these tendencies (in terms of frequency of the peak and correspondent level) is shown in Figure 5.13 for P1 at design pitch and in Figure 5.14 for P2 at design pitch. The values reported are relative to the minimum value in each plot. It is again confirmed that the frequency decreases

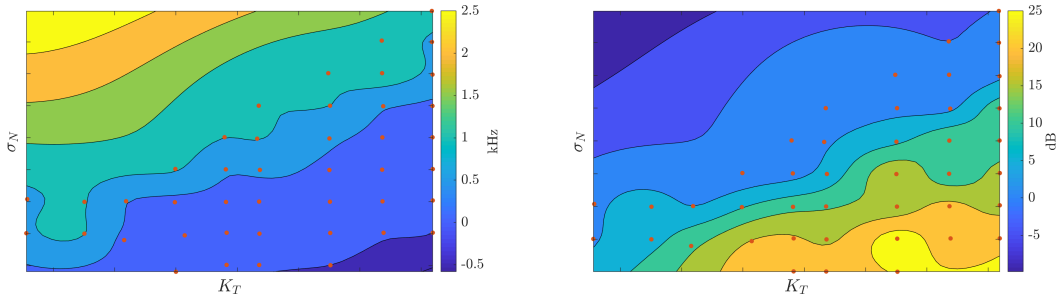

(a) Tip vortex cavitation, central frequency of the peak.

(b) Radiated noise level at the peak.

Figure 5.13: P1-DES, noise samples tendencies for machine learning dataset.

moving to lower σ_n, and/or higher K_T, hence moving from points characterised by weaker TVC to those featuring larger TVC extents. Furthermore, the dependency of the frequency on the cavitation extent is more evident for overloaded conditions,

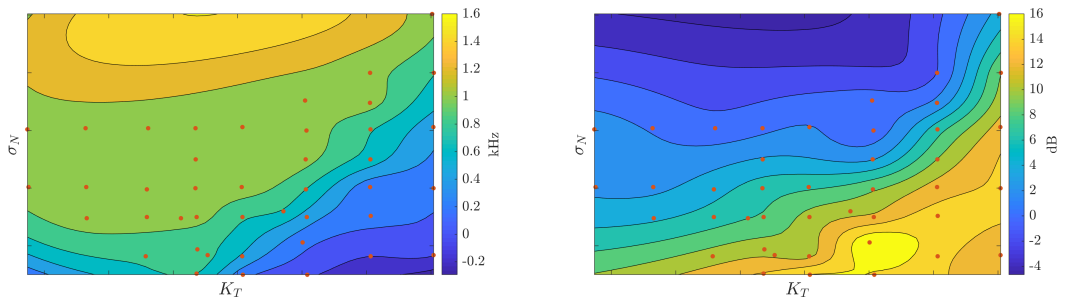

(a) Tip vortex cavitation, central frequency of the peak.

(b) Radiated noise level at the peak.

Figure 5.14: P2-DES, noise samples tendencies for machine learning dataset.

while reducing propeller load, variations with respect to the cavitation number are considerably lower, confirming what observed previously.

The amplitude of the peak behaves accordingly, with higher levels generally measured where cavitation is more intense (both tip vortex and sheet cavitation). These trends are clear but some outliers are presents: this is due to a double reason, the first is that these peaks are detected manually by the operator in the post-processing phase and the second is that some anomalies in the noise generation are found as already explained. Besides, the peak can be spread over a wide range of frequencies making impossible a well defined detection of the resonance frequency. Lastly, the peak levels and frequencies can be the sum of the contributions of the TVC and of the S.S. sheet.

In general, these contour plots demonstrate that the main features of noise spectra depends upon propeller loading and cavitation extent, in good agreement with theories of cavitation noise. The models developed in present work have to reproduce these tendencies and their correlation with relevant parameters defining the propeller functioning conditions, the propeller geometry and the wake field.

The previous considerations have been made for the net noise normalised following the spherical spreading loss (RNL) which is, as already discussed in Subsection 4.6.2, not truthful in a confined environment with sound reflections and reverberations. In principle, one should account mainly for the trasferred noise levels but, for some WPs, the source levels are unpredictably distorted if compared to the RNL and the aforementioned trends and similar characteristics may be lost. This happens especially at the mid-lower frequencies where the UNIGE cavitation tunnel TFs show an hump (Figure 4.22); this involves that, for many functioning points, the vortex peak is altered in shape and frequencies, or even it disappears.

In the following figures are shown the RNL versus the SL for three loaded conditions and different cavitation indexes. For instance, in Figures 5.15 and 5.17 (propellers behind twin screw wake) the vortex peaks present in the interval 400 Hz to 2000 Hz are flattened out, or shifted at lower frequencies. In Figure 5.16 are depicted spectra of the P1 propeller in uniform flow, hence the RNL vortex humps are naturally less pronounced than in the previous case. Here, the SL peaks become indistinguishable from the tonals (not visible in figure) until very low cavitation number is reached.

The RNL features more clear and stable shapes, then the spectrum parametrization described in the following section have been computed only for the RNL, while

for the SL only the one-third octave bands representation has been kept.

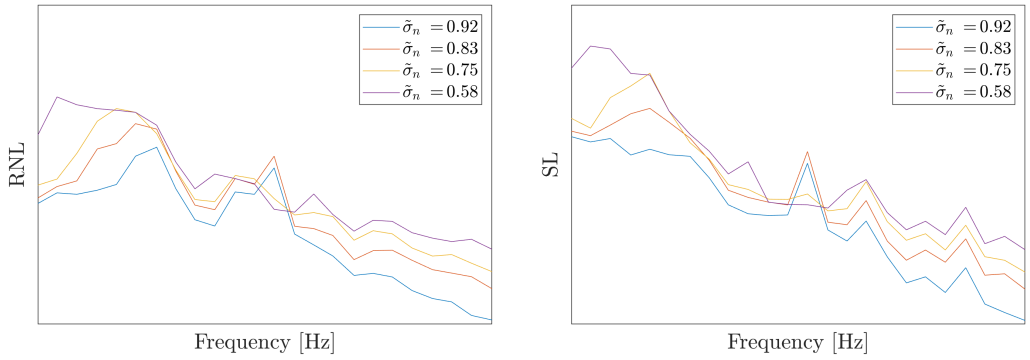

Figure 5.15: Comparison of RNL (left) and transferred (right) spectra for P2-DES.

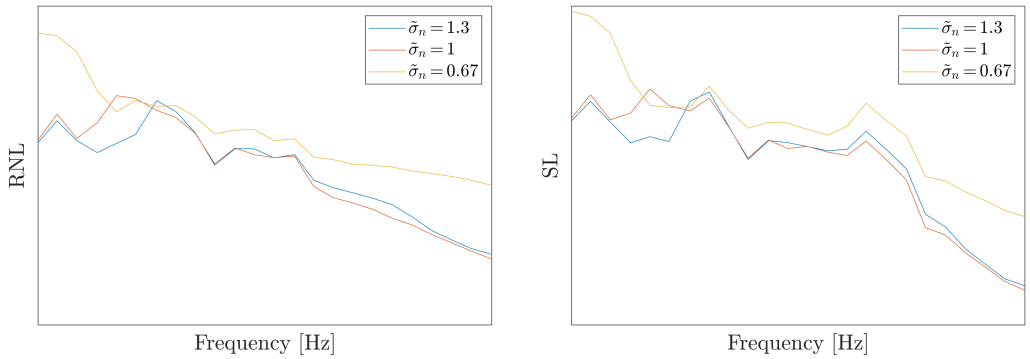

Figure 5.16: Comparison of RNL (left) and transferred (right) spectra for P1-W2.

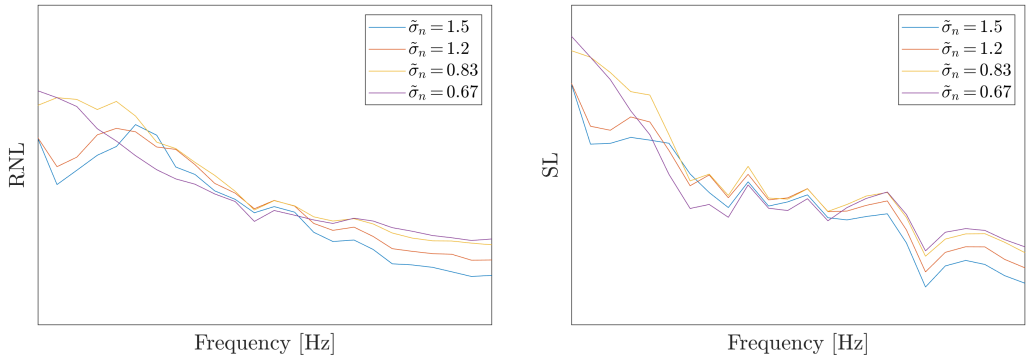

Figure 5.17: Comparison of RNL (left) and transferred (right) spectra for P3-W6.

5.3.1 Spectrum parametrization

The narrowband representation of noise spectra seen so far is useful since it allows to better identify the components of interest, such as the continuous spectrum associated to cavitation, distinguishing them from tonal noise or in general other

unwanted noise components; however, these spectra are definitely too detailed to be used in computational analysis. In addition, the trends featured by single spectral rows may be rather complex and not so meaningful, especially if compared to the general trends just described.

Due to this, three different representation of the spectrum will be exploited:

- a simplified spectrum defined by 4 points;
- the radiated noise levels in 1/3 octave band;
- the source levels in 1/3 octave band.

A simplified description of the spectra, allows to keep only those information of physical and practical relevance and to speed up the ML calculus. In the light of the previous considerations, the spectrum simplification shown in Figure 5.18 is adopted. This simplified spectrum is defined by the knowledge of the frequency and level of

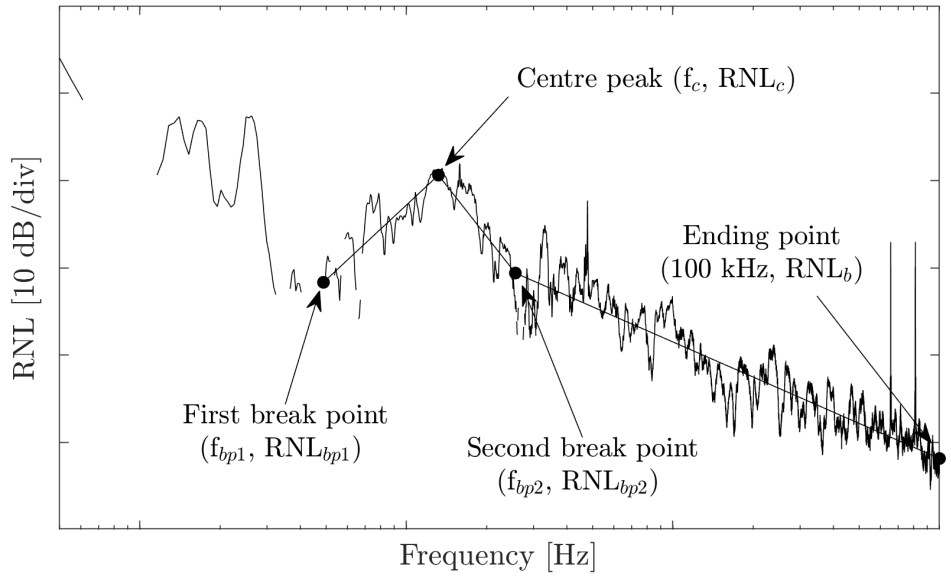

Figure 5.18: Adopted spectrum simplification.

only five points; these frequencies and levels, summarised also in Table 5.1, are the target of the models developed. The starting and the ending points frequency is fixed at 50 Hz and 100 kHz respectively. The center peak is of utmost importance and since it can be difficult to identify, automatic detection has been dropped in favor of manual detection. Instead the other targets are detected automatically within a code which aims to find the best fitting piece-wise function. Within the points used to define the spectrum, the first one is almost meaningless since in that part the spectra are typically dominated by background noise or by tonal noise components, hence not of interest for what regards the goal of present work. Actually, the part of the simplified spectrum which can be reasonably considered representative of cavitation noise is identified by frequencies higher than that of the first break point.

Alternative targets are the decay (or growth) of sound levels, these are computed from the previous defined target points.

Table 5.1: Dataset output variables.

Output Variable	Unit	Description	Dimension
f_{bp1}	[Hz]	Frequency at first breakpoint	1
$\mathrm{RNL}_{\mathrm{bp1}}$	[dB]	Noise level at first breakpoint	1
f_{c}	[Hz]	Central frequency	1
$\mathrm{RNL}_{\mathrm{c}}$	[dB]	Noise level at central frequency	1
f_{bp2}	[Hz]	Frequency at second breakpoint	1
$\mathrm{RNL}_{\mathrm{bp2}}$	[dB]	Noise level at second breakpoint	1
$\mathrm{RNL}_{\mathrm{b}}$	[dB]	Noise level at ending frequency (100 kHz)	1
α	[dB/oct]	Slope between breakpoint 1 and vortex peak	1
β	[dB/oct]	Slope between vortex peak and breakpoint 2	1
γ	[dB/oct]	Slope between breakpoint 2 and last point	1
$\mathrm{SL}_{1/3}$	[dB]	One-third Source Levels	24
$\mathrm{RNL}_{1/3}$	[dB]	One-third Radiated Noise Levels	24

Given $f_2 > f_1$, the slope of the RNL in dB/Hz is

$$\mathcal{K} = \frac{\mathrm{RNL}_2 - \mathrm{RNL}_1}{\log_{10}(f_2) - \log_{10}(f_1)}\,. \tag{5.1}$$

For convenience is better to convert $\mathcal{K}$ in dB/oct, in this way $\mathcal{M}$ represents the slope for each doubling of the frequency.

$$\mathcal{M} = \mathcal{K} \cdot log_{10}(2)\,. \tag{5.2}$$

Lastly, the power of the decay can be expressed dimensionless as

$$\mathcal{B} = \frac{\mathcal{K}}{10}\,. \tag{5.3}$$

In principle it is indifferent the definition adopted, but for the above mentioned convenience, the slope in dB/oct is considered as reported in Table 5.1.

Besides this simplified spectrum, also the radiated noise levels and the source levels in one-third octave are computed in the interval 400 Hz to 80 000 Hz. The 1/3 octave band act as a filter mitigating random fluctuations of the noise, then physical meaning of the levels is improved respect to the narrowband representation.

The advantage of using the 1/3 octave band is that the human error, of the simplification phase, is avoided. On the other side the target to be modelled by ML rise in number and complexity, hence more sophisticated ML algorithms are needed. As an example, it is easier to find the governing law of the high frequencies decay respect to a generic 1/3 band level.

An example of the target points for P2-DES is provided in Figure 5.19. It has to be remarked that this propeller is operating at conditions where the S.S. cavitation is rather stable and its development uniform, consequently the different target points are likely to evolve smoothly in the WPs domain. However, the automatic procedure of break-points detection can feature anomalies when the hollow between two piece-wises is not well defined. For instance in Figure 5.18 the BP2 is placed rather high in level respect to the hollow, this happens because right after (moving towards higher frequencies) the levels increase a little before to decrease steadily until 100 kHz.

These small hump, if related for instance to components of the background noise difficult to remove, can affect the detection of break-point meaningful from the point of view of the cavitation noise.

The uncertainties in the localisation of the break-points reflect on the correspondent contour plots (again, the values reported are relative to the minimum value in each plot). The BP1 frequency for P2-DES (Figure 5.19a) feature a large area where apparently the frequency is unvaried for the entire K_T range. Instead the BP1 level (Figure 5.19b) seem to be more affected by the change of WP. The second break-point apparently is more connected to the propeller functioning for the frequency (Figure 5.19c) even if some anomalies are visible, conversely the levels are rather unstable and they do not feature a smooth trend (Figure 5.19d). Lastly, the $\mathrm{RNL_b}$ (Figure 5.19e) is usually very stable and easy to detect with small error. The spectrum slopes in Figures 5.19f and 5.19g are affected by the uncertainties in the break-points detection too. Only the high frequency decay in Figure 5.19h seems to show a clear trend, in particular the spectrum gets more flat when the cavitation become more intense as when the load increase or the cavitation index gets lower.

5.4 Summary

The final spectra meet largely the shapes and the tendencies known from literature; this supposes that suction side cavitation noise spectra can be predicted as a function of some parameters, hence this specific task may be successfully carried out by means of by machine learning algorithms if the right features and targets are found.

Noise spectra are firstly extracted from raw data in narrowband: this representation is rich in information if considered as a whole; however, if a higher detail is considered, looking at spectral rows, it is evident that many fluctuations are random. Given that, the general pattern of this type of noise is modelled like a broken-stick function made by five points, only these will be the ML output to be learned.

This approximation is well-functioning for many samples, with some exceptions. In particular it is tricky the localisation of the break-points because sometimes they feature anomalies which cannot be predicted. The anomalies can be the outcome of components of the non-cavitating noise which are difficult to be quantified or due to the inherent instability of the noise. When a target does not show clear tendencies respect to the parameters it is probable that the ML models will not be able to map the inner bound between output and input. The possible solutions are two: introduce more features and/or define a more meaningful target. For this reason also the decay of each line segment has been calculated, the expectation is that this target will be more stable respect to the pair (f_n, RNL_n).

Alternative target to be modelled by the ML are the one-third octave band levels for the radiated noise and for the source noise.

The RNL, as for the simplified spectrum, is the cavitation net noise scaled considering the spherical propagation of the sound, therefore the spectrum is corrupted by the propagation effect of the UNIGE cavitation tunnel of the pressure waves. If the aim is to predict the noise of the cavitation propeller in free-field environment or to compare the noise acquired in different laboratories, the source levels must be considered. However transfer functions could not be available or the designer is interested in the RNL or only in the peak vortex; for these reasons, all the three different groups of targets will be modelled.

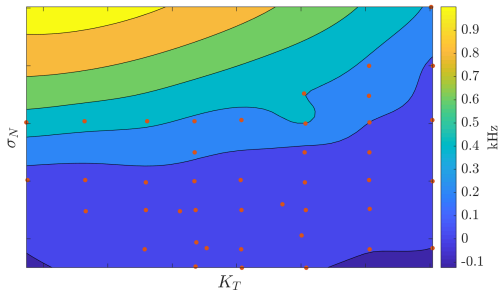

(a) BP1 frequency.

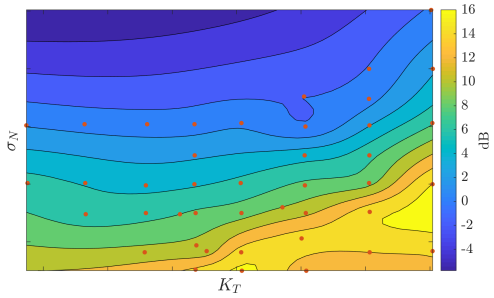

(b) BP1 Radiated Noise Level.

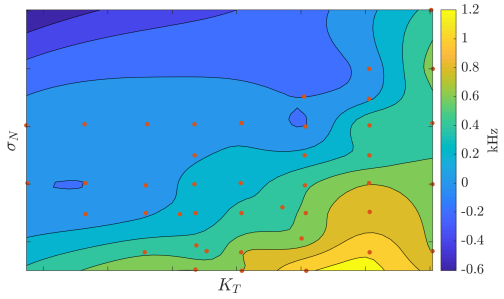

(c) BP2 frequency.

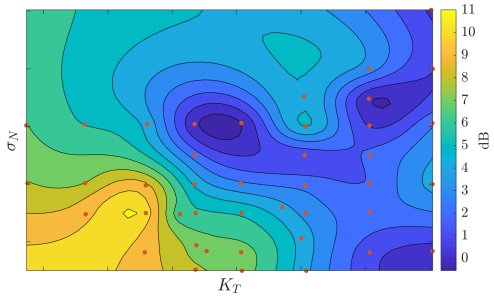

(d) BP2 Radiated Noise Level.

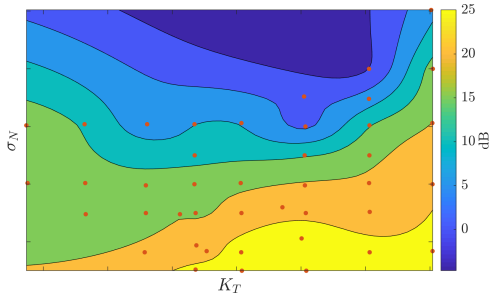

(e) RNL at ending frequency 100 kHz.

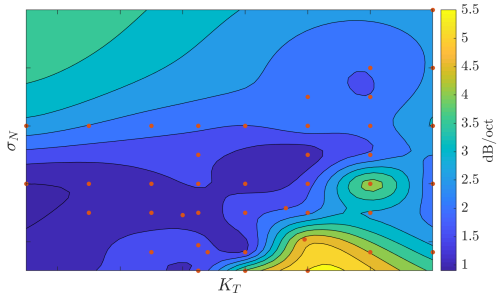

(f) Slope between BP1 and the central peak.

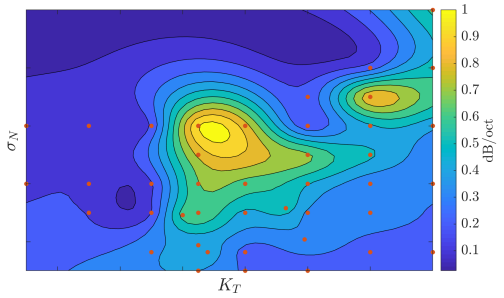

(g) Decay bet. the central peak and BP2.

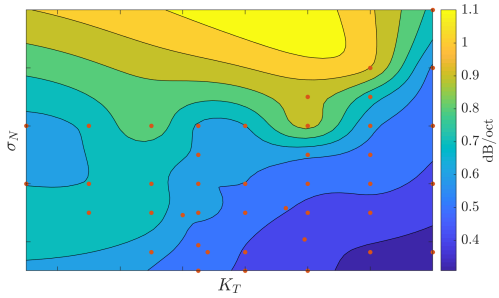

(h) Decay bet. BP2 and the level at 100 kHz.

Figure 5.19: P2-DES, noise target tendencies for machine learning dataset.

Chapter 6

Features extraction

In this chapter the input variables of the models are described. The features include some quantities describing the propeller geometry, the wake inflow and the propeller working conditions in terms of kinematic conditions, load and cavitation. In addition, some inputs coming from hydrodynamic computations carried out with a boundary element method, have been included.

6.1 Introduction

In supervised learning algorithms, the choice of features has an huge impact in the model's performance: the best set of features improves accuracy, reduces overfitting and training time. The features have to be extracted from the available data, according to the physical knowledge of the process involved or alternatively to exploit the experience matured on the field under examination. From experimental and practical observation the cavitation noise generation is linked to propeller geometry, its functioning point and to the quality of inflow wake.

In naval architecture many of the possible features (e.g. the thrust of a propeller) are commonly referred at their non dimensional form, which is a well established practice in marine engineering but it can undermine the machine learning because it can hide or change the effect that the predictor variables have on the target or they can make difficult to separate the individual effects. For this reason, when possible, for each dimensionless feature, its dimensional counterpart has been considered too.

Some inputs, as the inflow wake, are commonly provided by a matrix of values evaluated on a grid of points corresponding to coordinate of a vertical plane upstream the propeller. This is the most complete and useful characterisation for these kind of inputs but they require the use of rather complex ML algorithms, more computational time and processing power. Otherwise, a limited set of global descriptors can be found in place of the before mentioned matrices.

In order to consider progressively more complex tasks in this study, in the first running of ML (Chapter 8) the simplified features have been preferred. Then, with the goal to minimise the human error in the feature extraction and to boost the accuracy of the DDM, the features in the form of matrices have been introduced too (Chapter 9).

The working parameters features are described in Section 6.2, then the defined cavitation types in Section 6.3, lastly the inflow characterisation in Sections 6.4 and 6.5.

All these quantities are usually available at the propeller design phase, exception made for the inception indices which may be estimated anyway by dedicated CFD simulations with reasonable accuracy, see Gaggero et al. (2014); the CFD simulations needed to obtain the inception indices are still challenging but more feasible than those required to estimate directly the model scale noise.

From CFD simulations other useful quantities can be extracted such as the pressure field around the blade and the profile circulation; these alone are able to replace all the above features because they contain the whole hydrodynamic characterisation of the phenomenon. Assuming that the designer is interested to check many different geometries, the numerical simulations should require less time as possible without losing validity. The methods selected for present work is then the non-cavitating boundary element method. In Section6.6 an in-depth overview of the Boundary Element Method (BEM) features is shown.

6.2 Propeller geometry and working parameters

In principle, it is possible to provide to a machine learning tool the complete description of the model propeller geometry (e.g. as a 3D matrix) but to keep computation as simple as possible in these first steps, a limited number of geometrical descriptors has been selected (Table 6.1). These can be referred to the main dimension of the propeller such as the diameter D, the pitch P or the expanded area A_E, or to the blade sections as chord c, thickness t and camber f. The blade sectional features are taken in account only for the $0.7R$ because it is one of the most relevant for the sheet cavitation. The expanded area A_E or its dimensionless counterpart Blade Area Ratio (BAR) have been included because of the well-known correlation between the blade surface area, the load and the back cavitation.

$$\mathrm{BAR} = \frac{A_E}{\pi D^2/4}. \tag{6.1}$$

The pitch setting $\Delta\Phi$ is defined for CPP as the difference between the design pitch angle Φ at $0.7R$ and the tested pitch setting; for instance P1-RED5, $\Delta\Phi = -5$.

$$\Phi(r) = \arctan\left(\frac{P}{2\pi r}\right). \tag{6.2}$$

Besides the blade geometry, the cavitation generation is straightforward affected by the ship velocity and the water head. The advance coefficient, and the dimensionless thrust and torque are kept equal to the full-scale propeller (kinematic condition similarity). These dimensionless quantities are defined according to ITTC guidelines (ITTC Specialist Committee on Hydrodynamic Noise, 2017) like:

$$J = \frac{V_a}{nD}\,. \tag{6.3}$$

$$K_T = \frac{T}{\rho n^2 D^4}\,. \tag{6.4}$$

$$K_Q = \frac{Q}{\rho n^2 D^5}\,. \tag{6.5}$$

Table 6.1: Geometrical descriptors.

Input Variable	Description	Unit
D	Diameter	[m]
P	Pitch	[m]
P/D	Pitch ratio	[]
$\Delta\Phi$	Difference between actual and design pitch	[°]
A_E	Expanded area	[m^2]
BAR	Blade area ratio	[]
Z	Number of blades	[]
α_s	Shaft angle	[°]
c	Blade chord at $0.7R$	[m]
c/D	Chord ratio at $0.7R$	[]
t_{max}	Blade maximum thickness at $0.7R$	[m]
t_{max}/c	Thickness ratio at $0.7R$	[]
f_{max}	Blade maximum camber at $0.7R$	[m]
f_{max}/c	Camber ratio at $0.7R$	[]

$$\eta_o = \frac{J}{2\pi}\frac{K_T}{K_Q}\,. \tag{6.6}$$

The full scale hydrodynamic analogy is reproduced in principle by the cavitation number identity.

$$\sigma = \frac{p_{static,ref} - p_v}{0.5\rho V_{ref}^2}. \tag{2.2 revisited}$$

In Equation (2.2) $p_{static,ref} = p_{atm} + \rho g h$ and p_v vapour pressure of water. The height h can be the shaft immersion at the center disk or at the highest blade tip (the top dead center), depending upon the purpose.

Four formulations of the cavitation index have been considered: σ_n is the cavitation number evaluated at the shaft line, based on the peripheral speed ($V_{ref} = n\mathrm{D}$), σ_v is again evaluated at the shaft line, but based on the advance speed ($V_{ref} = V_a$), σ_{ntip} is the index based on peripheral speed ($V_{ref} = n\mathrm{D}$) but with respect to the static pressure at the blade tip and lastly σ_{tip} is based on resultant velocity at blade tip ($V_{ref} = \sqrt{V_a^2 + (\pi n\mathrm{D})^2}$), with static pressure at the tip. The functioning descriptors are listed in Table 6.2.

In the Approach 1 of the modelling phase thrust and toque have been taken from the MST; in the Approach 2, in view of keeping separate the features from the experimental tests, they have been provided from the BEM calculations.

6.3 Cavitation pattern

In experimental tests an accurate cavitation bucket has been drawn for every configuration. No other information about the cavitation areas or volume are available from tests, hence the only possible features must be obtained from the buckets. The idea was to get an indicator of the distance from the inception points for a given phenomena. Ideally when the indicator is greater than one the inception is still far, when it is equal at 1 the inception threshold has been reached and when it is

Table 6.2: Functioning descriptors.

Input Variable	Description	Unit
V_a	Advance velocity	$[^m/_s]$
n	Rate of propeller rotation	[Hz]
T	Propeller Thrust	[kgf]
Q	Propeller Torque	[kgf·cm]
J	Advance coefficient	[]
K_T	Thrust coefficient	[]
$10K_Q$	Torque coefficient	[]
RelPre	Relative pressure	[mBar]
σ_v	Cavitation index referred to advance velocity	[]
σ_n	Cavitation index referred to rotational speed	[]
σ_{tip}	Cavitation index referred to resultant speed at blade tip	[]
σ_{ntip}	Cavitation index referred to rotational speed at blade tip	[]

less than one the cavities are fully developed. Therefore, the propeller cavitation pattern can described by the parameter σ_n/σ_{ni}, that is the ratio between the actual cavitation number and the inception index for the phenomenon.

Cavitation types have been divided as common practice in suction side and pressure side phenomena; the first have been divided further according to the angular sector where they originate. Frequently behind wake some phenomena are overstimulated and hence the inception anticipated. For instance S.S. cavitation usually arises in proximity of the maximum angle of attack; this can be located at the top dead centre in single screw vessel or in the first half of the first quadrant for twin screw vessel (named 0° in the following) or also in the second quadrant for open water test with inclined shaft (named 90°).

Being the tip vortex cavitation (TVC) the most important types for the considered propellers, a further distinction have been made between a vortex showing only in the downstream (D.TVC, Detached tip vortex) or connected to the blade (TVC). Other distinctions are listed in Table 6.3.

Table 6.3: Cavitation pattern features.

Input Variable	Description	Unit
TVC 90°	Suction side tip vortex	[]
D. TVC	Detached tip vortex	[]
TVC 0°	Suction side tip vortex at 0°	[]
S.S. S	Suction side sheet	[]
S.S. S 0°	Suction side sheet at 0°	[]
S.S. RB	Suction side root bubbles	[]
S.S. B	Suction side bubbles	[]
VFSF	Vortex from sheet face	[]
P.S.TVC	Pressure side tip vortex	[]
P.S. S	Pressure side sheet	[]
P.S. RB	Pressure side root bubbles	[]

6.4 Axial wake inflow

The wake field strongly influences propeller cavitation and its dynamics, both because of its global intensity, usually represented by the average wake fraction, and its variations at different angular positions. The velocity with which the blade passes from the undisturbed flow to the reduced one, the severity of this negative peak and the time that elapses during this passage affects the growth and collapse of cavities and hence the generated noise. In particular, these aspects are of utmost importance for present cases because of the characteristics of considered wake fields. Actually, they are characterised by average values of the wake fraction rather close to zero (which could suggest undisturbed flow), and very close each other even if, as pointed out by Figure 4.8, the wakes are strongly different each other.

As an example in Figure 6.1 two photos taken at the same WP (same K_T and σ_n) for propeller P1 at design pitch are visible, behind twin screw wake, on the left, and without wake, on the right. The cavitation pattern is considerably different and this discrepancy is due to the inflow wake: behind wake it presents S.S. sheet that grows and quickly collapse due to sudden change in the axial wake, while from the sheet a thick and stable tip vortex is generated; conversely, when no wake is present and the only disturbance is given by the dynamometer, no sheet cavitation is present and the tip vortex at 0° is intermittent until the blade reaches the 90° position where it becomes attached because of the increased angle of attack.

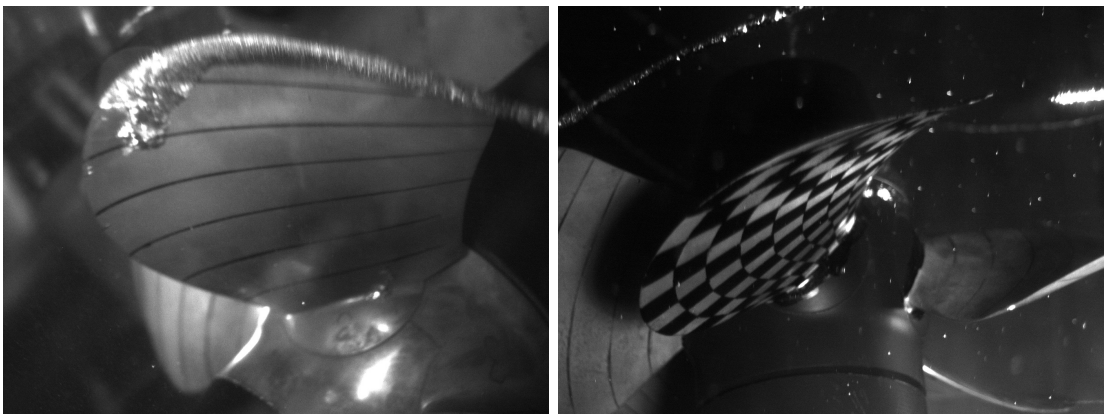

Figure 6.1: Effect of the wake on cavitation extent: P1 at design pitch, behind W1 (left) and W2 (right) for the same functioning point.

Due to this, it is necessary to define suitable parameters able to describe these kinds of wakes, discriminating between the considered cases whose differences may be rather important from the point of view of noise generation.

To this aim, wake parameters have been defined partially following Odabaşi and Fitzsimmons (1978) and are schematised in Figure 6.2. The left and right gradients are the the maximum and minimum derivatives of the wake with respect to the blade angular position, computed at a given radial position. The wake width is the angular sector where the wake fraction is greater than 0.05 (i.e. where the axial velocity on the propeller plane is reduced at least by the 5%). The wake depth is the maximum value of the wake fraction for a given radial position with respect to $w = 0$. The little decelerated peak visible at around $-30°$ is produced by the shaft bracket and it is neglected in this computation because from experimental evidence it is irrelevant in the driving mechanism of the cavitation.

The wake characteristics are reported for two radial positions, namely $0.7R$ and $0.9R$, since these two positions are considered as the most representative for sheet cavitation (both suction side and pressure side) and tip vortex cavitation.

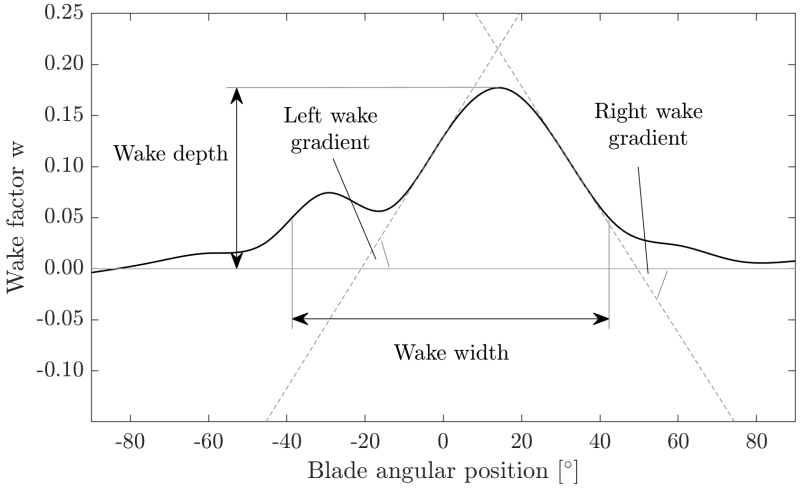

Figure 6.2: Wake parameters.

Lastly, the mean wake fraction is computed by Equation (6.7).

$$\overline{w} = \frac{\int_0^{2\pi} \int_{r_{hub}}^{R} w(r,\theta) r dr d\theta}{\pi(R^2 - r_{hub}^2)}. \tag{6.7}$$

In Table 6.4 the calculated values are summarised. For the uniform inflow (W2 and W5) a proper wake does not exist but only the little disturbance given by the dynamometer arrangement which by experimental evidence is known to have negligible influence on noise generation. Due to this the wake features are zero exception made for the wake width that is set to 360°. The wake factor at constant values of r/R are plotted for each wake at radial section $0.7R$ in Figure 6.3 and for $0.9R$ in Figure 6.4: from these plots it is evident how the average wake factor is not sufficient alone to provide a full characterisation of the wake.

The wake $(1 - w)$ has been also provided (for the Approach 2 only), for each samples, as a matrix with blade angular position by row and blade radial section by columns.

Table 6.4: The wake features.

Wake	$\overline{w}$	Left wake gradient		Right wake gradient		Wake width		Wake depth	
		$0.7R$	$0.9R$	$0.7R$	$0.9R$	$0.7R$	$0.9R$	$0.7R$	$0.9R$
W1	0.036	19.7°	29.6°	-43.4°	-40.9°	76°	86°	0.265	0.286
W2	0	0	0	0	0	360°	360°	0	0
W3	0.031	19.5°	27.7°	-19.1°	-27.7°	82°	82°	0.177	0.227
W4	0.022	27.8°	18.5°	-25.3°	-30.7°	41°	63°	0.177	0.215
W5	0	0	0	0	0	360°	360°	0	0
W6	0.020	17.7°	37.2°	-19.5°	-56.5°	9°	23°	0.067	0.148

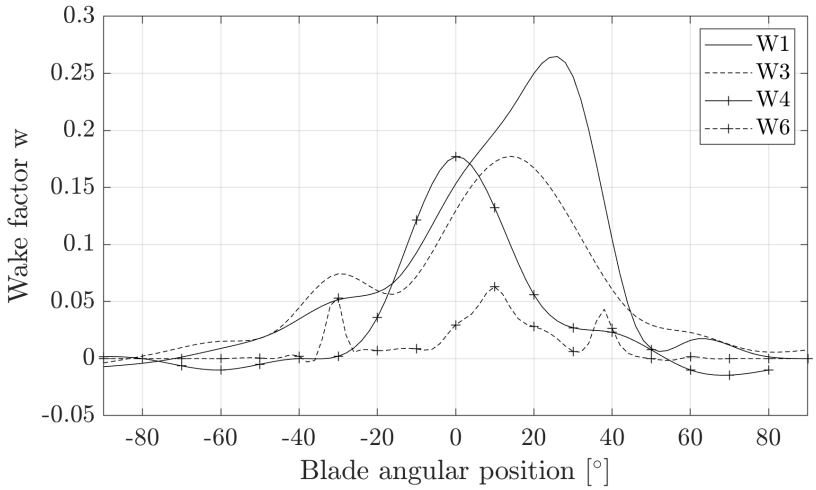

Figure 6.3: Axial wake distribution for section $r/R = 0.7$.

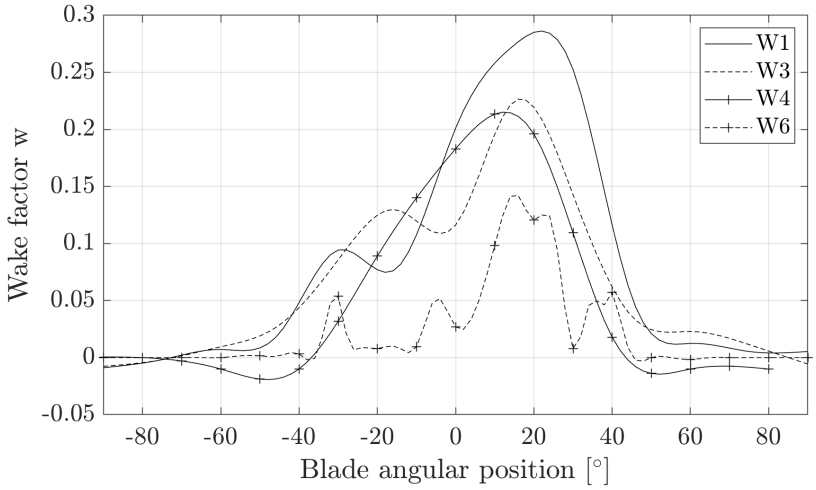

Figure 6.4: Axial wake distribution for section $r/R = 0.9$.

6.5 Geometric angle of attack

The angles of attack have been used with the particular aim to describe the hydrodynamic functioning of blades sections with special reference to suction side sheet cavitation. With respect to the wake field, the angle of attack allows to better take into account the effects of the pitch setting combined with the characteristics of the inflow, including also the shaft inclination. Since the propeller self-induced velocities are not known, the geometric angle of attack is used (Figure 6.5). These self induced velocities could be simply calculated using e.g. a lifting line code. However, it is believed that the additional information would not be very important, based also on the results reported in the following.

The geometric angle of attack α_G (ITTC Propulsion Committee, 2008) is defined as the difference between the advance angle $\beta(r, \theta)$ of a blade section, determined by Equation (6.8), and the local pitch angle Φ.

$$\beta(r,\theta) = \arctan\left(\frac{V_a(1-w)}{\pi \cdot D \cdot n \cdot r/R + V_a(1-w) \cdot sin(\alpha_s) \cdot sin(\theta)}\right). \tag{6.8}$$

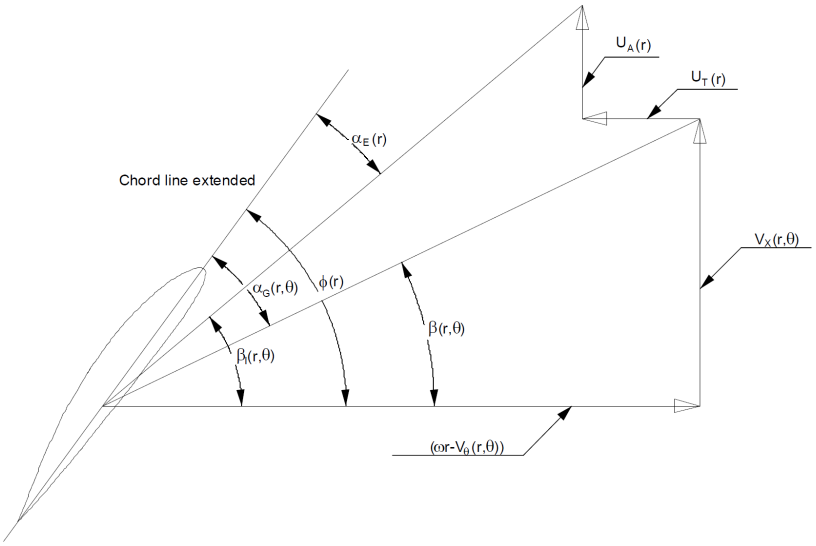

Figure 6.5: Velocity diagram for a propeller blade section at section r (image from ITTC Propulsion Committee (2008))

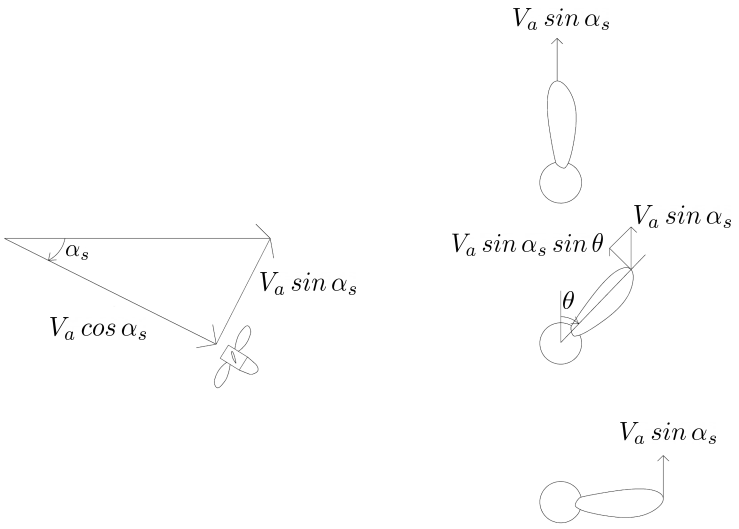

Figure 6.6: Inflow velocity components.

In Equation (6.8) α_s is the shaft angle, and θ is the blade angular position. The term $V_a(1-w)\cdot sin(\alpha_s)\cdot sin(\theta)$ is due to the influence of the shaft inclination on the tangential velocity seen by the propeller which include the tangential wake factor (Figure 6.6): this is zero when the blade is vertical and reaches the maximum when the blade is horizontal (positive at $\theta = 90°$, negative at $\theta = 180°$).

Figure 6.7 shows some examples of the variation of beta angle during the revolution and the effect of shaft angle on velocity modulation for two radial sections. The propeller is the P2 with an undisturbed velocity of 5.25 m/s and revolution speed 25 Hz. Uppermost, it is noticeable the ship wake effect on β, with the global minima at around 18° just as the corresponding wake curves. Further, with zero

shaft angle (dashed lines), β assumes the same value at 90° and 270°. Instead, when shaft inclination is accounted (solid line), in the first quadrant the advance angle decrease because the added velocity is positive (concordant with the propeller peripheral speed), otherwise in the fourth quadrant (from −90° to 0°). In this example, the difference due to shaft inclinations is quite small because in the tests have been performed with a reduced shaft angle.

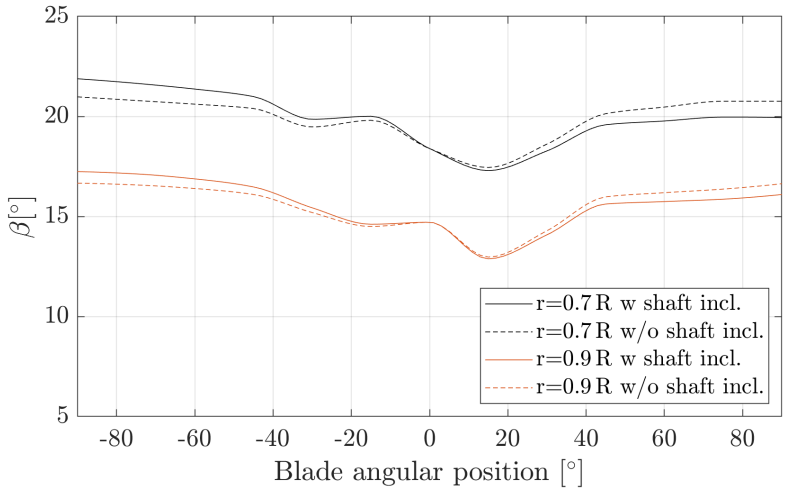

Figure 6.7: Shaft inclination effect on advance angle.

In Figure 6.8 an example of β for different wakes is given. The kinematic condition chosen is $V = 5.25\,\mathrm{m/s}$ and $n = 22.5\,\mathrm{Hz}$, the radial section is $0.7R$. W2, being the uniform wake inflow for P1, has only a sinusoidal modulation due to shaft angle (if were $\alpha_s = 0$, β would be steady along the revolution).

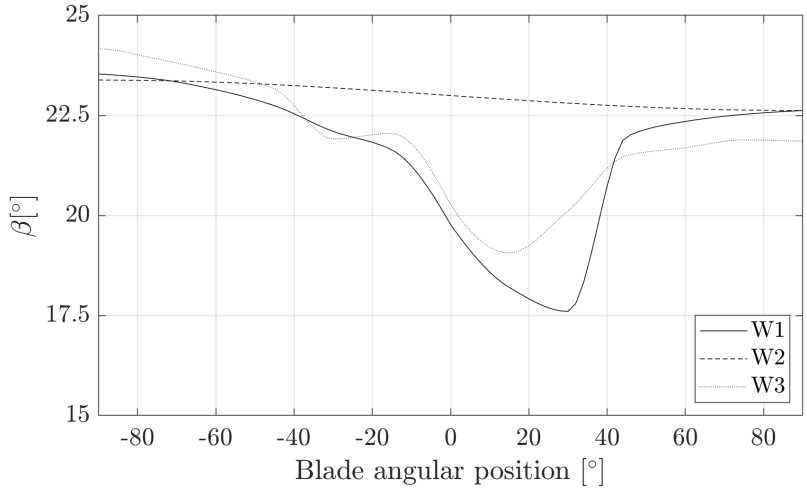

Figure 6.8: Wake effect on advance angle.

The geometric angle of attack is the angle between the flow, considering the effects of the wake and the inclined shaft, and the chord line pitch, neglecting the self-induced velocities.

$$\alpha_G(r,\theta) = \Phi(r) - \beta(r,\theta). \tag{6.9}$$

As expected the minimum α_G is always located at 270°, because of the effect of the inclined shaft, while the maximum is in correspondence of the decelerated wake peak (see Figure 6.9, propeller speed and flow velocity are again $V = 5.25\,\mathrm{m/s}$ and $n = 22.5\,\mathrm{Hz}$) but, in case of less pronounced wake peak and significant shaft inclination, it may be located also at 90°.

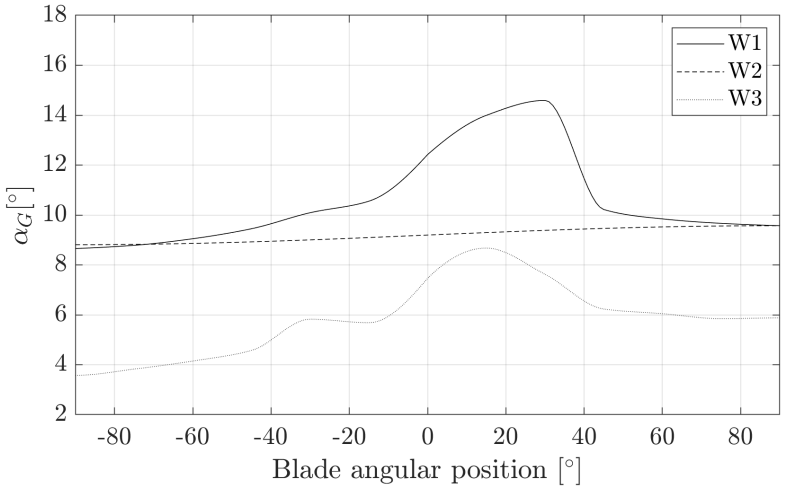

Figure 6.9: Angle of attack for three different propeller at design pitch (P1-W1, P1-W2, P2-W3) at $0.7R$.

The features extracted from the angle of attack are summarised in Table 6.5, they include the average value on the whole revolution, the maximum and minimum value, and the angular position of the maximum for two radial position.

Table 6.5: Geometrical angle of attack features.

Input Variable	Description	Unit
$\overline{\alpha}_{G07}$	Circumferential average α_G at $0.7R$	[°]
min α_{G07}	Minimum α_G at $0.7R$	[°]
max α_{G07}	Maximum α_G at $0.7R$	[°]
$\theta\|_{max\ \alpha_{G07}}$	Angular position of maximum α_G at $0.7R$	[°]
$\overline{\alpha}_{G09}$	Circumferential average α_G at $0.9R$	[°]
min α_{G09}	Minimum α_G at $0.9R$	[°]
max α_{G09}	Maximum α_G at $0.9R$	[°]
$\theta\|_{max\ \alpha_{G09}}$	Angular position of maximum α_G at $0.9R$	[°]

The angle of attack has been also provided (for the Approach 2 only), for each samples, as a matrix with blade angular position by row and blade radial section by columns.

6.6 Boundary Element Methods features

In the last part of this work of feature extraction, a series of non-stationary and non-cavitating BEM calculations have been performed by the research group with in-house software.

The actual propeller geometry has been modelled through 42 panels with cosinusoidal spacing in the chord wise direction, to increase the discretization accuracy at blade leading and trailing edge. Twenty-three sections are distributed, following a geometric progression, on the radial direction for a total of more than 900 panels on each blade including the related portion of the hub. The mesh grid for the propellers is visible in Figure 6.10. The trailing wake has been modelled for six complete propeller revolutions, with a time step corresponding to 6°.

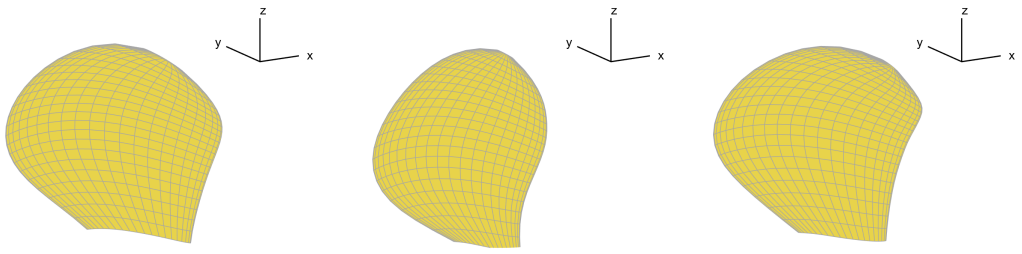

Figure 6.10: Panel representation of the model propellers P1 (left), P2 (middle) and P3 (right), at design pitch.

To reduce computational time, in view of establishing a routine procedure, the WPs have been modelled keeping fixed the propeller speed at 25 Hz and considering a limited number of inflow speed. Afterwards, the features for the actual working points have been obtained by means of interpolation on the inflow velocity and scaling for the revolution speed. Lastly, the features have been interpolated on nominal radial section from $r/R = 0.35$ to 0.95, in order to achieve a congruent grid for all the propellers; radial position very close to the tip have been discarded due to instability in the numerical results.

From the BEM calculations the following data are obtained:

- the hydrodynamic curves (K_{TBEM}, K_{QBEM});
- the matrix of coefficients of pressure C_P computed in correspondence to each panel (both chord and span wise) and time step;
- the blade circulation Γ in $[m^2/s]$ for every radial section and time step.

Recalling that the calculations have been performed at 25 Hz, and knowing that the BEM circulation (Γ_{25}) can be made non-dimensional as in Equation 6.10, the final circulation for the samples revolution speed is given in Equation 6.11.

$$\Gamma_{adim} = \frac{\Gamma_{25}}{\pi 25 D^2}\,, \tag{6.10}$$

$$\Gamma\,(n) = \Gamma_{adim}\pi\ nD^2 = \Gamma_{25}\frac{n}{25}\,. \tag{6.11}$$

6.6.1 Estimation of the cavitating area

In the physical model for the prediction of the cavitation noise driven by the S.S. sheet, described in Section 7.6, one of the input parameters is the area swept by cavitation. Brown (1976) does not provide further explanation on how to derive this area. For instance, the cavitation area varies almost periodically during the propeller revolution, especially if the propeller is operating behind wake.

The measure of the cavitation area can be accomplished with different methods and with different degree of accuracy. The most sophisticated is by means of high-speed cameras which can track the sudden dynamic of cavitation bubbles. If high-speed cameras are not available, also from normal photographs it can be retrieved a less accurate estimation of the cavitation area: in this case instantaneous, violent, change in cavitation area cannot be noticed, hence the area could be underestimated or overestimated.

CFD computations are nowadays used to predict cavitation extent, in particular for the sheet cavitation. RANS (Reynolds Averaged Navier-Stokes equation) are then a valid alternative to calculate the cavitation area, in place of MSTs. Anyhow, RANS will be computational expensive, in particular if they have to be applied to a large dataset, with many off-design working points.

In the first phase of this task, it has been preferred to compute the cavitation area A_C from non-cavitating BEM calculation. The cavitation extent is approximated by the condition $-C_P > \sigma_n$ on the suction side of the blade; from the condition, the cavitating panels are detected and their area measured. This operation is repeated for each angular position of the propeller and for each radial section. This is obviously only an approximation, not considering the development of cavitation, which results in an enlargement of the cavitating area on the blade; however, this may allow to discriminate between different conditions, avoiding long cavitating calculations.

In Figure 6.11 an example of the determination of the cavitating area for a given loading condition (defined by $\sigma_n = 2.5$) is shown, the dots are in correspondence of the edge of the panels at $r/R = 0.95$.

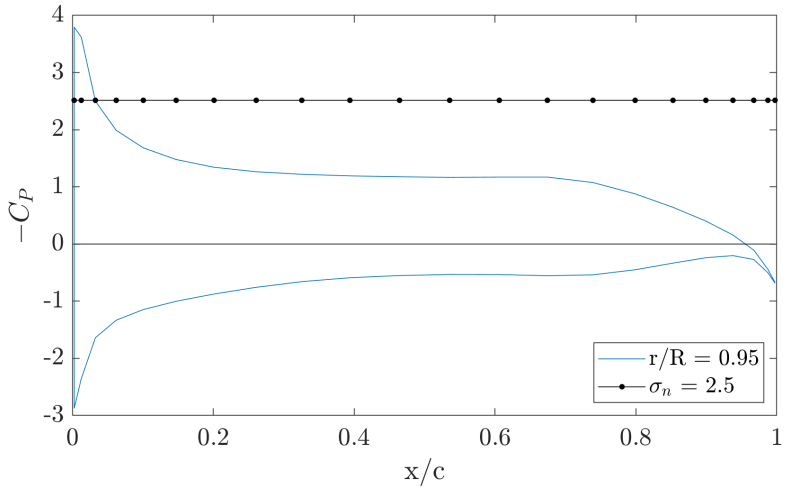

Figure 6.11: Example of cavitating area measure.

In Figure 6.12 are reported as example, the cavitating panels for P1-DES at a high load condition, the position is referred to the angular position of blade 1. The

propeller is seen by the back, and it is moving anti-clockwise from this point of view. In Figure 6.12a the blade 1 is at around half a quarter turn before the top dead center, it is reaching the decelerated wake. In Figure 6.12b the blade 1 is at 0° just behind the ship wake, the cavitating area for this blade is at its highest value. Then the blade moves away the decelerated zone and the cavitating area decreases accordingly.

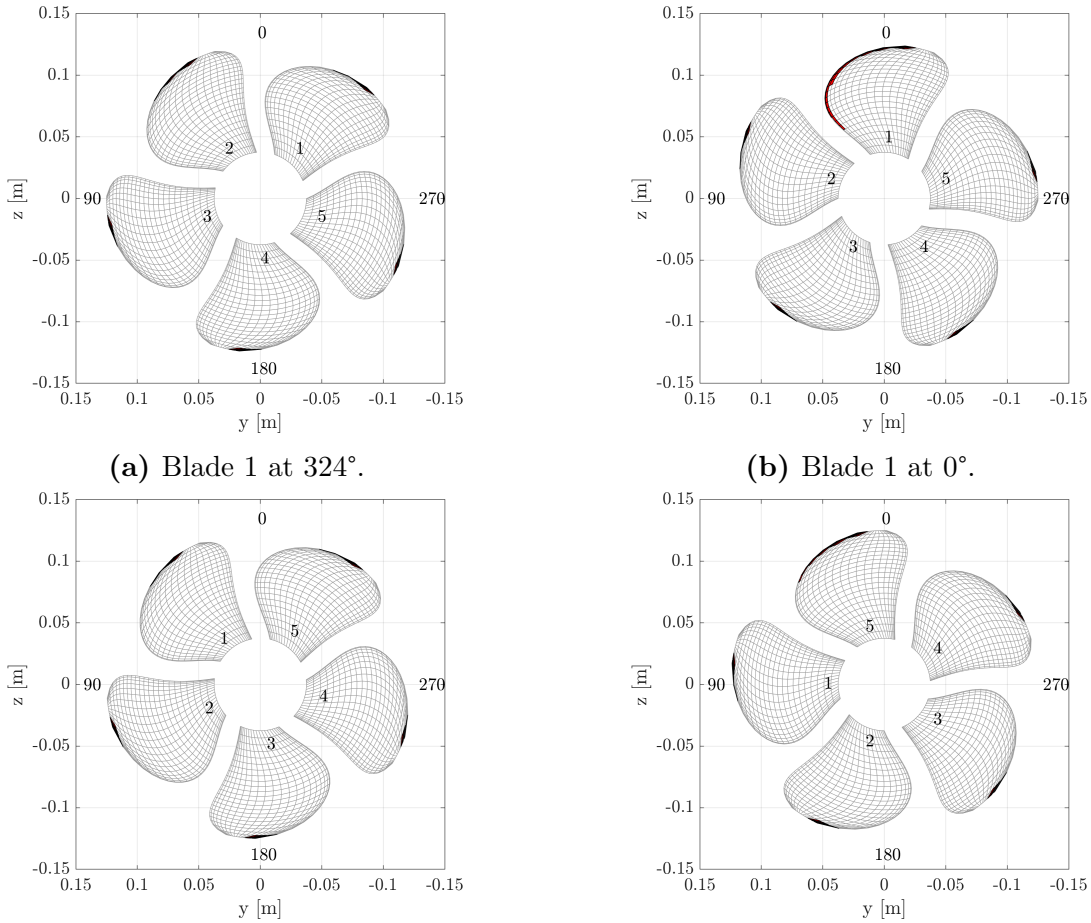

(a) Blade 1 at 324°.

(b) Blade 1 at 0°.

(c) Blade 1 at 42°.

(d) Blade 1 at 90°.

Figure 6.12: Cavitation area for propeller P1-DES at high load and average cavitation index.

In Figure 6.13, for the same load of the previous image, the total cavitating area for different cavitation numbers are plotted, with respect to the propeller disc area (the period is of $360/Z$). The maximum value of the area will be used as an input for the PM. In Figure 6.14 the definitive areas are shown: each colour represents a different configuration, and within each configuration, from left to right, the blade load increases. Some clusters are distinguishable in each configuration, with the appearance of a monotone rise: each of them is referred to the same K_T and to a progressive decrease in σ_n. In practice, even with all the limitation of this method, the cavitation swept area grows when the cavitation number decrease.

Due to limits in non-cavitating BEM, the most unloaded condition appears as cavitation free, this drawback will have to be learnt by the ML. However this does not undermine the advantage of the presented approach.

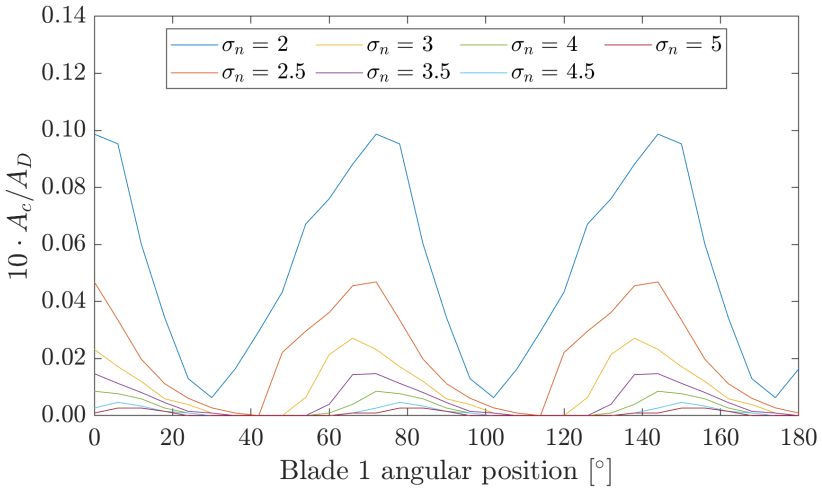

Figure 6.13: Cavitation area for propeller P1-DES at high load for various cavitation number.

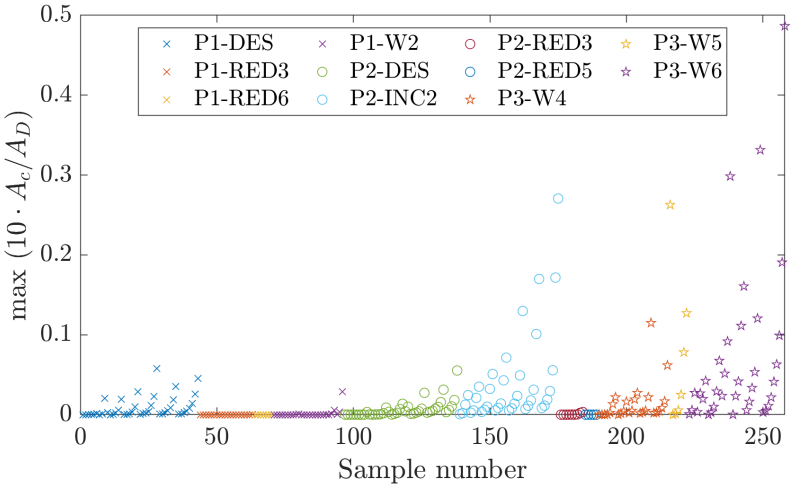

Figure 6.14: Maximum cavitation area during propeller revolution for the whole dataset.

6.7 Summary

Cavitation growth, collapse and rebounds is highly susceptible to propeller geometry and to the environmental conditions, such as water quality, etc. The selected features have been grouped in four categories:

- propeller geometry, these are the general dimensions of the propeller together with the expanded area and the thickness and camber of $0.7R$ section;
- working conditions, which comprises shaft angle, pitch setting and hydrodynamic forces;
- the cavitation extent as pure numbers related to the strength of each phenomena (expressed by the ratio σ_n/σ_{ni});

- and lastly the inflow due to the wake disturbance and the angle of attack with which the blade meet the flow.

Descriptors can be obtained from data acquired by sensors and other instruments within model scale tests, or in a totally numerical way thanks to CFD software. The robustness of the second approach relies on the total detachment from the MST for what concern the features. This is a key point for a tool aimed to be employed in place of MST but, on the other side, the DDMs will be more demanding. Indeed, the performance of the models assessed during the test phase are valid if all the inputs come from the same distribution (i.e. they are generated from the same process), then if some features are provided by the model tests, they will need to be always taken from MSTs.

A novel approach consists in considering features derived from BEM calculations, not only for the improvement of knowledge provided to the ML but also because inputs like thrust and torque can so be derived with a certain accuracy without performing MST.

In order to consider the possible advantages and drawbacks of the inclusion of numerical evaluation of propeller functioning conditions, different steps will be considered: first of all, only data from model tests will be considered (Chapter 8), then different sets of features coming from BEM calculations will be added (Chapter 9).

This page was intentionally left blank.

Chapter 7

Semi-empirical models for the cavitation noise prediction

The cavity radius of a cavitating vortex can be computed by different vortex models available in literature; a quick overview of the main cases is here discussed. Therefore, some relations for the prediction of the cavitation noise level are presented. In the conclusion a possible procedure to obtain the vortex resonance frequency and its maximum noise level, starting from BEM computations and experimental data, is outlined.

7.1 Introduction

In the last years much effort has been dedicated to the prediction of the cavitating broadband noise by computational methods, in particular to analyse the generation of noise by turbulent flows. Some example are RANSE, LES (Large Eddy Simulation), or DDES (Delayed Detached Eddy Simulation) solver of the flow field and the Ffowcs-Williams Hawkings "acoustic analogy" for the sound generation and propagation process. These methods are still computationally expensive and lack in the estimate of the noise level in the frequency range where the TVC is expected to have an important contribution (Li, Hallander, and Johansson, 2018).

Other solutions come from the coupling of potential flow methods with semi-empirical models (Matusiak, 1992; Lafeber, Bosschers, and van Wijngaarden, 2015; Fujiyama and Nakashima, 2017) derived from simplified analytical solutions, or from empirical relations, and that usually require tuning on full-scale or model-scale data. This approach, although less sophisticated, is computationally faster and it can be used in practical applications from designer or researcher.

Here two semi-empirical formula for the prediction of the tip vortex noise hump (frequency and power) and one empirical formula for the estimation of the broadband noise due to sheet cavitation will be presented, some of the inputs of these formulations may be obtained by BEM.

The centre frequency of the hump is expected to be related to the vortex natural frequency (Thomson, 1880; Morozov, 1974; Raestad, 1996; Bosschers, 2007). Theoretical models have been developed to describe the dispersion relation of inertial waves on the cavitating core, e.g. Thomson (1880) and Morozov (1974). Later, these theories have been demonstrated by many authors on the basis of experimental data (Maines and Arndt, 1997; Bosschers, 2009; Pennings, Westerweel, and van

Terwisga, 2016). Besides, the resonance frequency of a cavitating vortex has been related by many authors to the vortex cavity radius r_c, that is the thickness of the region filled with vapour. The radius is dependent upon the vortex strength, that in turn depends on blade load distribution. At first approximation, the cavity radius can be found as the radius where the local pressure reaches the water vapour pressure; to compute effectively the local pressure, the knowledge of the velocity field around the vortex is needed. This field is the sum of three components: axial, radial and azimuthal velocities (Figure 7.1). In the models here presented, the axial velocity is neglected because considered steady, while the magnitude of the radial velocity is assumed to be negligible with respect to the tangential velocity (hypothesis of 2-D vortex). Anyway, the pressure distribution is reasonably well predicted from the azimuthal velocity component alone (Hommes, Bosschers, and Hoeijmakers, 2015).

In the past years, a multitude of vortex models have been developed to shape the azimuthal velocity v around a vortex. The simplest model is the potential flow vortex which results in an infinite velocity in the vortex origin and then in infinite negative pressure. In real flows this singularity does not appear due to viscous effects that are responsible for the zero velocity in the origin. In the attempt to model this condition, Rankine proposed a formula where the circumferential velocity in the viscous core r_ν decrease linearly as if the core were a solid body rotating.

More complex models for non-cavitating vortical flows are the one by Lamb (1932) that is the analytical solution for the Navier-Stokes equations for an axisymmetric flow, and many semi-empirical models such as Vatistas, Kozel, and Mih (1991), Proctor et al. (2010), and Gerz et al. (2005). The Lamb-Oseen model is mostly known to overestimate the velocity (as the Rankine's), instead the semi-empirical models, that include a variable number of parameters to be fitted on experimental data, are found to give a more accurate prediction (Hommes, Bosschers, and Hoeijmakers, 2015).

The velocity field surrounding a developed cavitating vortex has been measured by LDV by Campos (1992) and the results showed that the velocity distribution away from the cavity interface is identical to the one of the non-cavitating vortex. The velocity near the cavity could not be measured accurately with LDV because of uncertainty in vortex center location due to wandering or meandering motion of the core, due to free stream turbulence or to instabilities of the vortex core. Moreover, the blade aperiodicity, i.e., the variation in blade location from one period to another also contributes to the perceived wandering motion of the tip vortex (Bhagwat and Ramasamy, 2012).

SPIV (Stereoscopic Particles Image Velocimetry) measurements with high spatial resolution (Pino et al., 2011; Pennings, Westerweel, and van Terwisga, 2015), show that the flow near the cavity interface (for a fully developed cavitating vortex) is decelerated more than in the case of non-cavitating vortex. When a vortex starts to cavitate, the vapour cavity pushes out the flow and the viscous core. As found by Bosschers, Janssen, and Hoeijmakers (2008) near the interface a very small region with solid body rotation can be observed, beyond which the slope of azimuthal velocity distribution with radius first increases and then decreases, without reaching the amplitude of the non-cavitating velocity.

In Figure 7.1 a vortex stream-line, and the azimuthal velocity v distribution in reference to the radial coordinate r are sketched. For a non-cavitating vortex,

the viscous radius is found in correspondence of the maximum azimuthal velocity. Instead, when a cavity starts growing (from r_{c1} to r_{c3}) the velocity peak shift outside and decrease in magnitude.

To capture this phenomenon Bosschers (2018b) presented a new formulation for the Lamb-Oseen model which include the boundary condition at the cavity interface, and, in the same paper, a new semi-empirical model for the cavitating vortices.

In this chapter, an overview of the main vortex models will be presented in Sections 7.2 and 7.3.

A section will be dedicated respectively to the theory behind the formula to predict the resonance frequency (Section 7.4) and the noise level related to the cavitating vortices (Section 7.5). Different relations will be presented according to different set of available data. Eventually, an empirical method by Brown (1976) will be presented in Section 7.6 to predict the broadband noise level related mostly to sheet cavitation, and partly to vortex cavitation, at mid-high frequencies (>10 kHz).

Lastly, a workflow for the prediction of the cavity radius according to the data available will be discussed in Section 7.7.

7.2 Analytical solution for a 2-D vortex

The vortex flow is analysed using a cylindrical coordinate system (r, θ, z) centred in the vortex origin, as in (Figure 7.1), with velocity components (u, v, w) in radial, azimuthal and axial direction. The governing equations of a 2-D, incompressible

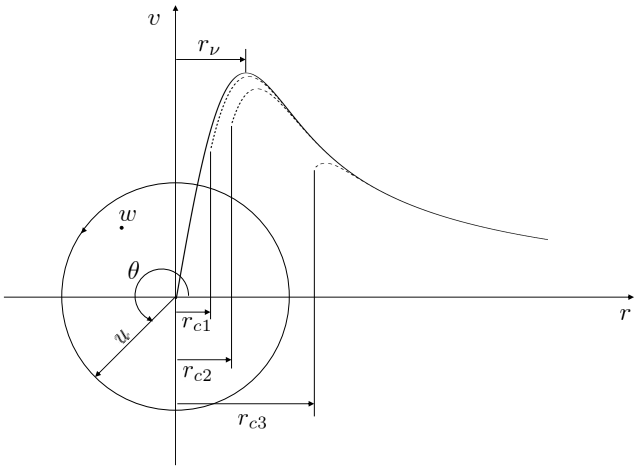

Figure 7.1: Vortex models reference system.

and axisymmetric flow are given by the continuity equation (Equation (7.1)) :

$$\frac{1}{r}\frac{\partial}{\partial r}(ur) = 0\,, \tag{7.1}$$

and by the momentum equations in radial (Equation (7.2)) and azimuthal (Equation (7.3)) direction.

$$\frac{\partial u}{\partial t} + u\frac{\partial u}{\partial r} - \frac{v^2}{r} = -\frac{1}{\rho}\frac{\partial p}{\partial r} + \frac{\mu}{\rho}\frac{\partial}{\partial r}\left[\frac{1}{r}\frac{\partial (ur)}{\partial r}\right]. \tag{7.2}$$

$$\frac{\partial v}{\partial t} + u\frac{\partial v}{\partial r} + \frac{uv}{r} = \frac{\mu}{\rho}\frac{\partial}{\partial r}\left[\frac{1}{r}\frac{\partial (vr)}{\partial r}\right]. \tag{7.3}$$

With t time, p pressure, ρ flow density, and μ dynamic viscosity. Assuming that the radial velocity is zero throughout the fluid domain, the momentum equations can be further simplified:

$$\frac{v^2}{r} = \frac{1}{\rho}\frac{\partial p}{\partial r}, \tag{7.4}$$

$$\frac{\partial v}{\partial t} = \frac{\mu}{\rho}\frac{\partial}{\partial r}\left[\frac{1}{r}\frac{\partial (vr)}{\partial r}\right]. \tag{7.5}$$

It follows that the pressure distribution only depends upon the azimuthal velocity.

For $r \to \infty$ the hypothesis of irrotational and non viscous flow is valid then the azimuthal velocity is given by the potential flow free vortex

$$v(r) = \frac{\Gamma_\infty}{2\pi r}. \tag{7.6}$$

This inviscid model results in $v \to \infty$ at $r = 0$ that is physically infeasible, hence more complex vortex models should be applied.

As a first approximation, the viscous core can be defined like a solid body rotating with viscous radius r_ν, plus a potential decay away from the solid boundary (Rankine model):

$$v(r) = \begin{cases} \frac{\Gamma_\infty}{2\pi r_\nu^2} r & 0 \le r/r_\nu \le 1 \\ \frac{\Gamma_\infty}{2\pi r} & r/r_\nu > 1 \end{cases} \tag{7.7}$$

A singularity is present at the viscous core boundary $r = r_\nu$.

Modeling the viscous core structure and temporal development of lift generated trailing vortices is still a challenge. A complete description of the turbulent viscous core requires the full solution of the Navier-Stokes (N-S) equations which is possible only numerically. Numerical solutions resulting in satisfactory turbulence models are currently available but they are out of the aim of this work. Closed-form solutions for vortex flow are inferable by further simplifying the governing equations.

For bi-dimensional, axisymmetric vortex, and laminar flow, imposing $v = 0$ at $r = 0$ the solution of the N-S leads to Lamb-Oseen vortex (Lamb, 1932):

$$v(r,t) = \frac{\Gamma_\infty}{2\pi r}\left\{1 - \exp\Big(-\frac{r^2}{4\nu\zeta t}\Big)\right\}, \tag{7.8}$$

ν is the kinematic viscosity and $4\nu\zeta t$ is the diffusive growth of the vortex core over time. Now, if viscous radius $r_\nu(t) = \sqrt{4\nu\zeta t}$ (core spreading method, Kuwahara and Takami (1973)) is a prescribed parameter, Equation (7.8) can be rewritten:

$$v(r) = \frac{\Gamma_\infty}{2\pi r}\left\{1 - \beta\exp\Big(-\zeta\frac{r^2}{r_\nu^2}\Big)\right\}, \tag{7.9}$$

$\zeta = 1.2564$ is set to obtain the maximum v at $r = r_\nu$. The parameter β is equal to 1 for non-cavitating flow, instead for a cavitating flow it can be obtained substituting

Equation 7.9 in the boundary condition given by the jump conditions for mass and momentum at the cavity interface (Bosschers, Janssen, and Hoeijmakers, 2008):

$$\beta = \frac{r_\nu^2}{r_\nu^2 + \zeta r_c^2} \exp\Big(\zeta \frac{r_c^2}{r_\nu^2}\Big) \,. \tag{7.10}$$

Then, the velocity at the cavity interface:

$$v(r_c) = \frac{\Gamma_\infty}{2\pi} \Big(\frac{\zeta r_c}{r_\nu^2 + \zeta r_c^2}\Big) \,. \tag{7.11}$$

The pressure variation along the radius can be computed with an acceptable error by integration of Equation 7.4 (Hommes, Bosschers, and Hoeijmakers, 2015):

$$p(r) - p_\infty = -\int_r^\infty \rho \frac{v^2}{r} dr \,. \tag{7.12}$$

Substituting Equation (7.9) in Equation (7.12) and integrating from zero to infinity leads to

$$\begin{aligned} p(r) - p_\infty = & -\frac{\rho \Gamma_\infty^2}{(2\pi r)^2} \Big\{ \frac{1}{2} - \beta \exp\Big(-\zeta \frac{r^2}{r_\nu^2}\Big) + \frac{\beta^2}{2} \exp\Big(-2\zeta \frac{r^2}{r_\nu^2}\Big) \\ & + \frac{\beta \zeta r^2}{r_\nu^2} E_1\Big(\zeta \frac{r^2}{r_\nu^2}\Big) - \frac{\beta^2 \zeta r^2}{r_\nu^2} E_1\Big(2\zeta \frac{r^2}{r_\nu^2}\Big) \Big\} \,, \end{aligned} \tag{7.13}$$

where E is the exponential integral $E_1(x) = \int_x^\infty \exp(-\tau)/\tau \, d\tau$.

In Figure 7.2 a comparison of non-cavitating vortex models is shown in terms of azimuthal velocity and pressure distribution. The reference value v and p are taken from the inviscid model for $r = r_\nu$. It is noticeable the infinite pressure resulting by the potential method at vortex core origin. The vortical region ends when the viscous model velocity equals the potential flow velocity (in Figure 7.2 at around $r/r_\nu = 2$).

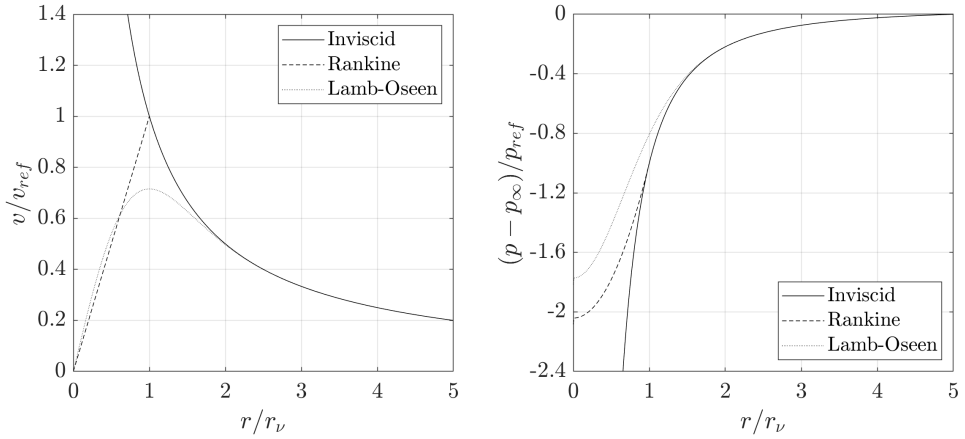

Figure 7.2: Azimuthal velocity (left) and pressure distribution (right) for three non-cavitating vortex models.

In case of absence of cavitation the minimum pressure is located at the vortex center and is given by:

$$p(r = 0) - p_\infty = p_{min} - p_\infty = -\frac{\rho \Gamma_\infty^2}{(2\pi r_\nu)^2} \zeta \log 2 \,. \tag{7.14}$$

Following the same path, the minimum pressure for the Rankine model is

$$p(r=0) - p_\infty = p_{min} - p_\infty = -\frac{\rho\Gamma_\infty^2}{(2\pi r_\nu^2)^2}\,. \tag{7.15}$$

Thus recalling the definition of inception index of cavitation and given the reference velocity V_{ref}, for the Lamb-Oseen vortex reads

$$\sigma_i = \frac{p_\infty - p_{min}}{\frac{1}{2}\rho V_{ref}^2} = \Big(\frac{\Gamma_\infty}{\pi V_{ref} r_\nu}\Big)^2 \frac{1}{2}\zeta \log 2\,. \tag{7.16}$$

The axial vorticity distribution $[s^-1]$ and the circulation $[m^2/s]$ follows from Equation (7.9):

$$\omega_z(r) = \frac{1}{r}\frac{\partial(rv)}{\partial r} = \frac{\Gamma_\infty}{\pi}\frac{\zeta}{r_\nu^2 + \zeta r_c^2}\exp\Big[-\frac{\zeta(r^2 - r_c^2)}{r_\nu^2}\Big]\,, \tag{7.17}$$

$$\Gamma(r) = v(r)\,2\pi r = \Gamma_\infty\Big[1 - \frac{r_\nu^2}{r_\nu^2 + \zeta r_c^2}\exp\Big[-\frac{\zeta(r^2 - r_c^2)}{r_\nu^2}\Big]\Big]\,. \tag{7.18}$$

In Figure 7.3 a comparison is shown between the inviscid model and the cavitating Lamb-Oseen ($\beta \neq 1$) for four different cavity radius. The model follows the experimental evidence of reduced tangential velocity and velocity peak displaced at outer radii, according to the boundary condition of zero shear stress. For larger cavity size ($r_c > 2r_\nu$), viscous effects on the pressure distribution become irrelevant, and the pressure distribution follows the inviscid model.

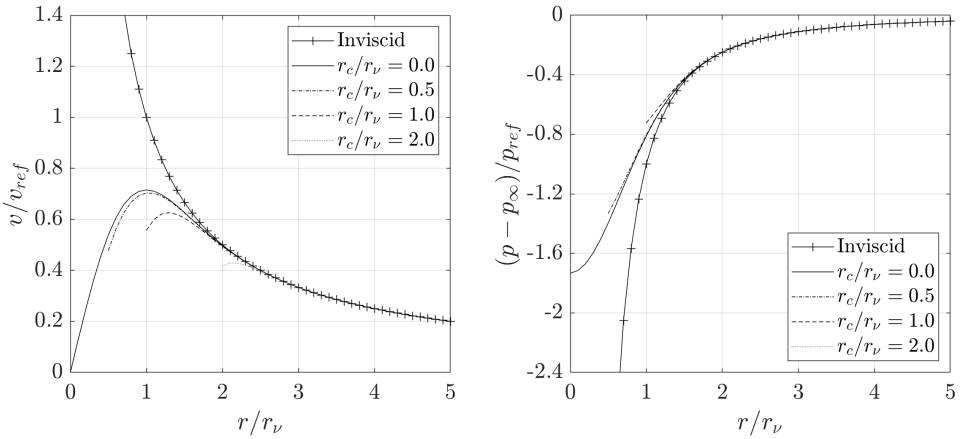

Figure 7.3: Azimuthal velocity (left) and pressure distribution (right) for the cavitating Lamb-Oseen model, for different cavity radius.

Figure 7.4 reports the cavity radius for different cavitation numbers, the ratio σ/σ_i is computed for a range of cavity size by $(p(r_c) - p_\infty)/(p_{min} - p_\infty)$ with the pressure expression of Equation 7.13.

$$\begin{aligned}\frac{\sigma}{\sigma_i} = \Big(\frac{r_\nu}{r_c}\Big)^2 \frac{1}{\zeta \log 2}\Big\{&\frac{1}{2} - \beta\exp\Big(-\zeta\Big(\frac{r_c}{r_\nu}\Big)^2\Big) + \frac{\beta^2}{2}\exp\Big(-2\zeta\Big(\frac{r_c}{r_\nu}\Big)^2\Big) \\ &+ \beta\zeta\Big(\frac{r_c}{r_\nu}\Big)^2 E_1\Big(\zeta\Big(\frac{r_c}{r_\nu}\Big)^2\Big) - \beta^2\zeta\Big(\frac{r_c}{r_\nu}\Big)^2 E_1\Big(2\zeta\Big(\frac{r_c}{r_\nu}\Big)^2\Big)\Big\}\,.\end{aligned} \tag{7.19}$$

As for the pressure distribution, the major difference in prediction of the cavity radius between the two models is for smaller sizes, when the cavity becomes larger than the viscous core the non-cavitating model can be used in place of the cavitating one.

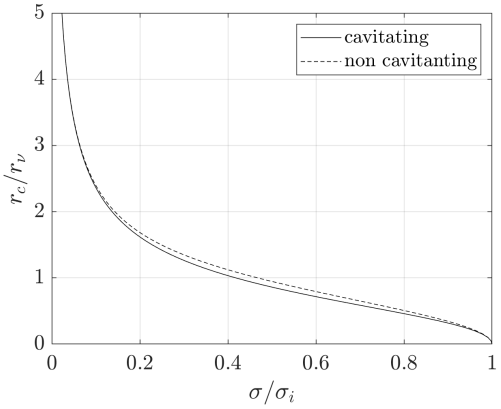

Figure 7.4: Predicted cavity size for the Lamb-Oseen vortex.

7.3 Semi-empirical models for cavitating vortices

The Lamb Oseen model is an analytical solution of the N-S equations where the viscous core of a non cavitating vortex has been spread only by diffusion, the roll-up effect on vorticity is then neglected. Proctor et al. (2010), starting from observation on decay times of counter-rotating vortices arising from an aircraft, proposed a formulation where the diffusivity is influenced also by the vortex sheet roll-up. Being B the wingspan (or depending on the case the length related to the roll-up, e.g. the propeller radius for ships), β and p empirical parameters to be fitted,

$$v(r) = \begin{cases} 1.0939\frac{\Gamma_\infty}{2\pi r}\left\{1 - \exp\left[-\beta\left(\frac{1.4r_\nu}{B}\right)^p\right]\right\}\left\{1 - \exp\left[-\zeta\left(\frac{r}{r_\nu}\right)^2\right]\right\} & r \leq 1.4r_\nu \\ \frac{\Gamma_\infty}{2\pi r}\left\{1 - \exp\left[-\beta\left(\frac{r}{B}\right)^p\right]\right\} & r > 1.4r_\nu \end{cases} \tag{7.20}$$

Suggested value for ζ is 1.2564 as before, while $\beta = 10$ and $p = 0.75$ are the parameters settled by Proctor that can be used as starting point. The drawback of this model is that it is composed by two formula that need to be matched at $r = 1.4\, r_\nu$.

Bosschers (2018b), following the Proctor's approach, introduced a new single-formula model

$$v(r) = \frac{\Gamma_\infty}{2\pi r}\left\{1 - \hat{\alpha}\exp\left[-\zeta_1\left(\frac{r}{B}\right)^p\right]\right\}\left\{1 - \exp\left[-\zeta_2\left(\frac{r}{r_\nu}\right)^2\right]\right\}. \tag{7.21}$$

The coefficients $\hat{\alpha}$, p and ζ_1 are fitting parameters to experimental velocity curves; $\hat{\alpha}$ should be comprised between 0 and 1 and it has been included to maintain a solid body rotation near the centre of the vortex, if 0 value is chosen the Lamb-Oseen is obtained.

The ζ_2 parameter has to be chosen so that the maximum velocity is at $r = r_\nu$. This is accomplished with a recursive procedure: at first stage $\zeta_2 = \zeta$, then at every iterative step it is updated as $\zeta_2^{new} = \zeta_2 \left[r(v_{max})/r_\nu \right]$, with $r(v_{max})$ the radius at which $v(r)$ reaches the maximum.

As done for the cavitating Lamb-Oseen, substituting the azimuthal velocity of Equation (7.21) in the boundary condition at the cavity interface (which requires that the tangential component of the shear stress at the cavity interface equals zero), the β is given by

$$\beta = \frac{2(1-\overline{\alpha})B^p r_\nu^q - \overline{\alpha}\zeta_1 p r_c^p r_\nu^q}{2(1-\overline{\alpha})B^p r_\nu^q - \overline{\alpha}\zeta_1 p r_c^p r_\nu^q + (1-\overline{\alpha})B^p q \zeta_2 r_c^q}\,, \tag{7.22}$$

with

$$\overline{\alpha} = \hat{\alpha}\exp\Big[-\zeta_1\Big(\frac{r_c}{B}\Big)^p\Big]\,, \tag{7.23}$$

and the radial distribution of azimuthal velocity for a cavitating vortex becomes

$$v(r) = \frac{\Gamma_\infty}{2\pi r}\left\{1-\hat{\alpha}\exp\Big[-\zeta_1\Big(\frac{r}{B}\Big)^p\Big]\right\}\left\{1-\beta\exp\Big[-\zeta_2\frac{r^q-r_c^q}{r_\nu^q}\Big]\right\}\,. \tag{7.24}$$

The default value for q is 2, but it can change to adapt the distribution of velocity to measured ones for the cavitating case, if needed.

Figure 7.5 reports the comparison for the three non-cavitating models: the Lamb-Oseen overestimates the pressure peak, instead the Proctor and the Bosschers models are quite comparable. The larger differences appear when comparing the Proctor

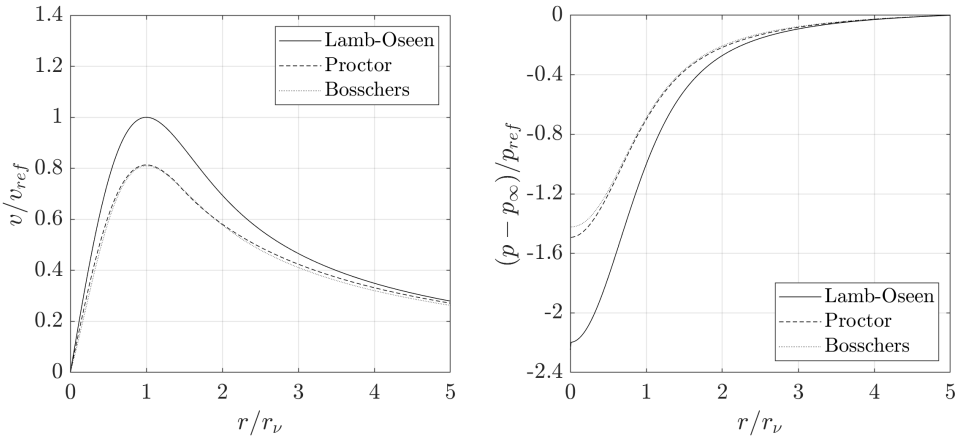

Figure 7.5: Azimuthal velocity (left) and pressure distribution (right) for the Lamb-Oseen, Proctor and Lamb-Oseen modified model (Bosschers), in non-cavitating condition.

model with the Bosschers model for three values of cavity size (Figure 7.6). The velocity field changes considerably for larger r_c and accordingly the pressure drop at the cavity interface decreases. The difference in predicted pressure between the more sophisticated Bosschers model and the Proctor model, decreases for well developed vapour cavity and becomes negligible for $r_c/r_\nu = 2$.

The detailed analysis on the effects of using different vortex models in the prediction of the experimental cavity radius goes beyond the purpose of this chapter and reference should be made to the work of Bosschers (2018b). Form this paper the

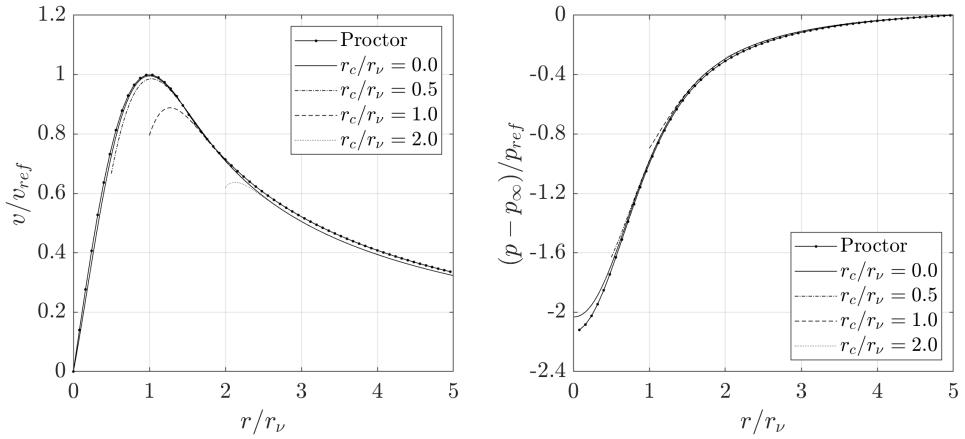

Figure 7.6: Azimuthal velocity (left) and pressure distribution (right) for the Proctor, and Lamb-Oseen modified model (Bosschers) for different cavity radius.

conclusions that can be draw on this matter are that when the vortex is attached to the tip, the non cavitating and the cavitating modified Lamb-Oseen vortex models give an accurate estimate of the cavity radius.

Conversely, when the vortex is detached from the tip and the cavity radius is small, the model that better fits the data is the modified cavitating Lamb-Oseen model with a correction applied to the viscous size ($r_{(\nu,corr)} \propto r_c/r_\nu$). Instead, for larger cavity size this models underpredicts r_c and the correction should be dropped.

7.4 Resonance frequency of a cavitating vortex

In this section formulations for the estimation of the cavitating vortex resonance frequency will be derived, starting from the theory of the single bubble of gas. The different formulations will differ according to increasing degrees of complexity, due to different set of inputs.

The resonance frequency of a single bubble of gas, immersed in an infinite domain of water (neglecting the effects of surface tension and viscous attenuation) can be found approximately from the relation of Minnaert (1933).

$$f_c = \frac{1}{r_c}\left(\frac{\Delta p}{\rho}\right)^{0.5}, \tag{7.25}$$

with Δp the pressure difference between inside and outside of the bubble, ρ the density of water and r_c the cavity radius. For the case of the cavitating tip vortex, the difference in pressure is related to the cavitation index σ_{tip} (Equation 2.2) evaluated at the blade tip. Equation 7.25 can be written as a function of σ_{tip}

$$f_c \propto \frac{1}{r_c}\sqrt{\sigma_{tip}} nD\,, \tag{7.26}$$

or alternatively

$$\frac{f_c}{BPF} \propto \frac{1}{r_c/D}\frac{\sqrt{\sigma_{tip}}}{Z}\,. \tag{7.27}$$

The cavity radius can be computed by the aforementioned vortex models.

Otherwise, the relation for a cavity radius near the hydrofoil tip can be written as a function of the tip circulation (Kuiper (1981, p. 136) and Tietjens and Prandtl (1957)):

$$\frac{r_c}{D} = \frac{1}{2\pi}\frac{\Gamma_{tip}}{nD^2}\frac{1}{\sqrt{\sigma_n}}\,, \tag{7.28}$$

where Γ_{tip} is the circulation at the propeller tip. This relation is found by the assumption of potential flow and viscous core as a rotating solid body. The cavity radius is obtained calculating the pressure distribution with the spiral vortex approach of Moore and Saffman (1973) and imposing the condition $p(r_c) = p_v$.

The Kutta's theorem expresses the lift of a 2-D airfoil when encountering a fluid at constant velocity in relation with the fluid density and the circulation around the foil. The propeller is a 3-dimensional body and the force of interest is the thrust rather than the lift, also the incident flow changes radially and is unstable due to inflow turbulence, so the total thrust can be only approximated by Kutta's theorem:

$$T = \rho n D^2 \overline{\Gamma} Z\,, \tag{7.29}$$

with $\overline{\Gamma}$ the mean circulation on the blade. The thrust can be rewritten in the usual non-dimensional form

$$K_T = \frac{\overline{\Gamma} Z}{nD^2}\,. \tag{7.30}$$

Hence, the circulation at the tip can be found by Equation 7.30 assuming that the thrust at the tip can be approximated by a factor τ, that is representative of the relative loading between blade and tip, hence Γ_{tip} becomes

$$\Gamma_{tip} = \frac{\tau K_T n D^2}{Z}\,. \tag{7.31}$$

Consequently, Equation 7.27 is rewritten as:

$$\frac{f_c}{BPF} \propto \frac{\sigma_{tip} n D^2}{Z\Gamma_{tip}}\,. \tag{7.32}$$

If the cavity radius is unknown, substituting the blade tip circulation of Equation 7.31 in Equation 7.28, the cavity radius can be expressed by propeller working parameters. Lastly, the resonance frequency becomes

$$\frac{f_c}{BPF} \propto \frac{\sigma_n}{\tau K_T}\,. \tag{7.33}$$

The same formulation to Equation 7.26 has been applied by Maines and Arndt (1997) to model the frequency for a singing vortex.

$$\frac{2\pi f_c r_c}{\pi n D} = 0.45\sqrt{\sigma_{\text{tip}}}\,. \tag{7.34}$$

With similar consideration as before, this leads to

$$f_c = \frac{0.45\sigma_{\text{tip}} n Z}{\tau K_T}\,. \tag{7.35}$$

The constant 0.45 has been found to fit the experimental data collected by Maines and Arndt (1997) on four elliptical hydrofoil' singing frequencies.

In Chapter 8 the Equation 7.35 will be used to predict the vortex resonance frequency on the current dataset. Hence, Equation 7.27 will be used together with the Proctor's model to compute the vortex cavity radius later in Chapter 9.

7.5 Noise level of a cavitating vortex

The acoustic power for a spherical pressure wave is proportional to the second power of the acoustic pressure. The power in decibel can be written as:

$$\mathrm{dB} = 20 \log_{10} \left(\frac{p}{p_{ref}} \right), \tag{7.36}$$

with p the root mean square of the pressure, and p_{ref} a reference pressure value that is $1\mu Pa$ for water. Considering now a cavitating vortex, its noise level in dB (called $\mathrm{RNL_c}$) can be computed with respect to non dimensional pressure as:

$$\mathrm{RNL_c} = 20 \log_{10} \left(\frac{p_a}{\rho n^2 D^2} \right), \tag{7.37}$$

p_a is the acoustic pressure of the vortex at a distance r from the source. Raestad (1996) found that the pressure data collected in full-scale trials by the DnV classification society, can be accurately modelled as a function of the volume acceleration of the tip vortex cavities, considering the noise from each vortex as incoherent sources, which results in:

$$p_a = C_1 \, \mathrm{TVI} \, \rho n^2 D^2 \, . \tag{7.38}$$

C_1 is a proportionality factor. The Tip Vortex Index (TVI) is a non-dimensional factor describing the pressure field from the propeller tip vortex.

$$\mathrm{TVI} = \left(\tau \frac{K_T}{Z} \right)^2 \frac{\sqrt{Z}}{\sigma_{tip}} \, . \tag{7.39}$$

Introducing TVI in Equation 7.37 gives:

$$\mathrm{RNL_c} = 20 \log_{10}(\mathrm{TVI}) + a_p \, , \tag{7.40}$$

the fitting term $20 \log_{10}(C_1)$ is renamed a_p. The last equation can be rewritten in different ways as done for f_c; for instance replacing TVI with Equation 7.39

$$\mathrm{RNL_c} = c_p + 20 \log_{10} \left[\left(\frac{\tau K_T}{Z \sqrt{\sigma_n}} \right)^k \sqrt{Z} \right], \tag{7.41}$$

where $k = 2$ as prescribed by Raestad, but Bosschers (2018a) suggested to treat it as a fitting factor to better adapt to data.

From Equation 7.39 the vortex noise level can be predicted by means of general working parameters of the propeller. Moreover, this relation can be rewritten in terms of the cavity radius enabling to include in the Raestad formula more advanced vortex models. Replacing the tip circulation by Equation 7.31:

$$\mathrm{RNL_c} = b_p + 20 \log_{10} \left[\left(\frac{\Gamma_{tip}}{2\pi \sqrt{\sigma_n} n D^2} \right)^k \sqrt{Z} \right]. \tag{7.42}$$

In the end, the cavity radius can be substituted to K_T by means of Equations 7.31 and 7.28:

$$\mathrm{RNL_c} = a_p + 20 \log_{10} \left[\left(\frac{r_c}{D} \right)^k \sqrt{Z} \right]. \tag{7.43}$$

Consequently, also the relation for the vortex noise level (as already given for the resonance frequency) can be expressed by means of different inputs according to the data availability and following increasing simplifications.

In Chapter 8 the Equation 7.41 will be used to predict the vortex noise level on the current dataset. Hence, Equation 7.43 will be used together with the Proctor's model to compute the vortex cavity radius later in Chapter 9.

7.6 Estimation formula for the sheet cavity noise

The prediction of the noise levels in the higher frequencies range (typically in the range 10-80 kHz), that are mostly dominated by the sheet and bubbles cavitation and less by the vortices, has been accounted with an empirical formula.

On the basis of studies on noise generated by propellers operating in free running and as side thruster, for naval vessels, Brown (1976) defined an upper bound for the acoustic intensity I when cavitation is fully developed, as shown in Equation (7.44):

$$I \leq ZDV_{tip}^3\sqrt{H}\,, \tag{7.44}$$

where V_{tip} is the tip speed and H is the absolute head above vapour pressure. From literature review and measurements, the cavitating noise spectral shape slope at mid frequencies appears to be typically between f^-1 and f^-2 (which is -3/-6 dB/octave), the second value is recommended when vortex cavitation is present. For frequencies above 10 kHz the spectrum shape appears to flatten from f^-2 to f^-1.

Starting from these considerations, Brown defined for a cavitating propeller, the spectrum of radiated noise level as:

$$L = K + \alpha\left[10\,log_{10}(ZD^4n^3f^{-1}) + 10\,log_{10}\Big(\frac{A_C}{A_D}\Big)\right], \tag{7.45}$$

with A_D the propeller disc area and A_C the swept area of cavitation. The pressure term has been removed because not relevant. The ratio A_C/A_D, lower than one in most cases, takes into account the noise variation at different levels of cavitation development. Hence, this term account for the reduced noise due to not fully developed cavitation. K and α are proportionality factors found by fitting to experimental data.

Bubble cavitation and the intermittent cavitation driven by the hull wake are very noisy phenomena but they are not explicitly included in the formulation; indeed, the contribution of unsteady cavitation is considered with equal weight in comparison with steady cavitation. This is of course not in line with real noise generation of a propeller experiencing bubble cavitation, however this is not very important since interest in posed on sheet and vortex cavitation, being bubble cavitation normally avoided as a design constraint.

The cavitation area may be determined directly by experiments (e.g. by photographs or high speed videos (HSV)) or computed by means of different numerical methods. In present work, the second solution has been chosen as reported in Subsection 6.6.1.

7.7 Semi-empirical procedure for the prediction of the cavitating vortex peak

The complete flow-chart for the prediction of the cavitating vortex noise is outlined in Figure 7.7, on the basis of what described in this chapter. Generally, the required input variables are the vortex strength, the propeller geometry, and the viscous core size. The vortex strength, for every propeller working point, can be taken proportional to the tip blade circulation calculated by BEM (or CFD), while the viscous radius can be obtained by data retrieved from literature (properly scaled to meet the Reynolds number, with McCormick's rule (McCormick, 1962)) or experimentally.

The azimuthal velocity can be calculated with the chosen vortex model. The pressure distribution is computed from the azimuthal velocity, and imposing the inception condition $p(r_c) = p_v$, the cavity radius is found for every propeller working point.

Two main sets of fitting parameters are visible in the schema: one for the vortex model and the other for the noise model(s), together with the recursive procedure adopted to tune them. Therefore, this process requires some iteration in order to tune all the necessary coefficients on the basis of the available experimental data (see Pennings, Westerweel, and van Terwisga (2015) and Bosschers (2018b) for an example). If the mismatch with the collected data is too large, it is possible to adjust also the viscous radius or the vortex strength by means of a multiplicative factor.

The aforementioned parameters can be found with an exhaustive search or with more sophisticated methods, depending upon search domain, number or fitting variables, computational capacity etc.

The vortex noise peak can be estimated with the formula analysed in Sections 7.4 and 7.5, and another set of parameters must be tuned. For the case of the vortex resonance frequency, the two parameters are found by a simple linear least square fitting on experimental data. The vortex peak noise level problem is non-linear and its minimum has to be found with an algorithm to optimize nonlinear functions, such as the ones presented in MATLAB library.

In particular, in the present thesis two approaches will be exploited:

- Approach 1 - Section 8.2: the vortex peak will be predicted by means of formulations exploiting general descriptors of the propeller and of the functioning point (Equations 7.33 and 7.41), hence no vortex model is needed. The noise models unknown parameters are found by fitting on experimental data (linear least squares for f_c and optimisation of nonlinear function for $\mathrm{RNL_c}$);

- Approach 2 - Section 9.2: the vortex peak will be predicted by means of formulations exploiting the cavity radius computed by the vortex model. Hence, Equations 7.27 and 7.43 will be used. In this case, neither experimental data on azimuthal velocity nor on cavity radius is known for the current propellers, hence all the tuning will be done directly on the vortex frequency. Eventually, the high frequency part of the spectrum will be predicted with the Brown method.

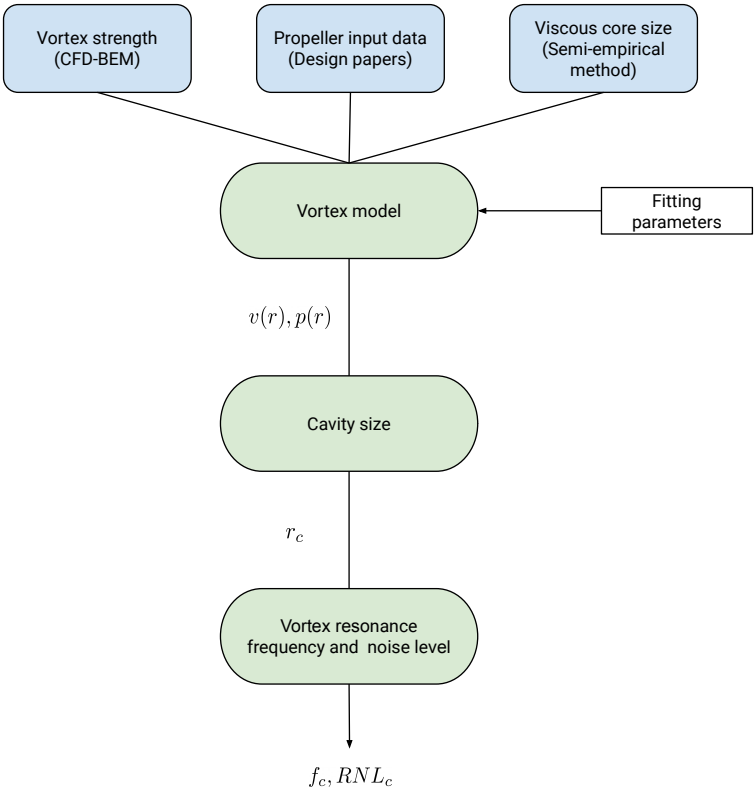

Figure 7.7: Schema of the general algorithm for the prediction of the vortex noise by means of semi-empirical models.

7.8 Summary

The resonance of cavitating vortices is in many cases responsible for the large hump in the spectrum of a cavitating propeller. The resonance frequency mainly depends on the vortex cavity radius; this size can be experimentally measured by dedicated SPIV test or, alternatively, it can be estimated assuming that in the vortical flow region where the pressure is lower than the vapour pressure, water changes into vapour. The total pressure can be computed with a reasonable accuracy by integration of the azimuthal velocity alone.

Conversely, the velocity field around a vortical flow can be solved with sophisticated numerical models or with semi-empirical 2-D vortex model coupled with BEM (Section 7.3). These models can be of two type: non-cavitating or cavitating, depending on whether the vapour-water interface effect on the azimuthal velocity is considered. Usually, these models require a certain number of fitting factors to better shape the data.

The cavity radius can be exploited in the vortex noise peak prediction with the formulas analysed in Sections 7.4 and 7.5; alternatively, with some assumptions, the same formulas can be rewritten as a function of general descriptors of the propeller functioning. Eventually, the contribution in the high frequency part of the spectrum will be predicted with the Brown method.

In Section 7.7 the procedure to couple the BEM calculations with the general semi-empirical models has been outlined; this will be further discussed in Section 9.2.

Chapter 8

Modelisation - Approach 1

The chapter presents the first modelling approach. The dataset employed is composed only by propellers P1 and P2 behind a typical twin-screw vessel wake. The noise target to be predicted is a simplification of the narrowband spectrum and the features are general descriptors of the working point, propeller geometry, cavitation pattern and wake.

8.1 Introduction

In this proposed context, a general modelisation framework can be defined, characterised by an input space $\mathcal{X} \subseteq \mathbb{R}^d$, an output space $\mathcal{Y} \subseteq \mathbb{R}$, and an unknown relation $\mu : \mathcal{X} \to \mathcal{Y}$ to be learned. For this first approach, $\mathcal{X}$ is composed by the features reported in Table 8.2, while the output space $\mathcal{Y}$ refers to the cavitation noise spectrum frequencies and levels reported in Table 8.1. Therefore the physical problem is simplified from the point of view of the targets and of the features to better fit more basic learning models (Section 1.3).

The propeller set-ups taken into account include similar wake inflow (Table 8.3) in various pitch configurations for a total of 164 samples. In the first phase of the work, transfer function corrections for the confined environment effect have not been applied, hence the developed models will describe the characteristics of noise spectra measured inside the UNIGE cavitation tunnel. This is due to the main interest of this activity, which is to check the validity of the proposed approach, rather than the prediction to full scale or the comparison with other facilities. It has to be remarked, anyway, that the experimental data considered in this phase (belonging

Table 8.1: Dataset output variables.

Output Variable	Unit	Description	Dimension
f_{bp1}	[Hz]	Frequency at first breakpoint	1
RNL_{bp1}	[dB]	Noise level at f_{bp1}	1
f_{c}	[Hz]	Central frequency	1
RNL_{c}	[dB]	noise level at central frequency	1
f_{bp2}	[Hz]	Frequency at second breakpoint	1
RNL_{bp2}	[dB]	Noise level at f_{bp2}	1
RNL_{b}	[dB]	Noise level at ending frequency (100 kHz)	1

Table 8.2: Dataset input variables.

Propeller working parameters			Cavitation types		
Variable	Unit	Description	Variable	Unit	Description
$^P/_D$	[]	Pitch ratio			
$\Delta\Phi$	[°]	Difference between actual and design pitch	TVC 90°	[]	Suction side tip vortex
J	[]	Advance coefficient	D. TVC	[]	Detached tip vortex
K_T	[]	Thrust coefficient	TVC 0°	[]	Suction side tip vortex at 0°
$10K_Q$	[]	Torque coefficient	S.S. S	[]	Suction side sheet
η_o	[]	Open water efficiency	S.S. S 0°	[]	Suction side sheet at 0°
σ_v	[]	Cavitation index based on advance velocity	S.S. RB	[]	Suction side root bubbles
σ_n	[]	Cavitation index based on rotational speed	S.S. B	[]	Suction side bubbles
σ_{ntip}	[]	Cavitation index based on rotational speed at blade tip	VFSF	[]	Vortex from sheet face
V_a	[m/s]	Advance velocity	P.S. TVC	[]	Pressure side tip vortex
n	[Hz]	Rate of propeller rotation	P.S. S	[]	Pressure side sheet
T_c	[kgf]	Thrust	P.S. RB	[]	Pressure side root bubbles
Q_c	[kgf·cm]	Torque			
$\mathrm{p_{rel}}$	[mBar]	Pressure relative to the ambient pressure			

Wake parameters			Angle of attack geometric		
Variable	Unit	Description	Variable	Unit	Description
			$\overline{\alpha}_{G07}$	[°]	Circumferential average α_G at $0.7R$
$w\,\mathrm{wd}_{07}$	[°]	Wake width at $0.7R$	min α_{G07}	[°]	Minimum α_G at $0.7R$
$\mathrm{D}_\theta w\vert_{07}^-$	[°]	Left wake gradient at $0.7R$	max α_{G07}	[°]	Maximum α_G at $0.7R$
$\mathrm{D}_\theta w\vert_{07}^+$	[°]	Right wake gradient at $0.7R$	$\theta\vert_{max\ \alpha_{G07}}$	[°]	Angular position of maximum α_G at $0.7R$
$w\,\mathrm{wd}_{09}$	[°]	Wake width at $0.9R$	$\overline{\alpha}_{G09}$	[°]	Circumferential average α_G at $0.9R$
$\mathrm{D}_\theta w\vert_{09}^-$	[°]	Left wake gradient at $0.9R$	min α_{G09}	[°]	Minimum α_G at $0.9R$
$\mathrm{D}_\theta w\vert_{09}^+$	[°]	Right wake gradient at $0.9R$	max α_{G09}	[°]	Maximum α_G at $0.9R$
			$\theta\vert_{max\ \alpha_{G09}}$	[°]	Angular position of maximum α_G at $0.9R$

Table 8.3: Propeller and wake configurations for modelisation Approach 1.

Pitch	Propeller	
	P1	P2
Design	W1	W3
Reduced (-3°)	W1	W3
Reduced (-5°)		W3
Reduced (-6°)	W1	
Incremented (+2°)		W3

only to P1 and P2) have been collected keeping the hydrophones and test section configuration unvaried for the whole campaign. Due to this, the transfer function correction is the same for all the experiments.

The model $h : \mathcal{X} \to \mathcal{Y}$ is an artificial simplification of μ: h can be obtained with different kinds of techniques, for example requiring some physical knowledge of the problem, as in PMs, or the acquisition of large amount of data, as in DDMs, or both of them, as in HMs. Independently of the adopted technique, any model h requires some data in order to be tuned (or learned) on the problem specificity and to be validated (or tested) on a real-world scenario. For these purposes, two separate sets of data $\mathcal{D}_n = \{(\boldsymbol{x}_1, y_1), \cdots, (\boldsymbol{x}_n, y_n)\}$ and $\mathcal{T}_m = \{(\boldsymbol{x}_1^t, y_1^t), \cdots, (\boldsymbol{x}_m^t, y_m^t)\}$ need to be exploited, to respectively tune h and evaluate its performances. It is important to note that $\mathcal{T}_m$ is needed since the error that h would commit over $\mathcal{D}_n$ would be too optimistically biased since $\mathcal{D}_n$ has been used to tune h.

Hence, the error that h commits on $\mathcal{T}_m$ in approximating the real process is usually measured with reference to different indexes of performance (Ghelardoni, Ghio, and Anguita, 2013):

- the Mean Absolute Error (MAE) is computed by taking the absolute loss value of h over $\mathcal{T}_m$

$$\text{MAE}(h) = \frac{1}{m} \sum_{i=1}^{m} |h(\boldsymbol{x}_i^t) - y_i^t|; \tag{8.1}$$

- the Mean Absolute Percentage Error (MAPE) is computed by taking the absolute loss value of h over $\mathcal{T}_m$ in percentage

$$\text{MAPE}(h) = \frac{100}{m} \sum_{i=1}^{m} \left| \frac{h(\boldsymbol{x}_i^t) - y_i^t}{y_i^t} \right|; \tag{8.2}$$

- the Pearson Product-Moment Correlation Coefficient (PPMCC) measures the linear dependency between $h(\boldsymbol{x}_i^t)$ and y_i^t with $i \in \{1, \cdots, m\}$

$$\text{PPMCC} = \frac{\sum_{i=1}^{m} (y_i^t - \overline{y})(h(\boldsymbol{x}_i^t) - \hat{\overline{y}})}{\sqrt{\sum_{i=1}^{m} (y_i^t - \overline{y})^2} \sqrt{\sum_{i=1}^{m} (h(\boldsymbol{x}_i^t) - \hat{\overline{y}})^2}}, \tag{8.3}$$

  where $\overline{y} = {}^1\!/_m \sum_{i=1}^{m} y_i^t$ and $\hat{\overline{y}} = {}^1\!/_m \sum_{i=1}^{m} h(\boldsymbol{x}_i^t)$.

Other state-of-the-art measures of error exist (such as R-squared and or the Mean Square Error) but in this work these three are kept because, from a physical point of view, they give a complete description of the quality of the model and moreover adding more measures would make the results less readable.

The chapter is organised as follows: in Section 8.2 the PMs adopted and their parameter tuning is shown, in Section 8.3 the training and the strategies exploited to build the DDMs are explained, the hybrid modelling approach is discussed in Section 8.4 and lastly the results of the proposed methods are presented in Section 8.5.

8.2 Physical models

In the present thesis, some physics-based models for f_c and RNL_c are derived with a twofold objective: provide a benchmark for comparison with DDMs and provide features for the HMs. The tuning of parameters for the physical models is done by

fitting on the whole data set, hence no distinction between $\mathcal{D}_n$ and $\mathcal{T}_m$ has been done. The frequency and the maximum level of the peak in the spectrum of tip vortex noise have been computed following the discussions of Section 7.4, the formula are here reported for convenience.

$$f_c = \frac{0.45\sigma_{\text{tip}} n Z}{\tau K_T} \,. \qquad \text{(7.35 revisited)}$$

According to the approach used (Maines and Arndt, 1997), the vortex strength is assumed to be proportional to the thrust coefficient by means of the coefficient τ which represents the relative tip loading, and it is here assumed to be dependent only on propeller geometry and wake field. The hump level has been evaluated with the formulation presented by Raestad (1996) and Bosschers (2018b), that is derived from the acoustic pressure for a spherical wave:

$$\text{RNL}_c = a_p + 20\log_{10}\left[\left(\frac{\tau K_T}{Z\sqrt{\sigma_n}}\right)^k \sqrt{Z}\right]. \qquad \text{(7.41 revisited)}$$

In line with the work of Raestad (1996), the value of the exponent k should be 2; however, as pointed out also in Bosschers (2018a), the fitting with data is improved considering higher values. For the present work, the parameter k has been chosen equal to 3. The unknown parameter are the coefficients τ and a_p, can be obtained by means of fitting the experimental data. Values obtained are reported in Table 8.4.

Table 8.4: PMs estimated parameters.

	Propeller	$\Delta\Phi$	τ	a_p
	P1	0	0.527	117.4
	P1	-3	0.504	116.2
	P1	-6	0.362	120.6
PM1	P2	0	0.563	120.8
	P2	+2	0.585	117.2
	P2	-3	0.359	125.8
	P2	-5	0.339	118.9
PM2	P1 & P2	-	0.5234	118.5

As expected the coefficient τ, for a given propeller, decreases while reducing the pitch, indicating the overall reduced load. When a new propeller is considered, the values of a_p and τ cannot be estimated from data fitting before experimental results are available. Hence, it is important to define procedures for their estimation before experimental tests are carried out. This problem could be overcome using procedures as proposed in Bosschers (2018a), according to which the vortex strength is directly derived by BEM computations and consequently the knowledge of τ is no more needed; alternatively, the value of these parameters may be correlated with available geometric or hydrodynamic characteristics of the propellers. Obviously, the latter solution requires the availability of a significant number of test cases. In case this is not possible, the average values of the two coefficients obtained from previous experiments may be used as a first rough estimate. In order to check how the accuracy of the PM is affected by this possible rough assumption, the coefficients have been hence calculated also on the total set of tests available, without differentiating among different propellers and pitch settings. In the following, two

PMs are considered. The first one, PM1, makes use of all the values of coefficients a_p and τ derived for each propeller configuration. The second one, PM2, uses only values resulting from the fitting on the complete dataset, without propeller and pitch setting distinction.

8.3 Data driven models

In this work, a method called Kernel Regularized Least Squares has been adopted in order to estimate the relation between f_{bp1}, RNL_{bp1}, f_{c}, RNL_{c}, f_{bp2}, RNL_{bp2}, and RNL_{b} and the variables of Table 8.2.

The KRLS problem is formulated by exploiting kernels as

$$\boldsymbol{\alpha}^* : \quad \min_{\boldsymbol{\alpha}} \quad \|Q\boldsymbol{\alpha} - \boldsymbol{y}\|^2 + \lambda \boldsymbol{\alpha}^T Q \boldsymbol{\alpha}\,, \tag{3.18 revisited}$$

where $\boldsymbol{y} = [y_1, \ldots, y_n]^T$, $\boldsymbol{\alpha} = [\alpha_1, \ldots, \alpha_n]^T$, the matrix Q such that $Q_{i,j} = K(\boldsymbol{x}_j, \boldsymbol{x}_i)$, and the identity matrix $I \in \mathbb{R}^{n \times n}$. By setting equal to zero the gradient with respect to $\boldsymbol{\alpha}$ it is possible to state that

$$(Q + \lambda I)\, \boldsymbol{\alpha}^* = \boldsymbol{y}, \tag{3.19 revisited}$$

that is a linear system for which effective solvers have been developed over the years, allowing coping with even very large sets of training data (Young, 2003).

The problems here faced is how to choose $\boldsymbol{\varphi}$, the kernel K, and how to set up the regularisation hyperparameter λ.

It is possible to start by setting $\boldsymbol{\varphi}$ and the kernel K. Generally, the input features of $\mathcal{D}_n$ are subject to a process of transformation. This process is usually referred as FM since the input features are mapped from an initial input space X to a new input space Ψ. In this way, the FM procedure allows to find a new suitable representation $\boldsymbol{\varphi}(\boldsymbol{x}) \in \Psi$ of the data $\boldsymbol{x} \in \mathcal{X}$ by defining a function $\boldsymbol{\varphi} : \mathcal{X} \to \Psi$ mapping $\boldsymbol{x}$ to a new feature space where it is possible to then learn a simple linear model like the one defined by the KRLS. FM is usually adopted since the new feature space Ψ could enhance the performance capability of the predictor, depending on the values of $\boldsymbol{x}$ and y. In this work, the adopted FM was selected considering the acquired expertise and knowledge of the cavitation noise phenomenon, by applying the following FM

$$\boldsymbol{\varphi}(\boldsymbol{x}) = \left[\prod_{i=1}^{5d} v_i^{k_i} : \sum_{i=1}^{5d} k_i = j, j \in \{0, 1, \cdots, p\} \right]^T \in \mathbb{R}^{\sum_{j=0}^{p} \binom{5d}{j}} \tag{8.4}$$

$$\boldsymbol{v} = \left[x_1, \cdots, x_d, {}^1\!/_{x_1}, \cdots, {}^1\!/_{x_d}, \ln(x_1), \cdots, \ln(x_d), e^{x_1}, \cdots, e^{x_d}, e^{-x_1}, \cdots, e^{-x_d}\right]^T \in \mathbb{R}^{5d}.$$

In fact, based on this FM, it is possible to represents, with a simple linear combination, all the possible functions, with an opportune value of p, and where each feature is a physically plausible term of the function.

The problem of the FM of Equation (8.4) is that its computation is computationally unfeasible if d or p are large since the problem is NP-hard. Nevertheless, remembering that, in KRLS, it is possible to exploit the kernel trick and noting that the proposed FM can be expressed with a simple polynomial kernel

$$\boldsymbol{\varphi}(\boldsymbol{a})^T \boldsymbol{\varphi}(\boldsymbol{b}) = (\boldsymbol{v_a}^T \boldsymbol{v_b} + c)^p = K(\boldsymbol{a}, \boldsymbol{b}) \tag{8.5}$$

$$\boldsymbol{v_a} = \left[a_1, \cdots, a_d, {}^1\!/_{a_1}, \cdots, {}^1\!/_{a_d}, \ln(a_1), \cdots, \ln(a_d), e^{a_1}, \cdots, e^{a_d}, e^{-a_1}, \cdots, e^{-a_d}\right]$$

$$\boldsymbol{v_b} = \left[b_1, \cdots, b_d, {}^1\!/_{b_1}, \cdots, {}^1\!/_{b_d}, \ln(b_1), \cdots, \ln(b_d), e^{b_1}, \cdots, e^{b_d}, e^{-b_1}, \cdots, e^{-b_d}\right].$$

it is possible to avoid the NP-hard problem and use the desired FM. Note that $p \in \{0, 1, \cdots\}$ is the desired degree of the polynomial and $c \in [0, \infty)$ is a parameter trading off the influence of higher-order versus lower-order terms in the polynomial. p and c together with λ are hyperparameters that need to be tuned in order to optimize the performance of the final model.

Unfortunately, during the FM, many unnecessary features have been generated, which are either redundant or not informative. As a result, a feature selection phase is required in order to increase the generalisation performance of the model by selecting only the most informative features which best represent the problem to be solved and discarding the others (Guyon and Elisseeff, 2003). For this purpose here is adopted the backward elimination techniques described in (Guyon and Elisseeff, 2003).

The last problem that it is possible to solve is how to tune the hyperparameters p, c, and λ of the proposed method.

Since every ML model is characterised by a set of hyperparameters $\mathcal{H}$ influencing their ability to estimate μ, a proper model selection procedure needs to be adopted (Oneto, 2018).

In this has been exploited the BTS procedure and consequently $n_r = 500$, $l = n$ and the resampling must be done with replacement (Oneto, 2018).

8.4 Hybrid models

For the last modelisation type, the goal is to construct a model able to both take into account the physical knowledge about the problem encapsulated in the PMs of Section 8.2 and the information hidden in the available data as the DDMs of Section 3.3. An HM, based on the previous observation, should be able to learn from the data without being too different, or far away, from the PMs.

From the Data Science point of view, this requirement can be straightforwardly mapped in a typical ML Multi Task Learning (MTL) problem (Baxter, 2000; Caruana, 1997; Evgeniou and Pontil, 2004; Bakker and Heskes, 2003; Argyriou, Evgeniou, and Pontil, 2008; Caruana, 1997). MTL aims at contemporary learning two concepts, in this case the PM and the available data, through a learning algorithm $\mathscr{A}_{\mathcal{H}}$ which exploits the data in $\mathcal{D}_n$ to learn a function h which is both close to the observation, the data $\mathcal{D}_n$ and the PM, namely its forecasts.

Since for building a HM also a PM is needed, it will be developed a model to estimate the relation between f_{c} and $\mathrm{RNL_c}$ and the variables of Table 8.2, since the PM is only available for f_{c} and $\mathrm{RNL_c}$. Consequently, in this case a slightly different scenario is presented where the dataset is composed by a triple of points $\mathcal{D}_n = \{(\boldsymbol{x}_1, y_1, p_1), \cdots, (\boldsymbol{x}_n, y_n, p_n)\}$ where p_i is the output of the PM in the point $\boldsymbol{x}_n$ with $i \in \{1, \cdots, n\}$. The target is to learn a function able to approximate both μ, namely the relation between the input $\boldsymbol{x} \in \mathcal{X}$ and the output $y \in \mathcal{Y}$, and the PM, namely the relation between the input and the output of the PM. Basically two tasks have to be learned. For this purpose there are two main approaches: the first approach is called Shared Task Learning (STL) and the second Independent Task Learning (ITL). While the latter independently learns a different model for each task, the former aims to learn a model that is common between all tasks. A well-known weakness of these methods is that they tend to generalize poorly on one of the two tasks (Baxter, 2000). In this study, it is shown that an appealing

approach to overcome such limitations is provided by MTL (Baxter, 2000; Caruana, 1997; Evgeniou and Pontil, 2004; Bakker and Heskes, 2003; Argyriou, Evgeniou, and Pontil, 2008). This methodology leverages on the information between the tasks to learn more accurate models.

In order to apply the MTL approach to this case, it is possible to basically just modify the KRLS problem of Equation (3.13) in order to contemporary learn a shared model and a task specific model which should be close to the shared model. In this way is obtained a model which is able to contemporary learn the two tasks. A shared model is defined as

$$h(\boldsymbol{x}) = \boldsymbol{w}^T \boldsymbol{\varphi}(\boldsymbol{x}) \,, \tag{8.6}$$

and two task specific models as

$$h_i(\boldsymbol{x}) = \boldsymbol{w}_i^T \boldsymbol{\varphi}(\boldsymbol{x}), \quad i \in \{y, p\} \,. \tag{8.7}$$

Then it is possible to state the MTL version of Equation (3.13)

$$\begin{aligned} \boldsymbol{w}^*, \boldsymbol{w}_y^*, \boldsymbol{w}_p^* : \min_{\boldsymbol{w}, \boldsymbol{w}_y, \boldsymbol{w}_p} \quad & \sum_{i=1}^{n} \left[\boldsymbol{w}^T \boldsymbol{\varphi}(\boldsymbol{x}) - y_i\right]^2 + \left[\boldsymbol{w}^T \boldsymbol{\varphi}(\boldsymbol{x}) - p_i\right]^2 \\ & + \sum_{i=1}^{n} \left[\boldsymbol{w}_y^T \boldsymbol{\varphi}(\boldsymbol{x}) - y_i\right]^2 + \left[\boldsymbol{w}_p^T \boldsymbol{\varphi}(\boldsymbol{x}) - p_i\right]^2 \\ & + \lambda \|\boldsymbol{w}\|^2 + \theta(\|\boldsymbol{w} - \boldsymbol{w}_y\|^2 + \|\boldsymbol{w} - \boldsymbol{w}_p\|^2) \,, \end{aligned} \tag{8.8}$$

where λ is the usual regularisation of KRLS and $\theta \in [0, \infty)$, instead, is another hyperparameter that forces the shared model to be close to the task specific models. Basically the MTL problem of Equation (8.8) is a concatenation of three learning problems solved with KRLS plus a term which tries to keep related all the three different problems.

By exploiting the kernel trick as in KRLS it is possible to reformulate Problem (8.8) as follows

$$\begin{aligned} \boldsymbol{\alpha}^* : \quad \min_{\boldsymbol{\alpha}} \quad & \left\| \begin{bmatrix} Q & Q & 0 & 0 \\ Q & Q & 0 & 0 \\ 0 & 0 & Q & 0 \\ 0 & 0 & 0 & Q \end{bmatrix} \boldsymbol{\alpha} - \begin{bmatrix} \boldsymbol{y} \\ \boldsymbol{p} \\ \boldsymbol{y} \\ \boldsymbol{p} \end{bmatrix} \right\|^2 \\ & + \boldsymbol{\alpha}^T \begin{bmatrix} (\lambda + 2\theta)Q & (\lambda + 2\theta)Q & -\theta Q & -\theta Q \\ (\lambda + 2\theta)Q & (\lambda + 2\theta)Q & -\theta Q & -\theta Q \\ -\theta Q & -\theta Q & \theta Q & 0 \\ -\theta Q & -\theta Q & 0 & \theta Q \end{bmatrix} \boldsymbol{\alpha}, \end{aligned} \tag{8.9}$$

where $\boldsymbol{p} = [p_1, \ldots, p_n]^T$. The solution of this problem is again equivalent to solving a simple linear system

$$\begin{bmatrix} Q + (\lambda + 2\theta)I & Q + (\lambda + 2\theta)I & -\theta I & -\theta I \\ Q + (\lambda + 2\theta)I & Q + (\lambda + 2\theta)I & -\theta I & -\theta I \\ -\theta I & -\theta I & Q + \theta I & 0 \\ -\theta I & -\theta I & 0 & Q + \theta I \end{bmatrix} \boldsymbol{\alpha}^* = \begin{bmatrix} \boldsymbol{y} \\ \boldsymbol{p} \\ \boldsymbol{y} \\ \boldsymbol{p} \end{bmatrix} . \tag{8.10}$$

The function of interest is the shared one that can be expressed as follows

$$h(\boldsymbol{x}) = \boldsymbol{w}^T \boldsymbol{\varphi}(\boldsymbol{x}) = \sum_{i=1}^{n} (\alpha_i + \alpha_{i+n}) K(\boldsymbol{x}_i, \boldsymbol{x}) \,. \tag{8.11}$$

By exploiting the same FM and Feature Selection of the DDMs the HMs are obtained. What changes is the MS phase where λ, c, and p have been tuned as for the DDMs, but also θ.

8.5 Results and discussions

In this section, the performances of the PMs, DDMs, and HMs, (Sections 8.2, 3.3, and 8.4) will be tested and compared in two different scenarios:

- interpolation scenario: in this case models try to predict the propeller noise spectra main characteristics in different working conditions within the ones exploited for building the model; these tests are useful to check the capability of the model to provide predictions starting from the knowledge of the characteristics and the cavitating behaviour of the propeller;
- extrapolation scenario: in this case models try to predict the propeller noise spectra main characteristics in groups of working conditions where the cavitation intensity is very different with respect to the one exploited for building the model; these tests are useful to check the capability of the models to predict the noise related to cavitation patterns which cannot be reproduced at model scale.

The idea to consider the two scenarios is based on the viscous effects on tip vortex cavitation inception as discussed in Subsection 2.3.1. Basically the two scenarios just differ in the way $\mathcal{D}_n$ and $\mathcal{T}_m$ have been built. In other words, the two scenarios differ in the subset of data exploited for building and testing the models.

For what concerns the PMs, the PM1 and PM2 described in Section 8.2 will be considered. As described, PM1 and PM2 are just able to predict f_{c} and $\mathrm{RNL_c}$ based on a subset of the input variables described in Table 8.2.

DDMs are able to predict f_{bp1}, $\mathrm{RNL_{bp1}}$, f_{c}, $\mathrm{RNL_c}$, f_{bp2}, $\mathrm{RNL_{bp2}}$, and $\mathrm{RNL_b}$ based on all the input variables reported in Table 8.2. The set of hyperparameters tuned during the MS phase are $\mathcal{H} = \{p, c, \lambda\}$ chosen in $\mathfrak{H} = \{1, 2, \cdots, 10\} \times \{10^{-4}, 10^{-3}, \cdots, 10^{+4}\} \times \{10^{-4.0}, 10^{-3.8}, \cdots, 10^{+4.0}\}$.

For the HMs the custom algorithm described in Section 8.4 will be exploited. HMs are able to predict only f_{c} and $\mathrm{RNL_c}$ based on all the input variables reported in Table 8.2 and the PMs of Section 8.2. Since two PMs are available, two HMs, HM1 and HM2, will be considered, exploiting the PM1 and the PM2, respectively. The set of hyperparameters tuned during the MS phase are $\mathcal{H} = \{p, c, \lambda, \theta\}$ chosen in $\mathfrak{H} = \{1, 2, \cdots, 10\} \times \{10^{-4}, 10^{-3}, \cdots, 10^{+4}\} \times \{10^{-4.0}, 10^{-3.8}, \cdots, 10^{+4.0}\} \times \{10^{-4.0}, 10^{-3.8}, \cdots, 10^{+4.0}\}$.

All the tests have been repeated 30 times and the average results are reported, together with their t-student 95% confidence interval, in order to ensure the statistical consistency of the results.

8.5.1 Interpolation Scenario

In this scenario $\mathcal{D}_n$ and $\mathcal{T}_m$ have been created by splitting randomly the whole 164 samples keeping 90% of the data in $\mathcal{D}_n$ and the remaining 10% in $\mathcal{T}_m$. In this way the models have been tested in their ability to predict the propeller noise spectra main characteristics in various, but different, working conditions within the ones exploited for building the model.

In Table 8.5 the performance of PMs, DDMs, and HMs in predicting the noise spectra main characteristics are reported. The performance are measured with the MAE, the MAPE, and the PPMCC. The table reports the full set of results for completeness. The best performing models are underlined in bold. From the table it is clear how the HMs are in the most cases the best performing ones followed by the DDMs. The PMs are usually the worse performing models. Unfortunately, the full table is not easy to interpret nor very informative and for this reason, in the next sections, a series of scatter plots is used to give a better interpretation of the results.

8.5.1.1 Physical Models Results

Figure 8.1 reports the scatter plots of the measured and predicted values of f_c and $\mathrm{RNL_c}$ for both PM1 and PM2.

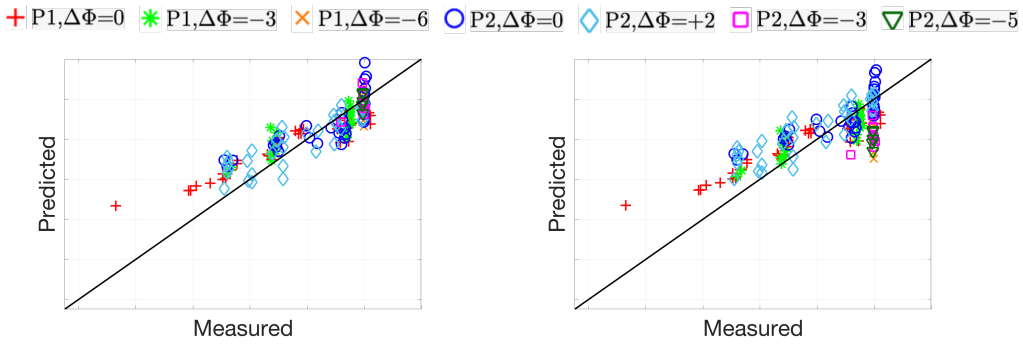

(a) f_c, PM1 [$0.2\log_{10}$(Hz)/div] **(b)** f_c, PM2 [$0.2\log_{10}$(Hz)/div]

(c) $\mathrm{RNL_c}$, PM1 [10dB/div] **(d)** $\mathrm{RNL_c}$, PM2 [10dB/div]

Figure 8.1: Interpolation Scenario PMs: scatter plots of the measured and predicted values of f_c and $\mathrm{RNL_c}$ for both PM1 and PM2.

From Figure 8.1 it is possible to observe that:

- there is a significant variance of the results depending on the different tests;
- especially for f_c, data points tend to distribute with an angle between the measured and predicted values which is slightly different from 45°, clearly

Prop. Model	$\Delta\Phi$	f_{bp1} DDMs	RNL_{bp1} DDMs	f_c PM1	f_c PM2	f_c DDMs	f_c HM1	f_c HM2	RNL_c PM1	RNL_c PM2	RNL_c DDMs	RNL_c HM1	RNL_c HM2	f_{bp2} DDMs	RNL_{bp2} DDMs	RNL_b DDMs
MAE																
P1	0	75±4	1.6±0.1	172±8	173±9	130±5	**78±4**	81±4	4.0±0.2	3.9±0.2	2.2±0.1	1.3±0.1	**1.2±0.1**	4168±212	4.3±0.2	1.2±0.1
P1	-3	64±3	1.8±0.1	168±9	169±7	143±7	88±5	**83±4**	3.2±0.2	4.0±0.2	2.6±0.1	**1.3±0.1**	1.5±0.1	10737±573	10.2±0.5	2.8±0.1
P1	-6	153±8	0.9±0.0	216±11	514±28	203±10	**122±5**	127±5	1.1±0.1	7.5±0.3	1.0±0.1	**0.7±0.0**	0.9±0.0	138±7	1.0±0.0	2.6±0.1
P2	0	90±5	1.6±0.1	207±11	205±10	92±4	**48±3**	53±2	3.1±0.2	5.1±0.3	1.2±0.1	0.8±0.0	**0.8±0.0**	174±7	1.0±0.1	1.6±0.1
P2	2	86±4	2.3±0.1	148±7	182±9	101±6	**55±3**	64±4	3.9±0.2	4.0±0.2	1.7±0.1	**0.8±0.0**	0.9±0.0	1375±71	2.1±0.1	1.7±0.1
P2	-3	97±3	1.8±0.1	145±7	499±26	97±5	**76±4**	81±5	4.3±0.2	4.5±0.2	3.2±0.1	**2.0±0.1**	2.6±0.1	117±6	3.5±0.2	4.5±0.2
P2	-5	85±4	0.7±0.0	116±6	560±27	70±4	**57±3**	62±3	**1.2±0.1**	10.9±0.7	2.9±0.1	2.2±0.1	1.9±0.1	89±5	4.1±0.2	5.9±0.3
P1	all	80±5	1.6±0.1	175±8	205±10	141±7	**85±5**	86±5	3.5±0.2	4.3±0.2	2.2±0.1	1.3±0.1	**1.3±0.1**	5610±269	5.7±0.2	1.7±0.1
P2	all	89±5	1.9±0.1	173±10	243±12	95±4	**54±3**	60±3	3.4±0.2	4.9±0.3	1.7±0.1	**1.0±0.1**	1.1±0.1	650±30	1.8±0.1	2.1±0.1
all	all	85±4	1.7±0.1	174±10	227±11	114±6	**68±3**	71±4	3.5±0.2	4.6±0.2	1.9±0.1	1.1±0.1	**1.1±0.1**	2780±144	3.5±0.2	2.0±0.1
MAPE																
P1	0	26.8±1.2	40.7±1.9	22.6±1.2	22.9±1.0	13.8±0.6	**8.2±0.4**	8.7±0.5	29.7±1.3	31.5±1.3	13.7±0.7	7.4±0.4	**6.7±0.3**	29.1±1.5	61.2±3.1	6.2±0.3
P1	-3	10.0±0.5	392.9±15.7	17.7±1.0	16.7±0.7	13.6±0.7	8.2±0.4	**7.9±0.4**	32.1±1.5	46.2±2.2	20.8±1.1	**11.2±0.7**	11.9±0.5	55.3±2.5	328.4±16.3	14.1±0.8
P1	-6	21.1±1.2	40.2±1.8	13.7±0.7	32.7±1.7	12.9±0.6	**7.7±0.3**	8.0±0.5	11.7±0.6	76.7±3.8	10.4±0.5	**7.6±0.4**	10.0±0.5	7.6±0.3	468.7±25.6	9.1±0.4
P2	0	34.6±1.9	41.9±2.2	17.3±0.7	18.1±1.1	8.5±0.4	**4.5±0.2**	4.8±0.2	28.2±1.3	39.2±2.0	8.0±0.3	5.8±0.3	**5.5±0.3**	7.7±0.4	24.9±1.4	8.5±0.5
P2	2	30.6±1.4	118.3±5.9	17.4±0.7	23.3±1.3	10.3±0.6	**6.0±0.4**	6.5±0.3	23.0±1.1	22.6±0.8	9.4±0.5	**5.0±0.3**	5.4±0.3	21.8±1.0	53.0±3.0	10.7±0.5
P2	-3	14.4±0.6	155.4±7.3	9.3±0.5	32.3±1.8	6.3±0.3	**4.9±0.2**	5.2±0.2	51.3±3.1	63.1±3.2	33.5±1.5	**20.9±1.1**	24.0±1.3	5.7±0.2	382.8±19.2	27.9±1.3
P2	-5	11.8±0.6	18.8±1.2	7.4±0.4	35.7±1.9	4.5±0.2	**3.7±0.2**	4.0±0.2	**60.8±2.5**	594.3±29.2	169.0±6.9	124.8±6.5	110.0±6.0	4.9±0.2	861.2±41.5	19.1±1.0
P1	all	21.7±1.2	141.3±6.4	20.3±1.0	22.1±1.1	13.6±0.5	**8.1±0.3**	8.4±0.3	28.6±1.4	40.1±2.2	15.4±0.7	8.5±0.4	**8.5±0.4**	34.3±1.9	257.0±27.0	8.5±0.4
P2	all	30.2±1.5	80.8±3.6	16.0±0.8	22.5±1.1	8.8±0.5	**5.1±0.3**	5.5±0.3	30.1±1.3	64.8±3.4	20.2±0.9	**12.4±0.5**	13.1±0.7	13.1±0.6	116.5±6.1	11.6±0.6
PPMCC																
P1	0	.74±.03	.98±.05	.92±.04	.92±.05	.91±.05	.96±.05	**.97±.05**	.88±.04	.88±.04	.93±.05	**.98±.05**	.98±.06	.77±.04	.62±.03	.96±.05
P1	-3	.81±.04	.90±.05	.84±.04	.84±.03	.85±.04	.95±.05	**.95±.05**	.74±.04	.74±.04	.80±.04	**.97±.05**	.96±.05	-.09±.00	-.24±.01	.89±.04
P1	-6	.91±.05	.98±.05	**-.84±.04**	-.84±.05	-.59±.03	-.77±.04	-.70±.03	.90±.04	.90±.05	.84±.04	**.97±.05**	.96±.05	-.55±.03	.87±.05	.91±.05
P2	0	.65±.04	.90±.05	.74±.04	.74±.04	.94±.05	**.98±.04**	.98±.06	.70±.04	.70±.04	.95±.05	.98±.05	**.98±.05**	.78±.04	.90±.04	.95±.04
P2	2	.86±.05	.97±.05	.90±.04	.90±.05	.94±.06	.98±.04	**.98±.04**	.40±.02	.40±.02	.89±.04	.97±.04	**.97±.04**	.19±.01	.61±.03	.94±.04
P2	-3	.71±.03	.89±.05	.49±.02	.49±.02	.56±.02	.51±.03	**.71±.03**	.06±.00	.06±.00	.45±.02	**.89±.05**	.87±.04	.63±.04	.33±.02	.84±.05
P2	-5	.99±.04	.96±.05	.27±.01	.27±.01	.27±.01	**.55±.05**	.45±.02	.89±.05	**.89±.05**	.38±.02	.65±.03	.63±.03	.05±.00	.33±.02	.63±.03
P1	all	.78±.03	.97±.05	.88±.05	.82±.04	.90±.05	.96±.05	**.96±.05**	.85±.05	.83±.03	.92±.04	.98±.05	**.98±.05**	.48±.02	.39±.02	.94±.05
P2	all	.83±.04	.96±.05	.84±.05	.66±.04	.95±.05	**.99±.05**	.98±.05	.70±.03	.46±.02	.92±.04	**.97±.06**	.96±.05	.30±.02	.72±.04	.93±.05
all	all	.81±.04	.96±.04	.86±.03	.72±.03	.93±.05	.97±.05	**.97±.05**	.77±.04	.59±.03	.92±.04	**.98±.05**	.97±.05	.45±.02	.47±.02	.93±.05

Table 8.5: Interpolation Scenario: PMs, DDMs, and HMs, performance measured with the MAE, the MAPE, and the PPMCC. Winning method in bold.

underlining a problem in the PM adopted;
- as expected, the accuracy of the PM1 model is significantly better than the one of the model PM2. However, from a qualitative point of view, results reported in the scatter plots evidence the same problems in both cases.

The PM implemented in this work seems to provide only a rough approximation of the dependency of f_c and RNL_c on the input parameters. In the case of the PM1, the values of the parameter τ have been tuned on the available experiments, assuming its value is not dependent on the operational conditions, but only on propeller configuration, while for PM2 τ it is assumed constant on the whole data set. The observed results point out also the limits of these assumptions. Furthermore, one of the main problems related to PMs is that in some cases the noise spectra within the available data present a behaviour similar to the one schematised by the PM whereas in other cases a significantly different behaviour is observed, with the frequency of the maximum weakly depending on cavitation size (this is especially true for the near to inception samples, characterised by high frequency and low noise level). The PM is not able to discriminate between these different situations and its accuracy decreases when the cavitation noise is not mainly driven by the tip vortex pulsation, e.g. when the propeller pitch is lower. This may contribute to the significant variance observed.

8.5.1.2 Data Driven Models Results

Figure 8.2 reports the scatter plots of the measured and predicted values of f_{bp1}, RNL_{bp1}, f_c, RNL_c, f_{bp2}, RNL_{bp2}, and RNL_b for the DDMs. From Figure 8.2 it is possible to observe that:
- considered targets are predicted with a reasonable accuracy by the model, demonstrating that trends present in the experimental data can be effectively modelled by the DDMs;
- the DDMs seems to correctly predict the targets considering also the different behaviours of cavitation noise spectra observed, which represented one of the limits of the considered PMs;
- the results show significantly different trends depending on the considered target
  - a reasonable agreement between measured and predicted data is observed for targets f_c, RNL_c and RNL_b, even if some variance is present;
  - a good agreement is observed also for the target RNL_{bp1}, but in this case there seems to be a deterioration of the prediction performance for the highest values in the distribution;
  - the distributions of points on the scatter diagrams highlight some problems for what regards targets f_{bp1}, f_{bp2} and RNL_{bp2}. Points are partially clustered around certain values, with a significant number of samples spread over the plot without a clear tendency.

Additionally, some examples of the predicted spectra are given in Figure 8.3. It has to be remarked that these are only two examples obtained from one of the several computational iterations performed during the model selection phase, which are reported here in order to discuss some issues of the present approach. For what regards the overall quality of the model, the representative indexes are those reported in Table 8.5. These results point out some limits of the definition of the targets for the prediction of noise spectra. The simplified spectral shape adopted effectively

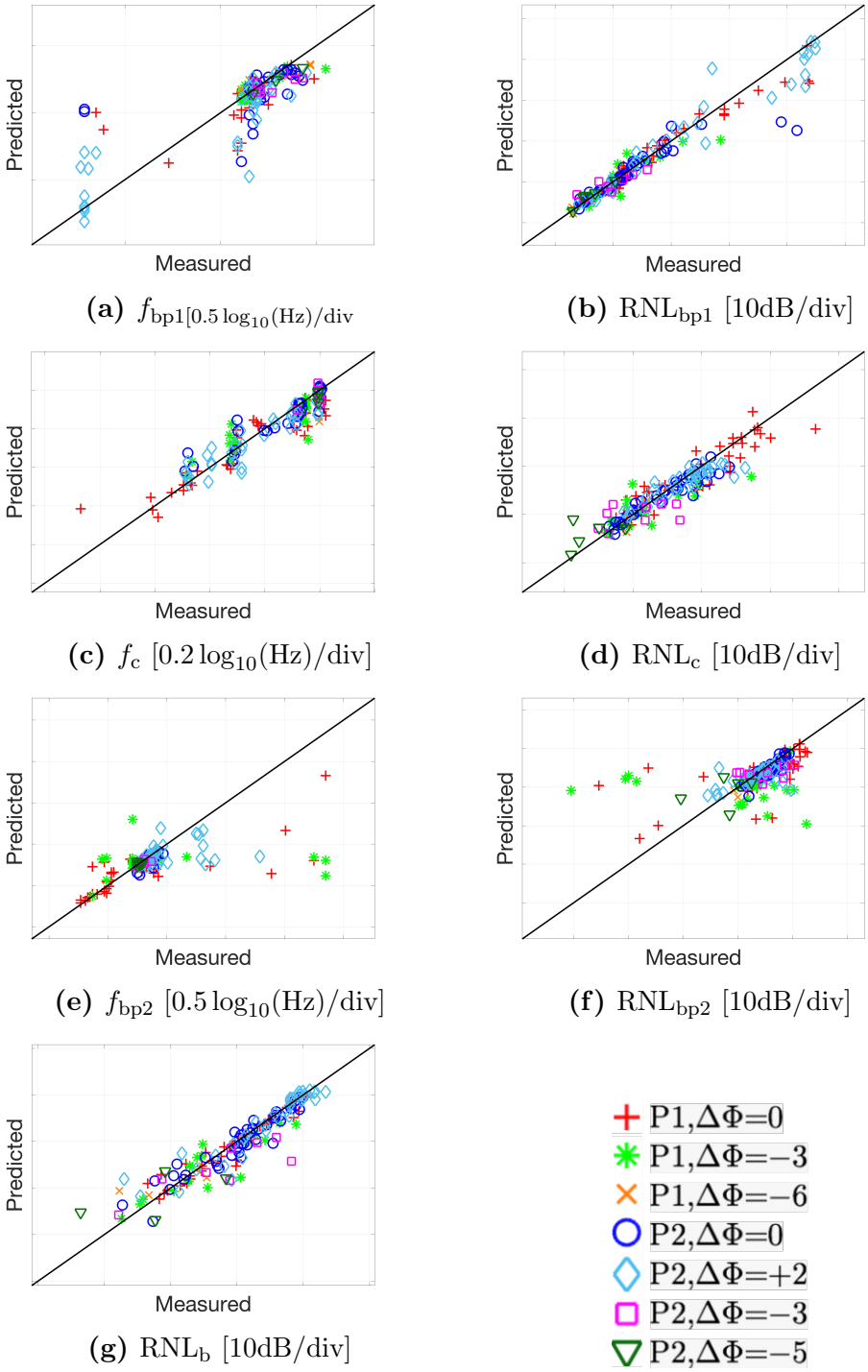

(a) f_{bp1}[0.5 $\log_{10}$(Hz)/div] **(b)** $\mathrm{RNL}_{\mathrm{bp1}}$ [10dB/div]

(c) f_{c} [0.2 $\log_{10}$(Hz)/div] **(d)** $\mathrm{RNL}_{\mathrm{c}}$ [10dB/div]

(e) f_{bp2} [0.5 $\log_{10}$(Hz)/div] **(f)** $\mathrm{RNL}_{\mathrm{bp2}}$ [10dB/div]

(g) $\mathrm{RNL}_{\mathrm{b}}$ [10dB/div]

Figure 8.2: Interpolation Scenario DDMs: scatter plots of the measured and predicted values of f_{bp1}, $\mathrm{RNL}_{\mathrm{bp1}}$, f_{c}, $\mathrm{RNL}_{\mathrm{fc}}$, f_{bp2}, $\mathrm{RNL}_{\mathrm{bp2}}$, and $\mathrm{RNL}_{\mathrm{b}}$.

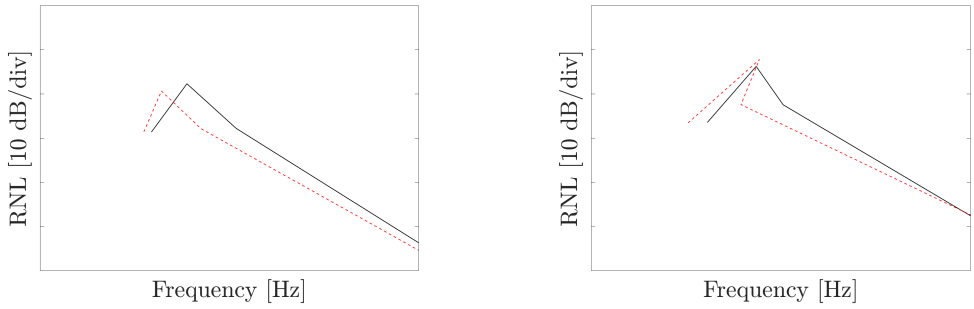

(a) P1-DES, mid-loading condition, $\sigma_n = 3.5$.

(b) P2-DES, low-loading condition, $\sigma_n = 1.91$.

Figure 8.3: Interpolation Scenario DDM: simplified spectrum target (solid black) and predicted (dashed red) for different WPs.

succeeds in modelling measured noise spectra, even considering both spectral shapes observed, namely with and without prominent peak.

The issues may be related to the definition of the parameters used to describe the simplified spectra, namely frequencies and levels of the points. Actually, the frequency and levels of the two breakpoints used to define the simplified shape do not feature a clear physical meaning and consequently they are not characterised by clear tendencies as other targets. The first break point, roughly corresponds to the frequency above which the cavitation noise spectrum is perceived over the background noise. As a consequence the frequency of this point, and its corresponding level, depends not only on the characteristics of cavitation noise, but also on the spectrum of the background noise in the tunnel.

The second break point divides the spectrum into two regions characterised by different decay ratio of noise with respect to frequency: the decreasing part of the peak, when present, with a larger decay ratio, and the high frequency spectrum with lower decay. These two regions are clearly distinguished only when a prominent peak is identified, otherwise an almost constant decay is observed from the maximum point of the spectrum towards higher frequencies. In the latter case, the definition of the break point is uncertain and consequently f_{bp2} and $\mathrm{RNL}_{\mathrm{bp2}}$ may assume anomalous values.

Considering the two example spectra in Figure 8.3, another issue related to the DDM itself is evident; in particular, the model is composed by seven independent DDMs (one for each target), not related to each other, thus allowing for unwanted results like the one reported in Figure 8.3b, where the second break point predicted is at a lower frequency with respect to the center peak. Such kind of problems are likely to appear especially for the points which are more difficult to be predicted, as the second breakpoint in this case. Conversely, it is clear that the peak in the same spectrum is very well captured. Whereas, Figure 8.3a may be considered as an example of a possible result, with a not completely satisfactory capturing of the peak frequency f_{c} but the discrepancy for all other parameters in line with the MAE reported in Table 8.5.

In order to have a better insight into this result, errors computed on the two example cases, for the various parameters are reported in the Table 8.6, compared to those declared in Table 8.5.

Prop.	$\Delta\Phi$	f_{bp1}	RNL_{bp1}	f_c	RNL_c	f_{bp2}	RNL_{bp2}	RNL_b
Model		DDMs	DDMs	DDMs	DDMs	DDMs	DDMs	DDMs
MAE								
P1-DES F. 8.3a		65.6	0.07	381.6	1.65	1298.0	0.05	1.7
P2-DES F. 8.3b		164.5	0.12	91.5	1.56	1334.6	0.05	0.2
all	all	85±4	1.7±0.1	114±6	1.9±0.1	2780±144	3.5±0.2	2.0±0.1

Table 8.6: DMMs accuracy comparison between the final model in Table 8.5 and the two test cases of Figure 8.3.

These issues might be overcome in different ways: modifying the simplified representation of spectra or simply employing different parameters to describe it. As an example, the decay ratio (i.e. the slopes of the curve) in the two mentioned regions of the spectrum could be considered in place of the break point. Actually, these parameters should allow to correctly describe the spectra as well, and they should not present anomalous values, even when the distinction between the two regions becomes meaningless. The adoption of alternative parameters and its effect will be shown in Chapter 9.

Evaluating the performance of the DDMs in terms of accuracy is just the first step toward understanding them. In fact, these models are black-box and consequently the learned relation between inputs and outputs is not explicitly known. Since Kernel Methods were exploited to extract the explicit form of the model, evaluating the relationship between inputs and outputs would be in most cases impossible while in some cases computational intractable (Shawe-Taylor and Cristianini, 2004). In order to overcome this limitation it was decided to perform a Feature Ranking (FR) procedure (Guyon and Elisseeff, 2003; Liu and Motoda, 2007) which allows to rank the features based on their effect on the model output. For this purpose, a very statistically sound and robust approach called permutation test was exploited (Good, 2013; François, Wertz, and Verleysen, 2006).

Table 8.7 reports the result of the FR procedure on the models which predict f_c and RNL_c. Before analysing the result of the FR procedure in details, it is worth noting that most of the considered features are strongly dependent or even redundant (e.g. propeller thrust and torque or the alternative definitions of the cavitation number). This means that FR can detect as important just one or all of this strongly correlated features, some of them, or all of them, which basically contain the same information. In fact, one has to remember that the FR procedure is a statistical procedure and consequently subject to uncertainties and statistical fluctuations and, consequently, it does not make sense to make very specific comments while it is more reasonable to observe global trends. Having said this, it is possible observe that:

- not surprisingly, the inception indexes of the driving phenomena (i.e. Tip Vortex at 0°, Detached Tip Vortex and Suction Side Sheet at 0° are always in the Top 3. This confirms the strong relation between measured noise and the cavitation intensity;

- the knowledge summarised in Equation (7.35) about the resonance frequency of the vortex can be found also in the FR, indeed the torque coefficient (in place of the thrust coefficient), the relative pressure (in place of the cavitation index)

and the propeller rotational speed are in the Top 10 features for importance;

- similarly, the sound pressure level of the vortex peak, whose theoretical expression of Equation (7.41) identifies in the propeller load and the cavitation index the most valuable parameters, is checked by FR;

- in general it can be observed the most influencing variables in the noise generation are among the most important ones according to the FR. Furthermore, it is interesting to notice the absence in the top positions of features assumed to be strongly related to the cavitation noise, as an example the wake parameters. This can be justified recalling that some features, such as the cavitation inception, directly depend on the wake, or some others, as the angle of attack, are derived from it. Hence, wake features could be redundant.

Table 8.7: Top 20 results of FR on f_c and RNL_c.

	f_c		RNL_c
#	Feature	#	Feature
1	TVC 0°	1	TVC 0°
2	D.TVC	2	S.S. S 0°
3	S.S. S 0°	3	D.TVC
4	max α_{G09}	4	TVC
5	$10K_Q$	5	V_a
6	p_{rel}	6	S.S. RB
7	TVC	7	J
8	n	8	$10K_Q$
9	max α_{G07}	9	P/D
10	Q	10	η_o
11	$\overline{\alpha}_{G09}$	11	σ_v
12	σ_v	12	max α_{G07}
13	S.S. S	13	n
14	σ_{ntip}	14	σ_{ntip}
15	σ_n	15	σ_n
16	S.S. RB	16	RelPre
17	P/D	17	Q
18	min α_{G09}	18	$\Delta\Phi$
19	K_T	19	max α_{G09}
20	T	20	T

8.5.1.3 Hybrid Models Results

Figure 8.4 reports the scatter plots of the measured and predicted values of f_c and RNL_c for both HM1 and HM2. From Figure 8.4 it is possible to observe that there is a significant enhancing of the performances of the DDMs by using the PMs. Moreover, the results show that the use of a more generic set of coefficients (PM2) does not lead to a noticeable degradation of the performance of the HMs, making them very attractive and promising in view of future enlargements of the experimental dataset. Only a sample, at very low peak frequency and high noise level, belonging to P1-DES, slips-out from the model prediction trend; it is clearly an outlier wrongly included in the dataset and it will be removed.

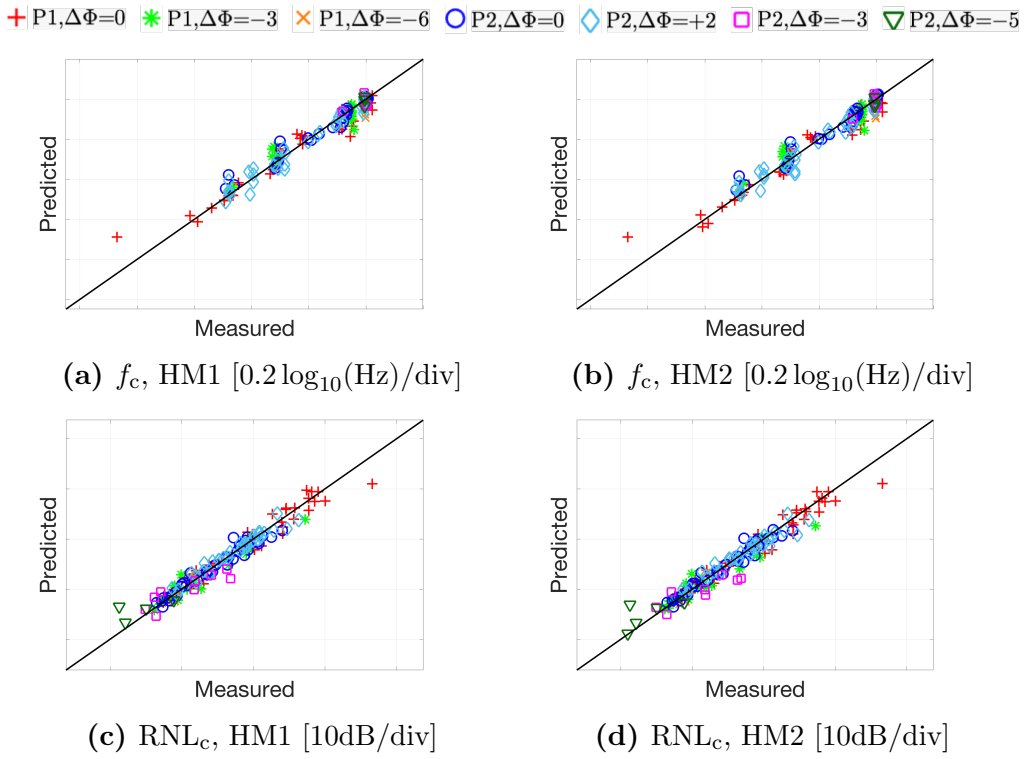

(a) f_c, HM1 [$0.2\log_{10}$(Hz)/div] **(b)** f_c, HM2 [$0.2\log_{10}$(Hz)/div]

(c) $\mathrm{RNL_c}$, HM1 [10dB/div] **(d)** $\mathrm{RNL_c}$, HM2 [10dB/div]

Figure 8.4: Interpolation Scenario HMs: scatter plots of the measured and predicted values of f_c and $\mathrm{RNL_c}$ for both HM1 and HM2.

8.5.2 Extrapolation Scenario

From a practical point of view, it is of great interest to test the capability of the models to predict radiated noise for cases not included in the variable domain of the data used to build them. Actually, new cases of interest might be characterised by values of the input variables not included between those considered, but still similar to them. This may be the case of a new propeller designed with operating requirements different from those considered.

As already anticipated, another important application of the models developed is related to those ship operational conditions for which the cavitation pattern cannot be correctly reproduced in model scale, requiring an extrapolation (Subsection 2.3.1). In order to better present the problem, the typical cavitation bucket of a model scale propeller is schematised in Figure 8.5. The full scale working point is characterised by the values of the thrust coefficient and cavitation number of the full scale propeller. In some cases, for this combination of values the model scale propeller does not cavitate, because of viscous scale effects affecting the development of vortices. However, applying scaling formulas like those proposed by McCormick (1962) or Shen, Gowing, and Jessup (2009), it is possible to assess if TVC is present in full scale and roughly estimate its extent by means of the σ_n/σ_{ni} ratio or similar quantities. In order to reproduce the same cavitation extent in model scale, some scaling criterion must be applied, such as the identity of the ratio σ_n/σ_{ni}. The test conditions obtained following this approach (i.e. the scaled working point in the example) are, in some cases, located on the bucket in the hatched area. In this area the presence of unwanted phenomena, like bubble cavitation or other measuring issues (e.g. bubble scattering), may alter the measured noise and also the development

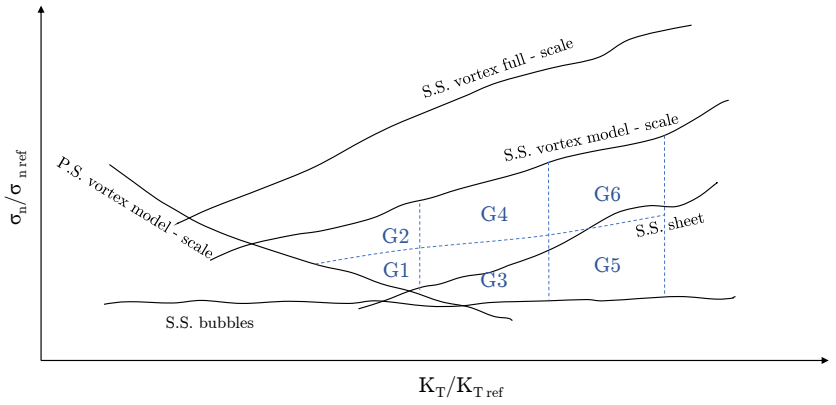

Figure 8.5: Sketch of data domain subdivision for extrapolation tests.

of the vortex cavitation itself. As a consequence, the direct measurement in such conditions is deemed not meaningful. Radiated noise in the hatched area should be predicted eliminating the unwanted effects, thus obtaining a sort of ideal model scale experiment. The proposed approach basically consists in developing a model based only on operational conditions without unwanted phenomena. These conditions correspond to the areas identified by numbers from G1 to G6 in Figure 8.5. These areas are defined by combinations of the quantities K_T/K_{Tref} and σ_n/σ_{ni} of the TVC. The model based on these data is able to predict noise for different extents of TVC and different combination of input parameters without modelling the unwanted phenomena. The target conditions in the hatched area are characterised by a combination of input parameters not included in the set of data used to define the model, hence an extrapolation is needed. Since validation data for the target region is not available, it is not possible to directly test the capability of the model to extrapolate in this area.

In order to obtain an indication of such capability, the extrapolation performance between different subsets of data, corresponding to the numbered areas in Figure 8.5, has been assessed. In particular the extrapolation test consists in including in $\mathcal{D}_n$ only five of the six groups and use the sixth group as $\mathcal{T}_m$. From the point of view of the physical problem here summarised (i.e. the prediction of the hatched area), the most interesting extrapolation cases are those for which $\mathcal{T}_m$ is represented by points belonging to the zones 1, 2, and 3.

In Table 8.8, analogously to Table 8.5 in Subsection 8.5.1, the full set of results are reported, and they are complemented with a series of scatter plots in order to better comment them. Note that, in this case, the results are not checked based on the propeller characteristics but based on the group membership (see Figure 8.5). Looking at Table 8.8, it is clear that the DDMs and the HMs are able to effectively make predictions in the extrapolation case and to provide estimation which can be reliable in a real world application of the method showing their ability to extrapolate and not just interpolate. Figures 8.6, 8.7, and 8.8, analogously to Figures 8.1, 8.2, and 8.4 in Subsection 8.5.1, report the scatter plots of the measured and predicted values of f_{bp1}, RNL_{bp1}, f_{c}, RNL_{c}, f_{bp2}, RNL_{bp2}, and RNL_{b} for the PMs (if available), the DDMs, and the HMs (if available) respectively. The extrapolation performance

Group	f_{bp1}	RNL_{bp1}	f_c			RNL_c			f_{bp2}	RNL_{bp2}	RNL_b
Model	DDMs	DDMs	PM1	PM2	HM1	HM2	PM1	PM2	DDMs	HM1	HM2	DDMs	DDMs	DDMs
MAE														
G1	66±3	0.7±0.0	199±9	177±9	143±8	**55±2**	55±3	7.1±0.4	8.8±0.4	3.5±0.2	1.6±0.1	**1.5±0.1**	3666±172	4.0±0.2	1.9±0.1	
G2	82±4	1.0±0.1	292±12	263±13	288±15	138±6	**133±7**	4.4±0.2	5.9±0.3	0.9±0.1	0.6±0.0	**0.6±0.0**	5346±364	5.1±0.2	2.4±0.1	
G3	105±5	4.0±0.2	162±9	166±9	96±5	**36±2**	37±2	4.6±0.2	4.2±0.2	3.7±0.2	1.0±0.0	**0.9±0.0**	1204±60	5.2±0.3	1.7±0.1	
G4	60±3	1.1±0.1	180±11	225±12	181±9	**56±3**	62±3	3.2±0.2	4.1±0.2	2.6±0.2	**0.9±0.0**	0.9±0.1	4797±219	3.5±0.2	2.8±0.2	
G5	101±5	6.3±0.3	205±10	272±13	219±12	**118±5**	139±6	4.1±0.2	4.1±0.2	4.5±0.2	2.5±0.1	**2.4±0.1**	2309±118	3.9±0.2	3.1±0.2	
G6	133±7	1.6±0.1	198±10	229±12	249±14	**95±5**	114±7	4.5±0.2	5.8±0.3	3.0±0.2	1.0±0.1	**1.0±0.0**	1800±86	3.1±0.2	3.6±0.2	
all	95±5	2.9±0.2	201±10	233±12	205±9	**87±4**	97±6	4.2±0.2	4.8±0.2	3.1±0.2	1.3±0.1	**1.3±0.1**	3045±173	3.9±0.2	2.8±0.1	
MAPE																
G1	13.5±0.7	10.6±0.6	19.7±1.1	20.4±1.0	13.5±0.6	7.3±0.4	**7.2±0.3**	32.0±1.4	40.9±2.2	14.8±0.7	6.6±0.4	**6.5±0.3**	27.0±1.3	89.6±4.5	19.1±0.9	
G2	12.2±0.7	223.3±10.5	19.4±0.8	17.2±0.9	20.1±0.8	9.5±0.4	**9.2±0.4**	41.4±2.1	54.7±2.6	8.1±0.4	5.3±0.3	**5.0±0.2**	15.8±0.8	77.5±3.7	11.5±0.6	
G3	44.9±2.2	28.3±1.4	22.9±1.4	24.7±1.1	12.7±0.6	**4.8±0.2**	5.1±0.3	22.6±1.1	20.3±1.1	17.4±0.8	4.8±0.3	**4.4±0.2**	43.2±2.1	64.9±2.8	12.9±0.6	
G4	10.4±0.5	313.7±12.0	14.7±0.7	17.3±0.8	14.1±0.8	**4.4±0.3**	4.8±0.2	32.5±1.7	58.4±2.8	29.5±1.3	14.8±0.8	**14.4±0.6**	17.3±0.7	115.8±5.9	11.1±0.5	
G5	70.2±3.4	70.3±3.0	30.5±1.6	35.5±1.7	23.0±1.1	**12.4±0.6**	13.6±0.7	26.2±1.5	31.2±1.3	23.2±1.2	12.2±0.6	**11.6±0.6**	29.1±1.6	67.7±3.4	22.5±1.1	
G6	20.1±1.1	174.3±8.5	13.8±0.7	16.1±1.0	17.3±0.8	**6.6±0.3**	7.8±0.4	60.9±3.4	115.0±5.5	38.1±1.7	20.6±1.1	**20.6±1.1**	18.2±1.0	354.3±16.8	13.4±0.7	
all	33.0±1.5	161.9±8.5	20.4±1.0	22.8±1.1	17.6±1.0	**7.7±0.4**	8.3±0.5	36.6±1.9	57.2±3.2	25.1±1.3	12.6±0.6	**12.3±0.6**	24.2±1.3	142.0±7.6	15.1±0.8	
PPMCC																
G1	.70±.03	.99±.04	.87±.05	.90±.05	.83±.04	**1.00±.05**	.99±.06	.75±.04	.90±.05	.87±.04	.99±.05	**.99±.05**	-.11±.01	-.41±.02	.98±.06	
G2	.65±.03	.95±.04	.70±.03	.74±.04	.90±.05	.94±.06	**.94±.05**	.73±.04	.55±.03	.90±.05	.97±.05	**.97±.05**	-.34±.01	.51±.03	.70±.04	
G3	.83±.04	.96±.05	.70±.03	.72±.04	.85±.04	.98±.06	**.98±.05**	.02±.00	.35±.01	.60±.03	.98±.05	**.98±.04**	.27±.01	.09±.00	.91±.04	
G4	.69±.04	.86±.05	.69±.04	.50±.02	.76±.03	.98±.05	**.98±.05**	.48±.02	.04±.00	.59±.03	**.97±.04**	.97±.05	-.28±.02	.40±.02	.78±.04	
G5	.75±.04	.80±.03	.88±.04	.50±.03	.50±.02	**.92±.05**	.83±.05	.66±.03	.65±.03	.67±.03	.92±.05	**.93±.05**	.05±.00	.43±.02	.84±.04	
G6	.57±.03	.87±.05	.56±.03	.24±.01	.60±.03	**.93±.05**	.83±.04	.70±.04	.03±.00	.72±.03	**.98±.05**	.97±.05	-.24±.01	.49±.02	.80±.05	
all	.77±.04	.91±.04	.81±.04	.71±.03	.80±.04	**.96±.05**	.93±.05	.68±.03	.55±.03	.82±.04	.97±.04	**.97±.04**	-.01±.00	.31±.02	.88±.03	

Table 8.8: Extrapolation Scenario: PMs, DDMs, and HMs, performance measured with the MAE, the MAPE, and the PPMCC. Winning method in bold.

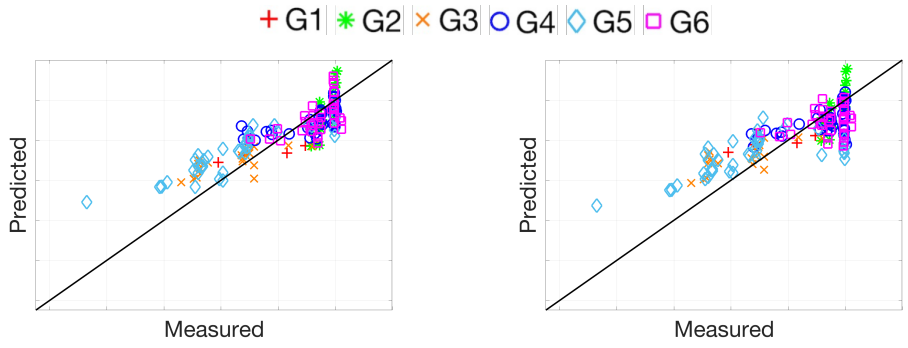

(a) f_c, PM1 [$0.2\log_{10}$(Hz)/div] **(b)** f_c, PM2 [$0.2\log_{10}$(Hz)/div]

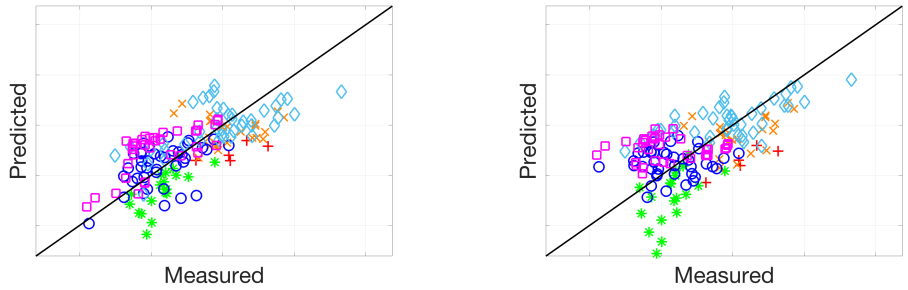

(c) RNL_c, PM1 [10dB/div] **(d)** RNL_c, PM2 [10dB/div]

Figure 8.6: Extrapolation Scenario PMs: scatter plots of the measured and predicted values of f_c and RNL_c for both PM1 and PM2.

of the DDMs and HMs are promising, and related results seem to confirm the validity of the proposed approach. The accuracy of the extrapolation is remarkable for all the groups except G5 for which however results are still acceptable. Anyway it has to be remarked that, for the sake of extrapolation to critical conditions previously described, the extrapolation of group G5 is not so important, presenting this group the highest deviations, in terms of cavitating behaviour, from the design conditions. On the contrary, results obtained for the extrapolation of groups G1, G2 and G3 are definitely encouraging.

8.6 Summary

In this chapter the first procedure to estimate propeller cavitation noise by means of numerical models has been presented. The goal is to predict the significant characteristics of the cavitation noise spectra using a limited amount of data available at propeller design stage. Within this purpose in mind, a simplification of the propeller noise spectra has been proposed. Three different modelisation strategies have been presented: one based on the physical knowledge of the problem, one based on data science and one based on a hybrid approach able to exploit both the two sources of information. An extensive set of cavitation tunnel tests performed with different propellers and different configurations allowed the creation of a database exploited to develop and testing the different models.

An in depth comparison of the performance of the different models has been performed. In particular two sets of evaluations have been carried out. In the first set, the capability of the models to predict the propeller noise spectra main

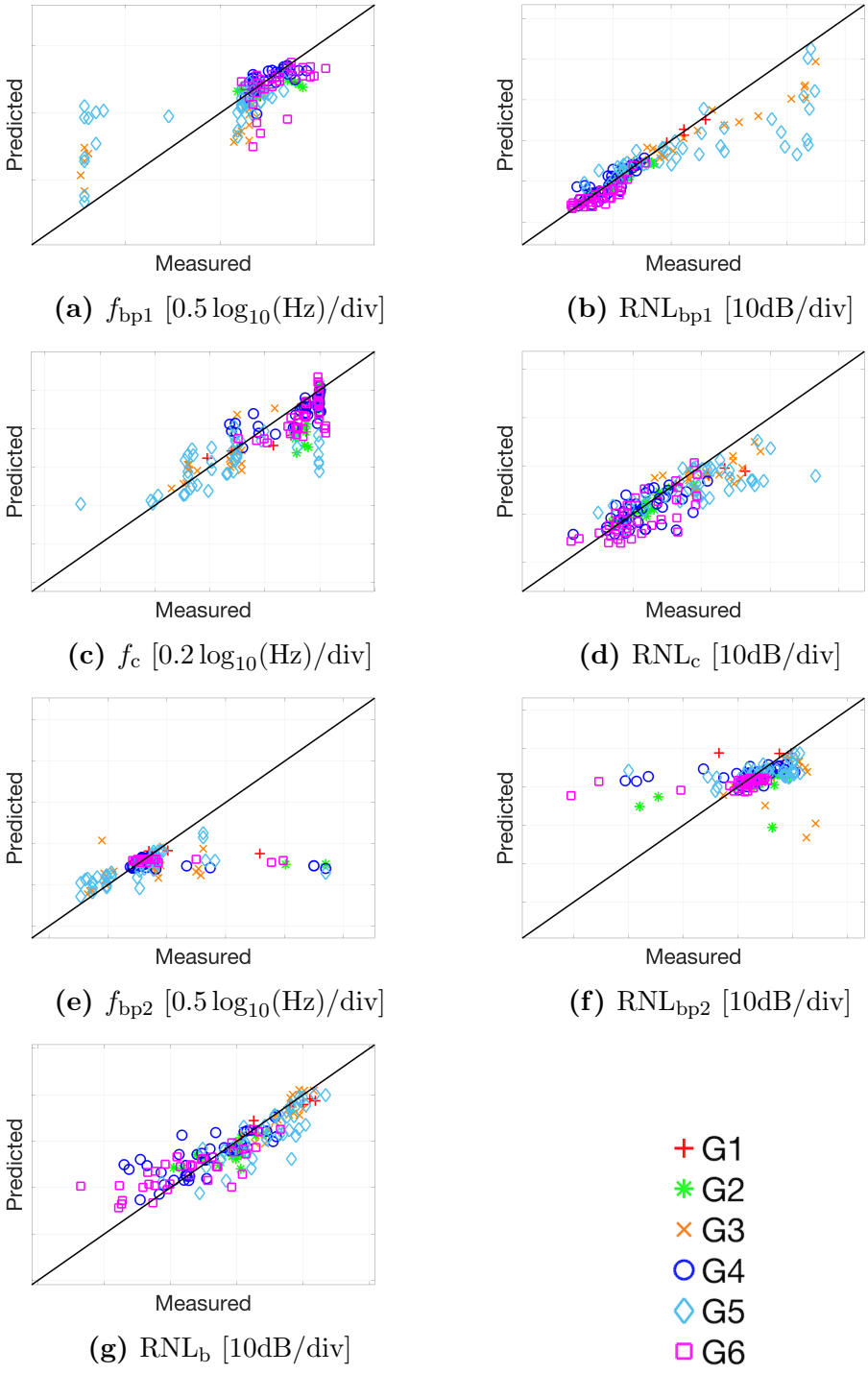

(a) f_{bp1} [$0.5\log_{10}$(Hz)/div] **(b)** $\mathrm{RNL}_{\mathrm{bp1}}$ [10dB/div]

(c) f_{c} [$0.2\log_{10}$(Hz)/div] **(d)** $\mathrm{RNL}_{\mathrm{c}}$ [10dB/div]

(e) f_{bp2} [$0.5\log_{10}$(Hz)/div] **(f)** $\mathrm{RNL}_{\mathrm{bp2}}$ [10dB/div]

(g) $\mathrm{RNL}_{\mathrm{b}}$ [10dB/div]

Figure 8.7: Extrapolation Scenario DDMs: scatter plots of the measured and predicted values of f_{bp1}, $\mathrm{RNL}_{\mathrm{bp1}}$, f_{c}, $\mathrm{RNL}_{\mathrm{c}}$, f_{bp2}, $\mathrm{RNL}_{\mathrm{bp2}}$, and $\mathrm{RNL}_{\mathrm{b}}$.

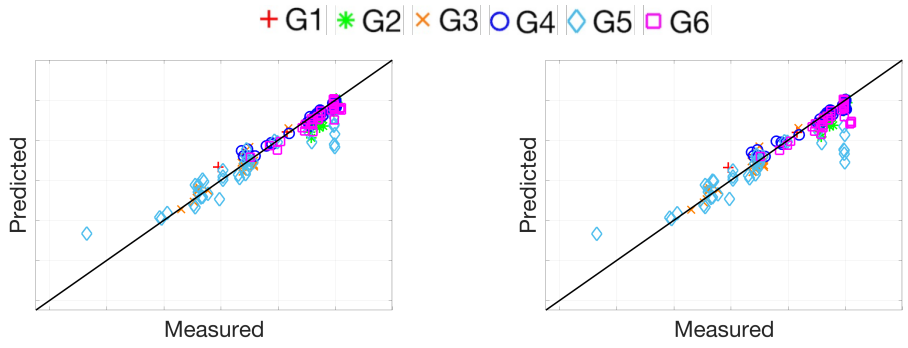

(a) f_c, HM1 [$0.2\log_{10}$(Hz)/div] **(b)** f_c, HM2 [$0.2\log_{10}$(Hz)/div]

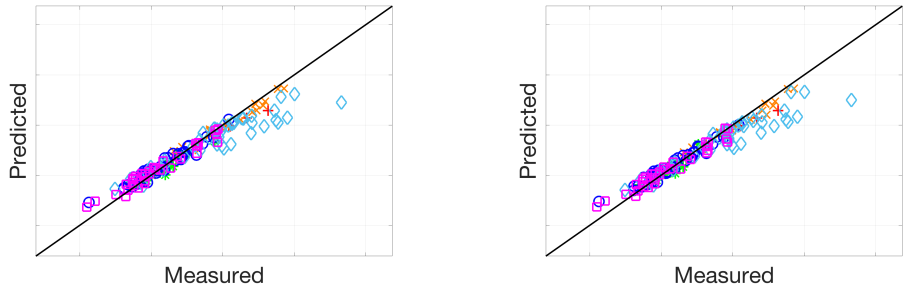

(c) RNL_c, HM1 [10dB/div] **(d)** RNL_c, HM2 [10dB/div]

Figure 8.8: Extrapolation Scenario HMs: scatter plots of the measured and predicted values of f_c and RNL_c for both HM1 and HM2.

characteristics in working conditions within the ones exploited for building the model has been analysed; in all cases, conditions different from those used to build the model have been used for the test, but always remaining inside the initial domain. In the second set of trials, instead, the capability of the models to predict the propeller noise spectra main characteristics in groups of working conditions where the cavitation intensity is different with respect to the one exploited for building the model has been tested. In both scenarios HMs have shown remarkable and promising results opening the way to future works in this direction.

Next step of the research (Chapter 9) will include several improvements of the promising modelling procedure, including some aspects summarised in the following.

The presented analysis has been limited only to a class of similar propellers and configurations deemed of remarkable interest, in order to generate a collection of data with a tolerable variance. The data collection will be enlarged considering further propellers and wake fields. This will require the use of an enlarged set of features, including more parameters describing propeller geometries (e.g. expanded area ratio, camber, chord, etc.).

Furthermore, transfer function corrections will allow including in the model the effect of the confined environment, providing an estimate of propeller source levels in free field conditions.

Numerical computations such as BEM, can provide interesting and complete features that can enhance the prediction capabilities (e.g.the pressure field on blades). In this first approach some features have been extracted from MSTs such as thrust and torque collected by the dynamometer. This, in principle, require that in the future applications of the models, these features have to be collected by similar MSTs because the indexes of performance of the models are valid if the inputs come from

the same probability density functions (i.e. if the inputs are obtained with the same methodologies). To disengage the predictive models features from the MSTs, the hydrodynamic curves computed by BEM will be used in place of the experimental ones.

Lastly, results obtained with the Hybrid Model suggest investigating this approach considering also other physical models or semi-empirical formulations available in literature, with the aim of further improve the already remarkable results of the developed models.

Chapter 9

Modelisation - Approach 2

The chapter presents the second modelling approach. The dataset employed is composed by propellers P1, P2 and P3 behind different types of wakes. The noise targets include a simplification of the narrowband spectrum, and the one-third octave band spectra for both radiated noise levels and source levels. Different groups of features have been considered including general descriptors, and more complex variables such as the complete wake, the pressure coefficients on the blade and the circulations.

9.1 Introduction

In this chapter an approach similar to the one already presented in Chapter 8, namely physical, data driven and hybrid models will be exploited to predict the cavitating noise spectra. The main differences consist of: increased samples size, additional propeller geometries and wakes, different types of spectrum parametrization, and multidimensional features. Therefore, more complex machine learning algorithms will be exploited.

The propellers and set-ups accounted are summarised in Table 9.1; as already exposed in Section 4.4, W2 and W5 are similar to an undisturbed flow. The other wake fields are reproductions of twin screw vessel wakes. The total number of samples is 258.

Table 9.1: Propeller and wake configurations for modelisation Approach 2.

Pitch	Propeller		
	P1	P2	P3
Design	W1-W2	W3	W4-W5-W6
Reduced (-3°)	W1	W3	
Reduced (-5°)		W3	
Reduced (-6°)	W1		
Incremented (+2°)		W3	

For simplicity, the features have been subdivided in groups called Feature Sets (FS) and reported in Table 9.2. The FS from 1 to 5 have been exploited in the DDMs and HMs. FS0 has been used in the PMs. The FS1 includes a series of scalar similarly to the Approach 1. The FS2, FS3, and FS5 are two-dimensional tensors representing respectively the axial wake, the propeller geometric angle of attack and the blade circulation. FS4 is the pressure coefficient distribution on the blades at

different angular positions, reported as three-dimensional tensor. FS4 and FS5 are calculated by non cavitating BEM (Section 6.6), all the other features are obtained by data available in the propeller design stage (Chapter 6). Features included in FS0 are the direct inputs for the noise physical models, whereas FS0[1] includes those variables that are exploited to calculate some PMs inputs.

Different target definitions have been used, based on the chosen Noise Spectra Parametrisation (NSP in Table 9.3):

- NSP1 is the pair vortex peak frequency and noise level;
- NSP2 is the same narrowband spectrum simplification adopted in Approach1;
- NSP3 is similar to NSP2 but with the power decay in [dB/oct] in place of the breakpoints expressed by the couple (f_i, RNL_i);
- NSP4 are the one-third octave band levels (OTO) of the transferred radiated noise;
- NSP5 are the OTO levels obtained with the spherical-spreading loss;

It should be noted that NSP2-3-5 represent the same spectrum (net noise with the spherical-spreading loss) but shaped with different approaches. The NSP1 is just a part of NSP2-3, i.e. the vortex frequency and level. This distinction has been made in order to analyse separately these targets, which represent some of the most important characteristics of noise spectra and they can be compared with relevant PMs.

As usual, the noise prediction is achieved by means of some physical models, a data driven model and an hybrid model. The theory behind the PMs has been described in Chapter 7, here in Section 9.2 the practical implementation of those formulations is explained. The PMs, differently from the DDMs, are available only for a limited number of targets as flagged by the ✓in Table 9.3; the apex 1 means that the target can be predicted only partially.

Two typologies of DDMs have been tested: the first is a simpler model called Conventional Data Driven Model (CDDM), the second is an Advanced Data Driven Model (ADDM). The ML models have been developed by the working team and hence are presented in Section A.1. The ADDMs has been combined with the PMs to get the HMs, it is presented in Section A.2.

The measure of the error that the modelled function h would commit in approximating the real process can again be measured by the mean absolute error, the mean absolute percentage error, and by the Pearson Product-Moment Correlation Coefficient (Equations 8.1, 8.2, 8.3).

To assess the predictive performance on the NSP4 and NSP5 the error is computed as the average of the errors on the noise levels predicted for all the OTO bands. This can be done since NSP4, and NSP5 simply count homogeneous quantities.

For what concerns instead NSP2 and NSP3 the approach adopted for NSP4, and NSP5 cannot be directly applied. In fact, the parameters of NSP2 and NSP3 represent different physical quantities, such as frequency and noise levels, expressed in non-homogeneous unit of measure. In order to estimate the error for NSP2 and NSP3 with an approach comparable to that adopted for NSP4 and NSP5, the simplified spectrum corresponding to the predicted values of NSP2 and NSP3 is

reconstructed. In such a way, the error can be computed comparing this spectrum with the real simplified spectrum. Obviously, it could be also possible to report the error (measured with the MAE, MAPE, and PPMCC) in estimating each parameter of the cavitation noise spectra parametrisation but this would not result in a concise and readable information. For this reason, this approach will be used just in few cases, in order to focus on the performance of the models in predicting specific targets, e.g. the frequency and level of the spectral hump. Eventually, the error on NSP1 as a whole as be computed only by the MAPE because this parametrisation counts for non-homogeneous quantities.

The chapter is organised as follows: in Section 9.2 the procedure adopted to exploit the PMs on the dataset is presented, for the vortex peak in Subsection 9.2.1, and for the broadband noise in Subsection 9.2.2. Some preliminary results are shown in Sub subsections 9.2.1.1 and 9.2.2.1. The theory behind the DDMs and the HMs is explained in Appendix A. The overall results of the proposed modelling approaches are discussed in Section 9.3, and finally Section 9.4 draws the conclusions of the chapter.

9.2 Physical models

9.2.1 Vortex peak prediction

The procedure described in Section 7.7 has been applied in the present context to estimate the characteristic frequency and level of noise spectral peak generated by cavitating vortices. The input data available are the propeller geometry, the wake inflow, and the blade circulation. In light of this, the vortex models shown in Chapter 7 can be exploited. Different vortex models have been discussed, among these the Proctor model has been chosen.

$$v(r) = \begin{cases} 1.0939\frac{\Gamma_\infty}{2\pi r}\left\{1 - \exp\left[-\beta\left(\frac{1.4r_\nu}{B}\right)^p\right]\right\}\left\{1 - \exp\left[-\zeta\left(\frac{r}{r_\nu}\right)^2\right]\right\} & r \leq 1.4r_\nu \\ \frac{\Gamma_\infty}{2\pi r}\left\{1 - \exp\left[-\beta\left(\frac{r}{B}\right)^p\right]\right\} & r > 1.4r_\nu \end{cases} \quad \text{(7.20 revisited)}$$

As suggested by Proctor, ζ is a prescribed parameter which takes the value of 1.2564 whereas p has been fixed at 0.75. B is the length scale related to the vorticity roll-up region, and for a propeller it becomes $D/2$. The Proctor model is a non-cavitating vortex model and it tends to overestimate the azimuthal velocity for not well developed cavities ($r_c \approx r_\nu$) and hence to overpredict the cavity radius. However, the cavitating vortex models require as an input the cavity radius, that is unknown in this context and hence the tuning procedure should have been spread to include an iteration on the r_c. Too many iteration cycles and tuning parameters must have been discouraged when the experimental data are limited because it is difficult to assess the influence of each tuning factor on the final results. For the same reason, the Proctor model has been chosen in place of the non-cavitating Bosschers (2018b) model.

The formulation of the Proctor model includes the following unknown quantities: r_ν, Γ_∞, β. Some of these, namely r_ν, Γ_∞, have specific physical meanings and their values should be found based on direct measurements of the azimuthal velocity distribution. Unfortunately, these measurements are not available for the current test

Table 9.2: Dataset input variables.

Variable	Unit	Description	Dimension	FS	PM
P/D	[]	Pitch ratio	1		
D	[m]	Diameter	1		FS0
A_E	$[m^2]$	Blade aspect ratio	1		
Z	[]	Number of blades	1	FS1	FS0
c/D	[]	Chord ratio at $0.7R$	1		
$t_{\max}/c$	[]	Blade maximum thickness at $0.7R$	1		
f_{max}/c	[]	Blade maximum camber at $0.7R$	1		
α_s	[°]	Shaft angle	1		
J	[]	Advance coefficient	1		
K_T	[]	Thrust coefficient	1		
$10K_Q$	[]	Torque coefficient	1		
V_a	[m/s]	Advance velocity	1	FS1	
n	[Hz]	Rate of propeller rotation	1		
σ_v	[]	Cavitation index ref. to advance velocity	1		
σ_n	[]	Cavitation index ref. to rotational speed	1		FS0
$\sigma_t ip$	[]	Cavitation index ref. to resultant speed at blade tip	1		
$\overline{w}$	[]	Average w	1		
max w_{07}	[]	Wake maximum at $0.7R$	1		
$w\,\mathrm{wd}_{07}$	[]	Wake width at $0.7R$	1		
$\mathrm{D}_\theta w\|_{07}^-$	[]	Left wake gradient at $0.7R$	1		
$\mathrm{D}_\theta w\|_{07}^+$	[]	Right wake gradient at $0.7R$	1	FS1	
max w_{09}	[]	Wake maximum at $0.9R$	1		
$w\,\mathrm{wd}_{09}$	[]	Wake width at $0.9R$	1		
$\mathrm{D}_\theta w\|_{09}^-$	[]	Left wake gradient at $0.9R$	1		
$\mathrm{D}_\theta w\|_{09}^+$	[]	Right wake gradient at $0.9R$	1		
$\overline{\alpha}_{G07}$	[°]	Circumferential average α_G at $0.7R$	1		
min α_{G07}	[°]	Minimum α_G at $0.7R$	1		
max α_{G07}	[°]	Maximum α_G at $0.7R$	1		
$\theta\|_{max\ \alpha_{G07}}$	[°]	Angular position of maximum α_G at $0.7R$	1	FS1	
$\overline{\alpha}_{G09}$	[°]	Circumferential average α_G at $0.9R$	1		
min α_{G09}	[°]	Minimum α_G at $0.9R$	1		
max α_{G09}	[°]	Maximum α_G at $0.9R$	1		
$\theta\|_{max\ \alpha_{G09}}$	[°]	Angular position of maximum α_G at $0.9R$	1		
w	[]	Axial wake	360×31	FS2	
α_G	[°]	Geometric angle of attack	360×31	FS3	
Γ	$[m^2/s]$	Blade circulation	60×25	FS5	FS0[1]

Table 9.3: Dataset output variables.

Variable	Unit	Description	Dimension	NSP	PM
f_c	[Hz]	Central peak frequency	1	1, 2, 3	✓
RNL_c	[dB]	Noise level at f_c	1	1, 2, 3	✓
f_{bp1}	[Hz]	Frequency of the first breakpoint	1	2	
f_{bp2}	[Hz]	Frequency of the second breakpoint	1	2	
RNL_{bp1}	[dB]	Noise level at f_{bp1}	1	2	
RNL_{bp2}	[dB]	Noise level at f_{bp2}	1	2	
RNL_b	[dB]	Noise level at ending frequency (100 kHz)	1	2, 3	✓
α	[dB/oct]	Slope between breakpoint 1 and central peak	1	3	
β	[dB/oct]	Slope between central peak and breakpoint 2	1	3	
γ	[dB/oct]	Slope between breakpoint 2 and last point	1	3	
$SL_{1/3}$	[dB]	Source Levels in OTO bands	24	4	✓[1]
$RNL_{1/3}$	[dB]	Radiated Noise Levels in OTO bands	24	5	✓[1]

cases, hence different strategies must be used to find the value of these unknowns. A first guess on the values of these parameters may be obtained from the analysis of literature data, however, since the characteristics of the flow vary case by case, values must be further tuned directly on noise data. In particular, the resonance frequency is considered for this purpose since its formulation is deemed more rigorous and more studies are available for this quantity. Furthermore, based on previous experiences, the resonance frequency is better predicted by the semi-empirical models than the noise amplitude, which may involve other complex aspects related to noise propagation.

Therefore, the only unknown coefficient β has been found by minimisation of the mean absolute error (Equation 8.1) in the vortex frequency prediction.

The viscous core radius r_ν has been obtained by the LDV measurements presented in Jessup (1989). Surveys were carried out in a cavitation tunnel and the test case was a 3 bladed model propeller, whose main characteristics are reported in Table 9.4.

Table 9.4: Jessup (1989) model scale propeller.

α_s	0°
Z	3
D	305.5 mm
$c_{0.95R}$	84.6 mm
J	0.833
n	10 Hz
V_a	2.54 m/s
$V_{0.95R}$	7.17 m/s
$Re_{0.95R}$	7.99×10^5
r_ν	0.915 mm

The Reynolds number is based on the chord length and on the resultant velocity

at $0.95R$. The Reynolds number for tests exploited in present thesis is generally different from the value reported in Table 9.4; since the viscous core size depends on it, the value derived by the mentioned LDV measurements must be scaled to the current test cases. This is done according to McCormick (1962) law:

$$\frac{r_\nu}{c} = \left(\frac{r_\nu}{c}\right)_{ref} \left(\frac{Re}{Re_{ref}}\right)^{-m/2} . \tag{9.1}$$

The exponent has been estimated by means of the formula proposed by Shen, Gowing, and Jessup (2009). According to this approach, the value of m decreases as the values of Re increase, approaching zero at the limit of very high Reynolds numbers. This agrees with the evidence that the effects of viscosity on cavitation diminishes as the Reynolds number approaches infinity, analogous to the general trend of flows to become inviscid at higher Reynolds numbers.

$$m = 5.16 \log\left(\frac{\log Re}{\log Re_{ref}}\right) / \log\left(\frac{Re}{Re_{ref}}\right) . \tag{9.2}$$

However, the viscous core size may depend also on other variables not considered in the scaling and then the scaled values may not allow to obtain a very good agreement with current data in terms of predicted resonance frequency of the vortex. Therefore it is envisaged to tune also the viscous radius by multiplying it by a factor constant on the whole dataset: following an exhaustive search in a reasonable interval, the best agreement has been found using the factor 0.5.

The vortex strength Γ_∞ is generally not known but it can be related to the blade circulation at large blade radius, computed by BEM (Bosschers, 2018a). This circulation, for a propeller operating in a non-uniform inflow, is dependent upon the blade position. This results in a variable vortex strength during the propeller revolution. As a consequence, also the cavitating radius and the corresponding resonance frequency depends on the blade angular position. In the measured noise spectrum the peak is unique and it likely corresponds to an average of the noise generated by every blade during the revolution, weighted according to the variable noise intensity. Therefore, a unique value of the circulation should be used in the vortex model, representing the prevalent vortex strength. Different possibilities have been exploited, such as the average over the revolution, the maximum, or some percentiles. The best performance of the model on present dataset have been obtained considering the 70% of the circulation at $r/R = 0.95$, averaged on the complete revolution.

Finally, the dynamic pressure can be computed from the azimuthal velocity, by Equation 7.12. The cavity radius is then found as the radial position where:

$$p_v \geq p(r) - p_\infty . \tag{9.3}$$

The model for the prediction of the vortex noise frequency is obtained combining this cavitating radius with Equation 7.26:

$$\frac{f_c}{nZ} = c_1 \frac{1}{r_c/D} \frac{\sqrt{\sigma_n}}{Z} + c_2 , \tag{9.4}$$

while Equation 7.43 has been used to model the corresponding noise level:

$$\mathrm{RNL_c} = a_p + 20 \log_{10}\left[\left(\frac{r_c}{D}\right)^k \sqrt{Z}\right] , \tag{7.43 revisited}$$

where c_1, c_2, a_p, and k are unknown parameters. For the case of the vortex resonance frequency, the two parameters are found by a simple linear least square fitting on f_c experimental data. The vortex peak noise level problem is non-linear and the best fit has been found with an algorithm to optimize non-linear functions in least square sense (Lagarias et al., 1998). Hereinafter this model will be named r_c-model.

For the sake of clarity the schema of the proposed algorithm is visible in Figure 9.1. The fitting parameters are the two multiplicative factors a_i and b_i for the vortex strength and for the viscous radius respectively, and the β coefficient for the Proctor model. The parameters are iteratively changed until the best fitting on the experimentally measured frequency is achieved (a^*,b^*,β^*). Instead, the unknown variables for the vortex peak prediction are found by a least square optimisation.

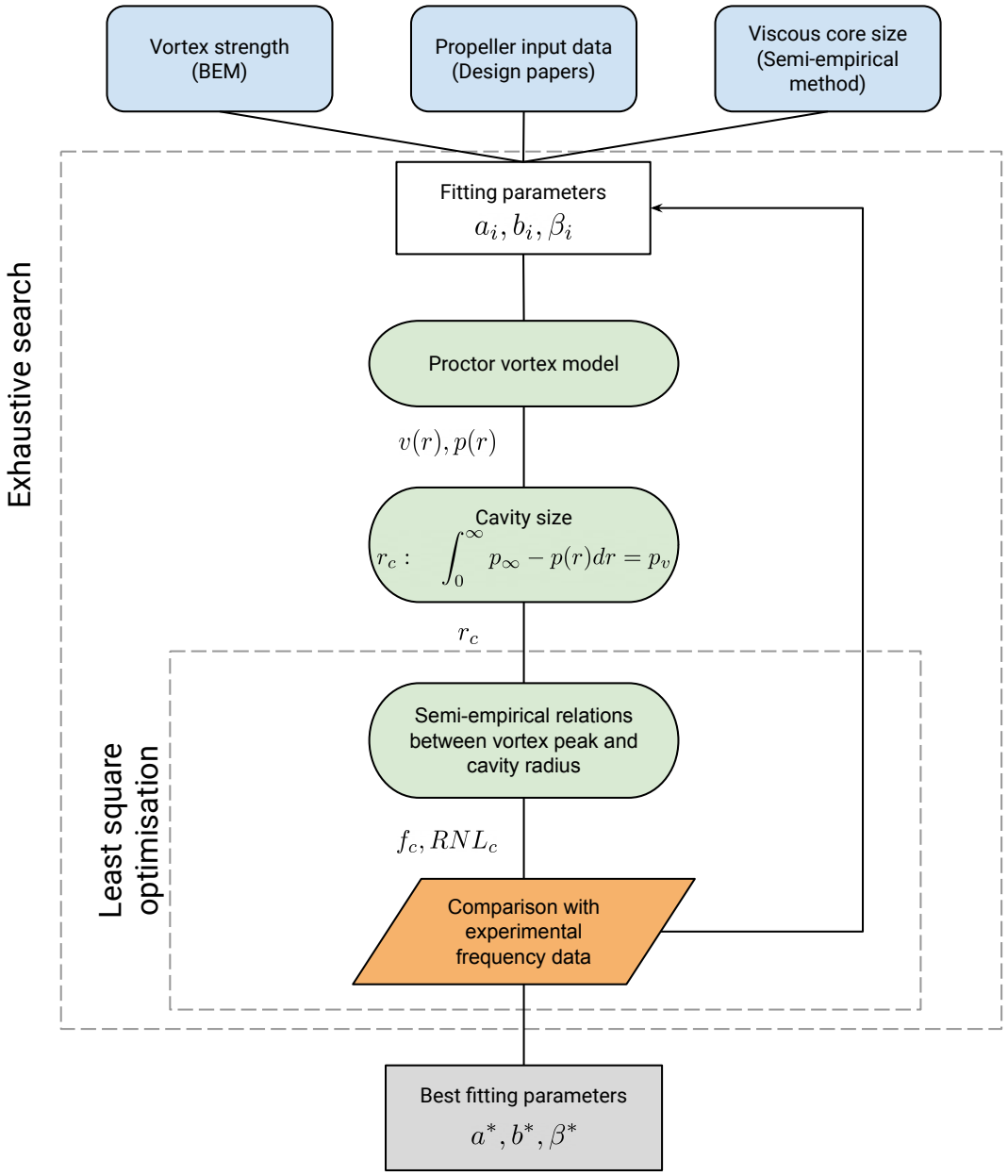

Figure 9.1: Schema of the tuning algorithm for the prediction of the vortex peak.

As discussed in Sections 7.4 and 7.5, alternative formulations for the noise peak

prediction can be used. These models are reported for the sake of comparison with the r_c-model that will be employed in the HMs.

One of the proposed models is the so called Γ-model:

$$\frac{f_c}{nZ} = c_3 \frac{\sigma_n n D^2}{Z \Gamma_{tip}} + c_4 \,, \tag{9.5}$$

$$\mathrm{RNL_c} = b_p + 20 \log_{10} \left[\left(\frac{\Gamma_{tip}}{2\pi \sqrt{\sigma_n} n D^2} \right)^k \sqrt{Z} \right]. \tag{7.42 revisited}$$

c_3, c_4, b_p, and k are tuning factors, fitted on the available experimental values. A possible alternative is represented by the τ-model, already used in Chapter 8:

$$\frac{f_c}{nZ} = c_5 \frac{\sigma_n}{K_T} + c_6 \,, \tag{9.6}$$

$$\mathrm{RNL_c} = c_p + 20 \log_{10} \left[\left(\frac{\tau K_T}{Z \sqrt{\sigma_n}} \right)^k \sqrt{Z} \right]. \tag{7.41 revisited}$$

c_5, c_6, c_p, and k are tuning factors, fitted on the experimental dataset.

Differently from the r_c-model, these last two formulations do not need expressly the cavity radius, hence no tuning is needed.

A review of the tuning procedure of the vortex model, and the comparison among the different noise models, is presented in Sub subsection 9.2.1.1.

9.2.1.1 Parameters estimation for the vortex noise models

In the tuning phase the samples that divert from the behaviour shaped by the PMs have been discarded, such as unloaded or close to inception conditions; the new set is named $\mathcal{S}$ and will be exploited to tune the fitting parameters.

In Figure 9.2 on the left the predicted vortex frequencies and on the right the dB levels are shown, for the three noise models each of them tuned on $\mathcal{S}$. The mean absolute error is reported in Table 9.5: the error has been computed both for each configuration and on the whole set $\mathcal{S}$.

The most promising model for the prediction of the central frequency is the r_c-model, especially for the propeller operating behind severe wake. Instead results for P1-W2 and P3-W6 (see Figure 9.2a) tend to distribute on the scatter plot with an angle inferior than 45°. For the P3-W5 the number of samples is too small to make reliable considerations about it. The other two models are generally less accurate to shape the behaviour of such different configurations.

Lastly, the prediction of the vortex noise levels is more challenging, as previously seen in the previous Approach 1, given that the $\mathcal{S}$ comprises mostly WPs where TVC and S.S. sheet cavitation coexist; hence the measured levels can be due to the combination of both phenomena.

To improve accuracy, at least for the f_c prediction, the set is splitted in two subsets: the first one contains only the propellers operating in strong wake ($\mathcal{S}_1$) and the second the configurations characterised by weaker wake fields ($\mathcal{S}_2$). In the first group fall the wakes, as W1-W3-W4, for which the minimum $(1 - w) < 0.9$, in the second group the remaining wakes W2-W5-W6 for which the minimum $(1 - w) > 0.9$.

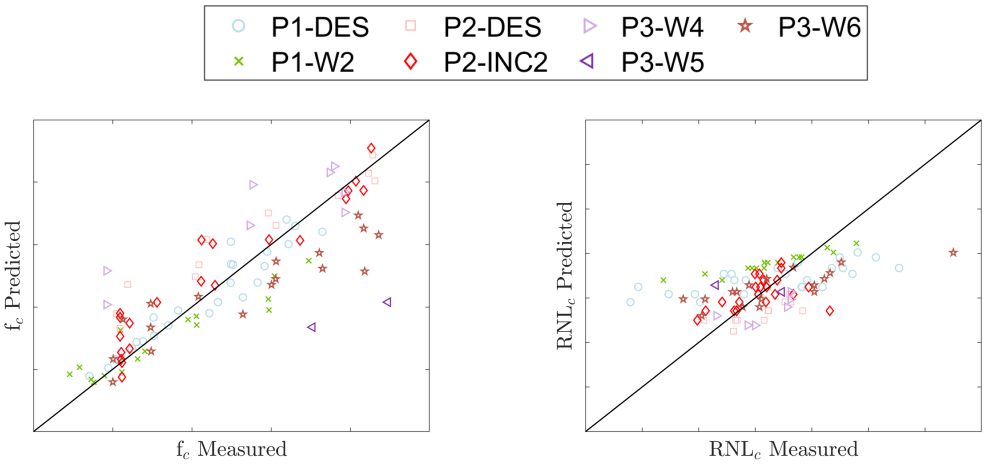

(a) r_c-model.

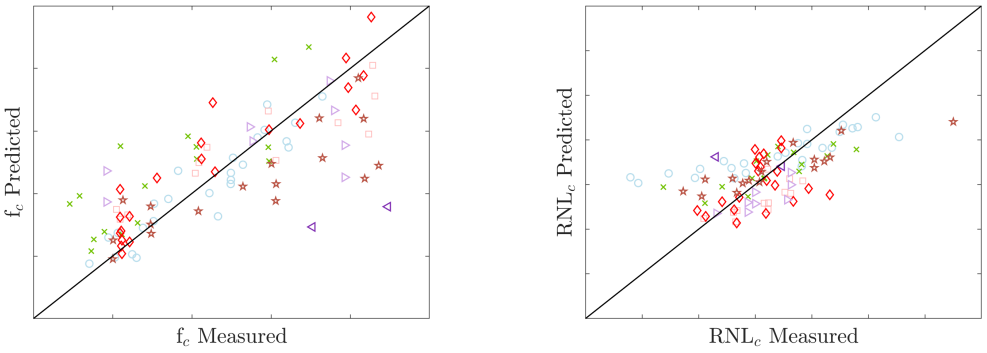

(b) Γ-model.

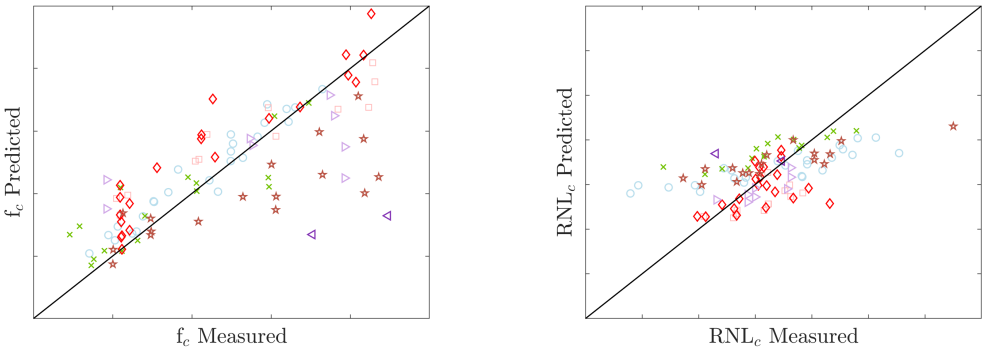

(c) τ-model.

Figure 9.2: Scatter plots of the measured and predicted values of f_c and $\mathrm{RNL_c}$ for different noise models, set sample $\mathcal{S}$.

Following this approach, the predictive performances of the new r_c-model improve as confirmed by the scatter plots Figures 9.3 and 9.4 and by the error collected in Tables 9.6 and 9.7, for $\mathcal{S}_1$ and $\mathcal{S}_2$ respectively.

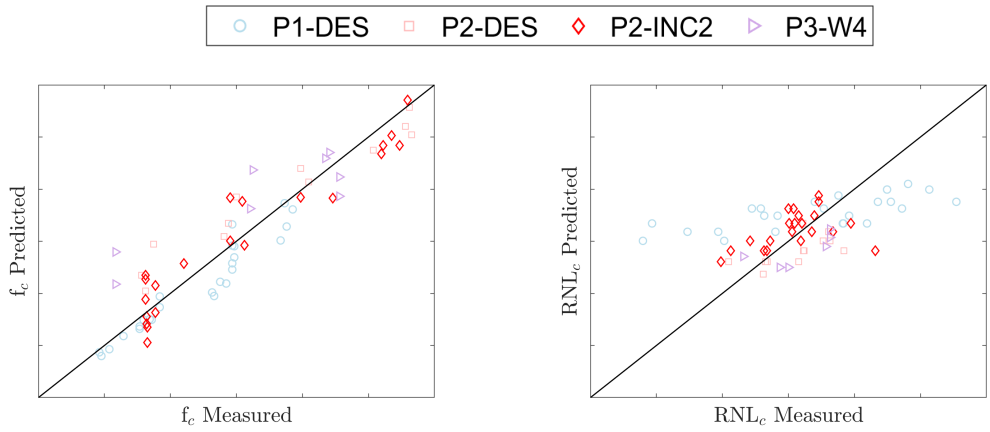

(a) r_c-model.

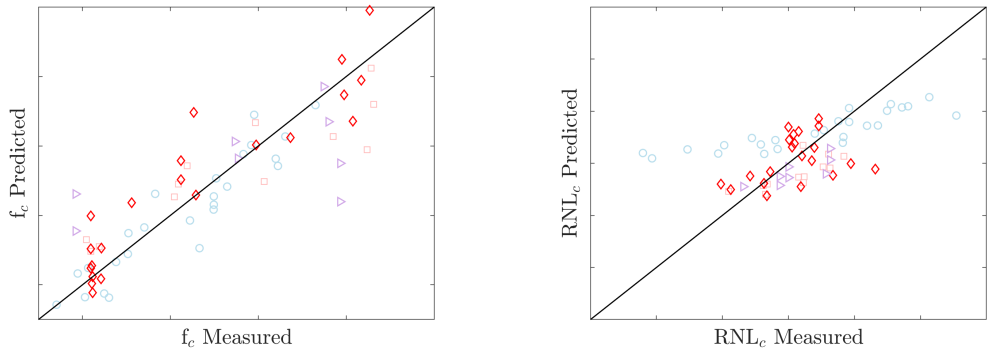

(b) Γ-model.

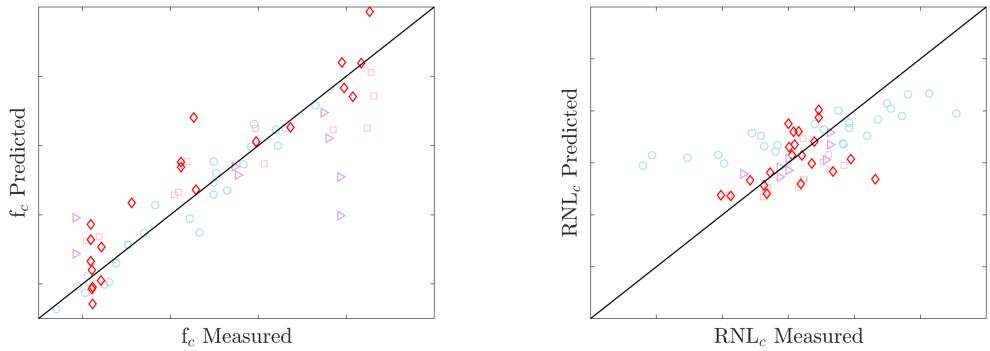

(c) τ-model.

Figure 9.3: Scatter plots of the measured and predicted values of f_c and $\mathrm{RNL_c}$ for different noise models, set sample $\mathcal{S}_1$.

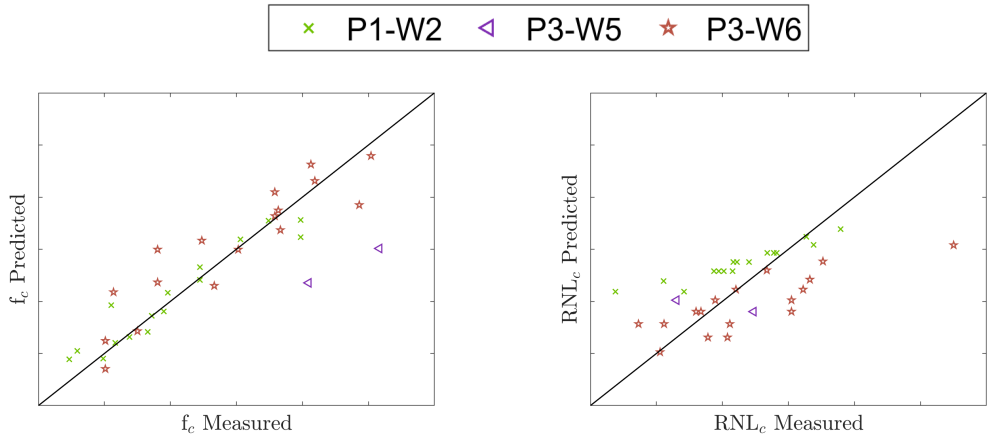

(a) r_c-model.

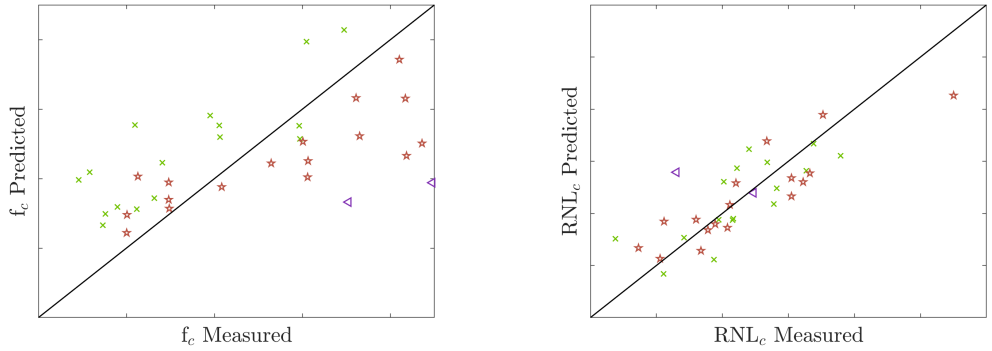

(b) Γ-model.

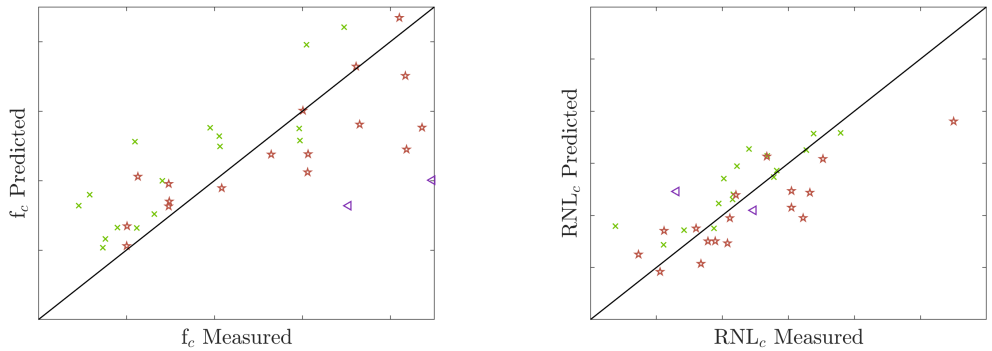

(c) τ-model.

Figure 9.4: Scatter plots of the measured and predicted values of f_c and RNL_c for different noise models, set sample $\mathcal{S}_2$.

Table 9.5: Predictive accuracy of the vortex peak for set $\mathcal{S}$ for different PMs.

	f_c - MAE [Hz]			RNL_c - MAE [dB]		
	r_c-model	Γ-model	τ-model	r_c-model	Γ-model	τ-model
P1-DES	42.3	54.0	49.4	4.5	3.7	4.0
P1-W2	81.9	156.6	80.5	3.2	2.3	3.0
P2-DES	122.4	141.2	136.2	2.4	2.5	2.7
P2-INC2	83.6	97.5	114.7	1.8	2.5	2.0
P3-W4	166.9	173.2	165.4	2.7	2.1	1.5
P3-W5	478.2	534.3	564.2	3.3	3.4	3.6
P3-W6	131.7	147.0	169.6	3.3	2.9	3.5
	100.3	124.2	117.8	3.1	2.8	3.0

Table 9.6: Predictive accuracy of the vortex peak for set $\mathcal{S}_1$ for different PMs.

	f_c - MAE [Hz]			RNL_c - MAE [dB]		
	r_c-model	Γ-model	τ-model	r_c-model	Γ-model	τ-model
P1-DES	56.3	56.5	34.6	4.5	3.9	3.9
P2-DES	96.8	131.0	112.5	2.1	2.0	2.3
P2-INC2	79.7	92.2	89.8	2.1	2.2	2.2
P3-W4	143.5	171.9	170.9	2.3	1.7	1.1
	81.7	95.4	82.8	3.0	2.8	2.7

Table 9.7: Predictive accuracy of the vortex peak for set $\mathcal{S}_2$ for different PMs.

	f_c - MAE [Hz]			RNL_c - MAE [dB]		
	r_c-model	Γ-model	τ-model	r_c-model	Γ-model	τ-model
P1-W2	50.3	173.4	134.7	2.8	2.3	1.9
P3-W5	388.9	495.0	490.3	3.5	3.9	3.8
P3-W6	86.5	150.0	118.9	3.2	2.2	2.9
	87.2	180.4	147.3	3.0	2.4	2.5

9.2.2 Broadband noise prediction

In this second approach the cavitating noise spectra, in the range 10 kHz to 80 kHz, have been predicted with the Brown's empirical formula discussed in Section 7.6 and here recalled. The cavitating area has been computed, as shown in Subsection 6.6.1, by the pressure distribution obtained by non-cavitating BEM computations. Such approach, neglecting the real development of the cavity, probably results in under-estimated predictions of the cavity areas.

$$L = K + \alpha \left[10\, log_{10}(Z D^4 n^3 f^{-1}) + 10\, log_{10}\Big(\frac{A_C}{A_D}\Big) \right]. \qquad \text{(7.45 revisited)}$$

In the formula, the constant K is the only unknown parameter, since $\alpha = 1$, and it has been found by fitting in least square sense, to the experimental radiated noise levels and source levels, respectively.

It is not surprising to find that K is the same value both for the RNL and the SL: in this facility, at higher frequencies, the effects of the confined environment are weaker and the propagation loss can be approximated with the spherical spreading (see Figures 5.15, 5.16, and 5.17).

The analysis of the predictive performances of this method are reported in Sub subsection 9.2.2.1.

9.2.2.1 Preliminary results for the broadband noise model

A better insight on the accuracy of this prediction method is reported in the following figures.

In Figure 9.5 the MAE, calculated for each configuration, is reported as a stacked bar graph for every RNL one-third octave band considered. The MAE seems less influenced by the frequency and more by the configuration, and as expected the propeller working in a strongly decelerated wake are better predicted. From Figure 9.6

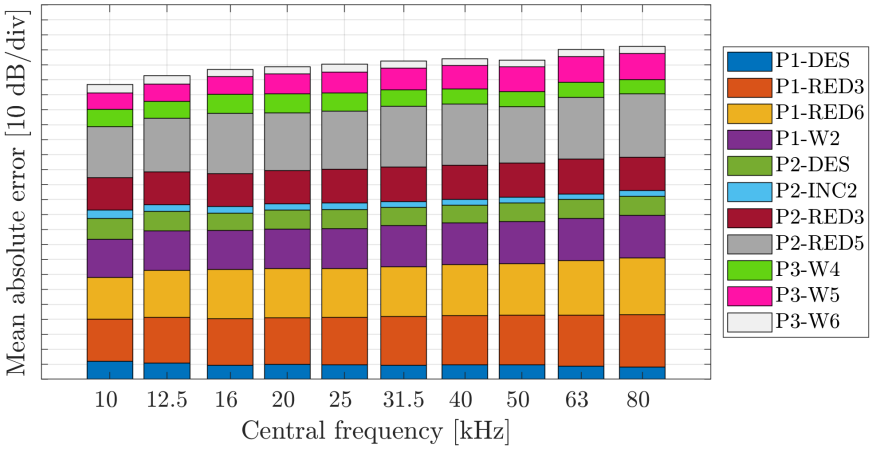

Figure 9.5: RNL, Brown prediction method, MAE [dB] computed for each configuration.

to Figure 9.8 the scatter plots of predicted versus experimental values are plotted, for the radiated noise levels at 80 kHz. The noise of P1 (Figure 9.6) is generally overestimated, this is reasonably due to a combination of underestimation of the cavitating area and in the power decay exploited in the prediction formula. Con-

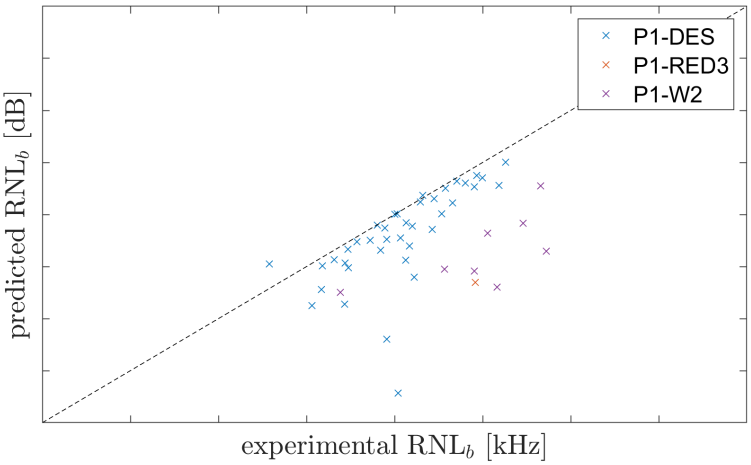

Figure 9.6: Propeller P1, RNL at 80 kHz predicted vs measured.

versely, the incremented pitch of P2 is well approximated (Figure 9.7), but again if reduced pitch configurations are considered, the performances are deteriorated. The cavitation noise of P3 seems to be better described (Figure 9.8) as confirmed by the

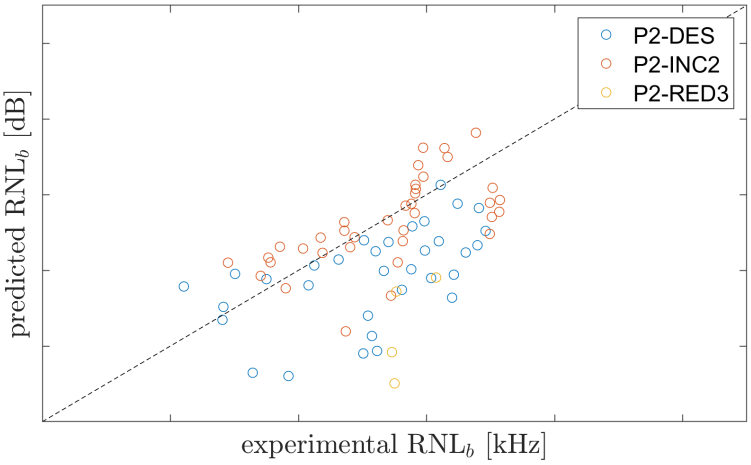

Figure 9.7: Propeller P2, RNL at 80 kHz predicted vs measured.

overall increased accuracy in the prediction, apart from the P3-W5 that, as said, is composed by a limited number of samples. Reasonably, the underrated cavitation

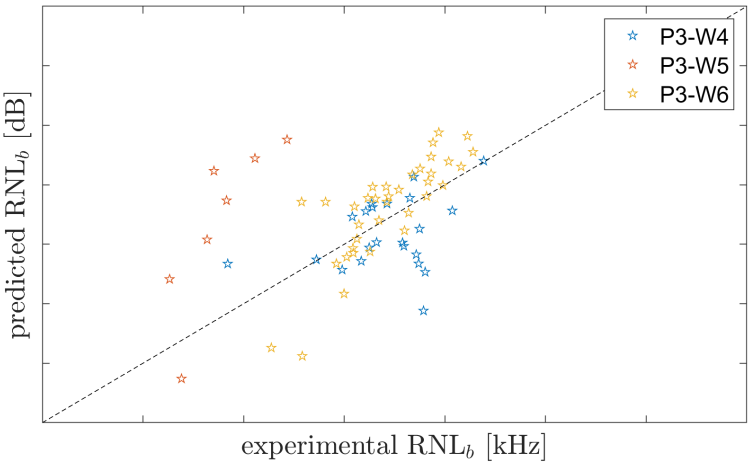

Figure 9.8: Propeller P3, RNL at 80 kHz predicted vs measured.

extent is one of the source of error. Besides, the power decay suggested by Brown for noise prediction purposes is f^{-1}; in the current dataset the decay at higher frequency is mostly comprised between f^{-2} and f^{-1} (see Figure 9.9). Usually it gets lower in magnitude when the cavitation is fully developed, indeed the propeller P3-W6 is really well predicted because its decay is centred around f^{-1}.

Detailed plots for the SL prediction are not reported, being almost identical to those already presented: the same considerations apply also in this case.

9.3 Results and discussions

In this section, the performances of the PMs, DDMs, and HMs (Sections 9.2, A.1, and A.2) will be tested and compared in two different scenarios, analogously to

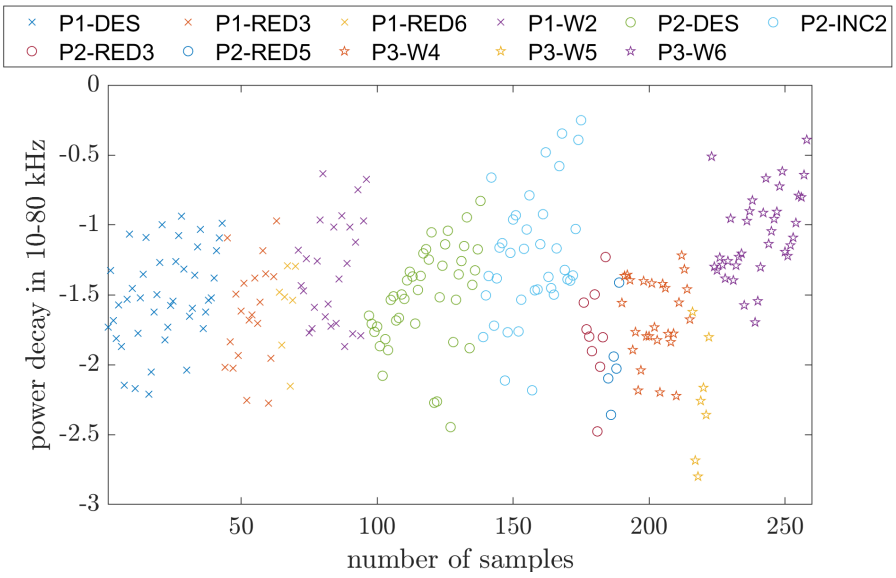

Figure 9.9: Spectrum frequency power decay (10 kHz to 80 kHz).

what has been done in Chapter 8 and following the theoretical considerations of Subsection 2.3.1.

As a reminder, the two modelisation scenarios are:

- interpolation scenario: in this case models try to predict the propeller noise spectra in various, but different, working conditions within those exploited for building the model; these tests are useful to check the capability of the model to provide predictions starting from the knowledge of the characteristics and the cavitating behaviour of the propeller;
- extrapolation scenario: in this scenario models try to predict the propeller noise spectra in groups of working conditions where the cavitation extent is very different with respect to those exploited for building the model (see Figure 8.5), these tests are useful to check the capability of the models to predict the noise related to cavitation patterns which cannot be reproduced at model scale due to viscous scale effects.

Basically the two scenarios just differ in the way training set $\mathcal{D}_n$ and test set $\mathcal{T}_m$ have been built for DMMs and the HMs training and testing.

The interpolation case is the simplest one. In this scenario $\mathcal{D}_n$ and $\mathcal{T}_m$ have been created by splitting randomly all the samples of the datasets described in Section 9.1 keeping 90% of the data in $\mathcal{D}_n$ and the remaining 10% in $\mathcal{T}_m$. In this way the models have been tested in their ability to predict the propeller noise spectra main characteristics in various, but different, working conditions within those exploited for building the model.

The extrapolation scenario tests the capability of the models to predict radiated noise for cases not included in the variable domain of the data used to build them. In order to obtain an indication of the extrapolation performance, samples of only five of the six groups of different operational conditions are included in $\mathcal{D}_n$ and use the sixth group as $\mathcal{T}_m$.

All the tests have been repeated 30 times and the average results are reported, together with their t-student 95% confidence interval, in order to ensure the statistical consistency of the results. The aforementioned subdivisions between training

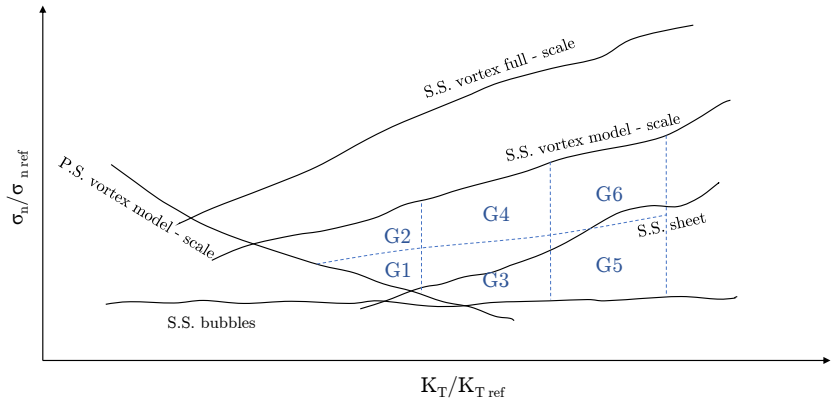

Figure 8.5: Sketch of data domain subdivision for extrapolation tests (repeated from page 119).

and test set have not been made for the PMs: the vortex peak models parameters have been found by fitting on selected working points as explained in Sub subsection 9.2.1.1, instead the parameter of the Brown's model for the broad band spectrum has been found by fitting in the whole dataset as presented in Sub subsection 9.2.2.1.

In the following, the main aspects and the most relevant comparisons of the models results are presented and discussed, in detail:

1. CDDMs vs ADDMs
2. PMs vs CDDMs vs HMs
3. The effect of Using the different FSs on the ADDMs and the HMs
4. The effect of Using different NSPs
5. The best PMs, ADDMs, and HMs
6. Interpolation vs extrapolation

9.3.1 CDDMs vs ADDMs

In order to compare the CDDMs and the ADDMs proposed in this work, the errors measured with the MAPE have first reported in Table 9.8, in the interpolation and extrapolation scenarios with different FSs and for the different NSPs. The CDDMs show comparable performances to ADDMs only when the FS1 is considered alone, hence when the cardinality of the FS is not too high with respect to the number of samples (see Section A.1). If multidimensional features are considered, the error for CDDMs is at least doubled with respect to ADDMs. Conversely, the minimum prediction error is obtained, for the ADDMs, when all the features are considered. Observed errors are lower than 5% in the interpolation scenario, and lower than 9% in the extrapolation scenario.

In summary, this suggests that only by using the ADDMs it is possible to improve the performance of the model exploiting more rich and complex features. On

the other hand it must be noted that the errors obtained with the CDDMs and the simplest feature set FS1 are only few percentages higher than the minimum errors obtained with the ADDMs. This comment highlights the fact that, within the tested scenarios, the improvements achieved exploiting the ADDMs with more complete and physically meaningful features are significant, but not outstanding. Nevertheless, the general performances of the models are definitely satisfactory.

		NSP1		NSP2		NSP3		NSP4		NSP5	
	FS	CDDM	ADDM	CDDM	ADDM	CDDM	ADDM	CDDM	ADDM	CDDM	ADDM
Interpolation	1	4.2±0.2	4.4±0.3	5.5±0.3	5.5±0.3	6.4±0.3	6.4±0.3	4.5±0.2	4.5±0.2	4.5±0.3	4.5±0.3
	1,2	9.0±0.3	3.5±0.2	10.4±0.3	4.6±0.3	11.2±0.3	5.5±0.3	8.3±0.3	3.8±0.2	8.8±0.3	3.7±0.2
	1,3	8.9±0.3	3.3±0.2	10.6±0.3	4.7±0.3	11.3±0.3	5.5±0.3	8.3±0.3	3.8±0.2	8.8±0.3	3.7±0.2
	1,4	12.1±0.3	3.5±0.2	13.5±0.3	4.6±0.3	14.3±0.3	5.6±0.3	10.5±0.3	3.9±0.2	11.4±0.3	3.7±0.2
	1,5	7.3±0.3	3.7±0.2	8.5±0.3	4.8±0.3	9.5±0.3	5.5±0.3	6.8±0.3	3.8±0.2	7.0±0.3	3.7±0.2
	All	14.8±0.3	**2.8±0.2**	16.4±0.3	**3.9±0.2**	17.4±0.3	**4.7±0.3**	12.8±0.3	**3.2±0.2**	14.0±0.3	**3.0±0.2**
Extrapolation	1	8.0±0.3	8.0±0.3	9.3±0.3	9.5±0.3	10.6±0.3	10.3±0.3	7.5±0.3	7.5±0.3	7.9±0.3	7.9±0.3
	1,2	13.0±0.3	6.9±0.3	14.5±0.3	8.4±0.3	15.3±0.3	9.4±0.3	11.2±0.3	6.8±0.3	12.2±0.3	7.0±0.3
	1,3	12.9±0.3	7.1±0.3	14.5±0.3	8.5±0.3	15.3±0.3	9.4±0.3	11.3±0.3	6.7±0.2	12.2±0.3	7.0±0.3
	1,4	16.1±0.3	7.2±0.3	17.4±0.3	8.5±0.3	18.4±0.3	9.3±0.3	13.5±0.3	6.8±0.2	14.8±0.3	7.0±0.3
	1,5	10.9±0.3	6.9±0.3	12.5±0.3	8.5±0.3	13.4±0.3	9.2±0.3	9.8±0.3	6.8±0.3	10.5±0.3	7.0±0.3
	All	19.0±0.3	**6.0±0.3**	20.4±0.3	**7.4±0.3**	21.4±0.3	**8.3±0.3**	15.8±0.3	**6.1±0.2**	17.5±0.4	**6.1±0.3**

Table 9.8: Comparison between CDDMs and the proposed ADDMs. Table reports the errors measured with the MAPE in the interpolation and extrapolation scenarios with different FSs for the different NSPs.

9.3.2 PMs vs ADDMs vs HMs

In order to compare the PMs, ADDMs, and HMs Table 9.9 reports the errors measured with the MAPE in the interpolation and extrapolation scenarios with different FSs and for the different NSPs. Note that the PMs are only able to fully predict the NSP1 and they always exploit only the feature set FS0. Instead, since the PM is able to predict part of the NSP2-NSP3 (the vortex peak), and of NSP4-NSP5 (the dB levels in 10 kHz to 80 kHz) it is possible to build the HMs also for those NSPs.

The PMs performances are always rather poor, as expected. The HMs generally allow improving the performance of the ADDMs. This improvement is larger when all the features are considered and, in particular, in the extrapolation scenario, where the MAPE for the HMs is about 2% lower than the ADDMs. This result agrees with the higher capabilities of HMs to generalise, thanks to the information included in the PMs.

9.3.3 The effect of using the different FSs on the ADDMs and the HMs

As commented in the relevant subsection, the CDDMs are not able to exploit the detailed information included in multidimensional features, whose presence results instead in a deterioration of the performances of the models. The worst performances for the CDDMs are attained for FS1+FS4 (FS4 is the single feature with the higher cardinality) and for FSAll.

The lowest error for the CDDMs, when multidimensional features are considered, is in the case FS1,5 probably because FS5 is (the blade circulation) the smallest

		NSP1			NSP2		NSP3		NSP4		NSP5	
	FS	PM	DDM	HM	DDM	HM	DDM	HM	DDM	HM	DDM	HM
Interpolation	1	11.6±1.0	4.4±0.3	4.3±0.3	5.5±0.3	5.6±0.3	6.4±0.3	6.3±0.3	4.5±0.2	4.5±0.2	4.5±0.3	4.5±0.3
	1,2		3.5±0.2	2.8±0.2	4.6±0.3	3.9±0.3	5.5±0.3	4.7±0.3	3.8±0.2	3.2±0.2	3.7±0.2	3.0±0.2
	1,3		3.3±0.2	2.8±0.2	4.7±0.3	3.9±0.3	5.5±0.3	4.7±0.3	3.8±0.2	3.2±0.2	3.7±0.2	3.0±0.2
	1,4		3.5±0.2	2.9±0.2	4.6±0.3	3.9±0.2	5.6±0.3	4.7±0.3	3.9±0.2	3.2±0.2	3.7±0.2	3.1±0.2
	1,5		3.7±0.2	2.8±0.2	4.8±0.3	3.9±0.2	5.5±0.3	4.8±0.3	3.8±0.2	3.2±0.2	3.7±0.2	3.1±0.2
	All		2.8±0.2	**2.4±0.2**	3.9±0.2	**2.7±0.2**	4.7±0.3	**3.4±0.2**	3.2±0.2	**2.2±0.2**	3.0±0.2	**2.3±0.2**
Extrapolation	1	12.1±1.1	8.0±0.3	8.0±0.3	9.5±0.3	9.4±0.3	10.3±0.3	10.4±0.3	7.5±0.3	7.5±0.3	7.9±0.3	7.9±0.3
	1,2		6.9±0.3	6.1±0.3	8.4±0.3	7.3±0.3	9.4±0.3	8.2±0.3	6.8±0.3	6.0±0.2	7.0±0.3	6.2±0.3
	1,3		7.1±0.3	5.8±0.3	8.5±0.3	7.6±0.3	9.4±0.3	8.5±0.3	6.7±0.2	6.0±0.2	7.0±0.3	6.2±0.3
	1,4		7.2±0.3	6.0±0.3	8.5±0.3	7.5±0.3	9.3±0.3	8.5±0.3	6.8±0.2	6.0±0.2	7.0±0.3	6.1±0.3
	1,5		6.9±0.3	5.8±0.3	8.5±0.3	7.4±0.3	9.2±0.3	8.3±0.3	6.8±0.3	6.0±0.2	7.0±0.3	6.1±0.3
	All		6.0±0.3	**4.3±0.3**	7.4±0.3	**5.6±0.3**	8.3±0.3	**6.4±0.3**	6.1±0.2	**4.6±0.2**	6.1±0.3	**4.5±0.3**

Table 9.9: Comparison between PMs, DDMs, and HMs. Table reports the errors measured with the MAPE in the interpolation and extrapolation scenarios with different FSs for the different NSPs.

among the multidimensional features. Hence, the increased error in CDDMs can be attributed to lack in the management of multidimensional inputs.

On the other hand, the ADDMs seem able to exploit these multidimensional inputs. When one multidimensional feature (FS2, FS3, FS4, FS5) is added to FS1, results are generally improved. Surprisingly, the effects of the different multidimensional features are all rather similar, preventing to rank these features based on their importance. The best performances are achieved with the ADDMs, when all the possible features are considered. However, the improvement with respect to the use of one single multidimensional feature added to FS1 is modest.

The same patterns are reflected in the HMs (Table 9.9). Nevertheless, the HMs seem to be even less influenced by the different combinations of FS1 and multidimensional features. If all the features are considered, the HMs show the best performances among all the considered models.

9.3.4 The effect of using different NSPs

Ranking the different target definitions based on the models performances in predicting them, the same order is obtained for CDDMs, ADDMs, and HMs. In particular, going from the best case to the worst, the order is: NSP1, NSP4 and 5 (similar outcome), NSP2 and lastly NSP3. However, the differences in performances are rather small, hence the proposed spectrum simplification is suitable to be used in place of the one-third octave bands.

The lowest error observed for NSP1 was reasonably expected. Actually, this target has a strong physical meaning and usually shows clear trends among the dataset. Most important, NSP1 is composed by a single point instead of a complete spectrum, therefore comparing it with the other target definitions may be questionable. Less trivial was the good performances observed in the prediction of the whole one-third octave spectrum (NSP4 and 5). This result is remarkable because the one-third octave spectra are a representation of the noise recognised in acoustic field. Moreover, its definition is easier than the simplified spectrum, being less prone to human error or susceptible to outliers. Therefore its use may simplify the dataset building phase. Some remarkable examples of the predicted spectra are given in Figure 9.11, for the NSP4 target in the interpolation scenario. As for previous Figure 8.3, it has to be remarked that these are only two examples obtained from one of the several compu-

tational iterations performed during the model selection phase, which are reported here in order to discuss the outcomes of the present approach. For what regards the overall quality of the model, the representative indexes are those reported in Table 9.9. It is clear, in this case, that the approach proposed in this section allows to eliminate some of the issues faced in the first attempt; in particular, the shape of the spectrum intrinsically is well predicted, without the presence of spurious points, as in the previous Figure 8.3b.

(a) P1-DES, low-loading condition, $\sigma_n = 2.5$.

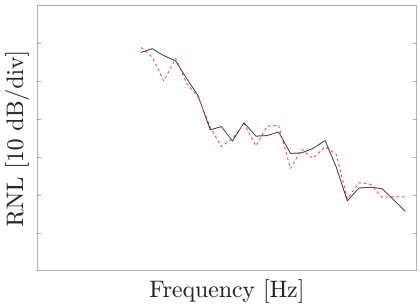

(b) P3-W4, high-loading condition, $\sigma_n = 3$.

Figure 9.11: Interpolation Scenario HM: NSP4 spectrum target (solid black) and predicted (dashed red) for different WPs.

Hence, a ML tool able to reproduce accurately both the NSP4, NSP5 and the center peak (NSP1) represents an optimal solution for the task at hand. The two alternative versions of simplified spectrum NSP2 and NSP3 are afflicted by the same problems pointed out in Sub subsection 8.5.1.2. The use of spectral slopes in NSP3 was an attempt to overcome the issues related to the complex trends featured by the breakpoints. These results demonstrate that this modification to description of the simplified spectrum does not provide any further improvements of the model capabilities. Actually, the errors for NSP3 are slightly larger than for NSP2, yet the accuracy is acceptable.

9.3.5 The best PMs, ADDMs, and HMs

In order to better detail the quality of the best PMs, ADDMs, and HMs in predicting the different parameters of the different NSPs, the errors measured with the MAE, MAPE, and PPMCC in the interpolation and extrapolation scenarios, with the best FS according to Table 9.9 are reported in Tables 9.10 - 9.14. The word "best" is used to intend the model which produces the best accuracy, or lower error, between the ones which uses different FSs according to Table 9.9. The vortex peak (frequency and level) is present in NSP1, NSP2 and NSP3 and it is reported in Tables 9.10-9.12, in terms of MAE, MAPE and PPMCC. The best interpolation MAE for f_c is below 60 Hz and for RNL_c it is lower than 1 dB, both for DDMs and HMs. In extrapolation the accuracy slightly decreases but it is still remarkable. In Figure 9.12 the comparison reported shows the PM, and the best ADDM and HM predicting the NSP1, for the interpolation scenario. Looking more in detail, it can be noticed that the ADD/HMs are able to predict cases in which the PM fails, i.e. when FS0 is not sufficient to characterise the samples. In the extrapolation (Figure 9.13) the

			FS*	f_c	RNL_c
MAE	Int.	PM	-	202.0±21.5	4.6±0.3
		DDM	all	57.2±4.1	1.0±0.1
		HM	all	**48.4±3.8**	**0.8±0.1**
	Ext.	PM	-	206.2±21.4	4.9±0.4
		DDM	all	122.6±5.5	2.1±0.1
		HM	all	**84.7±5.4**	**1.5±0.1**
MAPE	Int.	PM	-	9.9±1.1	13.2±1.0
		DDM	all	2.8±0.2	2.9±0.2
		HM	all	**2.4±0.2**	**2.4±0.2**
	Ext.	PM	-	10.1±1.0	14.1±1.1
		DDM	all	6.0±0.3	5.9±0.3
		HM	all	**4.1±0.3**	**4.4±0.3**
PPMCC	Int.	PM	-	0.76±0.01	0.52±0.02
		DDM	all	**0.99±0.01**	**0.99±0.01**
		HM	all	**0.99±0.01**	**0.99±0.01**
	Ext.	PM	-	0.76±0.01	0.39±0.12
		DDM	all	**0.99±0.01**	**0.99±0.01**
		HM	all	**0.99±0.01**	**0.99±0.01**

Table 9.10: Comparison between the best PM, DDM, and HM in predicting the different parameters of NSP1 according to Table 9.9. Table reports the errors measured with the MAE, MAPE, and PPMCC in the interpolation and extrapolation scenarios with the best FS.

samples are more scattered, hence the accuracy is lower but it is still satisfactory. In both cases, some outliers are visible in the ADDMs and HMs: these samples should be investigated and properly treated, e.g. adjusting the position of the peak or removing them from the dataset.

The spectrum level at 100kHz (RNL_b) is present in NSP2 and NSP3 (Tables 9.11-9.12). As reported, the MAE is less than 1 dB both in interpolation and extrapolation. Similar to the vortex peak, the last frequency noise level is easy to be predicted because its value changes rather smoothly according to the working points, hence the current features are able to fully characterise its behaviour. The NPS2 is the

			FS	f_c	RNL_c	RNL_b	f_{bp1}	f_{bp2}	RNL_{bp1}	RNL_{bp2}
MAE	Int.	PM	-	202.0±21.5	4.6±0.3	14.3±1.5	-	-	-	-
		DDM	all	58.7±4.3	1.0±0.1	1.6±0.1	39.3±2.4	2757.9±182.1	1.4±0.1	2.4±0.1
		HM	all	**48.9±3.9**	**0.8±0.1**	**1.0±0.1**	**27.6±2.0**	**2067.0±146.6**	**0.9±0.1**	**1.5±0.1**
	Ext.	PM	-	206.2±21.4	4.9±0.4	14.3±1.5	-	-	-	-
		DDM	all	128.3±5.9	2.0±0.1	2.9±0.1	73.1±2.7	5588.0±208.8	2.6±0.1	4.3±0.1
		HM	all	**86.6±5.6**	**1.5±0.1**	**2.3±0.1**	**55.6±2.8**	**4339.5±209.8**	**1.9±0.1**	**3.3±0.1**
MAPE	Int.	PM	-	9.9±1.1	13.2±1.0	38.5±4.0	-	-	-	-
		DDM	all	2.9±0.2	2.8±0.2	4.3±0.3	4.2±0.3	3.9±0.3	4.4±0.3	4.4±0.3
		HM	all	**2.4±0.2**	**2.3±0.2**	**2.7±0.2**	**3.0±0.2**	**3.0±0.2**	**2.9±0.2**	**2.8±0.2**
	Ext.	PM	-	10.1±1.0	14.1±1.1	38.5±4.0	-	-	-	-
		DDM	all	6.3±0.3	5.8±0.3	7.8±0.3	7.9±0.3	8.0±0.3	8.1±0.3	8.0±0.3
		HM	all	**4.2±0.3**	**4.4±0.3**	**6.2±0.3**	**6.0±0.3**	**6.2±0.3**	**6.0±0.3**	**6.0±0.3**
PPMCC	Int.	PM	-	0.76±0.02	0.52±0.02	0.12±0.02	-	-	-	-
		DDM	all	0.99±0.01	0.99±0.01	0.99±0.01	0.99±0.01	0.98±0.01	0.99±0.01	0.98±0.01
		HM	all	0.99±0.01	0.99±0.01	0.99±0.01	0.99±0.01	0.98±0.01	0.99±0.01	0.98±0.01
	Ext.	PM	-	0.76±0.01	0.39±0.06	0.12±0.05	-	-	-	-
		DDM	all	0.99±0.01	0.99±0.01	0.99±0.01	0.99±0.01	0.98±0.01	0.99±0.01	0.98±0.01
		HM	all	0.99±0.01	0.99±0.01	0.99±0.01	0.99±0.01	0.98±0.01	0.99±0.01	0.98±0.01

Table 9.11: Comparison between the best PM, DDM, and HM in predicting the different parameters of NSP2 according to Table 9.9. Table reports the errors measured with the MAE, MAPE, and PPMCC in the interpolation and extrapolation scenarios with the best FS.

best predicted spectrum simplification if it is considered as a whole (Table 9.9).

A detailed view of the estimation error is reported in Table 9.11 for each target composing NSP2.

In the prediction of the breakpoints frequencies and level, the MAPE is almost identical between BP1 and BP2, both for interpolation and extrapolation. This observation is misleading because the MAPE is a percentage hence the errors are weighted the same regardless of their absolute value. Indeed, the best MAPE for f_{bp1} and for f_{bp2} is 3.0 (HM, interpolation), but the correspondent MAE are 27.6 Hz and 2067 Hz. Therefore, f_{bp2} still suffer from worse prediction compared to f_{bp1}, because of some outliers due to the inherent physical phenomenon (for the same considerations pointed out in Subsection 8.5.1.2). The same tendency is visible for the levels of the two breakpoints but being the decibel already a ratio, the MAE is somewhat more contained.

In order to overcome the inherent weakness in the breakpoints detection, and improve the accuracy in the simplified spectrum prediction, the slopes of the different parts composing the simplified spectrum have been considered as an alternative target. They are expressed as dB/oct, hence they represent the change in dB corresponding to a doubling in frequency In Table 9.12 the accuracy in the NSP3 prediction is reported. It is evident that γ has a MAE of one order of magnitude inferior than α and β. This can be attributed to the higher stability (with respect to the WPs) of this portion of the spectrum, and to the aforementioned ease in the detection of one of the extreme points on which it is calculated (100 kHz, RNL_b). Conversely, the two other slopes still suffer of the same problem discussed for the

			FS	f_c	RNL_c	RNL_b	α	β	γ
MAE	Int.	PM	-	202.0±21.5	4.6±0.3	14.3±1.5	-	-	-
		DDM	all	60.3±4.6	1.0±0.1	1.6±0.1	2.4±0.1	3.0±0.1	0.5±0.0
		HM	all	**49.2±3.4**	**0.8±0.1**	**1.1±0.1**	**1.7±0.1**	**2.0±0.1**	**0.3±0.0**
	Ext.	PM	-	206.2±21.4	4.9±0.4	14.3±1.5	-	-	-
		DDM	all	127.2±6.0	2.1±0.1	3.0±0.1	3.9±0.1	4.7±0.1	0.8±0.0
		HM	all	**90.3±5.2**	**1.5±0.1**	**2.2±0.1**	**3.1±0.1**	**3.8±0.1**	**0.6±0.0**
MAPE	Int.	PM	-	9.9±1.1	13.2±1.0	38.5±4.0	-	-	-
		DDM	all	3.0±0.2	2.8±0.2	4.2±0.3	5.9±0.3	6.2±0.3	6.1±0.3
		HM	all	**2.4±0.2**	**2.4±0.2**	**2.9±0.2**	**4.2±0.3**	**4.3±0.3**	**4.0±0.3**
	Ext.	PM	-	10.1±1.0	14.1±1.1	38.5±4.0	-	-	-
		DDM	all	6.2±0.3	6.1±0.3	8.2±0.3	9.9±0.3	9.9±0.3	9.8±0.3
		HM	all	**4.4±0.3**	**4.2±0.3**	**5.9±0.3**	**7.7±0.3**	**8.1±0.3**	**8.0±0.3**
PPMCC	Int.	PM	-	0.76±0.03	0.52±0.01	0.12±0.07	-	-	-
		DDM	all	0.99±0.01	0.99±0.01	0.99±0.01	0.99±0.01	0.99±0.01	0.98±0.01
		HM	all	0.99±0.01	0.99±0.01	0.99±0.01	0.99±0.01	0.99±0.01	0.98±0.01
	Ext.	PM	-	0.76±0.05	0.39±0.01	0.12±0.14	-	-	-
		DDM	all	0.99±0.01	0.99±0.01	0.99±0.01	0.99±0.01	0.99±0.01	0.99±0.01
		HM	all	0.99±0.01	0.99±0.01	0.99±0.01	0.99±0.01	0.99±0.01	0.98±0.01

Table 9.12: Comparison between the best PM, DDM, and HM in predicting the different parameters of NSP3 according to Table 9.9. Table reports the errors measured with the MAE, MAPE, and PPMCC in the interpolation and extrapolation scenarios with the best.

breakpoints, even if the overall prediction accuracy is remarkable.

The NSP4 (noise corrected by means of transfer functions) and the NSP5 (noise corrected for spherical propagation) are visible in Tables 9.13 and 9.14, respectively. Each columns refer to a one-third octave band (from 1 to 24) in the range 0.4 kHz to 80 kHz for the ADD/HM, instead the PM is available only for the range 1 kHz to 80 kHz. The different levels are well predicted, both in interpolation and extrapolation, no particular trends seem to exist among the different parts of the spectrum.

	FS	$SL_{\frac{1}{3}}(1)$	$SL_{\frac{1}{3}}(2)$	$SL_{\frac{1}{3}}(3)$	$SL_{\frac{1}{3}}(4)$	$SL_{\frac{1}{3}}(5)$	$SL_{\frac{1}{3}}(6)$	$SL_{\frac{1}{3}}(7)$	$SL_{\frac{1}{3}}(8)$	$SL_{\frac{1}{3}}(9)$	$SL_{\frac{1}{3}}(10)$	$SL_{\frac{1}{3}}(11)$	$SL_{\frac{1}{3}}(12)$
MAE													
Ext.	DDM	all	1.7±0.1	1.2±0.1	1.5±0.1	1.5±0.1	1.2±0.1	1.2±0.1	1.4±0.1	1.2±0.1	1.2±0.1	1.0±0.1	1.0±0.1
	HM	all	1.1±0.1	0.8±0.1	1.0±0.1	1.0±0.1	0.9±0.1	1.0±0.1	1.0±0.1	0.8±0.1	0.9±0.1	0.6±0.1	0.7±0.1
Int.	DDM	all	3.3±0.1	2.4±0.1	2.8±0.1	2.6±0.1	2.6±0.1	2.7±0.1	2.6±0.1	2.2±0.1	2.1±0.1	2.2±0.1	1.9±0.1	1.8±0.1
	HM	all	2.4±0.1	1.7±0.1	2.1±0.1	2.1±0.1	1.8±0.1	2.0±0.1	2.0±0.1	1.6±0.1	1.6±0.1	1.7±0.1	1.4±0.1	1.4±0.1
MAPE														
Ext.	DDM	all	4.1±0.3	4.2±0.3	4.3±0.3	4.4±0.2	4.0±0.3	3.8±0.2	4.3±0.3	4.4±0.3	4.5±0.3	4.3±0.3	4.4±0.3	4.3±0.3
	HM	all	2.8±0.2	2.9±0.2	2.9±0.2	3.0±0.2	2.8±0.2	3.1±0.2	3.0±0.2	2.8±0.2	3.0±0.2	3.2±0.2	2.7±0.2	3.3±0.2
Int.	DDM	all	8.0±0.3	8.3±0.3	7.8±0.3	7.6±0.3	8.4±0.3	8.5±0.3	8.0±0.3	7.9±0.3	8.0±0.3	8.1±0.3	8.1±0.3	8.1±0.3
	HM	all	5.8±0.3	5.9±0.3	5.8±0.3	6.2±0.3	5.9±0.3	6.2±0.3	6.2±0.3	5.8±0.3	6.2±0.3	6.1±0.3	6.2±0.3	6.1±0.3
PPMCC														
Ext.	DDM	all	0.99±0.01	0.99±0.01	0.99±0.01	0.99±0.01	0.99±0.01	0.98±0.01	0.99±0.01	0.98±0.01	0.98±0.01	0.98±0.01	0.98±0.01	0.98±0.01
	HM	all	0.99±0.01	0.99±0.01	0.99±0.01	0.99±0.01	0.99±0.01	0.98±0.01	0.99±0.01	0.98±0.01	0.98±0.01	0.98±0.01	0.98±0.01	0.98±0.01
Int.	DDM	all	0.99±0.01	0.99±0.01	0.99±0.01	0.99±0.01	0.99±0.01	0.98±0.01	0.99±0.01	0.98±0.01	0.98±0.01	0.99±0.01	0.98±0.01	0.98±0.01
	HM	all	0.99±0.01	0.99±0.01	0.99±0.01	0.99±0.01	0.99±0.01	0.98±0.01	0.99±0.01	0.98±0.01	0.98±0.01	0.98±0.01	0.98±0.01	0.98±0.01

		FS	$SL_{\frac{1}{3}}(13)$	$SL_{\frac{1}{3}}(14)$	$SL_{\frac{1}{3}}(15)$	$SL_{\frac{1}{3}}(16)$	$SL_{\frac{1}{3}}(17)$	$SL_{\frac{1}{3}}(18)$	$SL_{\frac{1}{3}}(19)$	$SL_{\frac{1}{3}}(20)$	$SL_{\frac{1}{3}}(21)$	$SL_{\frac{1}{3}}(22)$	$SL_{\frac{1}{3}}(23)$	$SL_{\frac{1}{3}}(24)$
MAE														
Ext.	PM	-	-	-	14.0±1.1	14.8±0.9	14.1±1.1	13.8±1.3	14.7±1.3	14.1±1.4	15.0±1.2	14.2±1.5	14.6±1.5	14.9±1.5
	DDM	all	1.1±0.1	0.9±0.1	1.1±0.1	1.2±0.1	1.6±0.1	1.7±0.1	1.3±0.1	1.3±0.1	1.5±0.1	1.3±0.1	1.4±0.1	1.7±0.1
	HM	all	0.7±0.1	0.7±0.0	0.7±0.1	0.9±0.1	1.1±0.1	0.9±0.1	0.9±0.1	1.0±0.1	1.0±0.1	0.9±0.1	1.0±0.1	1.0±0.1
Int.	PM	-	-	-	14.0±1.1	14.8±0.9	14.1±1.1	13.8±1.3	14.7±1.3	14.1±1.4	15.0±1.2	14.2±1.5	14.6±1.5	14.9±1.5
	DDM	all	2.0±0.1	1.8±0.1	2.1±0.1	2.3±0.1	3.0±0.1	3.2±0.1	2.5±0.1	2.5±0.1	3.0±0.1	2.5±0.1	2.7±0.1	2.8±0.1
	HM	all	1.5±0.1	1.3±0.1	1.6±0.1	1.7±0.1	2.3±0.1	2.4±0.1	1.9±0.1	1.9±0.1	2.3±0.1	2.0±0.1	2.0±0.1	2.0±0.1
MAPE														
Ext.	PM	-	-	-	56.7±4.3	51.5±3.2	37.7±3.0	36.0±3.4	46.8±4.3	45.3±4.5	41.4±3.3	45.6±4.7	44.5±4.6	41.9±4.4
	DDM	all	4.2±0.2	4.1±0.3	4.3±0.3	4.3±0.3	4.2±0.3	4.3±0.2	4.3±0.2	4.1±0.2	4.3±0.3	4.3±0.3	4.3±0.3	4.7±0.3
	HM	all	2.9±0.2	3.1±0.2	2.8±0.2	3.1±0.2	2.9±0.2	2.8±0.2	2.8±0.2	3.0±0.2	2.9±0.2	2.7±0.2	3.0±0.2	2.8±0.2
Int.	PM	-	-	-	56.7±4.3	51.5±3.2	37.7±3.0	36.0±3.4	46.8±4.3	45.3±4.5	41.4±3.3	45.6±4.7	44.5±4.6	41.9±4.4
	DDM	all	7.8±0.3	8.0±0.3	8.4±0.3	8.1±0.3	8.0±0.3	8.3±0.3	8.0±0.3	8.1±0.3	8.3±0.3	8.0±0.3	8.3±0.3	8.0±0.3
	HM	all	5.9±0.3	6.0±0.3	6.3±0.3	6.0±0.3	6.2±0.3	6.4±0.3	6.0±0.3	6.1±0.3	6.4±0.3	6.4±0.3	6.1±0.3	5.7±0.3
PPMCC														
Ext.	PM	-	-	-	0.10±0.13	0.07±0.02	0.05±0.14	0.05±0.16	0.05±0.24	0.12±0.08	0.14±0.13	0.16±0.08	0.17±0.03	0.17±0.07
	DDM	all	0.99±0.01	0.98±0.01	0.99±0.01	0.99±0.01	0.99±0.01	0.99±0.01	0.99±0.01	0.99±0.01	0.99±0.01	0.99±0.01	0.99±0.01	0.99±0.01
	HM	all	0.99±0.01	0.98±0.01	0.99±0.01	0.99±0.01	0.99±0.01	0.99±0.01	0.99±0.01	0.99±0.01	0.99±0.01	0.99±0.01	0.99±0.01	0.99±0.01
Int.	PM	-	-	-	0.10±0.13	0.07±0.06	0.05±0.03	0.05±0.19	0.05±0.13	0.12±0.02	0.14±0.04	0.16±0.04	0.17±0.02	0.17±0.12
	DDM	all	0.99±0.01	0.99±0.01	0.99±0.01	0.98±0.01	0.99±0.01	0.99±0.01	0.99±0.01	0.99±0.01	0.99±0.01	0.99±0.01	0.99±0.01	0.99±0.01
	HM	all	0.99±0.01	0.99±0.01	0.99±0.01	0.99±0.01	0.99±0.01	0.99±0.01	0.99±0.01	0.99±0.01	0.99±0.01	0.99±0.01	0.99±0.01	0.99±0.01

Table 9.13: Comparison between the best PM, DDM, and HM in predicting the different parameters of NSP4 according to Table 9.9. Table reports the errors measured with the MAE, MAPE, and PPMCC in the interpolation and extrapolation scenarios with the best FS.

		FS	$RNL_{\frac{1}{3}}(1)$	$RNL_{\frac{1}{3}}(2)$	$RNL_{\frac{1}{3}}(3)$	$RNL_{\frac{1}{3}}(4)$	$RNL_{\frac{1}{3}}(5)$	$RNL_{\frac{1}{3}}(6)$	$RNL_{\frac{1}{3}}(7)$	$RNL_{\frac{1}{3}}(8)$	$RNL_{\frac{1}{3}}(9)$	$RNL_{\frac{1}{3}}(10)$	$RNL_{\frac{1}{3}}(11)$	$RNL_{\frac{1}{3}}(12)$
MAE	Int.	DDM	all	1.2±0.1	1.0±0.1	1.1±0.1	1.1±0.1	1.1±0.1	1.2±0.1	1.1±0.1	1.1±0.1	0.8±0.1	0.9±0.1	0.8±0.1	0.8±0.1
		HM	all	0.9±0.1	0.7±0.1	0.8±0.1	0.8±0.1	0.8±0.1	0.7±0.1	0.8±0.1	0.8±0.1	0.6±0.0	0.7±0.0	0.6±0.0	0.6±0.0
	Ext.	DDM	all	2.4±0.1	2.0±0.1	2.3±0.1	2.1±0.1	2.1±0.1	2.3±0.1	2.0±0.1	2.0±0.1	1.6±0.1	1.9±0.1	1.6±0.1	1.7±0.1
		HM	all	1.8±0.1	1.4±0.1	1.7±0.1	1.7±0.1	1.5±0.1	1.5±0.1	1.5±0.1	1.5±0.1	1.2±0.1	1.4±0.1	1.2±0.1	1.2±0.1
MAPE	Int.	DDM	all	3.6±0.2	3.3±0.2	3.4±0.2	3.5±0.2	3.6±0.2	3.8±0.2	3.6±0.3	3.6±0.2	3.4±0.2	3.3±0.2	3.4±0.2	3.5±0.2
		HM	all	2.6±0.2	2.6±0.2	2.6±0.2	2.7±0.2	2.5±0.2	2.4±0.2	2.7±0.2	2.6±0.2	2.6±0.2	2.6±0.2	2.6±0.2	2.7±0.2
	Ext.	DDM	all	6.9±0.3	6.9±0.3	7.2±0.3	7.0±0.3	6.9±0.3	7.4±0.3	6.6±0.3	7.0±0.3	6.8±0.3	7.0±0.3	6.9±0.3	7.3±0.3
		HM	all	5.1±0.3	4.9±0.3	5.3±0.3	5.4±0.3	5.0±0.3	4.9±0.3	5.0±0.3	5.1±0.3	5.2±0.3	5.1±0.3	5.3±0.3	5.3±0.3
PPMCC	Int.	DDM	all	0.99±0.01	0.99±0.01	0.99±0.01	0.99±0.01	0.99±0.01	0.99±0.01	0.98±0.01	0.98±0.01	0.99±0.01	0.99±0.01	0.98±0.01	0.99±0.01
		HM	all	0.99±0.01	0.99±0.01	0.99±0.01	0.99±0.01	0.99±0.01	0.99±0.01	0.98±0.01	0.98±0.01	0.99±0.01	0.98±0.01	0.98±0.01	0.98±0.01
	Ext.	DDM	all	0.99±0.01	0.99±0.01	0.99±0.01	0.99±0.01	0.99±0.01	0.99±0.01	0.98±0.01	0.98±0.01	0.99±0.01	0.99±0.01	0.99±0.01	0.99±0.01
		HM	all	0.99±0.01	0.99±0.01	0.99±0.01	0.99±0.01	0.99±0.01	0.99±0.01	0.98±0.01	0.99±0.01	0.98±0.01	0.98±0.01	0.99±0.01	0.99±0.01

		FS	$RNL_{\frac{1}{3}}(13)$	$RNL_{\frac{1}{3}}(14)$	$RNL_{\frac{1}{3}}(15)$	$RNL_{\frac{1}{3}}(16)$	$RNL_{\frac{1}{3}}(17)$	$RNL_{\frac{1}{3}}(18)$	$RNL_{\frac{1}{3}}(19)$	$RNL_{\frac{1}{3}}(20)$	$RNL_{\frac{1}{3}}(21)$	$RNL_{\frac{1}{3}}(22)$	$RNL_{\frac{1}{3}}(23)$	$RNL_{\frac{1}{3}}(24)$
MAE	Int.	PM	-	-	14.2±1.1	14.1±1.2	13.8±1.3	14.1±1.2	14.2±1.3	14.1±1.3	14.0±1.3	14.1±1.3	14.3±1.4	14.3±1.4
		DDM	all	0.8±0.1	0.7±0.0	0.8±0.1	1.0±0.1	1.2±0.1	1.1±0.1	1.2±0.1	1.1±0.1	1.2±0.1	1.1±0.1	1.2±0.1	1.2±0.1
		HM	all	0.6±0.0	0.5±0.0	0.6±0.0	0.6±0.1	1.0±0.1	1.0±0.1	0.8±0.1	0.8±0.1	0.9±0.1	1.0±0.1	0.9±0.1	0.9±0.1
	Ext.	PM	-	-	14.2±1.1	14.1±1.2	13.8±1.3	14.1±1.2	14.2±1.3	14.1±1.3	14.0±1.3	14.1±1.3	14.3±1.4	14.3±1.4
		DDM	all	1.8±0.1	1.4±0.1	1.6±0.1	2.0±0.1	2.5±0.1	2.2±0.1	2.4±0.1	2.2±0.1	2.3±0.1	2.3±0.1	2.5±0.1	2.4±0.1
		HM	all	1.3±0.1	1.0±0.1	1.2±0.1	1.5±0.1	1.8±0.1	1.8±0.1	1.7±0.1	1.8±0.1	1.7±0.1	1.7±0.1	1.8±0.1	1.8±0.1
MAPE	Int.	PM	-	-	62.4±4.8	50.7±4.3	39.4±3.6	40.6±3.6	42.7±3.8	43.3±4.0	42.7±4.1	41.6±3.9	40.4±3.9	41.2±4.1
		DDM	all	3.2±0.2	3.4±0.2	3.6±0.2	3.6±0.2	3.4±0.2	3.3±0.2	3.6±0.3	3.5±0.3	3.6±0.2	3.3±0.2	3.4±0.2	3.4±0.2
		HM	all	2.4±0.2	2.5±0.2	2.7±0.2	2.3±0.2	2.8±0.2	2.8±0.2	2.4±0.2	2.5±0.2	2.6±0.2	3.0±0.2	2.5±0.2	2.7±0.2
	Ext.	PM	-	-	62.4±4.8	50.7±4.3	39.4±3.6	40.6±3.6	42.7±3.8	43.3±4.0	42.7±4.1	41.6±3.9	40.4±3.9	41.2±4.1
		DDM	all	6.8±0.3	6.7±0.3	6.8±0.3	7.2±0.3	7.0±0.3	6.4±0.3	7.1±0.3	6.8±0.3	6.9±0.3	6.8±0.3	7.0±0.3	6.9±0.3
		HM	all	5.1±0.3	5.0±0.3	5.3±0.3	5.3±0.3	5.2±0.3	5.2±0.3	5.0±0.3	5.6±0.3	5.0±0.3	4.9±0.3	5.1±0.3	5.1±0.3
PPMCC	Int.	PM	-	-	0.14±0.02	0.15±0.04	0.08±0.07	0.10±0.12	0.08±0.07	0.09±0.11	0.11±0.02	0.10±0.22	0.11±0.04	0.13±0.08
		DDM	all	0.99±0.01	0.99±0.01	0.99±0.01	0.99±0.01	0.99±0.01	0.99±0.01	0.99±0.01	0.99±0.01	0.99±0.01	0.99±0.01	0.99±0.01	0.99±0.01
		HM	all	0.99±0.01	0.99±0.01	0.99±0.01	0.99±0.01	0.98±0.01	0.99±0.01	0.99±0.01	0.99±0.01	0.99±0.01	0.99±0.01	0.99±0.01	0.99±0.01
	Ext.	PM	-	-	0.14±0.01	0.15±0.01	0.08±0.04	0.10±0.01	0.08±0.02	0.09±0.11	0.11±0.02	0.10±0.02	0.11±0.07	0.13±0.07
		DDM	all	0.99±0.01	0.99±0.01	0.99±0.01	0.99±0.01	0.99±0.01	0.99±0.01	0.99±0.01	0.99±0.01	0.99±0.01	0.99±0.01	0.99±0.01	0.99±0.01
		HM	all	0.99±0.01	0.99±0.01	0.99±0.01	0.99±0.01	0.99±0.01	0.99±0.01	0.99±0.01	0.99±0.01	0.99±0.01	0.99±0.01	0.99±0.01	0.99±0.01

Table 9.14: Comparison between the best PM, DDM, and HM in predicting the different parameters of NSP5 according to Table 9.9. Table reports the errors measured with the MAE, MAPE, and PPMCC in the interpolation and extrapolation scenarios with the best FS.

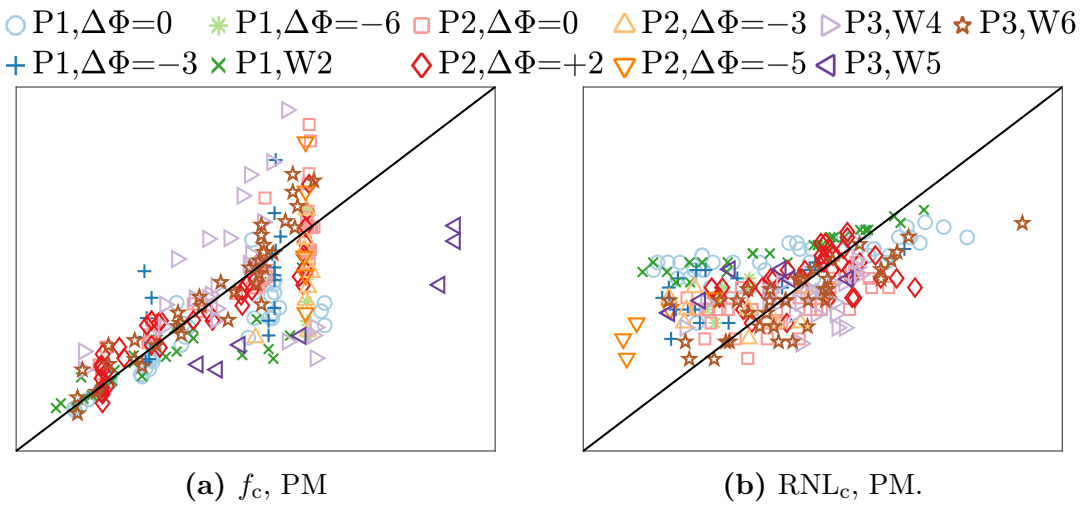

(a) f_c, PM

(b) RNL_c, PM.

(c) RNL_c, DDM, FSall.

(d) RNL_c, DDM, FSall.

(e) RNL_c, HM, FSall.

(f) RNL_c, HM, FSall.

Figure 9.12: Comparison between the best PM, DDM, and HM in predicting the different parameters of NSP1 according to Table 9.9. Figure reports the scatter plot (measured values on the x axis and predicted ones on the y axis) in the interpolation scenario with best FS for the different parameters of NSP1.

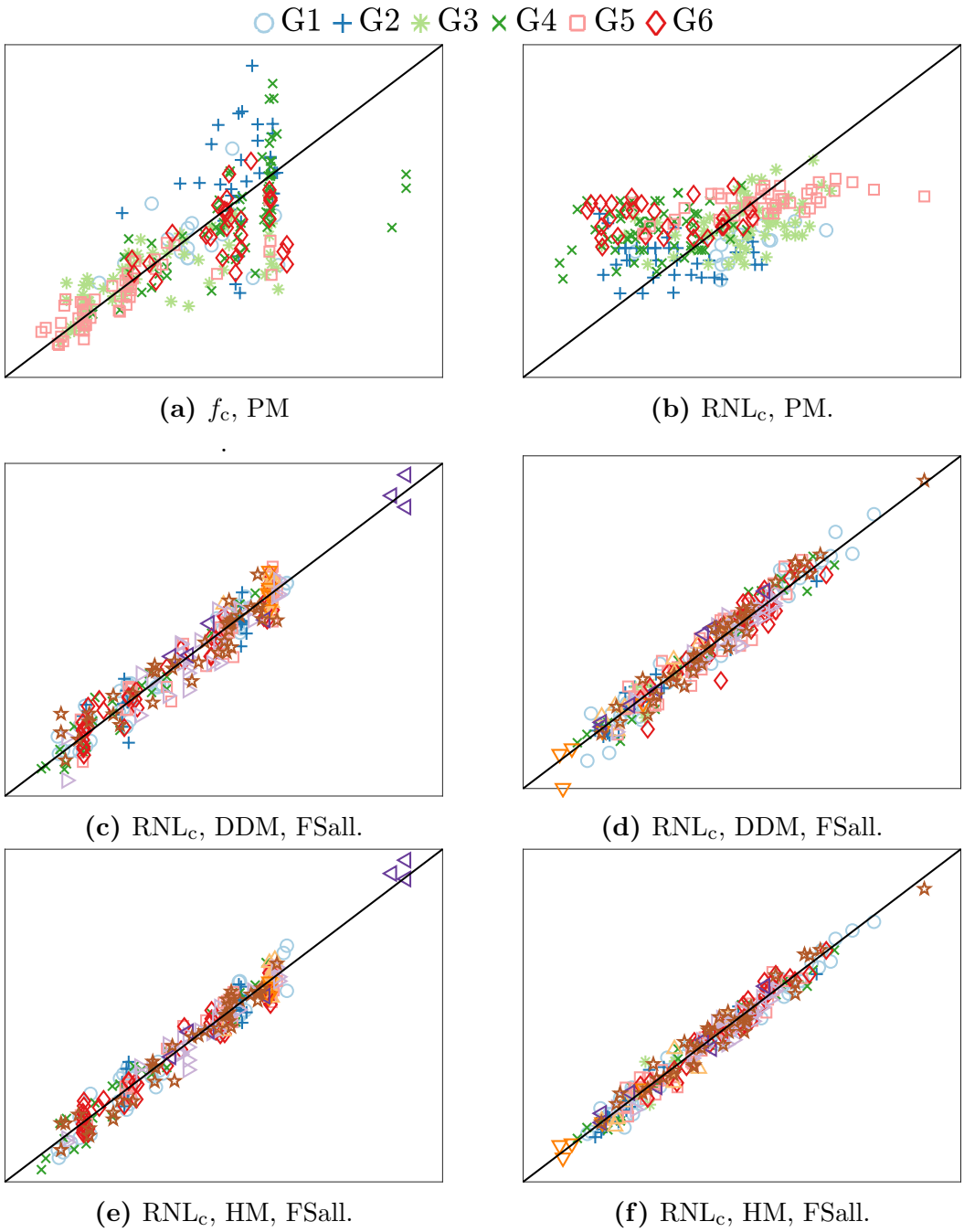

(a) f_c, PM

(b) RNL_c, PM.

(c) RNL_c, DDM, FSall.

(d) RNL_c, DDM, FSall.

(e) RNL_c, HM, FSall.

(f) RNL_c, HM, FSall.

Figure 9.13: Comparison between the best PM, DDM, and HM in predicting the different parameters of NSP1 according to Table 9.9. Figure reports the scatter plot (measured values on the x axis and predicted ones on the y axis) in the extrapolation scenario with best FS for the different parameters of NSP1.

9.3.6 Interpolation vs extrapolation

The models here presented show promising results both in the interpolation and in extrapolation scenario. Indeed, the error in extrapolation are doubled respect to the interpolation case, but being the latter really small, also the performances in extrapolation are widely acceptable. In extrapolation, the MAPE for the ADDMs and the HMs is lower than 10%.

9.4 Summary

In this chapter the second approach to estimate propeller cavitation noise by means of numerical models has been presented. The noise spectrum has been described in four different ways: the OTO bands for the source levels (NSP4), the OTO bands for the RNL (NSP5), and two different representation for simplified RNL (NSP2 and NSP3). The main difference between the present method and the one discussed in Chapter 8 is the use of multidimensional features, some of them coming from BEM computations. As explained in Appendix A.1 the conventional data driven models fail when the cardinality of the features domain is comparable or bigger than the samples size. For this reason, a new method based on advanced data driven models has been exploited. This ADDM has been able to predict accurately every NSPs. In particular, when all the possible features are considered, the performances are remarkably good. The PMs considered consist in the formulations for the vortex peak frequency, the vortex peak level and for the higher frequency part of the spectrum (in the range 10 kHz to 80 kHz); they are a derivation of semi-empirical or empirical models (Chapter 7). The PMs obtained from the vortex theory is quite accurate in the vortex resonance frequency estimation when only one configuration (or really similar configurations) and similar working points are accounted. Differently from the ADDMs, when multiple propellers/wake/WPs are considered, the performances of PMs drop. However, the physical knowledge encapsulated in the PMs, combined with the power of the pure numerical ADDMs give rise to the hybrid models, that again have been demonstrated to be best method to solve the task under study.

An in depth comparison of the performance of the different models has been performed. In particular two cases of evaluations have been carried out. In the first scenario, the capability of the models to predict the propeller noise spectra main characteristics in working conditions within the ones exploited for building the model has been analysed; in all cases, conditions different from those used to build the model have been used for the test, but always remaining inside the initial domain. In the second scenario, instead, the capability of the models to predict the propeller noise spectra main characteristics in groups of working conditions where the cavitation intensity is different with respect to the one exploited for building the model has been tested. In both scenarios ADDMs and HMs have shown remarkable and promising results.

For each model and scenario, different combinations of features have been considered: FS1, FS1+FS2, FS1+FS3, FS1+FS4, FS1+FS5, and all the features together. For every ADD/HM, the minimum error has been attained when all the features have been exploited, the maximum when only FS1 has been used, independently from the target definition; when FS1 is combined only with another of the two cases above mentioned. In the last situation, the models accuracy does not seems to be

susceptible to the multidimensional feature accounted.

A general insensitivity to the different combinations of features and targets it has been observed, as if the optimum had been reached.

This can attributed to the capability of the ADDM compared to the problem definition and the tested scenarios. Actually, the models are used to predict different working points (both in interpolation and extrapolation) of configurations (intended as propeller/wake) already known from the models. It can be noticed how in extrapolation the error is almost everywhere doubled respect to the interpolation. This could suggest that testing the models on propellers and configurations different from those used in the training phase, the performance would have been generally lower and most of all the effects of the different FS combinations and different spectrum parametrisation would have been more evident.

The results obtained so far are encouraging, and they lead to most challenging scenarios. From the above considerations the future analysis that will be undertaken could be an extrapolation scenario based on configurations and not on the WPs. For instance use WPs taken from similar wake configurations to predict WPs coming from a totally different wake. Or also, for a new interpolation scenario, to use two similar propellers to predict a propeller with intermediate geometric characteristics.

This page was intentionally left blank.

Chapter 10

Conclusions

In this PhD thesis the problem of the propeller back cavitation noise prediction has been addressed. The tools investigated have been physical models, data driven models and hybrid models. The former are semi-empirical or empirical formula taken from literature, the latter two are numerical approaches retrieved from the machine learning field.

The models have been built and tested on a set of noise spectrum samples collected at the UNIGE cavitation tunnel on three controllable pitch propellers, operating behind twin screw vessel wakes. The input data, i.e the features of the models, have been either collected in the model scale tests (as the cavitation inceptions) or derived from usual propeller design parameters (propeller geometry, wake at propeller). Moreover some inputs can be calculated with BEM tools as the pressure coefficients or the circulation around the blades.

From a test campaign at cavitation tunnel a series of cavitating propeller noise spectra have been collected, they represent the target to be predicted by the models. The net noise spectrum has been described in three alternative ways: the RNL in one-third octave bands, the SL in one-third octave bands or a piece-wise function simplification of the RNL. The latter is composed by 4 nodes, one of them is placed in correspondence of the center peak due to the back vortices cavitation.

Two different modelisation approaches have been exploited. At first, a simpler approach was used, considering as target the simplified spectrum and a not very large number of input parameters. In Approach 1 a simpler formulation of the problem have been addressed, namely the output was the broken-stick spectrum and the feature set was composed only by scalars (global characterisation of the propeller geometry, of the functioning point and of the wake). Hence, a simpler DDMs have been used. The PMs and the HMs used in this approach were only able to predict the cavitating tip vortex resonance frequency and noise level.

In Approach 2, four alternative targets have been predicted: the RNL, the SL, and two different representation of the broken-stick spectrum. Different combination of the following feature sets have been exploited: the generic scalars as in Approach 1, the matrix of the wake fraction, the matrix of the angle of attack, the blade pressure coefficients 3D-matrix and the blade circulations matrix. To manage features in multi dimension and to face a more complex formulation of the task, more advanced DDMs have been exploited. Moreover, the PMs and the HMs used in this approach were able to predict the cavitating tip vortex resonance frequency and noise level, and part of the broad band spectrum at higher frequencies.

In both approaches, the models have been tested in two scenarios: in interpola-

tion the models try to predict the propeller noise spectra in various, but different, working conditions within those exploited for building the model; in extrapolation the models try to predict the propeller noise spectra in groups of working conditions where the cavitation extent is very different with respect to those exploited for building the models. The latter scenario is a reproduction of the case when, due to scale effects, the cavitation pattern can not be reproduced in model scale for a working condition.

The DDMs and the HMs have shown remarkable results in both scenarios in terms of predictive accuracy. The HMs have been always the best, this demonstrates that combining the power of the machine learning methods with the physical knowledge encapsulated in the PMs is the best choice to address such complex task.

The DD/HMs are capable to accurately predict the vortex peak, the noise level at the maximum frequency and the OTO band both RNL and SL. However, the slopes of spectrum piece-wise parametrisation seem to be more difficult to be predicted; probably this is due to failures in the parametrisation phase than to lack in the DD/HMs. Indeed, for some working points the spectrum simplification can be difficult to be univocally defined.

The approaches proposed are therefore very promising, even if certainly further validations are needed, which have to be object of future work. The most important aspect is to test the method capability to predict cavitation noise also for other propeller geometries and/or ship wakes, different from those used for building the model. The previously mentioned extrapolation scenario is, from this point of view, a first test; however, extrapolating on propeller geometry or on wake is certainly more challenging. A further development is the enlargement of the database. The dataset so far applied is still limited both in sample size and in variance of the propeller geometries and wakes characteristics, hence future efforts will be made to enlarge the dataset to improve generalisation.

The PMs used in Approach 2 to predict the vortex noise are more sophisticated respect to the ones exploited Approach 1. Indeed, the vortex noise depends mainly upon the vortex cavity size, that in Approach 2 has been directly computed by means of non-cavitating vortex models. This prediction can be enhanced in two ways: the first is to exploit more complex model to better predict the cavity radius, the second is to adopt the dispersion relation as alternative noise model.

The broadband noise spectrum has been calculated by means of the Brown's empirical formula. The critical input is the cavitating area that has been calculated by the coefficients of pressure retrieved by non-cavitating BEM. This method is computationally inexpensive if compared to the most sophisticated RANSE, DDES and LES, however the cavitating area is usually under predicted and questions the accuracy of the Brown's formula.

Future developments will include a more precise cavitation extent estimation e.g. by means of RANSE calculations. The vortex noise prediction procedure may be implemented by a 3-D analysis of the flow around a cavitating vortex, as the dispersion relation of inertial waves propagating on the cavity interface (Thomson, 1880; Morozov, 1974; Pennings et al., 2015). Lastly, to better take into account the sheet cavity dynamics in the noise generation, the high frequency noise may be predicted with the Matusiak (1992) procedure to account for the break-off of the fixed sheet cavity in unsteady flow conditions.

Appendix A

Deep machine learning models

This appendix reports on the Deep Neural Network (DNN) strategy to build the DDMs and HMs explored in Chapter 9.

A.1 Data Driven Models

This section presents the proposed DDMs for predicting the different NSPs based on the different FSs as discussed in Chapter 9.

Even if the scenario of this approach is slightly different with respect to the one in Chapter 8, a first idea could be to exploit the same methodology for defining new DDMs and HMs and adapt it to the scope of this work. Unfortunately, for the reasons that will be clarified in this section (Shalev-Shwartz and Ben-David, 2014; Goodfellow, Bengio, and Courville, 2016), this approach would result in very low performance, in terms of accuracy, as will be shown in the experimental results of Section 9.3. The reasons behind this decay in performance need to be searched in the philosophy behind the methodology proposes in Chapter 8 that, from now on, will be named as Conventional DDMs (CDDMs) or Shallow DDMs (SDDMs). CDDMs

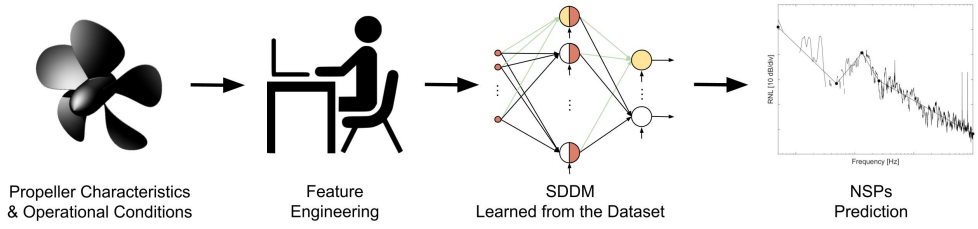

(a) CDDMs or SDDMs.

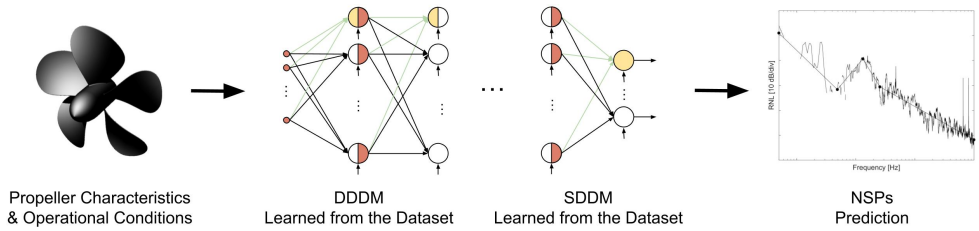

(b) ADDMs or DDDMs.

Figure A.1: Conventional (Shallow) DDMs vs Advanced (Deep) DDMs.

rely on the simple schema presented in Figure A.1a with the following details:

- from the available inputs, i.e. the propeller characteristics and operational conditions, the raw information about the FSs of Table 9.3 are extracted;
- from the raw FSs, experts of the problem together with data scientists extract a series of rich features, that should be able to provide all the information about the desired output, in this case the different parameters of the NSPs (this process is called Feature Engineering);
- a functional form of the predictive model, the SDDM, is defined by the data scientist. Then the parameters of the SDDMs are learned from the input/output samples, called dataset, where the input is coded with the features engineered in the previous step;
- finally the learned model can be exploited to make prediction about the NSPs.

This approach is very effective under a simple, but quite strict, assumption: the feature engineered by the experts should be rich enough to describe the phenomena, but characterised by a cardinality not too high compared to the number of samples of the dataset (Shalev-Shwartz and Ben-David, 2014; Goodfellow, Bengio, and Courville, 2016). If only FS1 is available, somehow analogously to the work of Chapter 8, then CDDMs would be the correct choice. As a matter of fact, in this case also FS2, FS3, FS4, and FS5 are available, and exploiting the CDDMs of Chapter 8 would result in an exploding number of features, because of the FSs intrinsic cardinality, and the model would be not able to learn the correct model with a dataset of limited cardinality like the one available for this study. Moreover, extract reach and representative features from the FS2, FS3, FS4, and FS5 is a complex task not suited for a human expert.

For these reasons, in this approach an Advanced DDMs (ADDMs) or Deep DDMs (DDDMs) will be exploited. ADDMs rely on the schema presented in Figure A.1b with the following details:

- as for the CDDMs, from the available inputs, (propeller characteristics and operational conditions), the raw information about the FSs of Table 9.3 are extracted;
- contrarily to the CDDMs, experts of the problem together with data scientists do not perform a Feature Engineering phase, but they define a functional form of the model, namely a structure of the model, to be learned from the data. This structure is composed by two levels: a first level (DDDMS) is dedicated to learn the features to be provided to the same SDDM exploited for the CDDMs;
- from the dataset, both the SDDM and the DDDM parameters are learned;
- finally the learned model can be exploited to make prediction about the NSPs.

The main differences between the CDDMs and the ADDMs rely on the fact that, in the ADDMs there is just minimal intervention of experts and data scientists in the definition of the model. In fact, in ADDMs, as it will be shown in this section, just the functional form of the features must be designed, while in CDDMs the features are basically handmade, everything else is learned from the dataset.

In this work, the CDDMs is not described in details, nevertheless, all the relevant details are reported in the original work of Chapter 8. For completeness, it is recalled that the CDDMs proposed in Chapter 8 is a combination of features engineered by experts Chapter 8 plus a KRLS (Shawe-Taylor and Cristianini, 2004) model plus a feature reduction phase (Guyon and Elisseeff, 2003) plus an advance model selection phase (Oneto, 2020).

Instead, from now on, a detailed description of the proposed ADDMs is reported,

starting from the basic principles that guided the definition of the proposed functional form until the final proposed model. In particular, it will be first explained the building blocks of the proposed ADDM, and then they will show how to combine them to derive the proposed architecture and solve the problem faced in this work. For simplicity, if not specified otherwise, the proposed ADDMs is simply referred as DDMs since, as it will be shown in Subsection 9.3.1, the ADDMs are the most effective ones for the purpose of this approach.

Let us start by making the hypothesis that $\mathcal{X} \subseteq \mathbb{R}^q$ with $q \in \mathbb{N}^*$, namely the input space is composed by different features stacked together in a vector (e.g. when only FS1 is considered), and that μ is a simple linear function. Note that, for each one of the different NSPs $\mathcal{Y} \subseteq \mathbb{R}^p$ with $p \in \mathbb{N}^*$, namely the output space is composed by different features stacked together in a vector. In this case, the best functional form of the model can be defined as follows

$$h(X) = WX + B\,, \tag{A.1}$$

where $W \in \mathbb{R}^{p \times q}$ and $B \in \mathbb{R}^p$, namely the functional form of the model is a multiple linear model in the space defined by $\mathcal{X}$ and $\{W, B\}$ are the parameters of the model. The functional form of the model can be also interpreted as p different neurons reacting to the input stimulus in different ways based on the different weights. The model of Equation A.1 is also graphically depicted in Figure A.2. $\{W, B\}$ need to

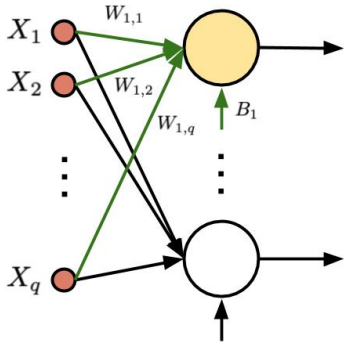

Figure A.2: Multiple linear model functional form for h. In red are identified the inputs, in green the weights, and in yellow the output of one neuron of the architecture.

be tuned in such a way that h is a good representation of μ. However, the quality of h in representing μ is defined by the index of performance defined in Section 9.1 for each of the NSPs computed on $\mathcal{D}_n$. These measure of accuracy will be refferred with the symbol $\hat{\mathtt{L}}(h, \mathcal{D}_n)$, namely the Empirical Error $\hat{\mathtt{L}}$ of the model h on the dataset $\mathcal{D}_n$. Consequently, the best parameters of h, namely $\mathtt{P}(h)$ (in the case of Equation A.1 $\mathtt{P}(h) = \{W, B\}$), are the ones which minimise the following problem

$$h^* : \min_{\mathtt{P}(h)} \quad \hat{\mathtt{L}}(h, \mathcal{D}_n)\,. \tag{A.2}$$

In general, Problem A.2 can be convex or not, depending on the functional forms of h or $\hat{\mathtt{L}}(h, \mathcal{D}_n)$ (Boyd and Vandenberghe, 2004; Pardalos and Romeijn, 2013). For this reason, if, at least, $\hat{\mathtt{L}}(h)$ is differentiable in $\mathtt{P}(h)$ (in the case of the model of Equation A.1 should be differentiable in $\{W, B\}$) it is possible to exploit one of the various forms of the gradient descend algorithm (Goodfellow, Bengio, and Courville,

2016) (e.g. SGD, RMSprop, Adagrad, Adadelta, Adam, etc.) to find the best set of $\mathtt{P}(h)$. Note that each algorithm has hidden hyperparameters that need to be tuned to reach satisfying solutions (Goodfellow, Bengio, and Courville, 2016) (e.g. Learning Rates, Momentum, Batch Sizes, etc.). Another critical aspect which deeply affects the results of the optimisation process in gradient-based methods is the starting point, or initialisation, of $\mathtt{P}(h)$; also in this case many options exist, but they are grouped in two big families (Goodfellow, Bengio, and Courville, 2016): the first one is the deterministic initialisation (e.g. Random Normal, Random Uniform, LeCun, Glorot, He, etc.) while the second one is the learned initialisation (e.g. Autoencoders, etc.).

This approach of Problem A.2 is known as empirical risk minimisation (Vapnik, 1998). However, ERM is usually avoided in DDMs as it leads to severe overfitting of the model on the training dataset. As a matter of fact, in this case the process of learning the $\mathtt{P}(h)$ could choose a model good just for describing $\mathcal{D}_n$ which has been exploited to learn $\mathtt{P}(h)$ (including noise, which afflicts $\mathcal{D}_n$). In other words, ERM implies memorisation of data rather than learning from them. For this reason, some regularisation effect in Problem A.2 has been included, allowing to find a $\mathtt{P}(h)$ good enough to both learn from $\mathcal{D}_n$ and generalise, namely have good performance, also on $\mathcal{T}_n$. Many ways exist to introduce this regularisation (Goodfellow, Bengio, and Courville, 2016) (e.g. Early Stopping, Weights Decay, Dropout, etc.) and with a little abuse of notation all of them will be modelled by modifying Problem A.2 into the following one

$$h^* : \min_{\mathtt{P}(h)} \quad \hat{\mathtt{L}}(h, \mathcal{D}_n) + \lambda \, \mathtt{R}(h), \tag{A.3}$$

where $\mathtt{R}(h)$ represents the regularisation term and $\lambda \in [0, +\infty)$ represents the regularisation hyperparameter, that need to be tuned, in order to find the best trade-off between ability of $\mathtt{P}(h)$ to learn from $\mathcal{D}_n$ and to generalise.

The limitations that are still considered are the hypothesis of the linearity of μ and then the linearity of functional form of the model presented in Equation A.1. In order to address this issue, it is possible to combine multiple linear models in this way

$$h(X) = W_2 \Gamma(W_1 X + B_1) + B_2 \,, \tag{A.4}$$

where Γ is an activation function (Goodfellow, Bengio, and Courville, 2016) (e.g. Sigmoid, Hyperbolic Tangent, Rectified Linear Unit, etc.), $W_1 \in \mathbb{R}^{h \times q}$ with $h \in \mathbb{N}^*$, $B_1 \in \mathbb{R}^h$, $W_2 \in \mathbb{R}^{p \times h}$, and $B_2 \in \mathbb{R}^p$. With a little simplification the same activation function element of the vector $W_1 X + B_1$ is exploited but in general it is possible to use different activation functions.

The model of Equation A.4 is also graphically depicted in Figure A.3. If Γ is, for example, a Sigmoid or a Hyperbolic Tangent it is possible to prove that, for h large enough, the model Equation A.4 can describe every possible function mapping points from $\mathbb{R}^q$ to $\mathbb{R}^p$ (Goodfellow, Bengio, and Courville, 2016). The type of activation function and h are hyperparameters which characterise the architecture that need to be tuned. The model of Equation A.4 is also called Shallow (SDDM) since it can be interpreted as the concatenation of multiple neurons with a single hidden layer of neurons. Note that this SDDM is somehow analogous to the one exploited in the CDDMs where the hidden layer represents the feature mapping, which is deterministic in CDDMs, while in this case is leaned from the data and the last layer is a simple linear function (note that, if the representation is good, linear

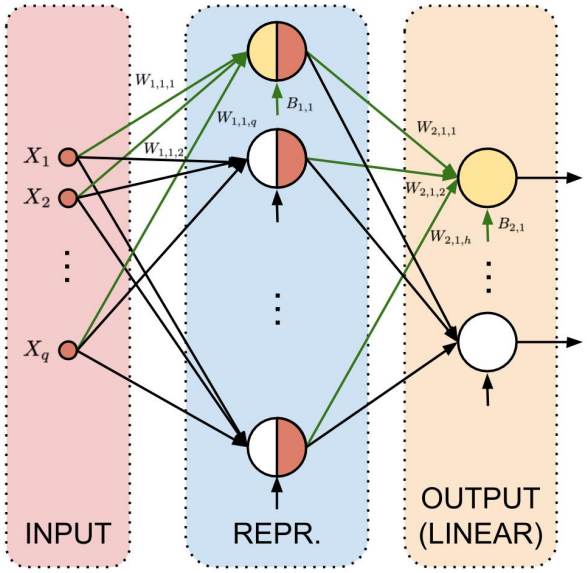

Figure A.3: Shallow DDM.

functions are powerful enough). Since the structure of the brain is not so simple but it has a deeper structure, in the last years (Goodfellow, Bengio, and Courville, 2016) Deep Models (DDDMs) have been developed and have shown to outperform many SDDMs in many real world problems involving natural signals (Goodfellow, Bengio, and Courville, 2016) (e.g. Image and Video Recognition, Natural Language Processing, Speech Recognition, etc.). In this case, the model is a concatenation of multiple neurons in a series of multiple hidden layers as follows

$$h(X) = W_H \Gamma_H(\cdots \Gamma_2(W_2 \Gamma_1(W_1 X + B_1) + B_2) \cdots) + B_H \,, \tag{A.5}$$

where Γ_i with $i \in \{1, \cdots, H\}$ and $H \in \mathbb{N}^*$ are the different activation functions at each layer, $W_1 \in \mathbb{R}^{h_1 \times q}$, $B_1 \in \mathbb{R}^{h_1}$, $W_H \in \mathbb{R}^{p \times h_{H-1}}$ with $h_{H-1} \in \mathbb{N}^*$, $B_H \in \mathbb{R}^p$, $W_i \in \mathbb{R}^{h_i \times h_{i-1}}$, and $B_i \in \mathbb{R}^{h_i}$ with $i \in \{2, \cdots, H-1\}$. Again, with a little simplification the same activation function in each hidden layer is exploited but in general each hidden layer may exploit different activation functions.

The type of activation function, H, and h_i with $i \in \{1, \cdots H-1\}$ are hyperparameters which characterise the architecture that need to be tuned. The model of Equation A.5 is also graphically depicted in Figure A.4. Note that in DDDMs, the representation that can be learned from the data is richer with respect to the SDDMs since it allows building more complex and, in principle, richer structures (Goodfellow, Bengio, and Courville, 2016).

The problem of the models of Equations A.4 and A.5 is that the cardinality of the matrices of parameters explodes too fast (curse of dimensionality) and then, in order to be able to learn them, millions of samples need to be available (Goodfellow, Bengio, and Courville, 2016). In this case, this is not possible since the cardinality of the dataset is very limited and fixed as described in Section 9.1 and this is also the reason why the CDDMs cannot be exploited.

One way to overcome this problem is to exploit the solution of the Extreme Learning Machines (ELMs) (Kasun et al., 2013; Tang, Deng, and Huang, 2016) which show that the ability of learning from data a good model, in the form of Equations A.4 and A.5, improves dramatically, in the case of limited number of

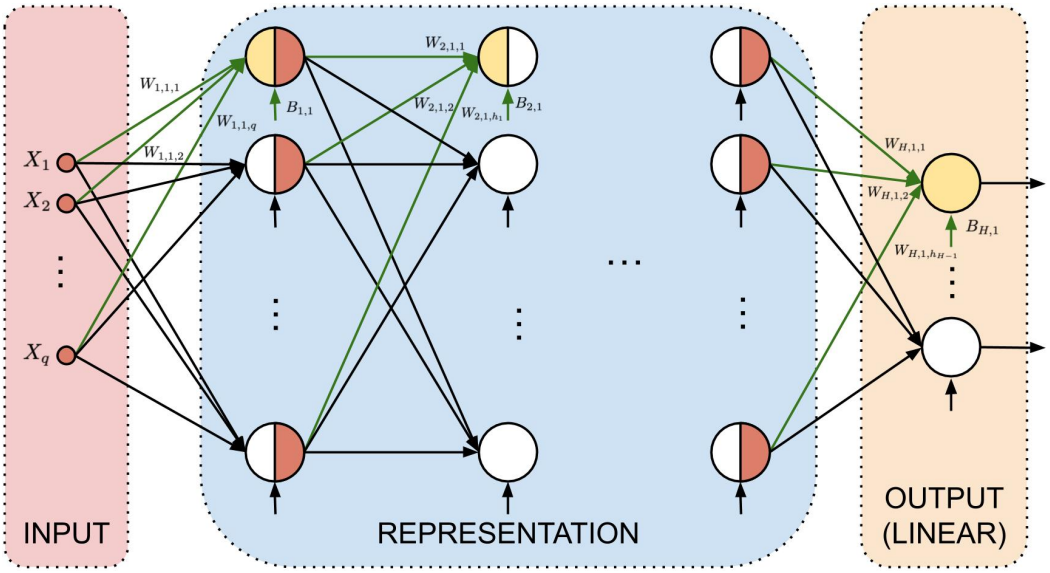

Figure A.4: Deep DDM.

samples, when W_1 for model Equation A.4 and $W_1, \cdots, W_{H-1}$ for the one of Equation A.5 are simply set randomly. Counterintuitively as it may seem, this solution represents the state of the art in many real world applications (Kasun et al., 2013; Tang, Deng, and Huang, 2016).

Another way to overcome the curse of dimensionality is to introduce the concept of sparsity on the architecture. Sparsity means that many weights in the architecture are zero or missing (an example, for simplicity on a SDDM, is reported in Figure A.5).

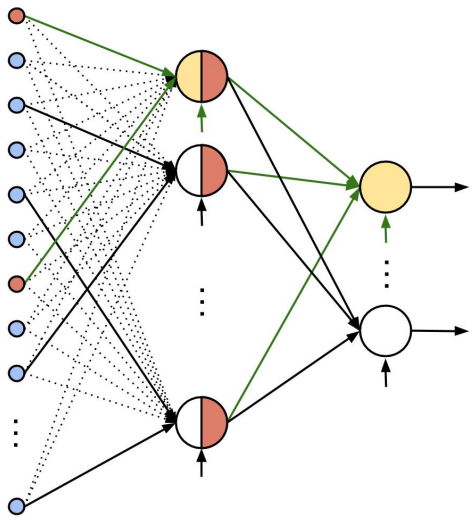

Figure A.5: Sparse version of the SDDMs of Figure A.3. Dotted rows means that that weight is set to zero, namely the connection is dropped.

This property can be achieved in two ways.

The first one, the naive one, is to use as $\mathtt{R}(h)$ the L1 (Tibshirani, 1996) or the L1-L2 (Zou and Hastie, 2005) regularisation which implies a sparse solutions in Problem A.3. Unfortunately, this approach does not really mitigate the curse of dimensionality and presents some intrinsic limitations (Goodfellow, Bengio, and

Courville, 2016). The reasons of these limitations lie in the fact that, simply adding a regularisation, does not help the model in reducing the intrinsic dimensionality of the space of the parameters since it still has to learn what parameters need to be set to zero.

The second option is to exploit the intrinsic structure of the FS. Until this point the hypothesis that was made considers that the input space is composed by different features stacked together in a vector (e.g. when just FS1 is considered) but, in the specific problem, some parts of the FS have a particular structure. In fact, FS2, FS3, and FS5 are two-dimensional (2D) tensors while FS4 is a three-dimensional (3D) tensor (please refer to Table 9.1 for simplicity or to Section 9.1 for the detailed explanation of these FSs). These 2D and 3D-tensors, contrarily to the FS1, have a particular property. Apart from the specific value of each particular element in the tensor, also the location in the tensor has a meaning related the tensor's construction (see Section 9.1). In a simpler case, like grayscale images, which can be represented as a 2D-tensor, pixels which are close to each other have some proximity property, called structure, which can help, for example, in distinguish things that are close or distant from each other or pixel which belongs to the same object (Goodfellow, Bengio, and Courville, 2016). In this case, it does not make any sense to stack neurons in layers which react to all the elements in the tensor contemporary (basically to build a structure like the ones in Figures A.2, A.3, and A.4) but each neuron should react to particular portion of the tensors, ignoring the other ones. This corresponds to deterministically set to zero some weights of the neurons and then, to fully process the tensor, to stack neurons which react to different portion of the tensors (namely a structure like the one of Figure A.5 is deterministically defined).

The problem that remains to be solved is how to define a structure of these neurons, and for this reason it will rely on a simple idea (Goodfellow, Bengio, and Courville, 2016): each neuron should react to part of the tensors which are close, in some sense, to each other. This idea comes from the use of convolution with Gabor applies in image processing (Russ, 2016), which emulates how the brain process the images to detect, for example, objects, distances, and contours. The only difference here is that these filters, instead of being deterministically defined to react to certain stimulus, are learned from the data. An example of the structure of the network for a 2D-convolution layer is reported in Figure A.6 where, for simplicity, just two neurons are fully depicted.

The architecture has several parameters. The input space, being a 2D-tensor, is a matrix of size $\mathbb{R}^{q_1 \times q_2}$. The patch, or the size of the filter to be learned, is $\mathbb{R}^{\lfloor r_f q_1 \rfloor_{\text{odd}} \times \lfloor r_f q_2 \rfloor_{\text{odd}}}$ where $r_f \in (0, 1)$ is an hyperparameter which regulates the ratio between the size of the 2D-input tensor and the filter while $\lfloor \cdot \rfloor_{\text{odd}}$ represents the closer smaller odd number.

The padding is the addition of elements at the border of the tensor to mitigate the edge effects, and its size is depicted in Figure A.6 (in this case the zero padding has been used, but also other types of padding exists like the "mirror" or "same" padding). The stride is the movement step of the filter on the tensor which is $\lfloor r_s q_1 \rfloor$ along the first dimension of the tensor and $\lfloor r_s q_2 \rfloor$ along the second dimension, $r_s \in (0, 1)$ is and hyperparameter which regulates this movement.

The dilation is a further sparsity capability of the filter reaction, which is $\lfloor r_d q_1 \rfloor$ along the first dimension of the tensor and $\lfloor r_d q_2 \rfloor$ along the second dimension, $r_s \in (0, 1)$ is and hyperparameter which regulates it. Obviously the number of neurons,

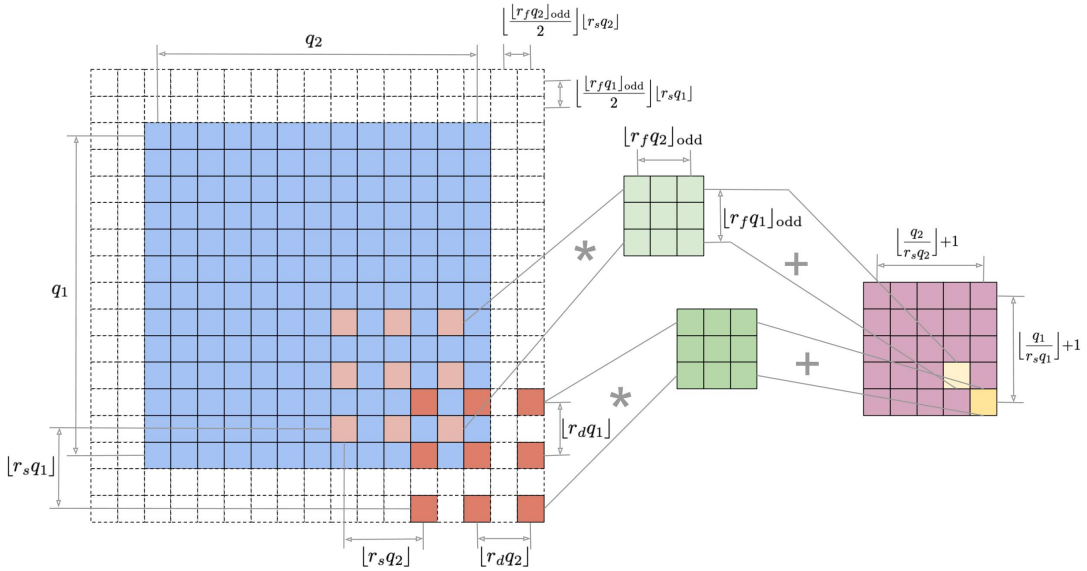

Figure A.6: Convolution on a two-dimensional tensor. The tensor has been indicated in blue, the learned filter (the sparse weights) in green, the output of one sparse neuron in yellow, the resulting two-dimensional tensor in purple, the padding in white.

and consequently the number of outputs of this 2D-convolution layer, depends on all these parameters and is reported in Figure A.6. Please refer to Goodfellow, Bengio, and Courville (2016) for a more detailed treatment of the convolutional networks.

The 2D-convolution can be defined by a learned filter but also by a deterministic function like the maximum, the average, or the median. For example, in Figure A.7 a 2D-max-pooling layer is reported, which is a 2D-convolution layer where, instead of learning a filter, the maximum operator is applied.

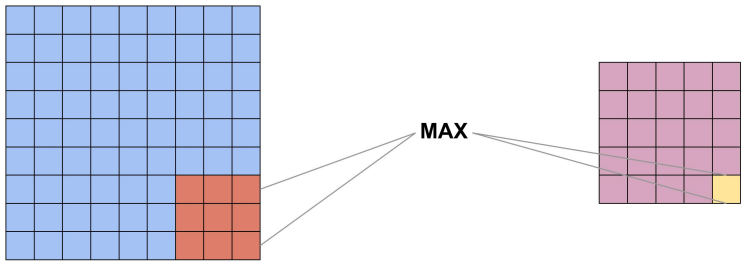

Figure A.7: Max pooling on a two-dimensional tensor: substitution of the deterministic function max to the learned filter in a convolution on a two-dimensional tensor (see Figure A.6). Note that, for simplicity, the padding, the dilation, and the stride have been not reported, since they are analogous to the ones of Figure A.6.

Using the same principles described for the 2D-tensors (FS2, FS3, and FS5) it is possible to build a convolutional network for 3D-tensors (in this case FS4). The input space, in this case, will be a tensor of size $\mathbb{R}^{q_1 \times q_2 \times q_3}$ and, consequently, the filter size will be $\mathbb{R}^{\lfloor r_f q_1 \rfloor_{\text{odd}} \times \lfloor r_f q_2 \rfloor_{\text{odd}} \times \lfloor r_f q_3 \rfloor_{\text{odd}}}$. In an analogous way the other dimensions (padding, stride, and dilation) will change. An example of 3D-convolutional network is represented in Figure A.8. Analogously, the 3D-max-pooling can be defined.

At this point all the building blocks required to build the proposed architecture and DDMs for estimating the different NSPs based on the different FSs are present.

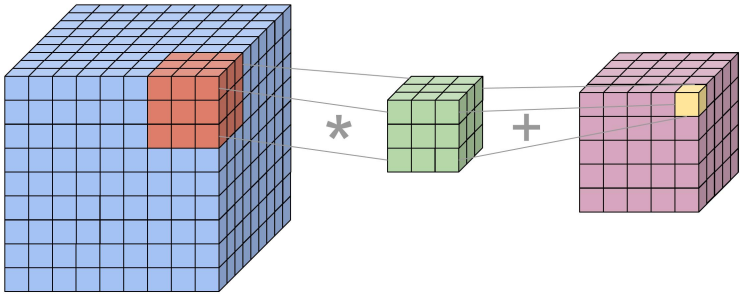

Figure A.8: Convolution on a three-dimensional tensor (see Figure A.6 for the meaning of the colors). Note that, for simplicity, the padding, the dilation, and the stride have been not reported, since they are analogous to the ones of Figure A.6.

In particular, a Dense Layer is defined (Figure A.3) with its different activation functions (e.g. RELU, Linear, Hyperbolic Tangent, etc.) and regularization (e.g. L2, Dropout, etc.), a Random Layer, namely a Dense Layer with random weights, the 2D and 3D Convolutional Layers (again with its activation functions), the 2D and 3D Max Pooling Layer. Since it will be required later, it has also been defined a Concatenation Layer, which simply takes in input whatever structure (e.g. scalars, vectors, or tensors) and reshape everything in a large vector. The point is then how to combine them to get a suited architecture for the problem under exam.

The architecture of the proposed DDMs will be built incrementally to explain the different choices.

For what concerns the FS1, this FS is somehow analogous to the one of Chapter 8 and for this reason a simple SDDMs like the one of Figure A.3 is enough. In order to limit the number of weights to be learned, the hidden layer will be a simple Random Layer (ELMs-style) with a hyperbolic tangent activation function to provide the necessary non-linearity, and the output layer will be a simple Dense Layer with linear activation function and the L2 regularisation to limit the overfitting. This structure basically emulates, with much fewer parameters to tune, the one proposed in Chapter 8. The hyperparameter to be tuned are just the number of neurons of the hidden layer $n_{\text{RL}} \in 2^{\{2,4,6,8,10\}}$ and the amount of regularisation defined by $\lambda \in 10^{\{-4.0,-3.5,\cdots,+3.0\}}$ (see Equation A.3) in the output layer since the number of inputs is defined by FS1 and the number of output neurons is defined by the particular NSP to be predicted. The initialisation of the output Dense Layer is a simple zero-valued initialisation.

For what concerns instead FS2, FS3, FS4, and FS5, the process is a bit more complicated. Firstly, it will be presented the proposed method for dealing with the 2D-tensors (FS2, FS3, and FS5) and the treatment of the 3D-tensor (FS4) will be just summarised because analogous. As already mentioned before, the 2D-tensors cannot be simply stacked with FS1 by means of a Concatenation Layer and fed to the architecture of Figure A.3 (see results of this approach in Subsection 9.3.1). For this reason, a more condensed representation of these FSs needs to be learnt, and, for this purpose, the convolution layers is the best choice. The only problem of the Convolutional Layers is that, based on the setting of their parameters, they are designed to react to just a particular scale of dimension and for this reason it would be good to have more layers which react to different scales. The solution that has been adopted in this approach is to use and Inception Layer (Szegedy et al., 2017) composed of three parallel Convolutional Layers (equipped with linear

activation functions to mitigate the gradient vanishing effect, that will be clarified later, and no regularisation because of the intrinsic sparsity of the architecture) reacting to different scales. In order to limit the number of weights to be learned, one of the three Convolutional Layers is a simple 2D Max Pooling Layer. Then, in order to agglomerate all the information at different scales and produce a condensed representation, the outputs of the two 2D Convolutional and the 2D Max Pooling Layers are combined adopting a Concatenation Layer and then exploiting a Dense Layer (equipped with linear activation functions, again to mitigate the gradient vanishing effect, and dropout as regulariser). This building block is depicted in Figure A.9. The architecture has multiple hyperparameters that have to

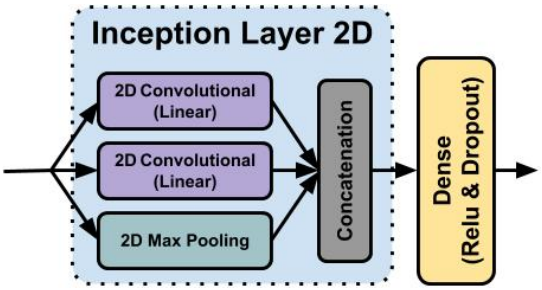

Figure A.9: Proposed architecture for extracting a good representation from the two-dimensional tensors (see FS2, FS3, and FS5 in Table 9.3) in the dataset described in Section 9.1.

be tuned. For the padding, a zero padding has been exploited. It is now necessary to tune for the 2D Convolutional and the 2D Max Pooling Layers the r_f ($r_f^{\text{C2D}_1}, r_f^{\text{C2D}_2}, r_f^{\text{MP2D}_1} \in \{0.1, 0.2, 0.4\}$), the r_s ($r_s^{\text{C2D}_1}, r_s^{\text{C2D}_2}, r_s^{\text{MP2D}_1} \in \{0.1, 0.2, 0.4\}$), and the r_d ($r_d^{\text{C2D}_1}, r_d^{\text{C2D}_2}, r_d^{\text{MP2D}_1} \in \{0.1, 0.2, 0.4\}$). Then, for the dense layer, it is necessary to tune the number of neurons $n_{\text{DL}} \in 2^{\{2,4,6,8,10\}}$ and the dropout rate $r_d \in 10^{\{-3,-4,-2,-1\}}$, namely the number of neurons to randomly deactivate during training (Goodfellow, Bengio, and Courville, 2016). The problem of this architecture is its initialisation phase since a deterministic or random initialisation would be not sufficient to guarantee good performances (Goodfellow, Bengio, and Courville, 2016). For this reason the architecture of Figure A.9 is initialised with a surrogate problem, using the autoencoders approach (Goodfellow, Bengio, and Courville, 2016). Basically, since the output of the dense layer in Figure A.9 should be a good and condensed representation of the FSs (FS2, FS3, and FS5), based on that representation it should be possible to retrieve the original FSs. Subsequently, the weights have been initialised using the approach proposed in He et al. (2015), hence to the Dense Layer of Figure A.9 is attached another Dense Layer where the outputs are the same FS provided to the block as input, and finally the network is trained using the algorithms that will be explained later in this section. The architecture of the autoencoder for pre-training the block of Figure A.9 is depicted in Figure A.10. After this pre-training phase the last Dense Layer added for the pre-training is removed, and the Inception Layer plus the dense layer after that have been kept.

The extension of this 2D block defined for FS2, FS3, and FS5 can be trivially extended to the case of FS4 where a 3D block need to be developed.

At this point, it is possible to combine all outputs of the blocks developed for FS2, FS3, FS4, and FS5 in a Concatenation Layer together with FS1 and fed them

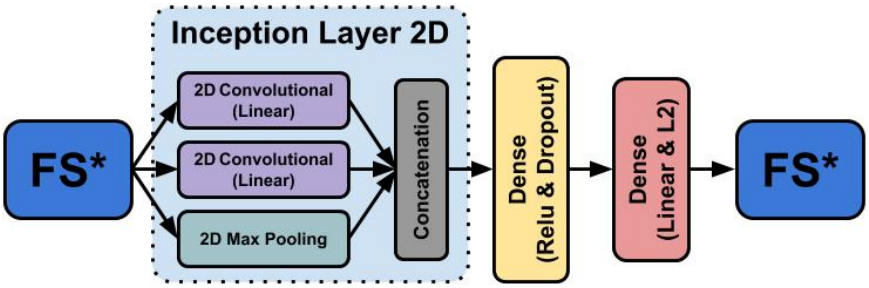

Figure A.10: Architecture of the autoencoder for initialising the architecture presented in Figure A.9.

to the same SDDMs described for FS1. It is possible to do perform this action since FS1 plus the outputs of the blocks developed for FS2, FS3, FS4, and FS5 is an informative and condensed information about all the features. The resulting architecture, namely the proposed DDM, is depicted in Figure A.11.

What still needs to be described is how the network has been trained (or pretrained the blocks just described for FS2, FS3, FS4, and FS5). As described before, many gradient descend-based algorithms (e.g. SGD, RMSprop, Adagrad, Adadelta, Adam, etc.) exist for solving the problem. The only issue of these algorithms is the Gradient Vanishing effect (Goodfellow, Bengio, and Courville, 2016), namely the fact that in deep network the gradient tend to go to zero exponentially in the number of layers. For this reason, in the proposed architecture, and in all the trained layers, is exploited a linear or RELU activation functions which mitigate this problem. Then, the Mini Batch Stochastic Gradient Descent (SGD) algorithm has been used, characterised by three hyperparameters: learning rate of the gradient, momentum that accelerates SGD in the relevant direction, and batch-size of each iteration.

The last problem that need to be solved is how to tune the hyperparameters of the proposed architecture. Since all DDMs are characterised by a set of hyperparameters $\mathcal{H}$ influencing their ability to estimate μ, a proper model selection procedure, namely the process of tuning them to achieve optimal performances, needs to be performed (Oneto, 2020). As already discusse, several methods exist for MS purpose but resampling methods, like the well-known k-Fold Cross Validation or the nonparametric Bootstrap approaches represent the state-of-the-art approaches (Oneto, 2020). Resampling methods rely on a simple idea: the original dataset $\mathcal{D}_n$ is resampled once or many (s) times, with or without replacement, to build two independent datasets called training, and validation sets, respectively $\mathcal{L}_l^i$ and $\mathcal{V}_v^s$, with $i \in \{1, \cdots, s\}$. Note that $\mathcal{L}_l^i \cap \mathcal{V}_v^i = \oslash$ and $\mathcal{L}_l^i \cup \mathcal{V}_v^i = \mathcal{D}_n$. Then, in order to select the best combination the hyperparameters $\mathcal{H}$ in a set of possible ones $\mathfrak{H} = \{\mathcal{H}_1, \mathcal{H}_2, \cdots\}$ for the proposed architecture or, in other words, to perform the MS phase, the following procedure has to be applied

$$\mathcal{H}^* : \ \arg\min_{\mathcal{H} \in \mathfrak{H}} \quad \frac{1}{s} \sum_{i=1}^{s} \hat{\mathtt{L}} \left(h^*_{\{\mathcal{H}, \mathcal{L}_l^i\}}, \mathcal{V}_v^i \right) , \tag{A.6}$$

where $h^*_{\{\mathcal{H}, \mathcal{L}_l^i\}}$ is the model with its set of hyperparameters $\mathcal{H}$ learned with with the data $\mathcal{L}_l^i$. Since the data in $\mathcal{L}_l^i$ are independent of the ones in $\mathcal{V}_v^i$, the idea is that $\mathcal{H}^*$ should be the set of hyperparameters which allows to achieve a small error on a data set that is independent of the training set. In this work will be exploited the

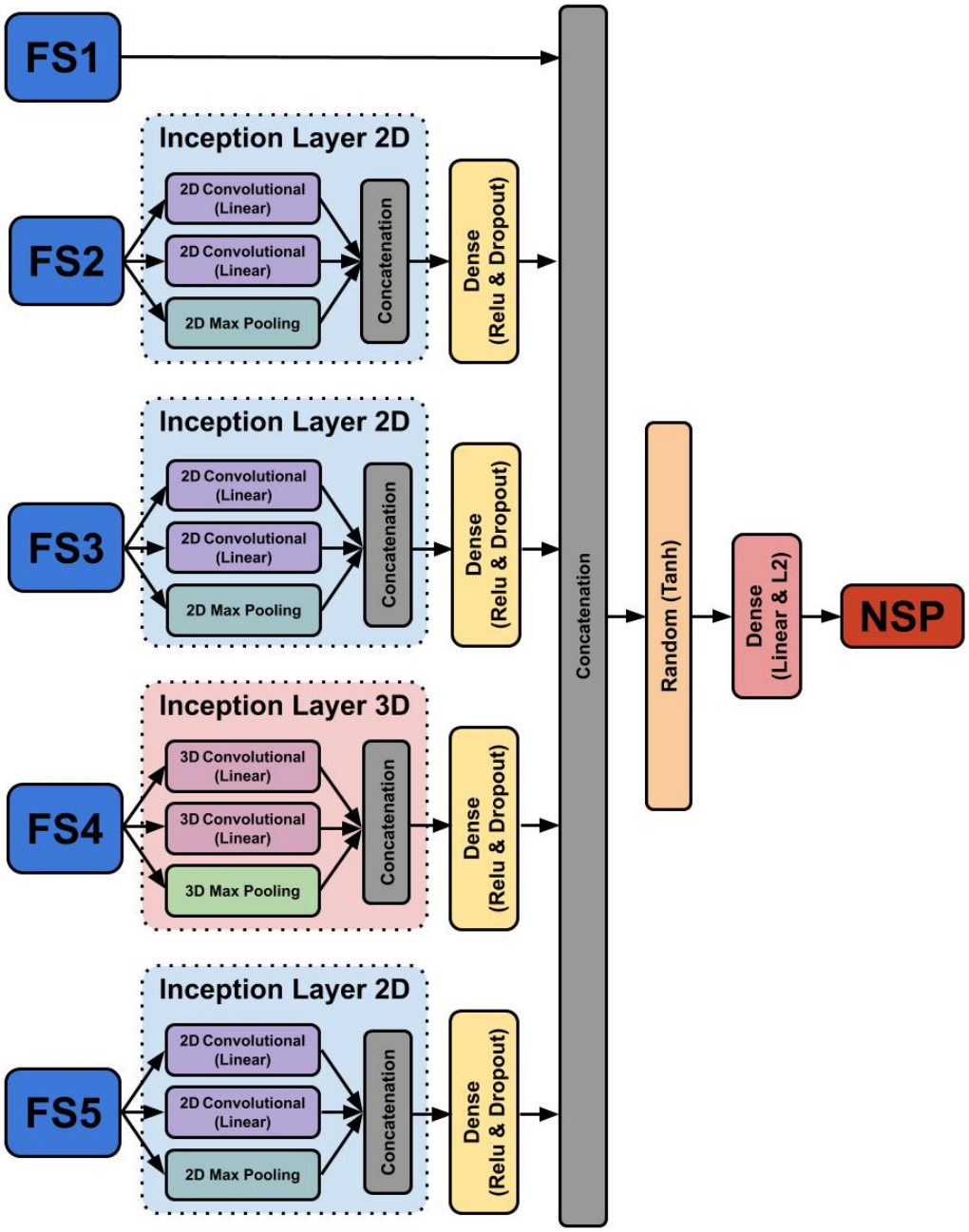

Figure A.11: Proposed DDM architecture.

BTS procedure and consequently $s = 100$, if $l = n$ and the resampling must be done with replacement (Oneto, 2020).

A.2 Hybrid Models

The problem that is addressed here is how to construct a model able to both take into account the physical knowledge about the problem encapsulated in the PMs of Section 9.2 and the information hidden in the available data described in Section 9.1 as the DDMs of Section A.1. For this reason the proposed HM is a combination of the PM and the DDM.

In order to reach this goal different approaches exist (see e.g. Coraddu et al.

(2018) and Coraddu, Baldi, and Anguita (2017)) but all these methods have been developed in the context of conventional DDMs (like the KLRS mentioned above) and not for advance DDMs (es the one based on DNNs described in Section A.1). In fact, for conventional DDMs there are many ways of including the knowledge encapsulated in the PMs. For example, in Coraddu et al. (2018) and Coraddu, Baldi, and Anguita (2017) authors simply add to the input space of the DDMs the prediction of the PMs, while in Coraddu, Baldi, and Anguita (2017) and Section 8.4 authors tried to build a model able to contemporary learn the target task and how the PMs behave.

These different flavours of HMs, for conventional DDMs, are due to the fact that the model functional form for conventional DDMs cannot be arbitrary modified without compromising their ability to effectively and efficiently learn from data or weakening they theoretical properties (Shalev-Shwartz and Ben-David, 2014; Goodfellow, Bengio, and Courville, 2016). Vice versa, the architecture of the advanced DDMs based on DNNs described in Section A.1 can be easily and almost arbitrary modified to meet the requirements of the particular application. Moreover, different ways of changing the architecture may results in the same effect because of the nature of the functional form of these DDMs, and for this reason the simplest solution can be chosen.

For example, in the case under examination, it could be possible to change the architecture of the proposed DDM depicted in Figure A.11 using the two main different philosophies introduced in Coraddu et al. (2018) and Coraddu, Baldi, and Anguita (2017) which consists in:

I changing the FS, namely the input space, or

II force the DDMs to learn contemporary the NSPs and the PMs, namely change the output space.

For what concerns the Option II the modification is trivial while the Option I is not as much trivial as it may seem since it is required to define where and how the prediction of the PMs should be fed to the DDM. Since the PMs already provide a good approximation of the propeller characteristic, in this particular case an actual NSP approximation, the most natural choice would be to consider this information at the same level of the FS1 that need to be fed to the layer which condensates all the information about the different FSs in order to improve its representativity. But such a choice is somehow equivalent to change the output space of the DDM since this would result in a consistent change of the last layers of the DDMs (in particular the expressivity, of size, of the random layer) (Goodfellow, Bengio, and Courville, 2016). Since these two modifications, in the proposed DDM, would have a similar effect, the Option I is used since it affects more directly the last layers, not influencing the other ones. The result is the HM architecture depicted in Figure A.12, where is underlined, for simplicity, the differences between the DDMs of Figure A.11 and the proposed HM.

Note that the HMs can be built just for the NSP for which a PM is provided, able to estimate all, or just a subset, of the parameters of the NSP. Hence, in this case, the HM can be defined just for all the NSPs (see Table 9.3).

Note also that the hyperparameters of the architecture, also for the HMs, need to be tuned with the same procedure described in Section A.1 for the DDMs, and that the set of hyperparameters tuned during the MS phase is the same as those of the DDMs.

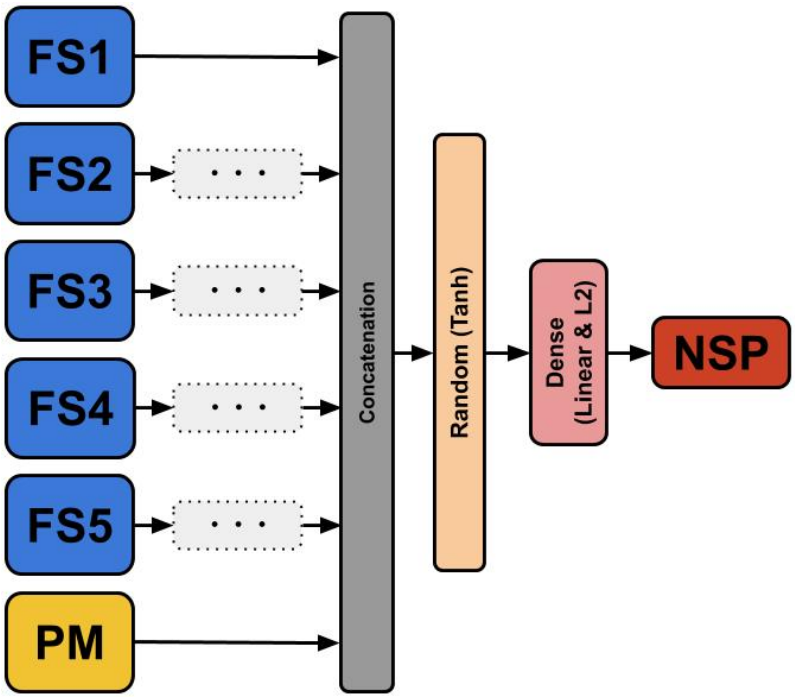

Figure A.12: DNN-based HM architecture (see Figure A.11 for the missing pieces).

References

Agrawal, R., Mannila, H., Srikant, R., Toivonen, H., and Verkamo, A. I. (1996). "Fast discovery of association rules." In: *Advances in knowledge discovery and data mining* 12.1, pp. 307–328.

Aktas, B. (2017). "A systematic experimental approach to cavitation noise prediction of marine propellers". PhD thesis. Newcastle University.

Argyriou, A., Evgeniou, T., and Pontil, M. (2008). "Convex multi-task feature learning". In: *Machine Learning* 73.3, pp. 243–272.

Arndt, R. E. A. and Ippen, A. T. (1968). "Rough surface effects on cavitation inception". In: *Journal of Basic Engineering* 90.2, pp. 249–261.

Arndt, R.E.A. and Maines, B.H. (1998). "Nucleation and bubble dynamics in vortical flows". In: pp. 143–148.

Bakker, B. and Heskes, T. (2003). "Task clustering and gating for bayesian multitask learning". In: *Journal of Machine Learning Research* 4, pp. 83–99.

Baxter, J. (2000). "A model of inductive bias learning". In: *Journal of artificial intelligence research* 12, pp. 149–198.

Bhagwat, M. J. and Ramasamy, M. (2012). "Effect of tip vortex aperiodicity on measurement uncertainty". In: *Experiments in Fluids* 53.5, pp. 1191–1202.

Billet, M. L. and Holl, J. W. (1979). "Scale Effects on Viscous Types of Limited Cavitation". In: *International Symposium on Cavitation Inception*, pp. 2–7.

Bishop, C. M. (2006). *Pattern recognition and machine learning*. Springer Science + Business Media.

Blake, W.K. (1984). *Aero-Hydroacoustics for Ships*. Report No. 84/010. Vol. 1 and 2. Bethesda, MD: David W. Taylor Naval Ship Research and Development Center.

Bosschers, J. (2007). "Broadband hull pressure fluctuations and cavitating vortices: an investigation of resonance frequencies". In: *Marine Engineering Forum, Propeller Cavitation Workshop*.

Bosschers, J. (2009). "Investigation of hull pressure fluctuations generated by cavitating vortices". In: *Proc. First Symposium on Marine Propulsors*.

Bosschers, J. (2018a). "A Semi-Empirical Prediction Method for Broadband Hull-Pressure Fluctuations and Underwater Radiated Noise by Propeller Tip Vortex Cavitation". In: *Journal of Marine Science and Engineering* 6.2, p. 49. DOI: 10.1016/j.ijmultiphaseflow.2018.03.021. URL: https://doi.org/10.1016/j.ijmultiphaseflow.2018.03.021.

Bosschers, J. (2018b). "An analytical and semi-empirical model for the viscous flow around a vortex cavity". In: *International Journal of Multiphase Flow* 105, pp. 122–133. DOI: 10.1016/j.ijmultiphaseflow.2018.03.021. URL: https://doi.org/10.1016/j.ijmultiphaseflow.2018.03.021.

Bosschers, J., Janssen, A.A., and Hoeijmakers, H.W.M. (2008). "Similarity solutions for viscous cavitating vortex cores". In: *Journal of Hydrodynamics, Ser. B* 20.6, pp. 679–688.

Boyd, S. and Vandenberghe, L. (2004). *Convex optimization*. Cambridge university press.

Briançon, L., Fournier, P., and Fréchou, D. (2013). "Marine propeller noise measurements techniques in hydroacoustics tunnel". In: *The 3rd International Conference on Advanced Model Measurement Technology for EU Maritime Industry, Gdansk, Poland*.

Brown, N.A. (1976). "Cavitation noise problems and solutions". In: *Proceedings of International Symposium on Shipboard Acoustics, Noordwijkehout, the Netherlands*.

Buist, J. (1993). "On the origin and acoustical behaviour of cloud cavitation." In:

Campos, J. A. C. Falcão de (1992). "Laser-doppler velocity measurements on tip vortices in non-cavitating and cavitating conditions". In: *ASME FED* 135.

Carlton, J. (2007). *Marine propellers and propulsion*. Butterworth-Heinemann.

Caruana, R. (1997). "Multitask Learning". In: *Machine Learning* 28.1, pp. 41–75.

Cipollini, F., Oneto, L., Coraddu, A.a, Murphy, A. J., and Anguita, D. (2018). "Condition-based maintenance of naval propulsion systems: Data analysis with minimal feedback". In: *Reliability Engineering & System Safety* 177, pp. 12–23.

Coraddu, A., Kalikatzarakis, M., Oneto, L., Meijn, G. J., Godjevac, M., and Geertsmad, R. D. (2018). "Ship diesel engine performance modelling with combined physical and machine learning approach". In: *International Naval Engineering Conference and Exhibition*.

Coraddu, A., Oneto, L., Baldi, F., and Anguita, D. (2017). "Vessels fuel consumption forecast and trim optimisation: a data analytics perspective". In: *Ocean Engineering* 130, pp. 351–370.

Coraddu A. Oneto, L., Baldi, F., and Anguita, D. (2017). "Vessels Fuel Consumption Forecast and Trim Optimisation: a Data Analytics Perspective". In: *Ocean Engineering* 130, pp. 351–370.

Council of European Union (2008). *MSFD 2008/56/EC*. `https://eur-lex.europa.eu/legal-content/EN/TXT/?uri=CELEX:32008L0056`.

Cristianini, N. and Shawe-Taylor, J. (2000). *An introduction to support vector machines and other kernel-based learning methods*. Cambridge university press.

Daily, J. W. (1956). "Turbulence and boundary layer effects on cavitation inception from gas nuclei". In: *Trans. ASME* 78, pp. 1695–1706.

Efron, B. and Tibshirani, R. J. (1994). *An introduction to the bootstrap*. CRC press.

Evgeniou, T. and Pontil, M. (2004). "Regularized multi-task learning". In: *ACM SIGKDD international conference on Knowledge discovery and data mining*.

Fitzpatrick, H.M. and Strasberg, M. (1956). "Hydrodynamic sources of sound". In: *Proc. First ONR Symp. on Naval Hydrodynamics*, pp. 241–280.

François, D., Wertz, V., and Verleysen, M. (2006). "The permutation test for feature selection by mutual information." In: *European Symposium on Artificial Neural Networks, Computational Intelligence and Machine Learning*.

Fujiyama, K. and Nakashima, Y. (2017). "Numerical Prediction of Acoustic Noise Level Induced by Cavitation on Ship Propeller at Behind-Hull Condition". In: *Fifth International Symposium on Marine Propulsors (smp'17), Espoo, Finland*.

Gaggero, S., Tani, G., Viviani, M., and Conti, F. (2014). "A study on the numerical prediction of propellers cavitating tip vortex". In: *Ocean engineering* 92, pp. 137–161.

Gerz, T., Holzäpfel, F., Bryant, W., Köpp, F., Frech, M., Tafferner, A., and Winckelmans, G. (2005). "Research towards a wake-vortex advisory system for optimal aircraft spacing". In: *Comptes Rendus Physique* 6.4-5, pp. 501–523.

Ghelardoni, L., Ghio, A., and Anguita, D. (2013). "Energy load forecasting using empirical mode decomposition and support vector regression". In: *IEEE Transactions on Smart Grid* 4.1, pp. 549–556.

Good, P. (2013). *Permutation tests: a practical guide to resampling methods for testing hypotheses*. Springer Science & Business Media.

Goodfellow, I., Bengio, Y., and Courville, A. (2016). *Deep learning*. MIT press.

Guyon, I. and Elisseeff, A. (2003). "An introduction to variable and feature selection". In: *The Journal of Machine Learning Research* 3, pp. 1157–1182.

He, K., Zhang, X., Ren, S., and Sun, J. (2015). "Delving deep into rectifiers: Surpassing human-level performance on imagenet classification". In: *IEEE international conference on computer vision*.

Hommes, T., Bosschers, J., and Hoeijmakers, H. W. M. (2015). "Evaluation of the radial pressure distribution of vortex models and comparison with experimental data". In: *Journal of Physics: Conference Series* 656, p. 012182.

IMO MEPC.1/Circ.833 (2014). *Guidelines for the reduction of underwater noise from commercial shipping to address adverse impacts on marine life*. London.

ISO 17208-1:2016 (2016). *Underwater acoustics — Quantities and procedures for description and measurement of underwater sound from ships — Part 1: Requirements for precision measurements in deep water used for comparison purposes*. `https://www.iso.org/standard/62408.html`.

ISO 17208-2:2019 (2019). *Underwater acoustics — Quantities and procedures for description and measurement of underwater sound from ships — Part 2: Determination of source levels from deep water measurements*. `https://www.iso.org/standard/62409.html`.

ITTC Propulsion Committee (2008). *Model Manufacture, Propeller Models Terminology and Nomenclature for Propeller Geometry*. Recommended Procedures and Guidelines 7.5-01-02-01. International Towing Tank Conference.

ITTC Specialist Committee on Hydrodynamic Noise (2014). *Final report and recommendations to the 27th ITTC*. Recommended Procedures and Guidelines. International Towing Tank Conference, pp. 1–45.

ITTC Specialist Committee on Hydrodynamic Noise (2017). *Model-Scale Propeller Cavitation Noise Measurements*. Recommended Procedures and Guidelines 7.5-02-01-05. International Towing Tank Conference.

ITTC Specialist Committee on Water Quality and Cavitation (2002). *Final Report and Recommendations to the 23rd ITTC*. Recommended Procedures and Guidelines. International Towing Tank Conference.

Jain, A. K. and Dubes, R. C. (1988). "Algorithms for clustering data". In: *Englewood Cliffs: Prentice Hall, 1988*.

Jessup, S.D. (1989). "An experimental investigation of viscous aspects of propeller blade flow". In: *PhD. Thesis, the Catholic University of America*.

Kasun, L. L. C., Zhou, H., Huang, G. B., and Vong, C. M. (2013). "Representational learning with extreme learning machine for big data". In: *IEEE intelligent systems* 28.6, pp. 31–34.

Keller, A. P. (1984). "Scale effects at beginning cavitation applied to submerged bodies". In: *Proceedings of the ASME international symposium on cavitation inception*.

Kohavi, R. et al. (1995). "A study of cross-validation and bootstrap for accuracy estimation and model selection". In: *International Joint Conference on Artificial Intelligence*.

Korkut E., Atlar M. (2000). "On the Importance of Effect of Turbulence in Cavitation Inception Tests of Marine Propellers". In: *Proceedings of Royal Society of London: Mathematical, Physical and Engineering Sciences* 458, pp. 29–48.

Kuiper, G. (1978). "Scale effects on propeller cavitation inception". In: *Twelfth International Symposium on Naval Hydrodynamics*, pp. 401–429.

Kuiper, G. (1981). "Cavitation Inception on Ship Propeller Models, Doctor's Thesis". PhD thesis.

Kuiper, G. (2001). "New developments around sheet and tip vortex cavitation on ships' propellers". In: *Fourth international symposium on cavitation, CAV 2001, California Institute of Technology, Pasadena*.

Kuwahara, K. and Takami, H. (1973). "Numerical studies of two-dimensional vortex motion by a system of point vortices". In: *Journal of the Physical Society of Japan* 34.1, pp. 247–253.

Lafeber, F. H., Bosschers, J., and van Wijngaarden, E. (2015). "Computational and experimental prediction of propeller cavitation noise". In: *OCEANS 2015-Genova*. IEEE, pp. 1–9.

Lagarias, J. C., Reeds, J. A., Wright, M. H., and Wright, P. E. (1998). "Convergence properties of the Nelder–Mead simplex method in low dimensions". In: *SIAM Journal on optimization* 9.1, pp. 112–147.

Lamb, H. (1932). "Hydrodynamics". In: *Cambridge University Press* 427.

Li, D., Hallander, J., and Johansson, T. (2018). "Predicting underwater radiated noise of a full scale ship with model testing and numerical methods". In: *Ocean Engineering* 161, pp. 121–135.

Liu, H. and Motoda, H. (2007). *Computational methods of feature selection*. CRC Press.

Lovik, A. (1981). *Scaling of propeller cavitation noise*. Nordforsk, Sweden.

Mack, L. M. (1977). "Transition prediction and linear stability theory". In: *AGARD conference proceedings*. 224, pp. 1–22.

Maines, B. and Arndt, R.E.A. (1997). "The case of the singing vortex". In: *Journal of fluids engineering* 119.2, pp. 271–276.

Matusiak, J. (1992). "Pressure and noise induced by a cavitating marine screw propeller". PhD thesis. Helsinki University of Technology.

McCormick, B. W. (1962). "On cavitation produced by a vortex trailing from a lifting surface". In: *Journal of Basic Engineering* 84.3, pp. 369–378.

Minnaert, M. (1933). "On musical air-bubbles and the sounds of running water". In: *J. Sci* 16, pp. 235–248.

Moore, D.W. and Saffman, P.G. (1973). "Axial flow in laminar trailing vortices". In: *Proceedings of the Royal Society of London. A. Mathematical and Physical Sciences* 333.1595, pp. 491–508.

Morozov, V.P. (1974). "Theoretical analysis of the acoustic emission from a cavitating line vortices". In: *Soviet physics acoustic-USSR* 19.5, pp. 468–471.

Norwood, C. *Noise from vessels and its control*. Tech. rep. Teaching materials, Defense Science and Technology Organization, Australia.

Odabaşi, A. Y. and Fitzsimmons, P.A. (1978). "Alternative methods for wake quality assessment". In: *International Shipbuilding Progress* 25.282, pp. 34–42.

Oneto, L. (2018). "Model Selection and Error Estimation Without the Agonizing Pain". In: *WIREs Data Mining and Knowledge Discovery* 8.4, e1252.

Oneto, L. (2020). *Model Selection and Error Estimation in a Nutshell*. Springer.

Pardalos, P. M. and Romeijn, H. E. (2013). *Handbook of global optimization*. Vol. 2. Springer Science & Business Media.

Pennings, P., Westerweel, J., and van Terwisga, T. (2016). "Cavitation tunnel analysis of radiated sound from the resonance of a propeller tip vortex cavity". In: *International Journal of Multiphase Flow* 83, pp. 1–11.

Pennings, P.C., Bosschers, J., Westerweel, J., and van Terwisga, T.J.C. (2015). "Dynamics of isolated vortex cavitation". In: *Journal of Fluid Mechanics* 778, pp. 288–313.

Pennings, P.C., Westerweel, J., and van Terwisga, T.J.C. (2015). "Flow field measurement around vortex cavitation". In: *Experiments in Fluids* 56.11, pp. 149–198. DOI: 10.1007/s00348-015-2073-9. URL: https://doi.org/10.1007/s00348-015-2073-9.

Petersen, J. P., Winther, O., and Jacobsen, D. J. (2012). "A machine-learning approach to predict main energy consumption under realistic operational conditions". In: *Ship Technology Research* 59.1, pp. 64–72.

Pino, C. del, Parras, L., Felli, M., and Fernandez-Feria, R. (2011). "Structure of trailing vortices: Comparison between particle image velocimetry measurements and theoretical models". In: *Physics of Fluids* 23.1, p. 013602. DOI: 10.1063/1.3537791. URL: https://doi.org/10.1063/1.3537791.

Plesset, M. S. and Chapman, R. B. (1971). "Collapse of an initially spherical vapour cavity in the neighbourhood of a solid boundary". In: *Journal of Fluid Mechanics* 47.2, pp. 283–290.

Proctor, F., Ahmad, N., Switzer, G., and Limon Duparcmeur, F. (2010). "Three-phased wake vortex decay". In: *AIAA Atmospheric and Space Environments Conference*, pp. 79–91.

Raestad, A.E. (1996). "Tip vortex index - an engineering approach to propeller noise prediction". In: *The Naval Architect*, pp. 11–15.

Raschka, S. *Predictive modeling, supervised machine learning, and pattern classification*. https://sebastianraschka.com/Articles/2014_intro_supervised_learning.html.

Rosasco, L., De Vito, E., Caponnetto, A., Piana, M., and Verri, A. (2004). "Are loss functions all the same?" In: *Neural Computation* 16.5, pp. 1063–1076.

Ross, D. (1976). *Mechanics of Underwater Noise*. Peninsula Publishing.

Russ, J. C. (2016). *The image processing handbook*. CRC press.

Scholkopf, B. (2001). "The kernel trick for distances". In: *Advances in neural information processing systems*.

Schölkopf, B., Herbrich, R., and Smola, A. J. (2001). "A generalized representer theorem". In: *Computational learning theory*.

Shalev-Shwartz, S. and Ben-David, S. (2014). *Understanding machine learning: From theory to algorithms*. Cambridge university press.

Shawe-Taylor, J. and Cristianini, N. (2004). *Kernel methods for pattern analysis*. Cambridge university press.

Shen, Y.T., Gowing, S., and Jessup, S.D. (2009). "Tip vortex cavitation inception scaling for high Reynolds number applications". In: *Journal of Fluids Engineering* 131.7.

Smith, T. W. P., O'Keeffe, E., Aldous, L., and Agnolucci, P. (2013). "Assessment of Shipping's Efficiency Using Satellite AIS data". In: *International Council on Clean Transportation*.

Szegedy, C., Ioffe, S., Vanhoucke, V., and Alemi, A. A. (2017). "Inception-v4, inception resnet and the impact of residual connections on learning". In: *AAAI Conference on Artificial Intelligence*.

Tang, J., Deng, C., and Huang, G.-B. (2016). "Extreme learning machine for multilayer perceptron". In: *IEEE transactions on neural networks and learning systems* 27.4, pp. 809–821.

Tani, G. (2015). "Experimental Study of Cavitating Propeller Radiated Noise". PhD thesis. University of Genoa.

Tani, G., Viviani, M., Ferrando, M., and Armelloni, E. (2019). "Aspects of the measurement of the acoustic transfer function in a cavitation tunnel". In: *Applied Ocean Research* 87, pp. 264–278.

Tani, G., Viviani, M., Villa, D., and Ferrando, M. (2017). "A study on the influence of hull wake on model scale cavitation and noise tests for a fast twin screw vessel with inclined shaft". In: London, England: SAGE Publications.

Thomson, W. (1880). "Vibrations of a columnar vortex". In: *Proceedings of the Royal Society of Edinburgh*.

Tibshirani, R. (1996). "Regression shrinkage and selection via the lasso". In: *Journal of the Royal Statistical Society: Series B (Methodological)* 58.1, pp. 267–288.

Tietjens, O. K. G. and Prandtl, L. (1957). *Applied hydro-and aeromechanics*. Vol. 2. Courier Corporation.

Tikhonov, A. N. and Arsenin, V. Y. (1979). *Methods for solving ill-posed problems*. Nauka, Moscow.

Urick, R. J. (1983). "Principles of underwater sound 3rd edition". In: *Peninsula Publising Los Atlos, California*.

van Rijsbergen, M.X. and van Terwisga, T.J.C. (2010). "Water quality effects on sheet cavitation inception on a ship propeller model". In: *Seventh International Conference on Multiphase Flow*.

van Wijngaarden, E., Bosschers, J., and Kuiper, G. (2005). "Aspects of the cavitating propeller tip vortex as a source of inboard noise and vibration". In: *ASME 2005 Fluids Engineering Division Summer Meeting*. American Society of Mechanical Engineers Digital Collection, pp. 539–544.

van Wijngaarden, L. (1994). "Bubble dynamics and the sound emitted by cavitation". In: *Bubble Dynamics and Interface Phenomena*. Springer, pp. 181–193.

Vapnik, V. N. (1998). *Statistical learning theory*. Wiley New York.

Vatistas, G. H., Kozel, V., and Mih, W.C. (1991). "A simpler model for concentrated vortices". In: *Experiments in Fluids* 11.1, pp. 73–76.

Young, D. M. (2003). *Iterative solution of large linear systems*. DoverPublications.

Zou, H. and Hastie, T. (2005). "Regularization and variable selection via the elastic net". In: *Journal of the royal statistical society: series B (statistical methodology)* 67.2, pp. 301–320.